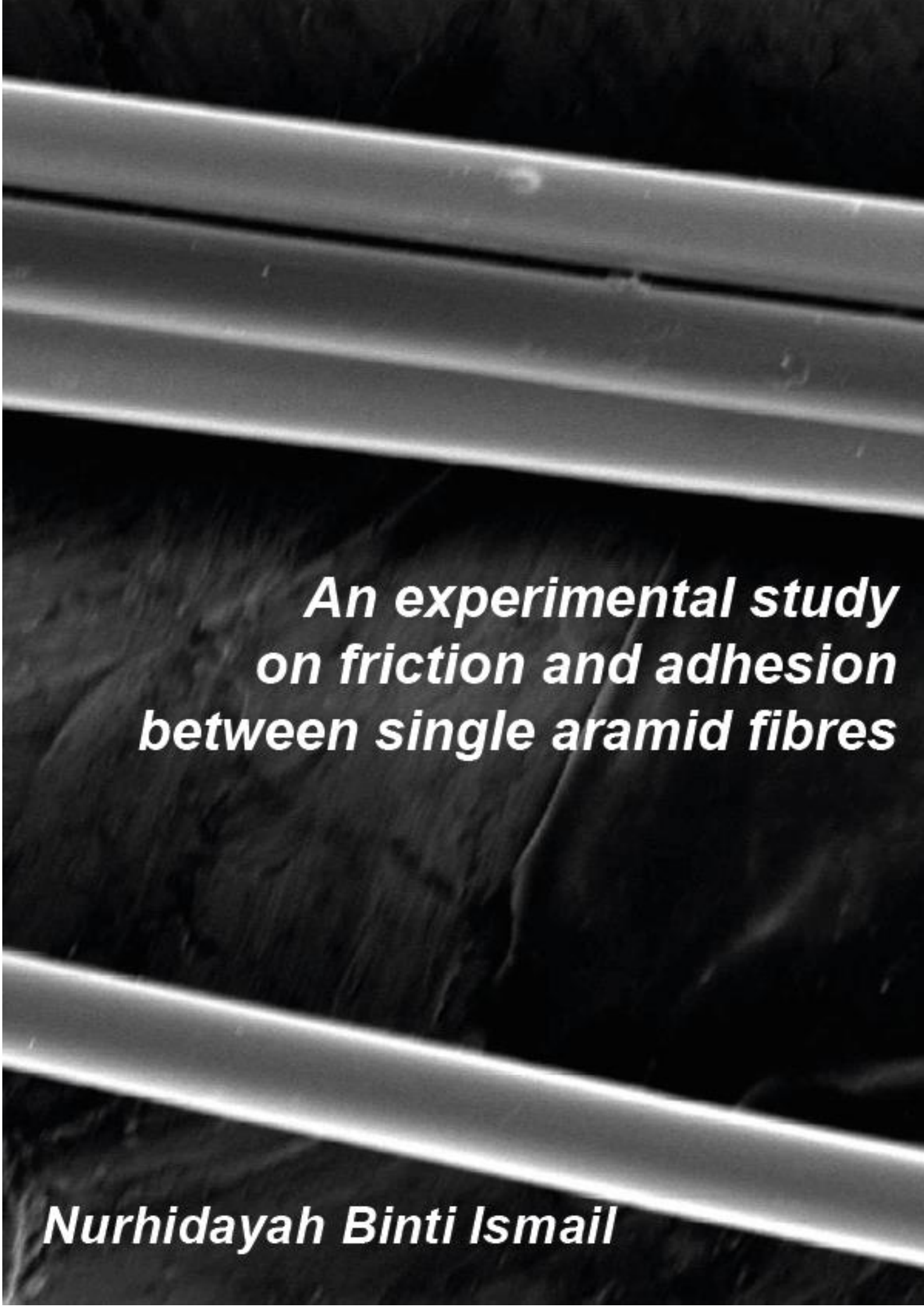

An experimental study on friction and adhesion between single aramid fibres

Nurhidayah Binti Ismail

An Experimental Study on Friction and Adhesion between Single Aramid Fibres

Nurhidayah Binti Ismail

AN EXPERIMENTAL STUDY ON FRICTION AND ADHESION BETWEEN SINGLE ARAMID FIBRES

DISSERTATION

to obtain
the degree of doctor at the University of Twente,
on the authority of the rector magnificus,
prof.dr. T.T.M. Palstra,
on account of the decision of the Doctorate Board,
to be publicly defended
on Friday the 21st of December 2018 at 12:45 hours

by

Nurhidayah Binti Ismail

born on the 14th of January 1985
in Terengganu, Malaysia

This dissertation has been approved by:

Supervisor:
dr. ir. M.B de Rooij
Co-supervisor:
prof. dr. ir. D.J Schipper

Cover design: Nurhidayah Binti Ismail
Printed by: Gilderprint, Enschede, The Netherlands
ISBN:978-90-365-4596-9
DOI:10.3990/1.9789036545969

GRADUATION COMMITTEE:

Chairman/secretary	Prof. dr. G.P.M.R Dewulf (University of Twente)
Supervisor	Dr. ir. M.B de Rooij (University of Twente)
Co-supervisor	Prof. dr. ir. D.J Schipper (University of Twente)
Members	Prof. dr. ir. R Akkerman (University of Twente)
	Prof. dr. ir. A Blume (University of Twente)
	Assoc. prof. dr. M.F.B Abdollah (Universiti Teknikal Malaysia Melaka)
	Prof. ir. dr. J.B A Ghani (The National University of Malaysia)
	Prof. dr. A Matthews (The University of Manchester)

Acknowledgement

First of all, I would like to take this opportunity to give a special appreciation to my supervisor, Dr.ir. Matthijn B. de Rooij for the guidance, courage, patience and constant support. I will always be grateful with the opportunity given to do a PhD under his supervision. I have learnt so many things during this four-year journey. His priceless comments and suggestions have made the completed of this thesis.

Special thanks also go to my co-supervisor, prof.dr.ir. Dik J. Schipper who always there to channel everything into a smooth journey. Thanks for being the person that cares about my research needs.

I would also like to express my gratitude to Erik and Walter for helping me out with the lab setup and always been there whenever I have problem with the measurements and setup. Their technical expertise and enthusiasm have really amazed me. It has been a pleasure to work with both of you. Also, not to forget my deep appreciation to Ivo and Dries who help me with the lab training. Not to forget, I also want to express my gratitude to Belinda and Debbie for their administration help.

My appreciation also goes to Bo Cornelissen and his colleagues from Teijin Aramid BV. I really appreciate their knowledge and expertise and not to forget the fruitful discussions on the related topic. To Hubert and prof. Julius Vancso, thank you for the collaboration. I really appreciate with all the scientific discussions that we had during this journey.

Special thanks also go to all the members of Surface Technology and Tribology group including Emile, Rob, Xavi, Mohammad, Tanmaya, Hilwa, Khafidh, Marina, Aydar, Shivam, Dominic, Melkamu, Yuxin, Ying Lei, Qangqiang, Michel, Matthijs, Yibo, and Febin. As a beginner in this field, I really appreciate all of your kindness especially from Hilwa, Xavi, Mohammad and Tanmaya in helping me with the coding and simulations. Thanks also to Hasib and Luigi who help me with the SEM.

I will never forget my UTeM colleagues who always help me with technical and scientific support. Their motivation keeps me stay strong to finish my PhD. Thanks a lot to Fadhilah who always find a time to review my papers and your comments really help me a lot. Also, thank you to Kak Bib, Mas, Wani, Kak Anum and Fathiah. Not to

forget, the new friends which I met during this journey; Kak Im and family, Mba Lulu, Mba Ratna, Mba Heksi, Mba Dwi, Mba Siti, Mba Sari, Ratri and her mother Ibu, and many others.

To my dearest husband, I really appreciate all the things that you have done along this year. Leaving your master's degree behind, just to be with me here in Enschede. Thank you for your love, trust, support and encouragement. I hope this piece of work will keep us remind all the tests and great loss that we had during this journey and how we both stay strong together. To my loving *Ma* and *Aboh*, thank you for all the supports and prayers. I hope you both will always be proud with me. Finally, I also would like to thank to my brother and sisters who have encouraged me in whatever I do.

Summary

Friction and adhesion properties between fibres is of great importance as it affects both the physical and mechanical performance of end products made from these fibres. At micro and nanoscale, friction and adhesion phenomena are driven primarily by a high volume-to surface ratio. Thus, understanding the mechanism of friction and adhesion between fibres is needed, for example to predict the mechanical behaviour of composites or fibrous structures. This thesis therefore addresses fundamental knowledge of the friction and adhesion behaviour between single aramid fibres.

A review of the experimental approach concerning friction and adhesion between single fibres is presented. It is shown that the principle of the linear motion method is the most suitable method that can be adapted to develop an experimental setup for measuring the friction and adhesion between single fibres.

Since the contribution of the surface physical properties is one of the important factors influencing the friction and adhesion, the wetting and surface energy of single aramid fibre is also studied. The surface energy is determined from the dynamic contact angle measurements using Wilhelmy's method. It is shown that the surface energy of aramid fibres is polar in character, exhibiting hydrophilic behaviour.

The influence of the parameters such as pre-tension load, fibre orientation (crossing angle), normal load and elastic modulus on the friction force is studied. A taut wire model is used to formulate the contact length between contacting fibre surfaces in perpendicular contact. With this model, the deflection of the fibre as well as the contact intimacy between fibres can be calculated and related to the measured friction force. However, it is found that the 'wrapping effect' due to pre-tension is small in comparison with the elastic deformation in contact. In an elliptical contact, it is found the role of pre-tension is relatively small and friction and contact area between fibres are dominated by the effect of fibre orientation (crossing angle). Generally the friction force decreases as the crossing angle increases. The Hertzian elliptical contact model is used to explain the changing size of the contact area due to the fibre orientations. Assuming the interfacial strength at the contact area is constant, the predicted friction force is in agreement with the measured friction force.

Further, the adhesion force between single fibres is explained using experiments and models. The effect of relative humidity and fibre orientation (crossing angle) on adhesion force is determined. At a relative humidity of 50%, the adhesion force shows a significant increase. The Young- Laplace and Kelvin equations are used to predict the adhesion force. At very low humidity levels (~8%), the adhesion force is reducing with increasing crossing angle. The contribution of the contact area due to the crossing angle effect is assessed using the JKR elliptical adhesive contact model. The experimental data fits with the model by considering the roughness effect as a scaling factor. However, in ambient conditions (~40% relative humidity), the adhesion force shows a minimum value at about 40° crossing angle due to the capillary torque.

In short, friction and adhesion between single aramid fibres have been explored successfully. Studies show that the role of the contact area between two contacting fibres is highly important in influencing the friction and adhesion force values.

Samenvatting

Wrijving en hechtingseigenschappen tussen vezels is van groot belang omdat het zowel de fysische als mechanische prestaties van eindproducten, gemaakt van deze vezels, beïnvloedt. Op micro- en nanoschaal worden wrijving en adhesie vooral veroorzaakt door een hoge oppervlakte-tot-volume verhouding. Meer kennis met betrekking tot het mechanisme van wrijving en adhesie tussen onderlinge vezels is dus nodig, bijvoorbeeld om het mechanisch gedrag van composieten of vezelachtige structuren te voorspellen. Dit proefschrift omvat fundamentele kennis met betrekking tot het wrijvings- en adhesiegedrag tussen aramidevezels.

Een overzicht van de experimentele benadering met betrekking tot wrijving en adhesie tussen afzonderlijke vezels wordt gepresenteerd. Het is aangetoond dat het principe van de lineaire bewegingsmethode een geschikte methode is die kan worden toegepast om een experimentele opstelling, voor het meten van de wrijving en adhesie tussen afzonderlijke vezels, te ontwikkelen.

Aangezien de bijdrage van de fysische eigenschappen van het oppervlak één van de belangrijke factoren is die de wrijving en adhesie beïnvloeden, worden ook de relatieve vochtigheid en de oppervlakte-energie van een enkelvoudige aramidevezel bestudeerd. De oppervlakte-energie wordt bepaald met behulp van de dynamische contacthoekmetingen die gebaseerd zijn op de Wilhelmy-methode. Het is aangetoond dat de oppervlakte-energie van aramidevezels meestal polair van karakter is en een hydrofiel gedrag vertoont.

De invloed van de parameters zoals voorspanning, vezeloriëntatie (onderlingehoek), normale belasting en elasticiteitsmodulus, op de wrijvingskracht, wordt bestudeerd. Een strak draadmodel is gebruikt om de contactlengte, tussen contact makende vezeloppervlakken die loodrecht staan op elkaar, te berekenen. Met dit model kunnen de afbuiging van de vezel en de contactcondities tussen vezels worden berekend en worden gerelateerd aan de gemeten wrijvingskracht. Er wordt aangetoond dat de grafische weergave tussen de wrijvingskracht en de voorspanning, en de grafisch weergave tussen het contactgebied en de voorspanning, een vergelijkbaar gedrag vertonen. Dit toont aan dat bij loodrecht contact de voorspanning de vezelbuigstijfheid, contactlengte - en hiermee dus ook - de wrijving beïnvloed. Bij een elliptisch contact is echter gebleken dat de

voorspanning relatief klein is en de wrijving en het contactoppervlak tussen de vezels worden gedomineerd door het effect van vezeloriëntatie (onderlingehoek). Over het algemeen neemt de wrijvingskracht af met het toenemen van de onderlingehoek. Het elliptisch contactmodel van Hertz wordt gebruikt om de veranderende grootte van het contactoppervlak als gevolg van de vezeloriëntatie uit te leggen. Aangenomen dat de afschuifsteihte in het contactgebied constant is, is de voorspelde wrijvingskracht in overeenstemming met de gemeten wrijvingskracht.

Verder wordt de adhesiekracht tussen enkele vezels verklaard aan de hand van experimenten en modellen. Het effect van de relatieve vochtigheid en vezeloriëntatie op de adhesiekracht is bepaald. Bij een relatieve vochtigheid van ~ 50% en meer vertoont de adhesiekracht een aanzienlijke toename. De Young-Laplace- en Kelvin - vergelijkingen worden gebruikt om de adhesiekracht te voorspellen. Bij zeer lage luchtvochtigheidsniveaus (~ 8%) neemt de adhesiekracht af met toenemende onderlingehoek. De bijdrage van het contactgebied als gevolg van het onderlingehoekeffect wordt beoordeeld met behulp van het JKR elliptisch adhesie contactmodel. De experimentele data is in overeenstemming met datgene voorspeld door het model, door het ruwheidseffect als een schaalfactor te beschouwen. Bij omgevingsomstandigheden (~ 40% relatieve luchtvochtigheid) vertoont de adhesiekracht echter een minimale waarde bij een onderlingehoek van ongeveer 40° ten gevolge van het capillair moment.

Samenvattend, zijn de wrijving en adhesie tussen enkele aramidevezels met succes onderzocht. Studies tonen aan dat de rol van het contactoppervlak tussen twee contactvezels van groot belang is bij het beïnvloeden van de wrijvings- en adhesiekrachten.

Nomenclature

Roman symbols

a_{cap}	Contact radius in capillary pressure equation	[m]
a_{ell}	Semi-major axis, elliptical contact	[m]
a_p	Contact radius, point (perpendicular) contact	[m]
A	Contact area	[m]
A_r	Real contact area	[m^2]
A_t	Cross-sectional area in taut wire model	[m^2]
A_{JKR}	Contact area in JKR model	[m^2]
b	Contact width, line contact	[m]
b_{ell}	Semi-minor axis, elliptical contact	[m]
e	Eccentricity ratio in elliptical contact	[-]
d	Linear density	[dtex]
E^*	Contact modulus	[Pa]
E_a	Axial elastic modulus	[Pa]
E_t	Transverse elastic modulus	[Pa]
$E(e), K(e)$	Complete elliptical integral	[-]
F_{adh}	Adhesion force	[N]
$F_{bouyancy}$	Buoyancy force in Wilhelmy equation	[N]
$F_{capillary}$	Capillary force in Wilhelmy equation	[N]
F_s	Surface tension force	[N]
F_p	Capillary pressure force	[N]
$F_{wetting}$	Total wetting force in Wilhelmy equation	[N]
g	Gravitational constant	[m/s^2]
I	Second moment of inertia	[m^4]
k_{ell}	Axis ratio in elliptical contact	[-]
k, n	Constant value in friction force model	[-]
l	Fibre free length	[m]
L_{line}	Contact length, line contact	[m]
m	Fibre line gradient, taut wire model	[-]
N	Normal load	[N]
p_o	Pressure maximum, elliptical contact	[Pa]
p/p_s	Relative humidity in capillary force equation	[%]
P	Ploughing effect in friction model	[N]
P_1	Pressure distribution in JKR model	[Pa]
P_{cap}	Capillary pressure in Laplace equation	[Pa]
r_1, r_2, r_k	Radii curvature in Laplace pressure	[m]
R	Fibre radius	[m]
R^*, R^e	Effective radius	[m]
R_a, R_b	Relative radii of curvature between bodies	[m]
R_g	Gas constant	[J/K mol]
T	Pre-tension load	[N]
T_1, T_2	Capstan tensional force	[N]
T_{abs}	Absolute temperature	[K]
V	Molar volume	[m^3]
$V_{immersed}$	Fibre immersed volume in Wilhelmy equation	[m^3]
x, x_c	Fibre length in cartesian coordinate x-axis in taut wire model	[m]
y, y_c	Fibre length in cartesian coordinate y-axis in taut wire model	[m]

Greek symbols

α	Coefficient in JKR adhesive elliptical contact model	[-]
β	Coefficient in JKR adhesive elliptical contact model	[-]
β_o	Constant value for resistance to bending equation	[-]
$\Delta\delta_x$	Fibre deflection in horizontal direction	[m]
$\Delta\delta_z$	Fibre deflection in vertical direction	[m]
ε	Shape factor for resistance for bending equation	[-]
μ	Coefficient of friction	[-]
θ	Crossing angle	[°]
θ_1, θ_2	Contact angles at solid surface in capillary force equation	[°]
φ	Filling angle	[°]
θ_{wrap}	Capstan method wrapping angle	[°]
θ_{twist}	Twisted method twisting angle	[°]
n_{twist}	Twisted method number of turns	[°]
η	Liquid viscosity	[mPas]
ρ	density	[kg/m^3]
v	Poisson ratio	[-]
ε	Approximate elliptical integral in elliptical contact	[-]
γ	Solid surface energy	[J/m^2]
γ_L	Liquid surface tension	[J/m^2]
γ_{SV}	Interfacial tension between solid and vapor	[J/m^2]
γ_{SL}	Interfacial tension between solid and liquid	[J/m^2]
γ_{LV}	Interfacial tension between liquid and vapor	[J/m^2]
γ_L^d	Dispersive component in liquid surface tension	[J/m^2]
γ_L^p	Polar component in liquid surface tension	[J/m^2]
τ	Shear strength	[Pa]

Abbreviations

AFM	Atomic force microscope
CAH	Contact angle hysteresis
RH	Relative humidity
SEM	Scanning Electron Microscope
VAFT	Vacuum Adhesion Friction Tester

Part A: Thesis

Contents

Chapter 1

Introduction

Aramid fibres are man-made high performance fibres that were first introduced in commercial applications in the early 1960s by DuPont [1]. The term ‘aramid’ is short for ‘aromatic polyamide’. Its popular combination of high strength and high stiffness, as well as the impressive strength-to-weight ratio that is higher than steel, has made the market demand for aramid fibres grow enormously. These fibres are used in many applications such in aerospace and military, for soft and hard ballistics protections, in deep sea and mooring lines for ropes and cables, in cut-protection products and also in heat and flame resistance garments, see Figure 1.1 for some examples.

Figure 1.1 The use of aramid fibre in commercial applications.

From the production of the aramid fibres to the material handling and use, each fibre undergoes several mechanical stresses in contacts with other fibres. One of the important phenomena is friction. In fibre production, friction between fibres is important as it governs

the quality and the efficiency of the fibre during processing such as twisting and winding of yarns, tow spreading, weaving, knitting and braiding of fabrics and forming and finishing of fibre final products. Surface physical properties such as roughness and mechanical properties such as shear, stiffness and strength are also influenced by this interaction. For example, the tensile strength value of the freshly drawn fibre can be reduced due to the rubbing contact between fibres [2]. On top of that, due to this interaction, the fibre could be damaged during material handling and transportation. For a fibre final product such as ropes and cables, an internal interaction between fibres that is induced during its usage may cause undesired structure deformation and hence shorten the structure lifespan.

Therefore, a basic understanding of the fibre interaction is needed as it plays an important role in influencing the structural integrity and the mechanical properties of the fibre as well as the final product. In the following section, fibre interactions in a context of friction and contact are discussed.

1.1 Friction between fibres

Generally, fibres are produced in small threadlike continuous filaments with a typical diameter of 10 μm. Thousands of individual continuous filaments are combined into a tow, while the tows themselves can be woven, braided or stitched together to form a fabric. Figure 1.2 illustrates the hierarchical levels of the fabric structure which can be classified into: (a) macroscale (fabric level), (b) mesoscale (tow level) and (c) microscale (filament level). The development of the final product is achieved through these hierarchical levels, in which the geometry of the construction or assembly is the link between consecutive levels. As a result, friction that occurs at each scale is crucial as it influences the performance of the final product. Several examples are given below to illustrate the friction between fibres.

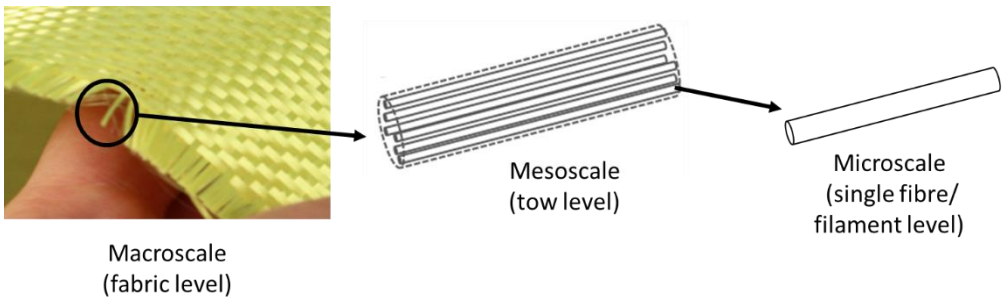

Figure 1.2 The hierarchical levels of fabric structure.

First, in the fibre production process especially during spinning to weaving, the interaction between tows and between tow and machine part can cause fibre defibrillation and can also lead to fibre breakage at filament level. As a result, this interaction can deteriorate the surface properties and the strength at tow and fabric level [3-6].

Second, in Liquid Composite Moulding (LCM), the deformability of the woven fabric is caused by the conformation of the woven structure into a local shape of tool. This is crucial as the tow orientation and filament distribution determine the mechanical properties of the final composite product. In the preforming process, an optimum setup is needed to avoid defects such as wrinkling and buckling in the fabric. The key parameters are friction between fibre and tool and between fibre and fibre contact [7]. For a non-crimp fabric (NCF) that is designed to have a better drapability in LCM, both the nature of the contact, and forces that are involved between contact surfaces are still very important. The combination of multiple layers of fibres stacked in just one fabric expose the fibres to a variety of contact configurations. Typically, fibre tows are arranged in different orientations (0, 45 and 90 degrees) as in Figure 1.3 to provide more isotropic properties of the fabric. The deformation of the biaxial and triaxial NCF under loading occurs through rotation, compaction and sliding of the tows. Furthermore, in this case the resistance to deformation is dependent not only on the density and the positions of the stitches but also on the tension. Therefore, is important to consider the effect of fibre tension on friction in the fibre-fibre contact as well.

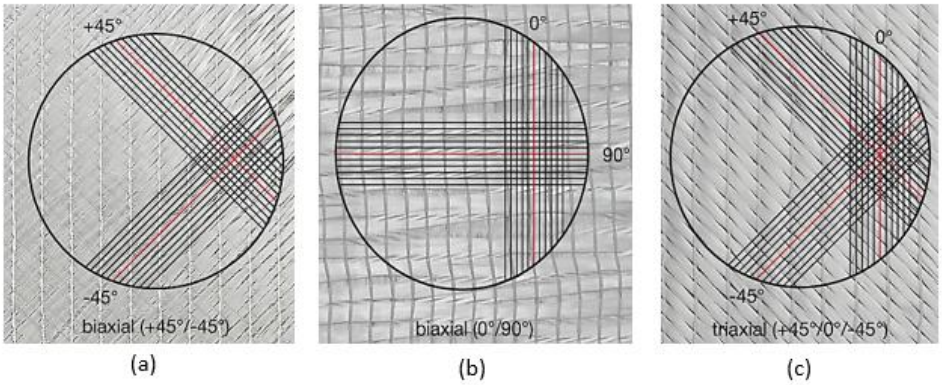

Figure 1.3 Multiaxial non-crimp fabric types: (a) +/- 45° biaxial, (b) +/- 90 ° biaxial and (c) +45°/0°/-45° triaxial.

Third, in mooring lines and oceanographic applications, friction between fibres can cause the premature failure of the fibre ropes and hence influence the mechanical properties and ropes lifespan [8, 9]. Tension in vertical direction due to the weight, as well as dynamic

response which is excited by longitudinal oscillation due to wave motion, will generate the internal friction in fibre ropes, see Figure 1.4. Also in this situation, tension in the fibres will potentially influence friction in the fibre-fibre contacts.

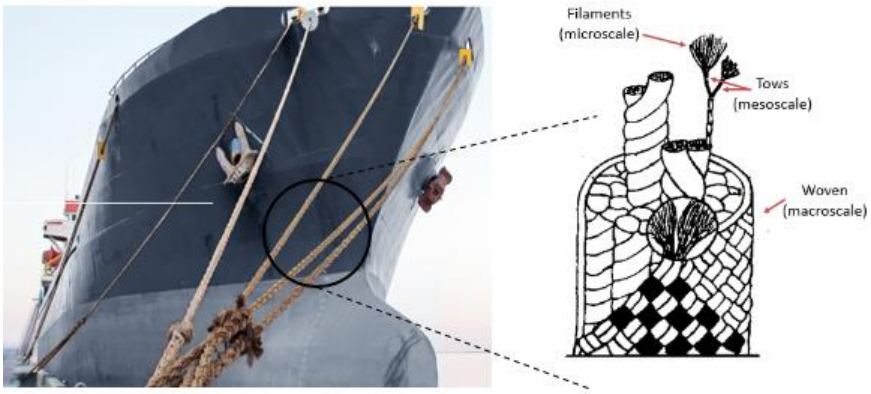

Figure 1.4 The structure of synthetic fibre ropes and cables for mooring lines application.

In ballistic applications, the performance of the impact resistance of the woven fabric in body armor is related to energy dissipation in the fabric. From an energy transfer point of view, it has been established that when a rigid projectile impacts a fabric, the lost projectile kinetic energy is absorbed by the fabric through three mechanisms. One of them is through frictional sliding between fibres [10]. So this frictional sliding between fibres is important for the ballistic limit and energy adsorption capacity of the woven fabric and therefore for the main functionality: impact resistance [11-14]. According to Briscoe and Motamedi [15], a fabric having higher internal friction absorbs more energy than a fabric with lower friction.

To conclude, knowledge of the fibre interaction is important as it plays a key role in governing the behaviour of fibre assemblies. The deformations that occur across the scales are inter-related and the frictional behaviour at filament level therefore needs to be understood. Besides, tension in fibres may also influence the frictional behaviour. Thus, in this thesis a study of frictional behaviour between fibres at filament level with the influence of pre-tension will be investigated. Here, this will be done by means of an experimental approach.

1.2 Contact modes

Friction is a surface phenomenon and is therefore always related to surface contact behaviour. This contact behaves differently depending the mode of contact between surfaces. Generally, contact modes can be classified into three types as illustrated in Figure 1.5. A line contact is realized between two fibres in parallel contact, a point contact happens when two fibres cross each other at 90° perpendicularly, while the elliptical contact mode is present when the two fibres cross each other between those two limits.

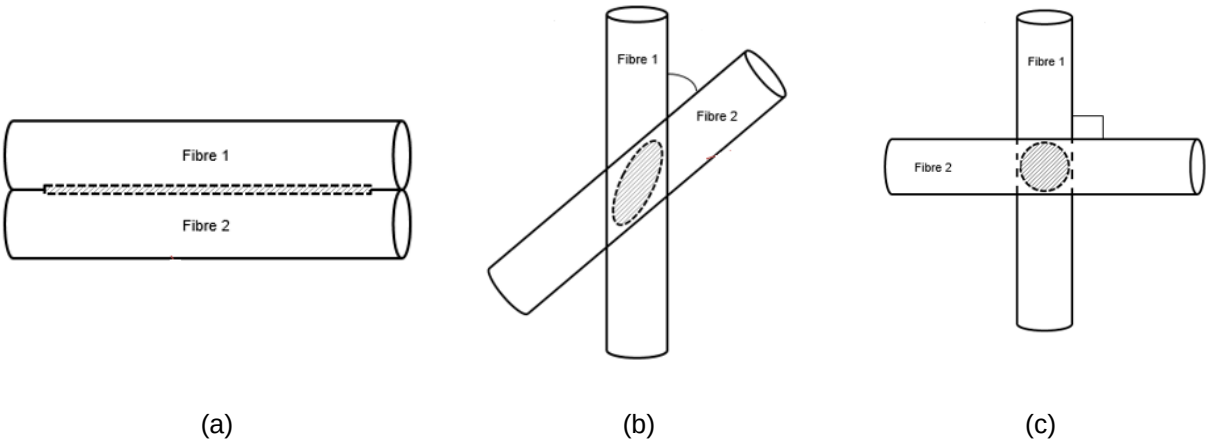

Figure 1.5 Illustration on three different contact modes:(a) line contact ($\theta = 0°/180°$), (b) elliptical contact ($0° < \theta < 90°$) and (c) point contact ($\theta = 90°$),fibres have the same radii.

The (static) friction force is considered as the force to break the contact in sliding direction. However, within the contacting surface itself, pressure and also adhesion force can be present. The adhesion force is the force required to separate the surfaces in normal direction. Thus, this study focuses on adhesion forces between fibres as well as on friction.

Besides the contact modes, the surface physical properties of the fibres such as surface energy play a role in the adhesion force. Physical and chemical treatments are often applied to the fibre surface such as the aramid fibre to enhance the functionality in terms of, for example, wetting and the ability to withstand the shear forces encountered during processing and use. Thus, to better comprehend the adhesion force between fibres, a knowledge of surface wetting and surface energy is important.

1.3 Research objectives

The aim of this thesis is to provide fundamental knowledge about the friction and adhesion behaviour between two contacting aramid fibres. Several research objectives are formulated below:

a) To develop an experimental approach to measure friction and adhesion between single aramid fibres.
b) To determine the surface properties including surface wettability and surface energy of single aramid fibres.
c) To determine the factors that affect the friction and adhesion between single aramid fibres including pre-tension and crossing angle.
d) To compare the experimental results obtained with the established models and theories.

1.4 Scope and limitations

This study addresses the frictional behaviour between two contacting aramid fibres. The investigation is limited to dynamic friction. The material of the fibres that are used in this study is limited to different types of Twaron® aramid fibre.

1.5 Thesis outline

Part A

This thesis consists of six chapters. A literature review on the experimental approach to measure the friction and adhesion force between fibres, contact mechanics and surface forces between contacts as well as the theoretical model which is related is described in **Chapter 2**. The friction and adhesion as related to the wetting and surface energy of single aramid fibre is determined experimentally and the results are discussed in **Chapter 3**. In more detail, the determination of contact angle and surface energy of single aramid fibres using the Wilhelmy method are described in this chapter. In **Chapter 4**, the development of the experimental setup to measure friction force between fibres is described. Also, friction force measurement methods and results will be presented. In particular, the effect of pre-tension load, crossing angle, elastic modulus and normal load on the friction force is discussed. In **Chapter 5,** the adhesion force measurement between fibres is studied. The AFM tip modification and also tip calibration is explained. The effect of relative humidity and crossing angle between fibres on adhesion force is studied. Finally, the general

discussion, conclusions of this work and recommendations for future research are presented in **Chapter 6.**

Part B

The body of this thesis is constructed based on the scientific papers which are prepared to be submitted and published. The content of the Paper C is presented in Chapter 3. Meanwhile the body of Chapter 4 is constructed based on the Paper A, B and D. Finally, the basis of Chapter 5 is based on Paper E.

References

[1] DuPont, Product overview Retrieved at: http://www.dupont.com/products-and-services/fabrics-fibers nonwovens/fibers/brands/kevlar.html

[2] Archer E. Buchanan S. McLlhagger AT. Quinn JP. The effect of 3D weaving and consolidation on carbon fiber tows, fabrics, and composites. *Journal of Reinforced Plastic Composites* 2010; 29(20):3162–70.

[3] Rudov-Clark S. Mouritz AP. Lee L. Bannister MK. Fibre damage in the manufacture of advanced three-dimensional woven composites. *Composites Part A Applied Science Manufacturing* 2003; 34(10):963–70.

[4] Lee B. Leong KH. Herszberg I. Effect of weaving on the tensile properties of carbon fibre tows and woven composites. *Journal of Reinforced Plastic Composites* 2001; 20:652–70.

[6] Decrette M. Mourad S. Osselin J-F. Drean J-Y. Jacquard UNIVAL 100 parameters study for high-density weaving optimization. *Journal of Industrial Textiles* 2015; 45 (6):1603-1618.

[7] Avgoulas EI. Mulvihill DM. Endruwiet A. Sutcliffe MPF. Warrior NA. De Focatiis DSA. Long AC. Frictional behaviour of non-crimp fabrics (NCFs) in contact with a forming tool*. Journal Tribology 2018*; 21, 71-77.

[8] Leech M. The modelling of friction in polymer fibre ropes. *International Journal Mechanical Sciences* 2002; 44: 621-643.

[9] Humeau C. Davies P. Engles TAP. Govaert LE. Vlasblom M. Jacquein F. Tension fatigue failure prediction for HMPE ropes. *Polymer Testing* 2018; 65:497-504.

[10] Lim CT. Tan VBC. Cheong CH. Perforation of high-strength double-ply fabric system by varying shaped projectiles. *International Journal of Impact Engineering* 2002; 27(6):577–91.

[11] Nilakantan G. Merrill RL. Keefe M. Gillespie JW. Wetzel ED. Experimental investigation of the role of frictional yarn pull-out and windowing on the probabilistic impact response of kevlar fabrics. *Composites Part B Engineering* 2015; 68:215–29.

[12] Duan Y. Keefe M. Bogetti TA. Cheeseman BA. Modeling friction effects on the ballistic impact behavior of a single-ply high-strength fabric. *International Journal of Impact Engineering* 2005; 31(8):996–1012.

[13] Parsons EM. King MJ. Socrate S. Modeling yarn slip in woven fabric at the continuum level: simulations of ballistic impact. *Journal of Mechanics and Physics of Solids* 2013; 61(1):265– 92.

[14] Das S. Jagan S. Shaw A. Pal A. Determination of inter-yarn friction and its effect on ballistic response of para-aramid woven fabric under low velocity impact. *Composites Structure* 2015; 120:129–40.

[15] Briscoe BJ. Motamedi F. The ballistic impact characteristics of aramid fabrics: the influence of interface friction. *Wear* 1992; 158(1–2):229–47.

Chapter 2

Experimental Study of Friction and Adhesion between Fibres

This chapter will focuses on the relevant literature of two important aspects in this thesis: (i) an experimental method to measure friction and adhesion in fibre-fibre contacts and (ii) an analysis of contact, friction and adhesion in fibre-fibre contacts. Based on this literature study, the general equations will be given which will be used in the remainder of this study.

2.1 Experimental Approaches

Frictional behaviour between fibres can be characterized either using an experimental method or a modelling method. To understand the nature of the fibre friction in fibrous materials, Gupta and El Mogahzy [1] have been developed the mathematical model based on the adhesion-shearing concept proposed by Bowden and Tabor [2, 3]. In addition, the importance of the contact mechanics during the fibre interactions attracted interest of Cornelissen and his co-workers [4, 5] and has resulted in the development of a contact model. There, tow-on-tow contact and tow-on-tool contact models have been developed to deepen the understanding of the frictional behaviour of carbon fibres.

However, the earliest studies on friction between fibres were carried out using experiments. Numerous experimental methods have been developed by previous researchers concerning fibre-on-fibre and fibre-on-metal at macro, meso and microscale. In fact, Gupta *et al.* [6] and Yusekkaya [7] also reviewed measured methods for friction. Those methods can be categorized and discussed in three different groups;

(a) Two fibres crossing and sliding in linear motion.

(b) The capstan method in which one material is wrapped over a cylindrical body.

(c) The twist method in which two materials (yarns or filaments) are twisted together at a certain number of turns and form a helix path.

2.1.1 Linear motion method

Several authors have used this technique [8-10] by utilizing the principle of cantilever. In this technique, friction is measured based on the principle of rubbing one fibre against another fibre in linear motion. As described by Pascoe and Tabor [11], this technique is very suitable with a very small load in the range of 10^{-6} N to 10^{-8} N, using the setup as shown in Figure 2.1.

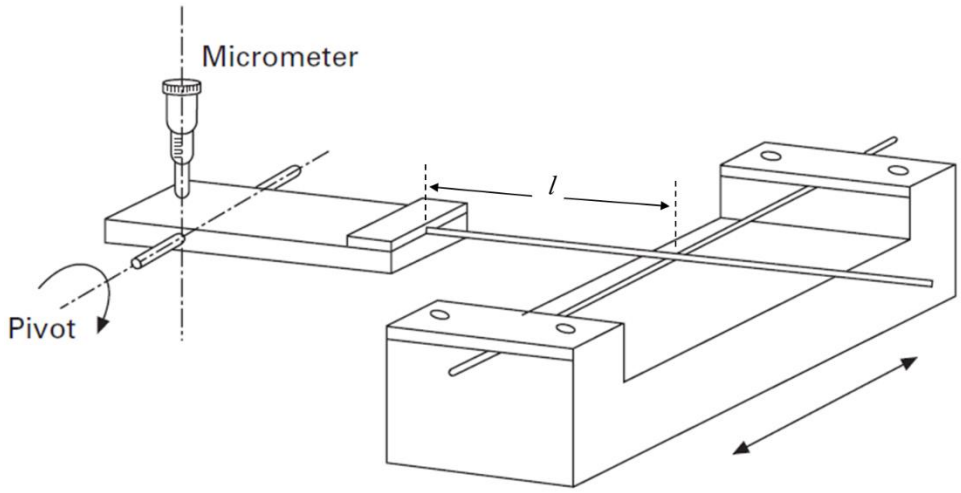

Figure 2.1 Setup developed by Pascoe and Tabor [11].

Briscoe *et al*. [12,13] have used this method to study the friction between polyethylene terephthalate monofilaments. In this setup, the top filament is pressed onto the bottom filament by rotating the pivot. The displacement of the top filament due to the deflection in vertical plane, $\Delta\delta_{z1}$ is used to estimate the normal force N. When the bottom filament is set to slide, the top filament is dragged with it and the deflection in horizontal direction of the top filament which is observed by the travelling microscope is used to calculate the friction force F_f. The normal and friction force can be calculated from vertical and deflection (see Figure 2.2 (a) and (b)). The relevant equations are:

$$\Delta\delta_z = Nl^3 /3E_aI \tag{2.1}$$

$$\Delta\delta_x = F_f l^3/3E_aI \tag{2.2}$$

where I is the second moment of inertia of the cross-section with radius R, E_a is the axial elastic modulus of the filament and l is the filament effective length from the contact point. Figure 2.2 (c) shows the friction force as a function of normal load which has been measured by Briscoe *et al.* [12] using the same principle method developed by Pascoe and Tabor [11].

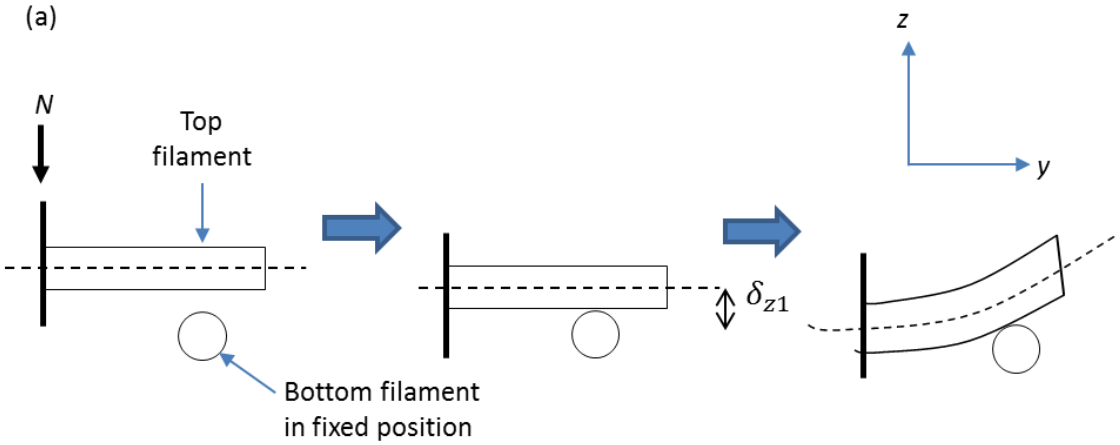
(a)
N
Top
filament
z
y
δ_{z1}
Bottom filament
in fixed position

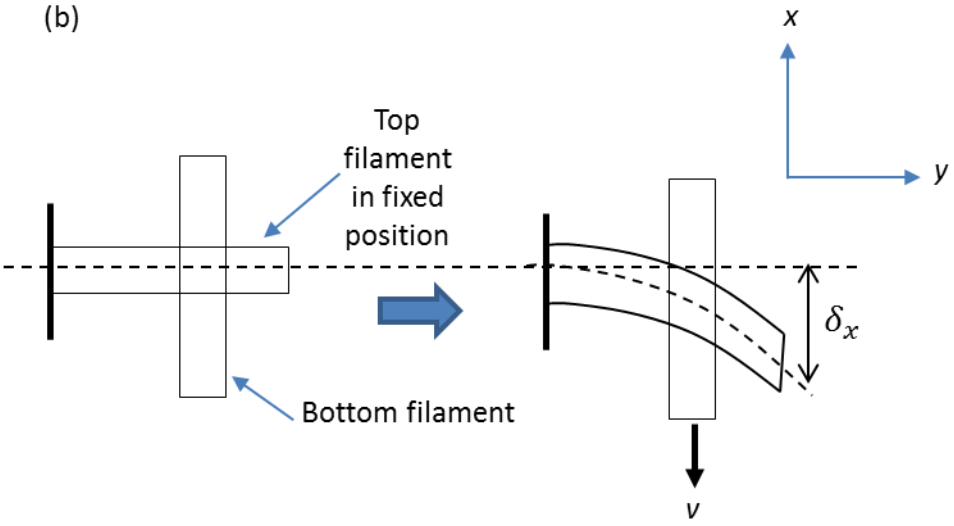
(b)
x
y
Top
filament
in fixed
position
δ_x
Bottom filament
v

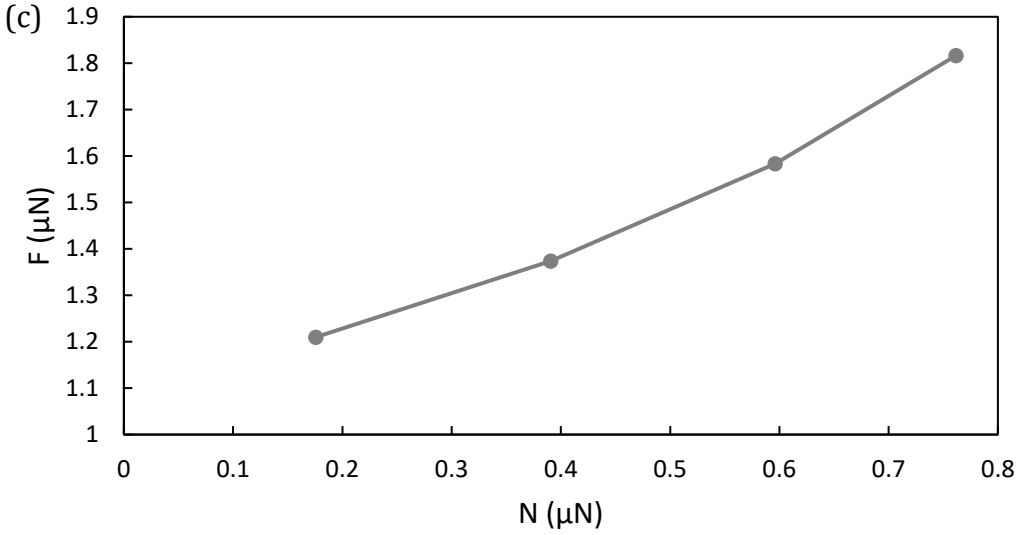

Figure 2.2 Measurements of normal and friction forces adapted by Briscoe *et al*. [12] (a) side view of the normal force on the specimen, (b) top view of the frictional force measured between monofilaments, (c) mean friction force as a function of normal load [12].

The contribution of adhesion force to the total normal load can be measured as well using this setup. Instead of pressing the top filament on the bottom filament to determine the normal force, here the top filament is initially allowed to just touch the bottom filament and is later pulled up gradually until the two filaments pull off. The separation distance, $\Delta\delta_{z2}$ (Figure 2.3 (a)) is substituted in Eq. 2 to allow calculation of the adhesive forces and the result of separation distance as a function of l^3 is depicted in Figure 2.3 (b).

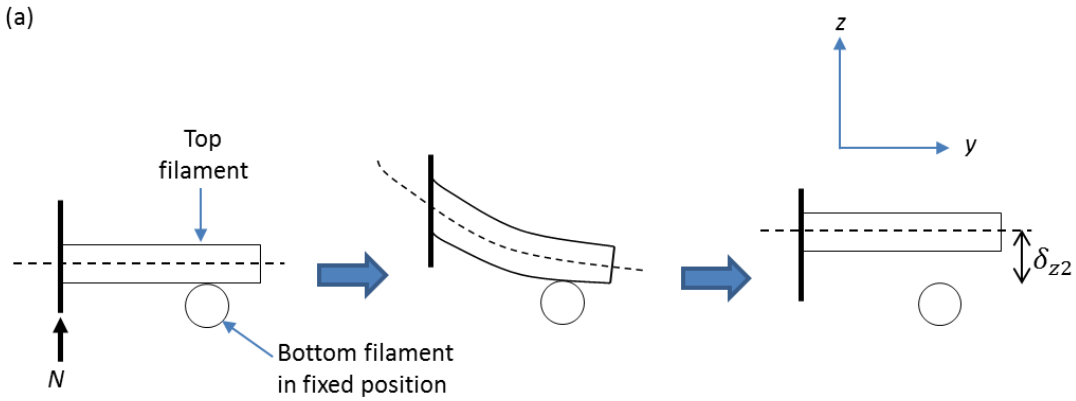

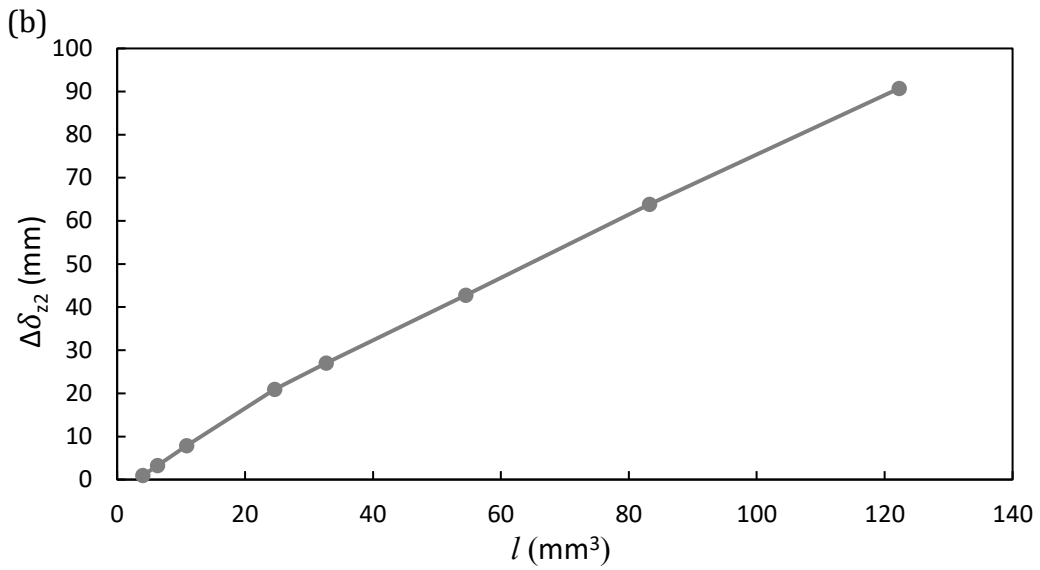

Figure 2.3 Measurements of adhesion forces adapted by Briscoe *et al*. [12] (a) side view of the adhesion force measured between monofilaments, (b) adhesion of crossed filaments, separation distance as a function of l^3 [12].

Recently, Tourlinas *et al.* [14] and Houssem *et al*. [15] have adapted this linear motion method in their setup to determine the friction force of polymer fibres such as carbon, polyamide and polyethylene. Also, Mulvihil et al. [16] modified this linear motion setup to suit his fundamental studies on friction at tow-on-tow and tow-on-metal contact situation. This setup is well suited to measure friction between filaments and tows as well as composite fabrics. Although Briscoe *et al.* [12,13] has used this method in their experiment to measure the adhesion force; the force obtained is very sensitive to the effective length of the filament *l.* An accurate measurement of the filament effective length *l* from the contact point is crucial.

2.1.2 Capstan method

For the capstan method, a fibre is wrapped over a cylindrical body and the frictional force that is developed is calculated based on a normal force generated by the tension exerted at both ends as shown in Figure 2.4.

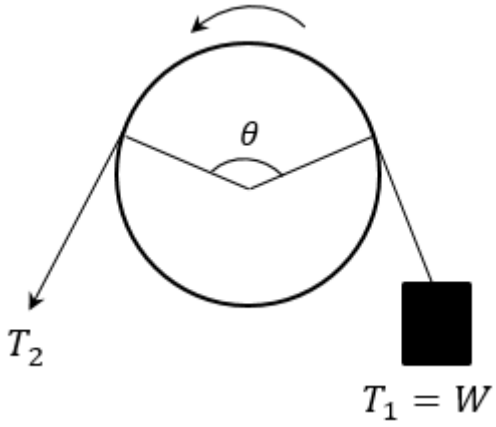

Figure 2.4 Capstan method.

The capstan relation gives an apparent coefficient of friction as a function of the tensional forces at T_1 and T_2 at both end and the wrapping angle θ_{wrap} of the fibre specimen on the cylindrical body. The relation is [17]:

$$\mu = \ln\left(\frac{T_2}{T_1}\right)\frac{1}{\theta_{wrap}} \tag{2.3}$$

Roselman and Tabor [18] have used this method to study friction at microscale level, while Cornelissen *et al*. [19] and Chakladar *et al.* [20] studied friction at mesoscale level. The factors influencing friction such as surface roughness [19], tow angle and tow size on carbon [20] have been investigated through this method. The cylindrical body can be metal, ceramic or another fibre. This method is useful for measuring the effects of speed and lubrication on the friction force. In fact, it is a tool to study frictional interfaces from a real production perspective. The metal capstan drum represents metal tooling such as in filament winding process. However, this method is less suited for a basic study of friction as the normal load applied results in a pressure distribution over a cylindrical body, where the maximum pressure is only at the middle point of the cylindrical body. So effectively, a friction force is measured over a range of pressures.

2.1.3 Twist method

Gralen, Olofsson and Lindberg [21-23] used the twist method to study the friction behaviour in textile materials. Two fibres are twisted together by a certain number of turns

and known weight and the friction is measured during the slippage as in Figure 2.5 (a). Later, Gupta *et al*. [24] adapted this method for use on a standard tensile tester.

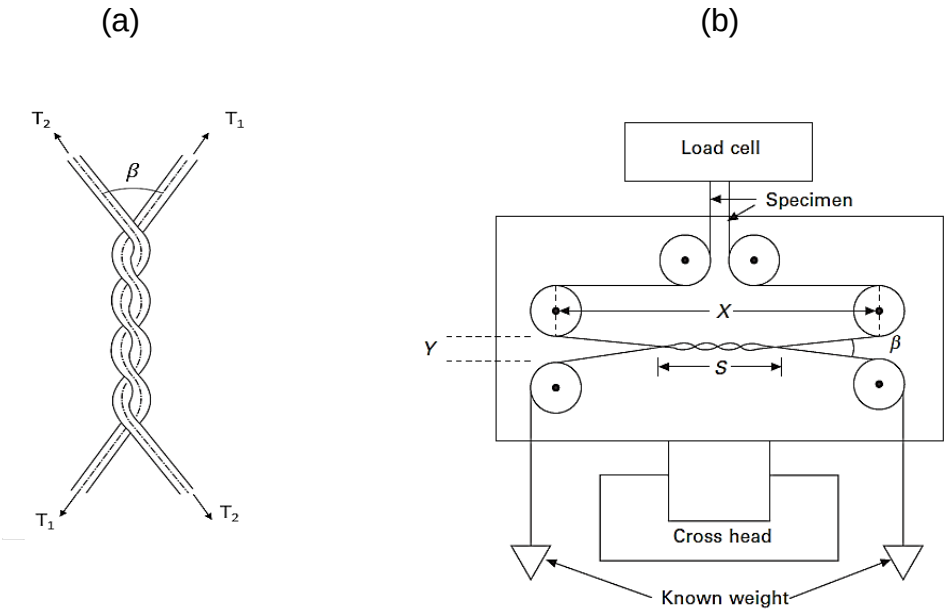

Figure 2.5 Twist method (a) schematic principle of measuring force using twist method, and (b) adaptation of twist method for use with a standard tensile tester [24].

In general, the fibres slip when the tension at T_1 increased above the critical value of T_2. The tensional force at both ends is measured in the same manner as capstan method. The general apparent coefficient of friction can be calculated as [17]:

$$\mu = ln\left(\frac{T_2}{T_1}\right)\frac{1}{n_{twist}\pi\theta_{twist}} \tag{2.4}$$

where T_1 and T_2 are the tensional forces at both ends, n_{twist} is the number of turns and θ_{twist} is the twisted angle. This method is limited to characterizing the friction between fibres at line type of contact. Although it is twisted and forms a helix path, the actual contact between surfaces is a line, parallel to the axis.

From the experimental approaches that has been discussed above, it is found that the linear motion method is the most suitable method that can be adapted in measuring the friction force between two single fibres. The friction force between fibres can be directly measured as one fibre is set to slide against another. The friction is measured using a relatively direct method. The pre-tension load is one of the control parameters in this

study. In this setup, the pre-tension load can be directly applied to the fibre (i.e. top or bottom fibre) and the fibre orientation could possibly be changed. This will provide several contact configurations between the contacting surfaces, whereas the capstan and twist method which is focused on line or point contact only. However, some modifications on the setup are required to suit the elastic material such as aramid fibre, which is not as stiff as carbon fibre.

2.2 Contact mechanics between fibres

To determine the friction and adhesion between two fibres, it is important to understand the nature of the contact between them. When two fibres are brought into contact, they will initially touch at either a point or along a line at the contacting surfaces. However, with the application of normal load, the elastic deformation will enlarge these contacts into contact area where the loads are distributed. As the size of the contact area influences the frictional behaviour, the contact area between the contacting surfaces is important and need to be considered.

2.2.1 Hertz contact model at different contact modes

As a foundation, Hertzian contact theory [25] can be used to predict the elastic deformation between two single fibres in contact. In this theory, the surface between two elastic solids is assumed to be smooth. Also, the size of the actual contact area must be smaller than the dimensions of each body. It is assumed that if two fibres with a cylindrical shape with equal radius are in parallel contact ($\theta = 0°/180°$), the contact area is rectangular with contact width *b* over the length of the contact *L* [25] as in Figure 2.6. The contact area is given by:

$$A = bL \tag{2.5}$$

with *b* is the contact width

$$b = \sqrt{\frac{4NR}{\pi L E^*}} \tag{2.6}$$

where *N* is the normal load, *R* is the fibre radius and *E** is the contact modulus. The contact modulus is calculated from the elastic modulus of the fibre, E_1 and E_2 and Poisson ratios v_1 and v_2 [25]:

$$\frac{1}{E^*} = \frac{1 - v_1^2}{E_1} + \frac{1 - v_2^2}{E_2} \tag{2.7}$$

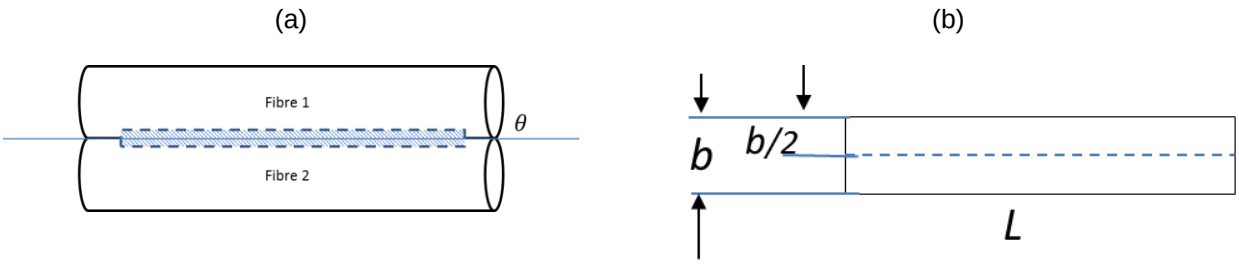

Figure 2.6 (a) Fibres in parallel contact, (b) geometrical contact area shape.

However, if two fibres cross each other in perpendicular contact, ($\theta = 90°$), the contact area is in a circular shape with the radius of the contact, *a* as shown in Figure 2.7. The contact area can be calculated by:

$$A = \pi {a_p}^2 \tag{2.8}$$

with a_p is the contact radius

$$a_p = \sqrt[3]{\frac{3NR^*}{4E^*}} \tag{2.9}$$

where *N* is the normal load, *R** is the effective radius and *E** is the contact modulus as in Eq. 2.7. The effective radius is calculated from the radii of the fibre, R_1 and R_2 [25]:

$$R^* = \frac{R_1 R_2}{R_1 + R_2} \tag{2.10}$$

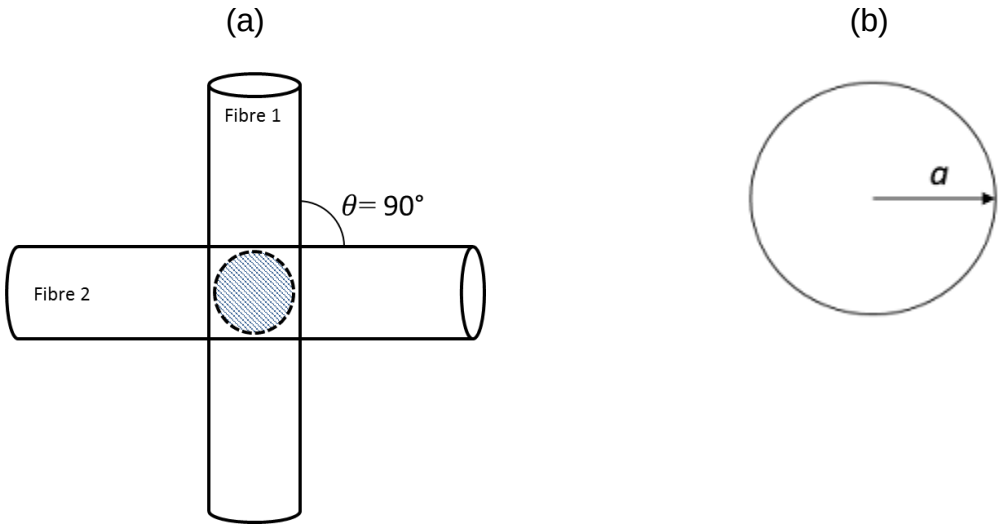

Figure 2.7 (a) Fibres in perpendicular contact, (b) geometrical contact area shape.

In the case of two cylinders at elliptical contact, the elliptical contact area can be calculated by determining the length of the semi-axes of the ellipse shape, *a* and *b* (see Figure 2.8). These can be calculated from the knowledge of geometric and elasticity of the bodies in contact. The principal relative radii of curvature between bodies can be related to the crossing angle θ and defined as follows [25]:

$$R_a = \frac{R}{1 - \cos\theta} \tag{2.11}$$

$$R_b = \frac{R}{1 + \cos\theta} \tag{2.12}$$

where the effective radius is given by:

$$R_e = \sqrt{R_a R_b} \tag{2.13}$$

Within the elliptical contact area, the pressure distribution can be expressed as:

$$P = p_o\sqrt{1 - (x/a_{ell})^2 - (y/b_{ell})^2} \tag{2.14}$$

$$(x/a_{ell})^2 + (y/b_{ell})^2 \leq 1$$

$$p_o = \frac{3N}{2\pi a_{ell} b_{ell}} \tag{2.15}$$

where *P* is the pressure, *N* is the normal load, p_o is the maximum pressure, a_{ell} and b_{ell} are the length of the semi-axes of the ellipse area. The relation between the geometric constant and semi-axes is given by [25]:

$$\frac{R_a}{R_b} = \frac{(a/b)^2 E(e) - K(e)}{K(e) - E(e)} \tag{2.16}$$

and

$$\frac{1}{2}\left(\frac{1}{R_a R_b}\right)^{1/2} = \frac{p_o}{E^*}\frac{b}{a^2 e^2}[\{(a^2/b^2)E(e) - K(e)\}\{K(e) - E(e)\}]^{1/2} \tag{2.17}$$

where *E*(e) and *K*(e) are complete elliptic integrals of the first and second kind respectively. The parameter *e* is the eccentricity of the contact ellipse given by:

$$e^2 = 1 - {b_{ell}}^2/{a_{ell}}^2 \tag{2.18}$$

With the equivalent contact radius $c = (a_{ell} b_{ell})^{1/2}$ and substitute p_o from equation (2.15) into (2.17) we can obtain:

$$c^3 = \frac{3NR_e}{4E^*}\frac{4}{\pi e^2}(b_{ell}/a_{ell)}{}^{3/2}\left[\left\{({a_{ell}}^2/{b_{ell}}^2)E(e) - K(e)\right\}\{K(e) - E(e)\}\right]^{1/2} \tag{2.19}$$

By solving the numerical integration of the elliptical integral *E*(e) and *K*(e), the size of the ellipse contact area can be calculated. However, due to the inconvenience of solving the numerical integration of the elliptical integral, an approximate relation has been developed.

Greenwood proposed an approximate equation to calculate the Hertzian elliptical contact area [26,27]. This method worked well for a mildly elliptical contact under engineering accuracy. The length of the semi-axes a_{ell} and b_{ell} of the ellipse can be calculated as [27]:

$$a_{ell} = \left(\frac{3{k_{ell}}^2 \varepsilon N R_e}{\pi E^*}\right)^{\left(\frac{1}{3}\right)} \qquad b_{ell} = \left(\frac{3\varepsilon N R_e}{\pi k_{ell}^2 E^*}\right)^{\left(\frac{1}{3}\right)} \tag{2.20}$$

where k_{ell} is the axis ratio (a_{ell}/b_{ell}), ε is the elliptic integral, *N* is the normal load, R_e is the effective radius and E^* is the contact modulus. Using the axis ratio, $k_{ell} = 1.0339({}^{R_b}/_{R_a})^{0.636}$ and elliptic integral, $\varepsilon = 1.0003 + 0.5968({}^{R_a}/_{R_b})$, the contact area of the ellipse shape at various crossing angles can be directly calculated.

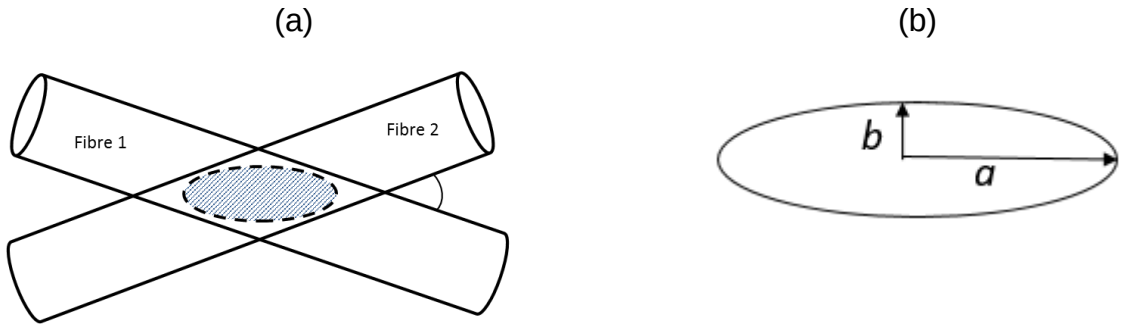

Figure 2.8 (a) Fibres in elliptical contact, (b) geometrical contact area shape.

2.2.2 Taut wire model at different pre-tension

When pre-tension is introduced, the fibre is stretched and the change in horizontal tension consequently influences the conformability between the contact surfaces. In this way, the contact is influenced by the wrapping length effects. In the analysis below, it is assumed that the pre-tension influences the elastic flattening of the fibre. Therefore, the area of contact or the contact length between fibres is solely governed by the fibre deflection. This will happen in the case of, for example, a fibre under high pre-tension. The deflection of the fibre which is in pre-tension under an applied normal load can be calculated as follows [28]:

$$2\left(\frac{\delta_z}{L_t}\right)^3 A_t.E + \left(\frac{\delta_z}{L_t}\right)T - \frac{N}{4} = 0 \tag{2.21}$$

where δ_z is the fibre deflection, L_t is the fibre length, A_t is the fibre cross-sectional area, *E* is the Young's modulus, *T* is the pre-tension load and *N* is the normal load. To study the relationship between pre-tension and contact length between contacting fibres, the deflection of the fibre must be determined first. Figure 2.9 shows the diagram of the fibre deflection due to pre-tension and normal load. Due to the application of normal load, both fibres that are in contact deform with a certain deflection δ_z. Thus, mathematically the behaviour of the lower fibre can be represented, assuming a straight line between the centre of the contact and the end of the top fibre:

$$y = mx - \delta_z \tag{2.22}$$

and the circumference of the bottom fibre that touch the lower fibre is represented by (see Figure 2.9):

$$(x - x_c)^2 + (y - y_c)^2 = R^2 \tag{2.23}$$

where *m* is the line gradient, δ_z is the fibre deflection, x_c and y_c are the coordinates of the centre of the contact and *R* is the fibre radius. If it is assumed that the contact geometry is triangular, the contact length a_δ between two fibres in contact at δ_z can be calculated, by evaluating the crossing points of equations (2.22) and (2.23) in the half -plane axis, as:

$$a_\delta = \sqrt{x^2 + (-\delta_z - y)^2} \tag{2.24}$$

In short, due to the pre-tension of the fibre and a wrapping effect, a contact area or in this case the contact length is generated due to the macroscopic bending of the fibre. Also, during loading, the bending stiffness of the fibre is increased due to the pre-tension. This

prevents deformation at the contact surfaces. This is different for the Hertzian contact theory where the contact area is generated due to the elastic deformation in the contact surface, and the pre-tension and the macroscopic bending of the fibre do not play a role.

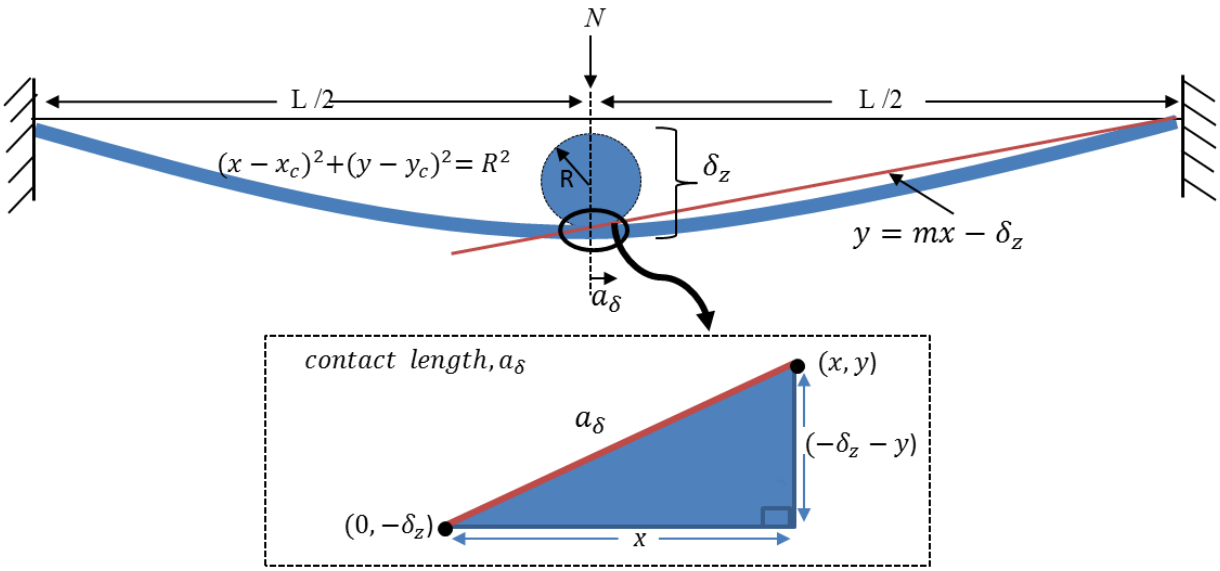

Figure 2.9 The diagram of the fibre deflection due to pre-tension and normal load.

2.3 Surface forces

Surface forces are the integral form of interaction forces between surfaces of macroscopic bodies through a third medium (e.g. vacuum and vapor). There can be different types of surface forces acting when two surfaces are brought closer to each other such as the van der Waals force, electrostatic force, capillary force, force due to chemical bonding and many others [29]. The combination of these forces gives rise to the adhesion force which can be expressed as:

$$F_{adhesion} = F_{van\ der\ Waals} + F_{capillary} + F_{electrostatic} + \cdots \tag{2.25}$$

However, the magnitude of these forces is dependent on several factors such as the size and the shape of the contacting surfaces, environmental conditions, the material properties, coatings and other factors. In humid conditions, the total adhesion force will be affected by the capillary force (meniscus force), caused by capillary effects. In dry contact conditions, the total adhesion will be composed of the van der Waals force, when the effects like electrostatic forces can be ignored. In the next section, the analytical equations to calculate these forces are presented.

2.3.1 Capillary force

The capillary forces or the meniscus forces of two spheres at low separation distance *D* (see Figure 2.10) are present due to condensation. Liquids that wet or have a small contact angle in combination surface will condense from vapour to bulk liquid forming a capillary neck or meniscus.

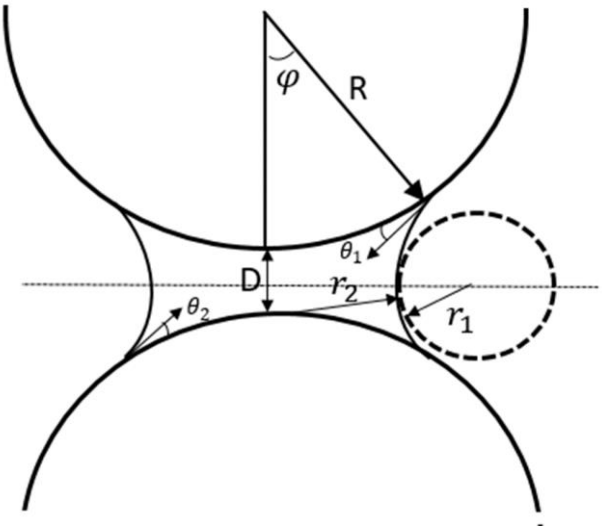

Figure 2.10 Geometry of sphere-sphere contact with meniscus formation [30].

The pressure that is generated by the curvature of the meniscus surface can be derived using the *Laplace* equation [29]:

$$P_{cap} = \gamma_L \left(\frac{1}{r_1} + \frac{1}{r_2}\right) \approx \frac{\gamma_L}{r_k} \tag{2.26}$$

where γ_L is the liquid surface tension (water) and r_1 and r_2 are curvature radii that define the curved surface as shown in Figure 2.10. In the *Kelvin* equation, the mean radius of curvature of the condensed meniscus is known as *Kelvin radius*, r_k, is dependent on the relative humidity and therefore can be calculated by [31]:

$$\left(\frac{1}{r_1} + \frac{1}{r_2}\right)^{-1} = r_k = -\frac{\gamma_L V}{R_g T_{abs} log\left(\frac{p}{p_s}\right)} \tag{2.27}$$

where p/p_s is the relative humidity (RH), V is the molar volume, R_g is the gas constant and T_{abs} is the absolute temperature. For water, γ_L = 73 mJ/m^2 at T = 293K, this gives $\gamma_L V / R_g T_{abs} = 0.54\ nm$. Since the pressure inside the capillary is lower than the pressure in the other vapour phase, the force due to the capillary pressure can be calculated as [31]:

$$F_p = -P_{cap}\pi\left({r_2}^2 - {a_{cap}}^2\right) = -\left[-\frac{R_g T_{abs}}{V_m} log\left(\frac{p}{p_s}\right)\right]\pi\left(R^2 - sin^2\varphi - {a_{cap}}^2\right) \tag{2.28}$$

However, there is another force component that arises from the surface tension of the liquid-vapour interface, which is the surface tension force to sustain the liquid surface. The surface tension force can be calculated as [31]:

$$F_s = -2\pi\gamma_L r_2 \sin(\theta_1 + \varphi) = -2\pi\gamma_L R \sin\varphi sin(\theta_1 + \varphi) \tag{2.29}$$

$$F_s = -L\gamma_L \sin\varphi sin(\theta_1 + \varphi)$$

Thus, the total capillary force, F_c is the sum of the capillary pressure F_p and surface tension force F_s [31]:

$$F_c = F_s + F_p \tag{2.30}$$

$$F_c = -L\gamma_L \sin\varphi sin(\theta_1 + \varphi) - \left[-\frac{R_g T}{V_m} log\left(\frac{p}{p_s}\right)\right]\pi(R^2 - sin^2\varphi - a^2)$$

In general, there are three distinct force regimes to describe the relationship between the adhesion force and relative humidity [32] as shown in Figure 2.11:

(i) Regime I (1-40%) is dominated by the van der Waals interactions.
(ii) Regime II (40-70%) represent a mixed regime between van der Waals and capillary effects.
(iii) Regime III (70-100%) is dominated by capillary effects.

It also has been claimed that there is no capillary neck developed at regime I, thus the adhesion force is dominated by van der Waals interactions only [32]. The capillary neck formation starts at about 40% RH and in this region the adhesion force is a combination of van der Waals and capillary force. From Figure 2.11, it can be seen that the adhesion force increases with increasing RH, however the adhesion force starts to decrease with increasing RH in regime III. According to Xiao and Qian [31], the decrease is due to the screening of the van der Waals force because of the presence of water in the gap.

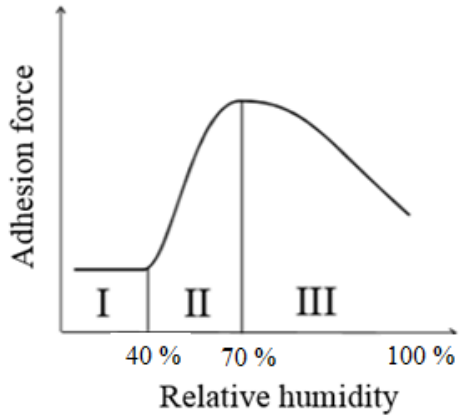

Figure 2.11 Generic sketch of a relation between adhesion force and relative humidity (RH) [32].

Accordingly, the capillary force model as described above is equivalent to a cylinder-cylinder interaction with equal diameters at perpendicular contact [29]. However, for an elliptical contact $(0° < \theta < 90°)$, it becomes difficult to compute the force as the capillary neck is distorted gradually with the increase in crossing angle θ [33]. To date, there is no experimental study done to relate the crossing angle and relative humidity on the capillary force. However, in numerical simulations, Soleimani *et al*. [34] showed that the capillary force is directly influenced by the crossing angle and the volume of the capillary neck. The wetting length of the capillary neck along the fibre axes shortens with increasing the crossing angle and thus reduces the capillary force [33,34].

2.3.2 Van der Waals force

The van der Waals force is the attractive or repulsive force acting between atoms, molecules or surfaces. In the case of two identical materials in contact or any two

materials in vacuum conditions, the van der Waals force is always attractive [29]. Further, in vacuum or at very low humidity levels (RH), this attractive van der Waals force is typically dominating. This attractive force is often characterized by the pull-off force which is needed to separate two bodies. At very low or zero normal load, this short-range force interactions can be determined for example using the Johnson-Kendall and Roberts (JKR) model. The JKR model can be considered as a modified Hertzian model. An important result of the JKR model is that it predicts a finite contact area between surfaces under zero normal load. This area can be calculated by the following general equation by putting *N*=0 [35]:

$$A_{JKR} = \pi(\frac{3R}{4E^*})^{2/3}\left(N + 3\pi\Delta\gamma R + \sqrt{6\pi\Delta\gamma RN + (3\pi\Delta\gamma R)^2}\right)^{2/3} \quad (2.31)$$

where *R* is the effective radius, *E** is the contact modulus, $\Delta\gamma$ is work of adhesion and *N* is the normal load. The JKR model assumes that the adhesive forces are confined inside the contact area and thus the pull-off force at point contact can be calculated using the following equation [35]:

$$F_{adh} = \frac{3}{2}\pi\Delta\gamma R \quad (2.32)$$

In the case of fibre-on-fibre at elliptical contact conditions, Johnson and Greenwood [36] extended the JKR for the point contact theory to a general elliptical adhesive contact model. In this model, it is assumed that the contact area remains elliptical, but the eccentricity varies continuously with the applied load. The pull-off force for an elliptical contact is substantially less than the value for a point contact and can be calculated as follows [36]:

$$F_{adh} = 2\pi a_{ell} b\left[P_1 - \frac{1}{3}\left(\alpha {a_{ell}}^2 + \beta {b_{ell}}^2\right)\right] \quad (2.33)$$

where P_1 is the pressure distribution (Eq. 2.33), α and β are the coefficient in pressure (Eq. 2.34) and, a_{ell} and b_{ell} are the semi-major and minor axes of the elliptical adhesive contact [36].

$$P_1 = \frac{\alpha {a_{ell}}^{5/2} - \beta {b_{ell}}^{5/2}}{{a_{ell}}^{1/2} - {b_{ell}}^{1/2}} \tag{2.34}$$

$$\alpha = \frac{E^*}{2bR_e}\alpha' \text{ and } \beta = \frac{E^*}{2bR_e}\beta' \tag{2.35}$$

$${a_{ell}}^{2/3} = 2R_e\sqrt{\frac{2\Delta\gamma}{\pi E^*}}\frac{(b_{ell}/a_{ell})^{\frac{1}{2}}(1-(b_{ell}/a_{ell})^{\frac{1}{2}})}{\beta'(b_{ell}/a_{ell})^2 - \alpha'} \tag{2.36}$$

2.4 Friction Model

The classical Amonton's laws of friction [37] is the most straightforward approach to describe dry friction between two sliding materials. This equation is typically valid for random rough surfaces in contact. The friction force F is directly proportional to the applied normal force N and the ratio of friction force to normal force is defined as coefficient of friction μ:

$$F_f = \mu N \tag{2.37}$$

However, studies conducted on synthetic and polymeric fibres have shown that the coefficient of friction does vary with the applied normal load, whereas the Amonton's law of friction implies a constant value. Bowden and Young [38] proposed a different equation and Lincoln [39] was the first to apply this equation to fibre friction then followed by several authors [21-23] who studied friction of fibrous materials. The following is widely accepted and shows that the friction force is not directly proportional to the normal force but follows a power law:

$$F_f = kN^n \tag{2.38}$$

where k and n have the constant value. The power of n is found to be less than but close to unity, typically between 0.7 to 0.9. These powers can be explained by assuming Hertzian contacts. As described by Bowden and Tabor [2,3] the friction force also can be written as follows:

$$F_f = \tau A_r + P \tag{2.39}$$

where τ is the shear stress, A_r is the real contact area between the contacting surfaces and P is ploughing. If the effect of ploughing is ignored, the friction force is caused only by shear in the microcontacts, with τ is the shear strength of the interface.

2.5 Summary

This chapter reviews the experimental methods that are used to measure the friction and adhesion force between fibres. Based on the three methods that have been discussed, the linear motion is the most suitable method to measure friction and adhesion between two single filaments. Using this method, the friction and adhesion force at a defined contact pressure can be measured. Since the aramid fibre is not as stiff as the carbon fibre, the setup shown needs to be modified. The top holder should be adapted to prevent the fibre from deforming before loading. To realize this, the top holder will be re-designed so that both fibre ends are clamped to the fibre holder. Also, with this method the orientation of the fibre can be easily controlled by rotating one of the fibres. In this way, the effect of crossing angle on fiction and adhesion force can be investigated. Moreover, the influence of crossing angle, specifically at angles between parallel to perpendicular contact, has not been studied in the literature. To understand the contact mechanics between fibres, the Hertz theory is used as a foundation to determine the area of the contacting surfaces. However, due to the introduction of pre-tension to the system, the theory of taut wire can become important in relating pre-tension and contact area between the fibre surfaces. Further, as the thickness of the fibre is relatively small, the contact can deviate from a

typical Hertzian contact. Meanwhile, the forces that are present at the contacting surfaces such as van der Waals and capillary force, have also been discussed. In dry contact conditions the van der Waals force is more dominant, whereas under humid conditions the capillary force is more significant. Additionally, the model to determine the capillary and van der Waals forces for different contact modes such as at point and elliptical contact has also been discussed. Finally, to describe the friction behaviour, several models were discussed, and it can be summarized that for polymeric materials the friction force is found not to be directly proportional to the normal force but tends to follow a power law. As a result, the coefficient of friction reduces as the normal load increases.

References

[1] Gupta BS. El Mogahzy YE. Friction in fibrous materials: Part I: structural model. *Textile Research Journal*. 1991;61(9):547-555.

[2] Bowden FP. Tabor D. Friction and lubrication of solids. Oxford, Clarendon Press. 1954.

[3] Bowden FP. Tabor D. Friction: An introduction to tribology. Anchor Press. New York.1973.

[4] Cornelissen B. de Rooij MB. Rietman B. Akkerman R. Frictional behaviour of high performance fibrous tows: a contact mechanics model of tow–metal friction. *Wear* 2013; 305(1–2):78–88.

[5] Cornelissen B. de Rooij MB. Rietman B. Akkerman R. Frictional behavior of carbon fibre tows: a contact mechanics model of tow–tow friction. *Textile Research Journal* 2014; 84(14):1476–88.

[6] Gupta BS. Ajayi AJ. Kutsenko M. Experimental methods for analyzing friction in textiles. Woodhead Publishing Limited. Cambridge. 2008.

[7] Yuksekkaya ME. More about fibre friction and its measurements. *Textile Progress* 2009;41(3):141–93.

[8] Mercer EH. Makinson KR. The frictional properties of wool and other textile fibres. *Journal of the Textile Institute Transactions* 1947; 38(5): T227–40.

[9] Howell HG. Inter-fibre friction. *Journal of the Textile Institute Transactions* 1951; 42(12): T521–33.

[10] Guthrie JC. Oliver PH. Inter-fibre friction of viscose rayon. *Journal of the Textile Institute Transactions* 1952;43: T579-T594.

[11] Pascoe MW. Tabor D. The friction and deformation of polymers. *Proceedings of Royal Society London A* 1956; 235(1201); 210–24.

[12] Briscoe BJ. Kremnitzer SL. A study of the friction and adhesion of Polyethylene terephthalate monofilaments. *Journal of Physics D: Applied Physics* 1979; 5:505-516.

[13] Briscoe BJ. Wrinkler A. Adams MJ. A statistical analysis of the frictional forces generated between monofilaments during intermittent sliding. *Journal of Physics D: Applied Physics* 1985;18: 2143-2167.

[14] Tourlinas M. Bueno M-A. Poquillon D. Friction of carbon tows and fine single fibers. *Composites Part A: Applied Science and Manufacturing*. 2017; 98: 116-123.

[15] Houssem EG. Barbier G. Kocher CW. Sinoimeri A. Pumo B. Experimental evaluation of transverse friction between fibers. *Tribology International* 2018; 119:112-122.

[16] Mulvihil D. Smerdova O. Sutcliffe M. Friction of carbon fibre tows. *Composites Part A: Applied Science and Manufacturing* 2016; 93:185–198.

[17] ASTM, D 3108 Test method for coefficient of friction - yarn to solid material.

[18] Roselman IC. Tabor D. The friction and wear of individual of carbon fibres. *Journal of Physics D: Applied Physics* 1977;10: 1181-1194.

[19] Cornelissen B. Rietman B. Akkerman R. Frictional behaviour of high performance fibrous tows: friction experiments. *Composites Part A: Applied Science and Manufacturing* 2013; 44:95–104.

[20] Chakladar ND. Mandal P. Potluri P. Effects of inter-tow angle and tow size on carbon fibre friction. *Composites Part A: Applied Science and Manufacturing* 2014;65;115–124.

[21] Gralen N. Olofsson B. Measurement of friction between single fibers. *Textile Research Journal* 1947;17(9): 488–496.

[22] Lindberg J. Gralén N. Measurement of friction between single fibers: II. Frictional properties of wool fibers measured by the fiber-twist method. *Textile Research Journal* 1948; 18(5):287–301.

[23] Gralen N. Olofsson B. Lindberg J. Measurement of friction between single fibers: Part VI: Physicochemical views of interfiber friction. 1953; 23:623.

[24] Gupta BS. Wolf KW. Postlethwait RW. Effect of structural material and construction on frictional properties of sutures. Surg. Gynecol. Obstet. 1985; 161:12-16.

[25] Johnson KL. Contact mechanics. Cambridge Uni Press. 1985.

[26] Greenwood JA. Formulas for moderately elliptical Hertzian contacts, Transactions of the ASME, J Trib. 1985;107 (4);501-504.

[27] Greenwood JA. Analysis of elliptical Hertzian contacts. *Tribology International* 1997;30[3]: 235-237.

[28] Charles I. Applied mechanics for engineers. The Syndic of The Cambridge University Press 1951:54-66.

[29] Israelachvili J. Intermolecular & Surface Forces. 2nd ed. London: Academic Press; 1991.

[30] Dormann M. Schmid H-J. Simulation of Capillary bridges between particles. *Procedia Engineering* 2015:102;14-23.

[31] Xiao X. Qian Li. Investigation of humidity-dependent capillary force. Langmuir 2000; 16; 8153-8158.

[32] He M. Blum AS. Aston DE. Buenviaje C. Overney RM. Critical phenomena of water bridges in nanoasperity contacts. Journal of Chemical Physics 2001;114(3):1355-1360.

[33] Bedarkar A. Wu X-F. Capillary torque in a liquid bridge between two angled filaments. *Journal of Applied Physics* 2009;106:113527.

[34] Soleimani M. Hill RJ. Van de Ven TGM. Capillary force between flexible filaments. *Langmuir* 2015:31;8328-8334.

[35] Johnson KL. Kendall K. Robert AD. Surface energy and the contact of elastics solids. in *Proceedings of Royal Society of London. Series A, Mathematical and Physical Sciences*, 1971.

[36] Johnson KL. Greenwood JA. An approximate JKR theory for elliptical contacts. *Journal of Physics D: Applied Physics* 2005; 38:1042.

[37] Amonton G. *Historie de l'Academie Royale des Sciences avec Memoires, de Mathematique et de Physique*. 1699. Page 206.

[38] Bowden FP. Young JE. Friction of diamond, graphite, and carbon and the influence of surface films. *Proceedings of Royal Society* 1951;208, 444.

[39] Lincoln B. Frictional and elastic properties of high polymeric materials. *British Journal of Applied Physics* 1952; 3:260.

Chapter 3

Wettings and Surface Energy Properties of Aramid Fibre

The physical properties of the solid surface play an important role in influencing the friction and adhesion force. Thus, in this study the wetting and surface energy of the three different types of aramid fibre is analyzed. The content of this chapter is the basis of Paper C in Part B.

3.1 Background

Aramid fibres are often treated with a physical or chemical treatment to control friction, facilitate processing and/or to improve their adhesive bonding. The chemical treatment, basically a chemical that is applied, must be spread and adhere to the surface so that it can withstand the shear forces encountered during processing and use. The deposition of the finishing material on the fibre surface will eventually change the surface properties, including the surface roughness and the surface energy, which directly influence the friction and adhesion behaviour. In composites, the adhesion between fibres or between fibres and matrix material is an important property as it influences the function of adhesive bonding between fibres in tow bundle, fibre to matrix and fibre coating.

In general, the surface energy of a solid can be determined through contact angle measurements between the solid and a series of test liquids. Several methods have been established to measure the contact angle of a solid surface, in the shape of a filament [1-4]. One of the most extensively used methods to measure the contact angle is the sessile drop method. Using this method, a proper amount of a liquid is dropped onto the solid surface. Then the contact angle is measured between the tangent to the liquid-vapor (LV) interface and the solid-liquid (SL) interface as shown in Figure 3.1.

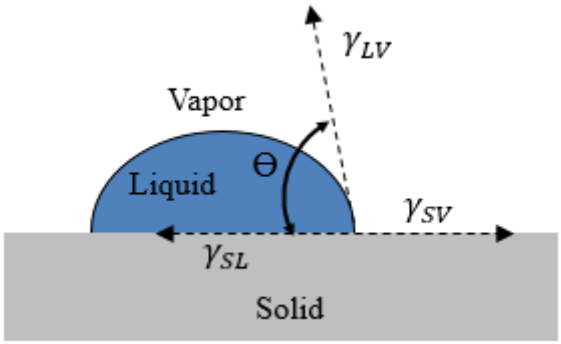

Figure 3.1 Contact angle measurement of a solid using sessile drop method [5].

This method is considered to be a static approach as the contact angle is measured of the static drop of the liquid on the fibre surface [6]. For a flat solid surface, measuring the contact angle using the sessile drop method is practical, but for a cylindrical shape surface such as a thin filament this method is quite challenging. Interestingly, a study done by Hao *et al.* [7] on modified aramid fibre surface using this method found that the volume of the liquid droplet influences the drop shape as well as the macroscopic contact angle between the drop and the fibre. Additionally, with a liquid that is prone to evaporation, measuring the accurate drop profile is difficult, leading to a poor reproducibility. For such a geometry, measuring the contact angle based on the Wilhelmy method is an alternative [8]. In this method, the contact angle is deduced from the wetting force which is measured during immersion and withdrawing the fibre from the liquid. According to the literature, this method has been applied on carbon [9-10] and basalt [11] fibres, but not on more flexible aramid fibres. Thus, in the next section, the experimental analysis of surface energy of a single aramid fibre utilizing the contact angle measurements using the Wilhelmy method will be discussed.

3.2 Materials

Three different types of Twaron® aramid fibres are used in this study. All fibres have been provided by Teijin Aramid B.V, Arnhem, The Netherlands. Table 3.1 shows the material properties of a single fibre. The A fibre is the standard fibre size while the OC is the fibre with larger thickness. Both A1 and A2 fibres are from the same fibre type. The only difference is that fibre A1 is a virgin fibre while the A2 fibre surface is treated with alkyl-phosphate salt. Three samples were tested for each fibre type. The samples are cut from the bobbin and directly measured. The length of each sample is approximately 10 mm.

The appropriate length is essential as a sample that is too long will cause the fibre to bend due to the low bending stiffness, thus the fibre will 'float' on the test liquid surface during the measurement. In order to assess the surface energy of the fibre, a set of liquids with a different range of polar and dispersive components has been used. The properties of the liquids are listed in Table 3.2.

Table 3.1 The material properties of Twaron® aramid fibre.

Properties	Unit	A1	A2	OC
Elastic modulus	GPa	109	109	29.3
Linear density	dtex	1.7	1.7	210
Breaking strength	mN	390	390	15400
Fibre diameter	um	12	12.2	140
Finish material		No	Alkyl-phosphate salt	Polyglycol ester

*linear density is the properties to express the size of the fibre in terms of mass per unit length.

Table 3.2 Properties of the test liquids.

Test liquid	γ_L (mN/m)	γ_L^d(mN/m)	γ_L^p(mN/m)	ρ(g/cm^3)	η(mPas)
n-hexane	18.43	18.43	0	0.6603	0.3080
distilled water	72.80	29.10	43.70	0.9982	1.002
ethylene glycol	48.00	29.00	19.00	1.1088	21.80

3.3 Results & discussion

3.3.1 Fibre surface characterization

The microstructure of the aramid fibres was examined using Scanning Electron Microscopy (SEM) and the roughness measurement in three-dimensional (3D) analysis was performed using a Nanosurf FlexAFM. The |Sq| parameter, the root mean square of the roughness over an area (3 µm x 3 µm), is calculated using the following formula [12]:

$$S_q = \sqrt{\frac{1}{A}\iint Z^2(x,y)\,dxdy} \tag{3.1}$$

Figure 3.3 shows the examples of a SEM image and an AFM image of the roughness measurement of the A1 fibre. The root mean square (RMS) value for roughness measured is Sq ≈ 1.6 nm. At microscopic scale, the roughness is present, but in the order of nm. More results on roughness measurement of the A2 and OC fibre can be found in Paper C.

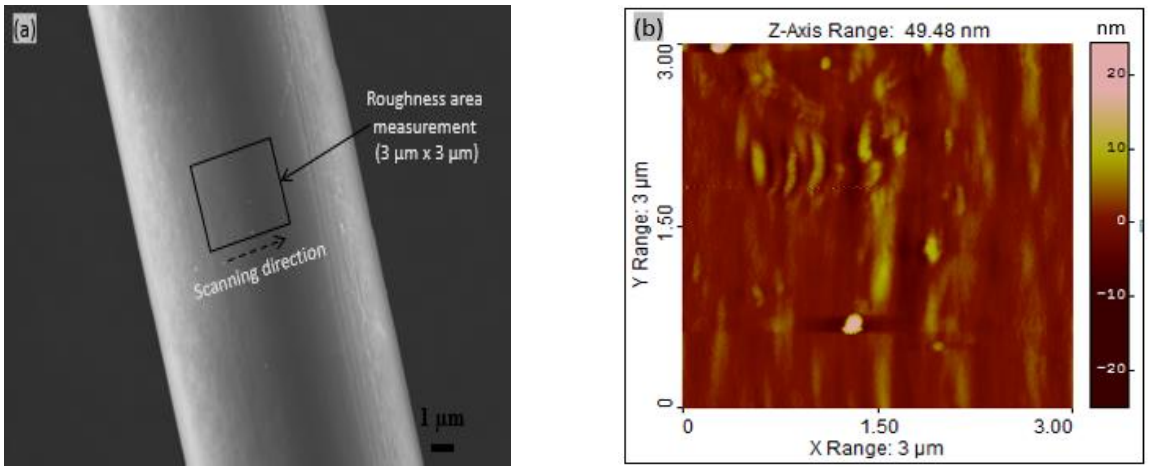

Figure 3.3 A1 fibre (a) SEM image and (b) Roughness measurement.

3.3.2 Contact angle measurement

In this study, the contact angle of single aramid fibre is determined based on the dynamic wetting force principle. The fibre is oriented perpendicular to the liquid interface and the force exerted on it during immersion and withdrawn due to wetting is measured by a tensiometer, as shown in Figure 3.2.

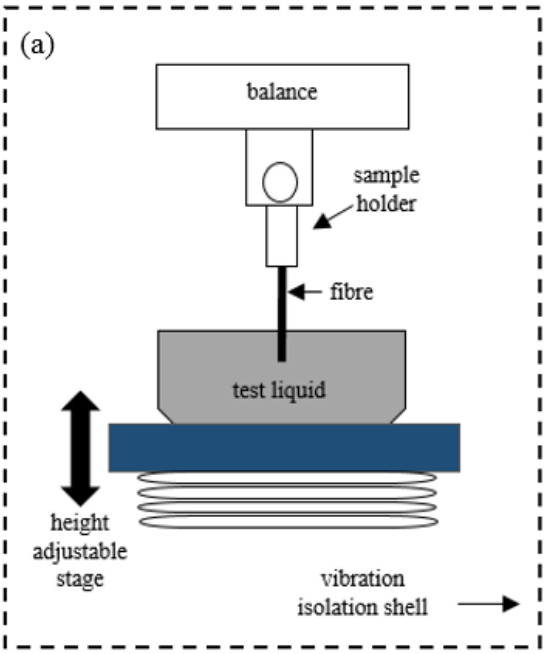

Figure 3.2 Experimental setup.

The total wetting force measured is a combination of the capillary force, buoyancy force and a mass which can be expressed as:

$$F_{wetting} = F_{capillary} - F_{bouyancy} + mass$$

$$= 2\pi R\gamma_L cos\,\theta - \rho g V_{immersed} + m_{fibre} g \quad (3.2)$$

where γ_L is the surface tension of the test liquid, R is the fibre radius and θ is the contact angle, m_{fibre} is the mass of the fibre, g is the gravitational acceleration, ρ is the density of the test liquid and $V_{immersed}$ is the immersed volume of the fibre. In this case, if 5 mm of fibre is immersed in distilled water, the buoyancy force is found to be in the order of 10^{-9} N which is very small and can be ignored in comparison with the capillary force, which is in the order of 10^{-5} N. Since the tensiometer is zeroed each time before starting the measurement, the mass contribution is zero. This means that the relationship between the force measured F and the contact angle θ becomes;

$$F_{wetting} = F_{capillary} = 2\pi R\gamma_L cos\theta \quad (3.3)$$

In this study, the dynamic contact angle measurements were performed using DCAT 11 by DataPhysics Instruments GmbH, with a resolution of 10^{-6} g and a lifting speed ranging from 0.7 um/s to 500 mm/min. The constant speed of 0.05 mm/s was used during both immersion and withdrawal of the fibre. According to Qiu and co-workers [10], a dynamic contact angle which is measured at a speed lower than 20 mm/min is considered to be a static advancing contact angle.

Figure 3.3 shows the typical force measured as a function of immersion depth of OC fibre type in water. The force signal is zero at the beginning as the fibre starts to approach the test liquid. There is a significant jump in the force signal at 1.2 mm in depth as the fibre starts contacting the test liquid surface and forming the contact angle. Afterwards, the force signal shows a steady value until reaching the desired depth. Then the reverse process takes place as the adjustable stage moves in the opposite direction and a steady force signal of receding angle is measured. When the fibre is out of the liquid as in Figure 3.4(a), the force signal continues to show a gradual increase. When reaching 0.8 mm, the force signal suddenly drops to zero which is exactly the same as at the beginning of the measurement. This behaviour was due to the ‘snap off’ between the fibre and the test liquid. A slightly higher force just before the ‘snap off’ was attributed to the meniscus force during separation between the fibre and the test liquid, as shown in Figure 3.4(b).

Table 3.3 shows the measurements for both advancing and receding contact angles. An average advancing contact angle of 65.1° was obtained for non-treated fibre A1. This is slightly higher than measured by Hao and co-workers (61.4°)[7] using a sessile drop method [12]. According to [3], the capillary force increases linearly with the diameter of the filament due to the higher wetted length, being linear with the diameter. Interestingly, our result shows that the fibre with a large thickness, the OC fibre type, has a lower contact angle than the A1 and A2 fibre type. It is believed that the lower contact angle may be due to the porosity of the OC fibre, as it is composed of microfilaments or thin fibrils. Further, it is noticed that the advancing contact angle is slightly higher than receding contact angles. These differences are defined as contact angle hysteresis (CAH). According to the literature, it is believed that this hysteresis is a thermodynamic irreversible process which is caused by several sources such as surface roughness [18], surface chemical heterogeneity [19], liquid adsorption and desorption [20] as well as molecular rearrangement [21]. In this study, it is unlikely that the primary cause of CAH is the surface roughness. From our AFM measurement results, the surface can be regarded as microscopically smooth with Sq being less than 5 nm for all fibres. The molecular

arrangement also cannot be connected to the CAH as the aramid fibre is a highly crystalline aromatic polymer which consists of immobile molecular chains [21]. Thus, one reason suggested in this study is that the CAH may be due to the surface chemical heterogeneity of the fibre.

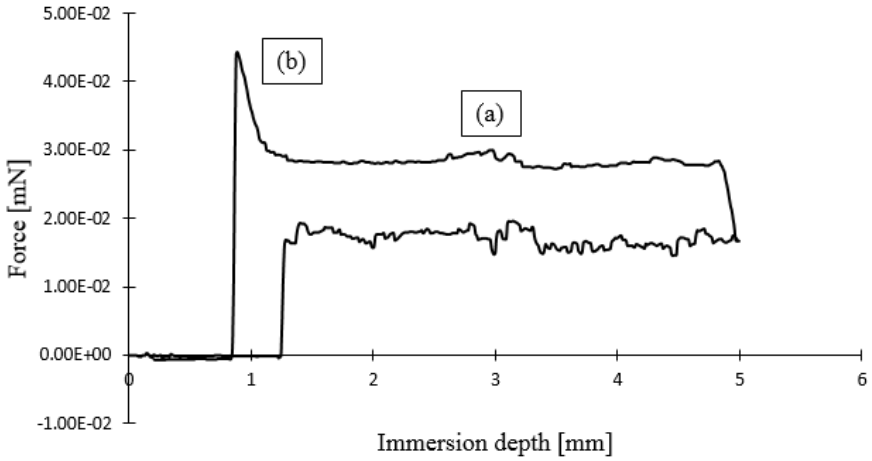

Figure 3.3 Typical force measurement for the OC fibre type in water.

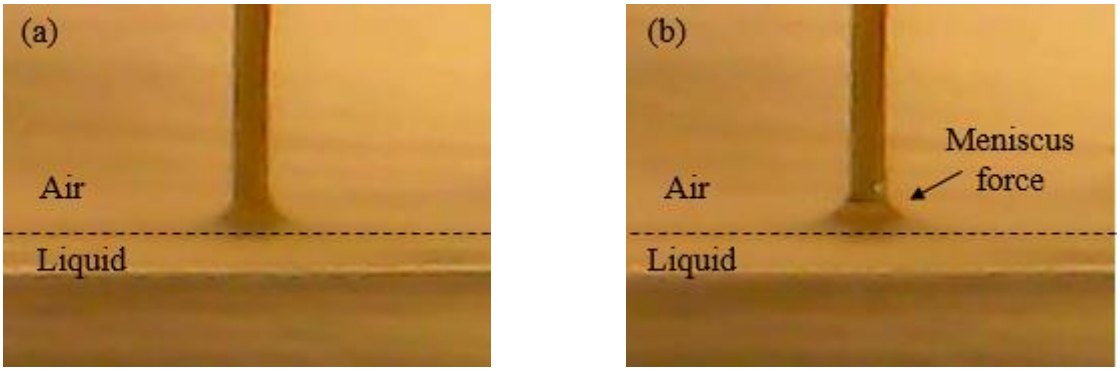

Figure 3.4 Real-time image of the meniscus formed between the OC fibre and water.

Table 3.3 The mean contact angle (CA) for all fibre type used in the experiment.

Fibre type	Contact angles (CA) ± SD		
	CA advancing	CA receding	CA hysteresis
A1	65.1 ± 1.4	41.9 ± 4.7	23.2
A2	61.3 ± 1.5	31.4 ± 5.6	29.9
OC	35.8 ± 0.9	12.5 ± 1.1	23.3

*SD = Standard deviation

3.3.3 Surface energy analysis

According to Young's equation [13], there is a relationship between the contact angle θ, the surface tension of the liquid γ_L, the interfacial tension between solid and solid γ_{SL} and the surface free energy γ_S of the solid which can be expressed as [13]:

$$\gamma_S = \gamma_L \cdot cos\theta + \gamma_{SL} \tag{3.4}$$

In order to be able to calculate the surface free energy of a single aramid fibre from the contact angle, the second unknown variable γ_{SL} must be determined. Building on the Fowkes method [14], the interfacial tension γ_{SL} is calculated based on the two surface tensions γ_S and γ_L and the similar interactions between the phases. These interactions are interpreted as the geometric mean of a dispersive part $\gamma^d$and a polar part γ^p of the surface tension or surface free energy, resulting in [15]:

$$\gamma_{SL} = \gamma_S + \gamma_L - 2\left(\sqrt{\gamma_S^d \cdot \gamma_L^d} + \sqrt{\gamma_S^p \cdot \gamma_L^p}\right) \tag{3.5}$$

The combination of equations (3.4) and (3.5) leads to:

$$\gamma_L(1 + cos\theta)/2\sqrt{\gamma_L^d} = \sqrt{\gamma_s^p}\sqrt{\frac{\gamma_l^p}{\gamma_l^d}} + \sqrt{\gamma_s^d} \tag{3.6}$$

The contact angle value is calculated from the capillary force using equation (3.2) and inserted in the Owens-Wendt equation, so resulting in equation (3.6) [15]. At least two liquids with known dispersive and polar parts of the surface tension are required to determine the surface free energy of the solid, where at least one of the liquids must have a polar part greater than zero. According to Chapman [16], using only two liquids results in an overestimation of the dispersive component and if more liquids are used, it increases the accuracy in the determination of the fibre surface energy [17].

Figure 3.5 shows a plot obtained by utilizing the values of contact angles to determine the surface energy of the A1 fibre for the three test liquids using the Owens-Wendt method. The result shows a reasonable agreement with the Owens-Wendt equation with a correlation coefficient above 0.85. Table 3.4 shows the surface energy of the A1, A2 and OC fibre with the dispersive and polar components obtained from Owens-Wendt analysis. The surface energy of the A1, A2 and OC fibre is 32.69 mJ m^{-2}, 44.69 mJ m^{-2} and 59.32 mJ m^{-2} respectively. Our result shows that the surface energy of A1 fibre (untreated) is lower than the surface energy of the untreated fibre measured in [22]. Their result shows that the surface energy of the untreated Twaron® aramid fibre is 50.6 mJ m^{-2} [22]. One possible reason for the difference is the fibre surface cleanliness. Our samples are directly tested without surface cleaning. The higher value for the polar component compared to a dispersive component in our results shows a good agreement with the values found in Gupta [23]. Also, it is found that treating the fibre surface with alkyl-phosphate salt increases the surface energy of the A fibre type with 27%.

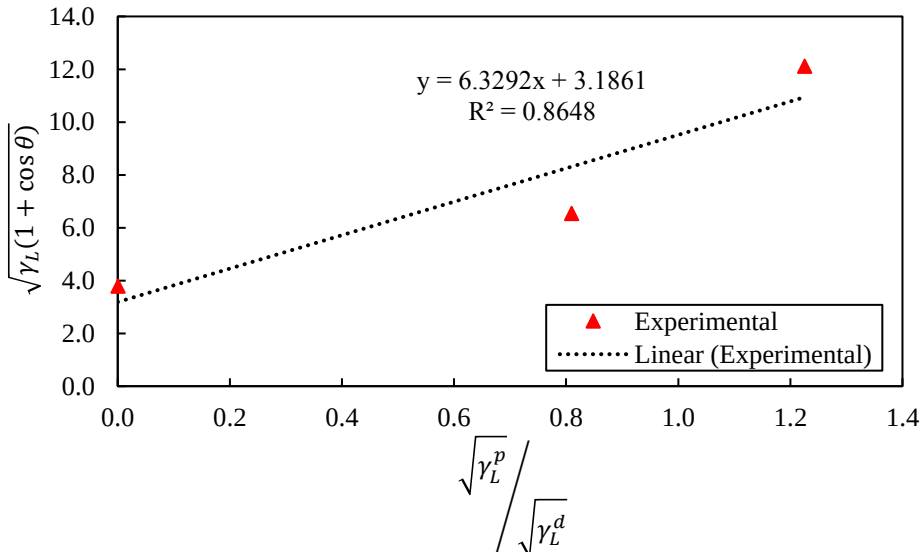

Figure 3.5 Linear fit for surface energy of the A1 fibre.

Table 3.4 The values of surface energy and its component (dispersive and polar).

Material	γ [mJ m^{-2}]	γ^d [mJ m^{-2}]	γ^p [mJ m^{-2}]
A1	32.69	15.01	17.68
A2	44.69	12.83	31.95
OC	59.32	14.6	44.72

3.4 Summary

The surface energy was determined by utilizing the dynamic contact angle measurements using the Wilhelmy method. The contact angle of three different Twaron® aramid fibres (A1, A2 and OC) is measured in a series of test liquids. The advancing contact angle is shown to be higher than the receding contact angle which causes the phenomenon of contact angle hysteresis. It is assumed that the hysteresis is due to the surface chemical properties such as the chemical heterogeneity which affects the difference in the advancing and receding contact angle. The surface energy of the Twaron® aramid fibres is mostly of polar character, exhibiting a hydrophilic behaviour.

References

[1] Miller B. Penn LS. Hedvat S. Wetting force measurements on single fibres. *Colloid Surfaces* 1983, 6(1); 49-61.

[2] Hseih Y-L. Wu M, Andres D. Wetting characteristics of Poly (p-phenyleneterephthalamide) single fibres and their adhesion to epoxy. *Journal of Colloid Interface Science* 1991; 144(1);127-144.

[3] van de Velde K. Kiekens P. Wettability and surface analysis of glass fibers, *Indian Journal of Fiber Textile Research* 2000; 25(1); 8-13.

[4] Barraza HJ. Hwa MJ. Blakley K. O'Rear EA. Grady BP. Wetting behaviour of Elastomer modified glass fiber, *Langmuir* 2001; 17(17); 5288-5296.

[5] Young T. III An essay on cohesion of fluids. *Philosophy Transaction Royal Society (London)* 1805; 5: 65.

[6] Yuan Y. Lee TR. Contact angle and wetting properties. *Surface Science* 2013; 51:3-34.

[7] Hao W. Yao X. Ke Y. Ma Y. Li F. Experimental characterization of contact angle and surface energy on aramid fibers. *Journal of Adhesion Science and Technology* 2013; 27(9): 1012-1022.

[8] Wu S. Polymer interface and adhesion. New York: Marcel Dekker; 1982. p.264.

[9] Si Q. Carlos AF. Dongxing Z. Aart Willem VV. David S. Wettability of a single carbon fiber. *Langmuir* 2016; 32:9697-9705.

[10] Jian W. Carlos AF. Dongxing Z. Xungai W. Aart WVV. David S. Wettability of carbon fibres at micro- and mesoscales. *Carbon* 2017; 120:438-446.

[11] Monica FP. Maria CS. Pierre-Jacques L. Fabrizio S. Jacopo T. Sylvain D. Surface characterisation and wetting properties of single basalt fibres. *Journal of Composite Part B* 2017; 109:72-81.

[12] ASME B46-1. Surface texture, surface roughness, waviness and lay. 2002.

[13] Young T. III An essay on cohesion of fluids. *Philosophy Transaction Royal Society (London)* 1805; 5: 65.

[14] Fowkes FM. Contact angle, wettability and adhesion. *American Chemical Society* 1964: 99.

[15] Owens DK. Wendt RC. Estimation of the free surface energy of polymers. *Journal of Applied polymers Science* 1969; 13: 1741-1747.

[16] Chapman II GB. Non-destructive Evaluation of adhesive bonds using 20 MHz and 25 kHz ultrasonic frequencies on metal and polymer assemblies. Author House, ISBN 978-1-4969-2553-4. 2014.

[17] Pasquini D. Belgacem MN. Gandini A. da Silva Curvelo AA. Surface esterification of cellulose fibres: characterization by drift and contact angles measurement. *Journal of Colloid Interface Science* 2006; 295(1): 79-83.

[18] Huang F. Wei Q. Wang X. Xu W. Dynamic contact angles and morphology of PP fibres treated with plasma. *Polymer Testing* 2006; 25; 22-27.

[19] Neumann AW. Contact angles and their temperature dependence: thermodynamic status, measurement, interpretation and application. *Advance in Colloid and Interface Science* 1974; 4:105-191.

[20] Timmons CO. Zisman WA. The effect of liquid structure on contact angle hysteresis. Journal of Colloid Interface *Science* 1966:22; 165-171.

[21] Lynn SP. Bernard M. A study of the primary cause of Contact Angle Hysteresis on Some Polymeric Solid. *Journal of Colloid and Interface Science*. 1980; 78(1): 238-241.

[22] Jia C. Chen P. Liu W. Li B. Wang Q. Surface treatment of aramid fiber by air dielectric barrier discharge plasma at atmospheric pressure. *Journal of Applied Surface Science* 2011; 257:4165-4170.

[23] Gupta BS. Textile fiber morphology, structure and properties in relation to friction. In: Gupta BS (ed) *Friction in Textile Materials*. Woodhead Publishing Limited, Cambridge, 2008.

Chapter 4

Friction Force Measurements in Fibre-Fibre Contacts

4.1 Introduction

In this chapter, a new experimental setup to measure the friction force between single fibres will be discussed. The friction force measurements were performed on the vacuum adhesion friction tester (VAFT) using several types of Twaron® aramid. These measurements were carried out in ambient conditions. The effects of several parameters on the friction force have been studied. The bending stiffness of the bottom fibre is controlled by controlling the pre-tension load. This method was used to analyze the effect of pre-tension on the friction force. The results are compared with the theory of taut wire as explained previously in Chapter 2. The fibre orientation of the top fibre has also been controlled to study the effect of the crossing angle on the friction force. The Hertzian contact model both at point (perpendicular) contact and elliptical contact as discussed in Chapter 2 have been used to correlate the friction force with the calculated contact area between the fibre surfaces. The effect of elastic modulus and normal load have been studied too. The surface energies of the fibres that were determined in Chapter 3 are used to relate the surface energy with the friction behaviour. The basis of the sections that are discussed below is constructed in accordance with the results of Paper A, B and D.

4.2 Materials

The properties of six types of Twaron® aramid fibres are listed in Table 4.1. In this study, the standard commercial aramid fibre (ST), low Young's modulus fibre (LM), high Young's modulus fibre (HM), the untreated (A1) and treated fibre type (A2) and large fibre thickness (OC) are used. Initially, the fibres were in the form of a tow bundle (see Figure 4.1(a)), with each yarn consisting of 1000 fibre filaments. Then the fibres were manually separated into a single filament; its Scanning Electron Microscope (SEM) image is shown in Figure 4.1(b). The samples were cut into specific a length according to the experimental needs using special cutter which was also provided by the manufacturer. The sample was cut three metres from the front end of the bobbin in order to make sure that the fibre was clean and undamaged.

Table 4.1 Manufacturer data of the material properties of the aramid fibres used in the friction experiments.

Description [unit]	ST	LM	HM	A1	A2	OC
Elongation at break [%]	3.2	4.4	2.9	3.2	4.4	2.9
Linear density [dtex]	1.7	1.2	1.6	1.7	1.7	210
Young's modulus [GPa]	99	60	115	109	109	29.3
Breaking strength [mN]	420	260	400	390	390	15400
Fibre diameter [µm]	12.2	10.8	11.9	12	12.2	140
Finish material	-	Alkyl-phosphate salt	Alkyl-phosphate salt	None	Ethoxylated /propoxylated butanol	Polyglycol ester

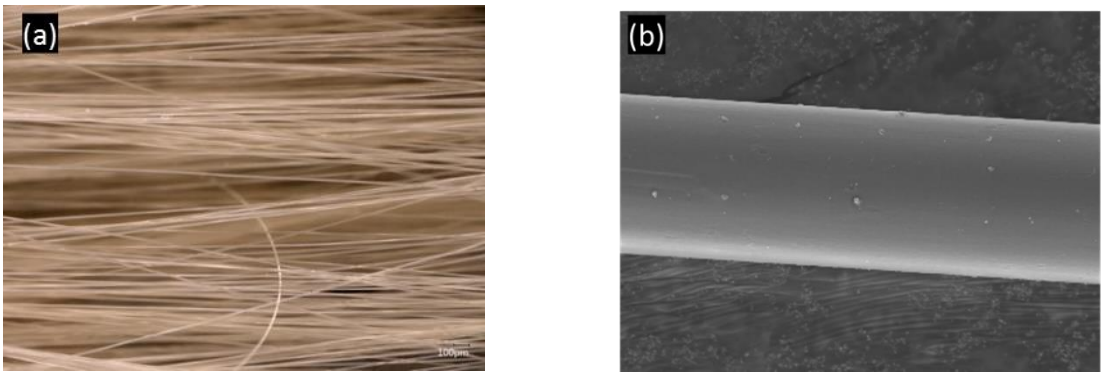

Figure 4.1 (a) Scanning electron microscope (SEM) fibre in tow bundle and (b) single fibre image.

4.3 Measurement setup and experimental procedure

Figure 4.2 shows the schematic of the experimental setup, crossed fibre arrangement and real experimental setup in VAFT to measure friction between two single fibres. The setup consists of a top and bottom holder to hold the fibres, a XY linear stage to place the lower holder and two capacitive sensors to measure normal and friction force along the *z* and *x* axis respectively. The resolution of the two capacitive sensors is 1 nm with a measuring range up to 50 µm. Both sensors are mounted on the force measuring mechanism (FMM). The forces are calculated based on the spring stiffness concept, in which deflection in the FMM is measured in *x* and *z* direction. A detailed explanation of the FMM can be found in Yaqoob [1]. With this load controlled setup, the maximum normal load that can be applied is 100 mN with an accuracy of 8 µN.

Since one of the main objectives of this study is to determine the effect of pre-tension on friction force, a pre-tension load is applied to the fibres. However, it is controlled only at the bottom fibre, while for the top fibre a minimal pre-tension is applied just to prevent the fibre from slacking. This had to be done due to the small length (2 mm) of the top fibre. A low viscosity glue type, Loctite 401 was used for gluing the fibre at fibre holders. One end of the bottom fibre is initially glued to a holder, then the other end is connected to a cable lug. The function of the cable lug is to clamp the end of the fibre into a loop shape so that the dead weight can be hooked to it to induce the pre-tension to the fibre. After the glue at the first end is cured, the dead weight is loaded to the fibre. Then the other end is glued. Next, the dead weight is removed after the glue is cured.

(a)

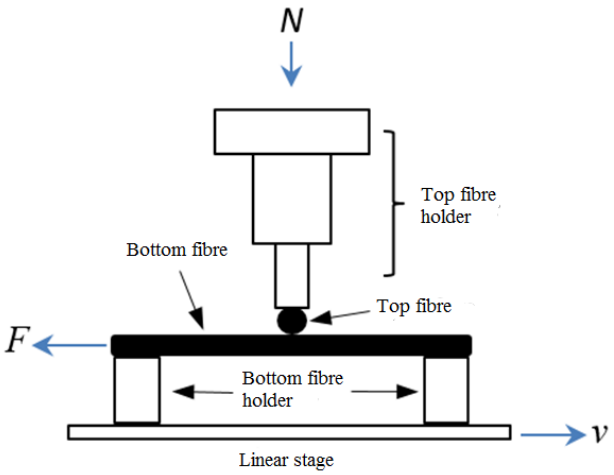

(b)

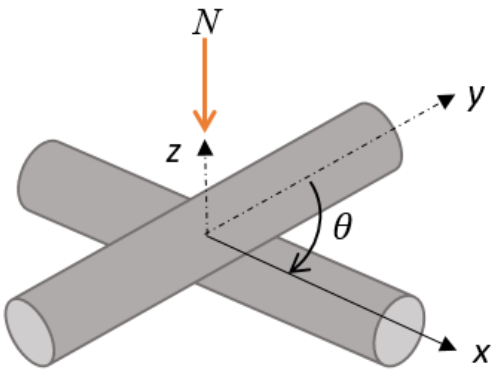

(c)

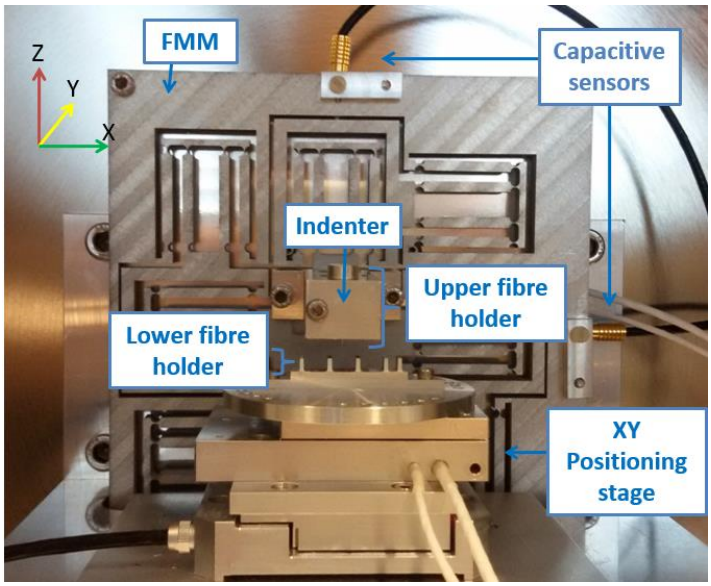

Figure 4.2 (a) Schematic description of friction experiment between fibres (b) crossed fibres arrangement (c) real experimental setup.

The top fibre orientation was controlled as well. While controlling the pre-tension of the bottom fibre, the top fibre is rotated clockwise to introduce a crossing angle during sliding. In this study, the friction force between two fibres is measured at a crossing angle of 30°, 40°, 50°, 75° and 90° under various normal and pre-tension loads.

Before starting the friction measurement, both fibres need to be brought into initial contact. During this procedure, no initial load is applied; therefore the normal and friction forces are zero just before the contact is made. The top fibre is moved downward approaching the bottom fibre slowly at a speed of 0.01 mm s^{-1} to find the rough contact. The speed is reduced to 0.001 mm s^{-1} until a few microns prior to contact. With the approach procedure, there is no deformation due to the applied load in the FMM system before contact is made, so the measured normal load is close to the applied load. Once the initial contact is reached, the desired normal load is applied to the contact. While the load is applied, the fibres start to deform as shown in Figure 4.3. The friction force is measured as the bottom fibre is sliding against the top fibre in *x* direction with the help of the linear stage. Multi-pass friction loops are executed to determine the repeatability and running-in effects. The measurements are repeated five times for data repeatability purposes. Three samples are tested for each crossing angle for reproducibility purposes. The parameters were used for the friction force measurement are listed in Table 4.2.

Table 4.2 Parameters that are used for friction measurements.

Description	symbol	value	units
Normal load	N	1- 50	mN
Pre-tension load	T	10-300	mN
Sliding speed	v	2	µm/s
Crossing angle	θ	30-90	degree
Sliding distance	d_f	100	µm
Fibre length		Top fibre: 2	mm
		Bottom fibre: 6	mm
Number of friction cycles		5	

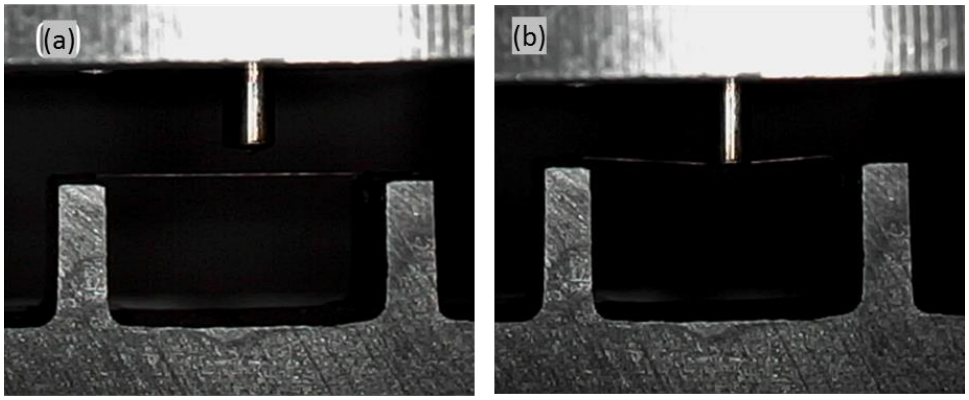

Figure 4.3 Normal load applied to the fibre (a) unloaded (b) loaded.

All friction measurements have been carried out in ambient with temperature of 20°C ± 2°C and 30% - 40 % RH. In this study, the experiment is repeated with three samples by replacing the bottom fibre while the top fibre is kept constant throughout the measurements of the similar fibre type. Figure 4.4 shows a typical friction force signal measured. To complete one friction cycle, the fibre is set to slide with a stroke of 100 µm both in forward and backward direction, as shown in Figure 4.4. At the first 10 µm of sliding distance, the friction force signal shows a transient response when the normal load is applied to the contact fibres. This is due to the lateral stiffness of the friction force mechanism (FFM) and the deformation of the contact. After reaching the desired normal load, the fibre starts sliding and the friction signal becomes stable. The pattern of the friction curve during forward and backward direction is similar, showing that the value of the friction measured is the same in both directions. To complete one friction test, the friction cycle is repeated five times. However, due to the potential effect of contamination, the average friction force is calculated based on the next four cycles only (cycle numbers 2 – 5) both during forward and backward sliding within a sliding distance of between 20

and 80 µm. It can be seen from the Figure that the variation between each cycle is very small. Also, Figure 4.5 gives the different samples (1, 2 and 3) under the same conditions (T = 50 mN, N = 10 mN), showing that the standard deviation is less than 0.1 mN. This demonstrates that the experiments have very a good reproducibility.

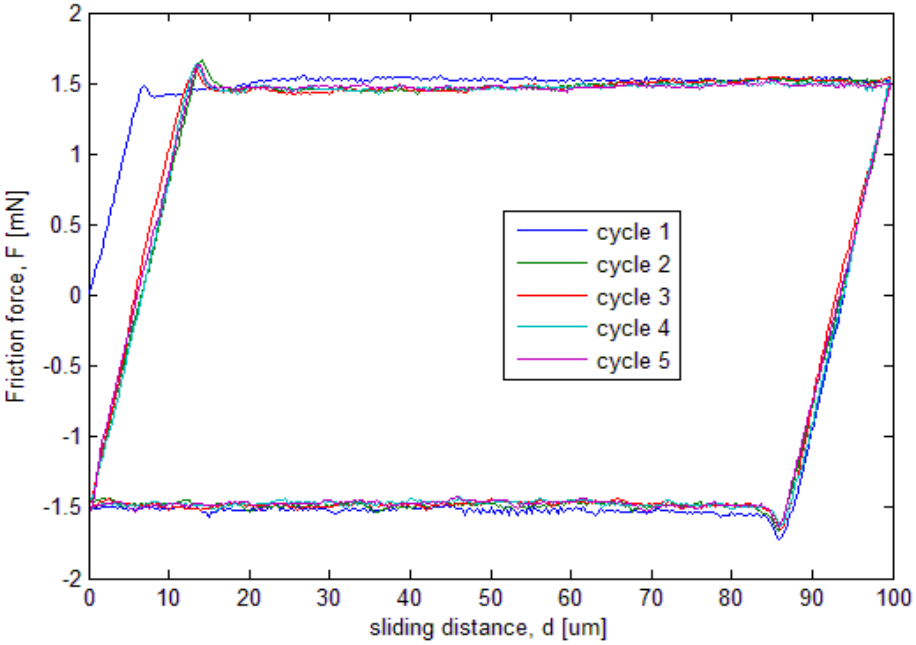

Figure 4.4 Typical friction force measured, N= 10 mN, T = 50 mN, v = 0.002 mm/s and θ = 90°.

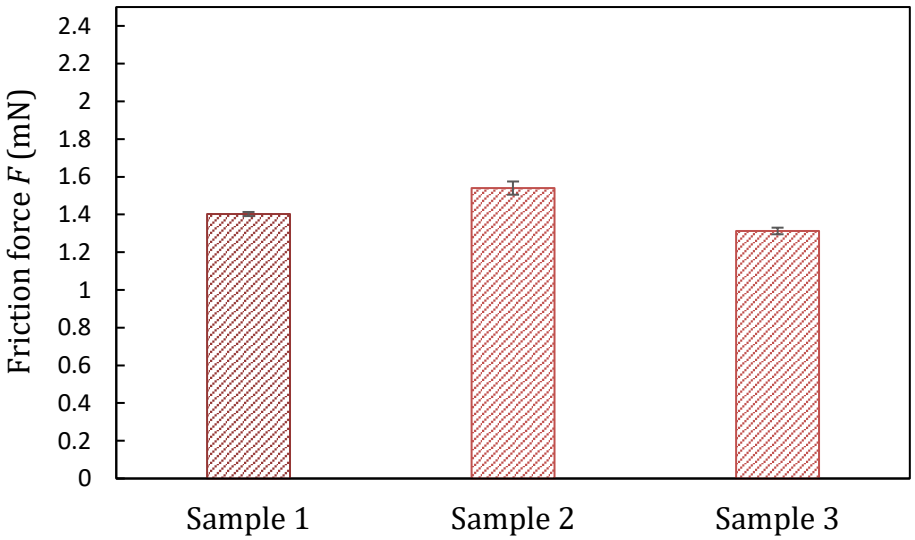

Figure 4.5 Friction force measured between three samples.

4.4 Result & discussion

4.4.1 The effect of the pre-tension load

Figure 4.6 gives the average friction force measured at various pre-tension load and normal load of the HM fibre. The results show that the friction force is reduced with increasing pre-tension load.

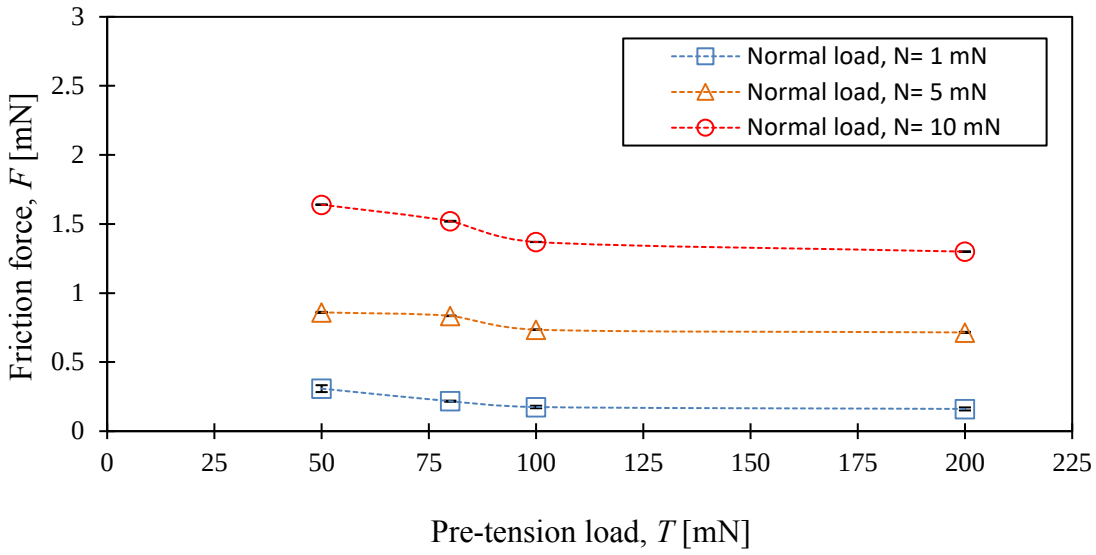

Figure 4.6 Friction force as a function of pre-tension load at various normal load of the HM fibre, v = 0.002 mm/s and θ = 90°.

Here, the theory of the taut wire model as described in Chapter 2 is used to analyse the 'wrapping effect' between the fibres. The deflection of the fibre due to the pre-tension load and normal load is measured during the experiments and the predicted value of the fibre deflection is calculated using equation (2.20) as described in Chapter 2. Figure 4.7 gives the comparison of the predicted and experimental results on the fibre deflection of the HM fibre. The result shows that the calculated value of the fibre deflection is always lower than the measured value. Note that the experimental values represent the total deflection of both top and bottom fibre, while the theoretical value only predict the deflection of the bottom fibre. So, the difference between the experimental and predicted values is a measure of the deflection of the top fibre.

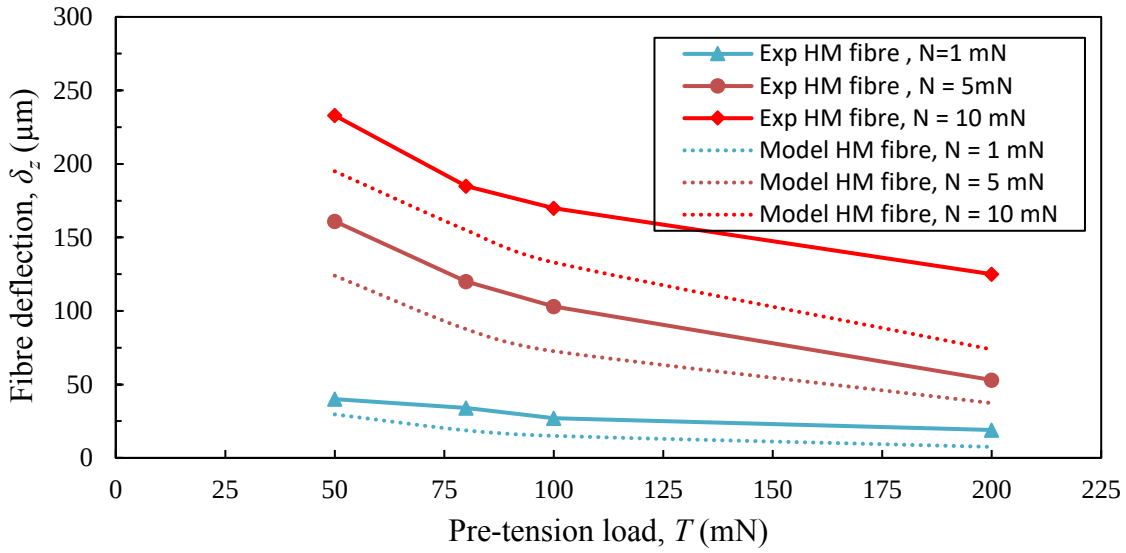

Figure 4.7 Comparison of the predicted and experimental results on the fibre deflection.

From Figure 4.7, it also can be seen that the fibre deflection is reduced with increasing pre-tension load. This means that as the pre-tension load increased, the 'bending stiffness' of the fibre is also increased, resulting in a lower fibre deflection. This will potentially reduce the conformability of the contact between the fibres and directly reduce the area of contact between the fibres and the friction force. With the information of the fibre deflection, the contact length between fibres can be calculated using the theory of the taut wire [2] as formulated in Chapter 2. The equation of the contact length is rewritten as follows:

$$a_\delta = \sqrt{x^2 + (-\delta_z - y)^2} \tag{5.1}$$

where a_δ is the half contact length, δ is the fibre deflection and x and y are the intercept point in coordinates which is determined using the equations (2.22) and (2.23) of Chapter 2. From calculations, it is found that at 50 mN pre-tension load with 1 mN applied normal load, the contact length between the fibres is only about 0.1 μm. When this value is compared with the radius of the contact due to elastic deformation using the Hertzian contact model as described in equation (2.9) of Chapter 2, it is found that the contact radius between the fibre-fibre contact is about 1.3 μm, which is greater than the contact length due to the 'wrapping effect'. This means that although the pre-tension affects the

macroscopic bending of the fibre, the role of pre-tension on the contact area is small in comparison to the elastic deformation in fibre-fibre contact (see Figure 4.8).

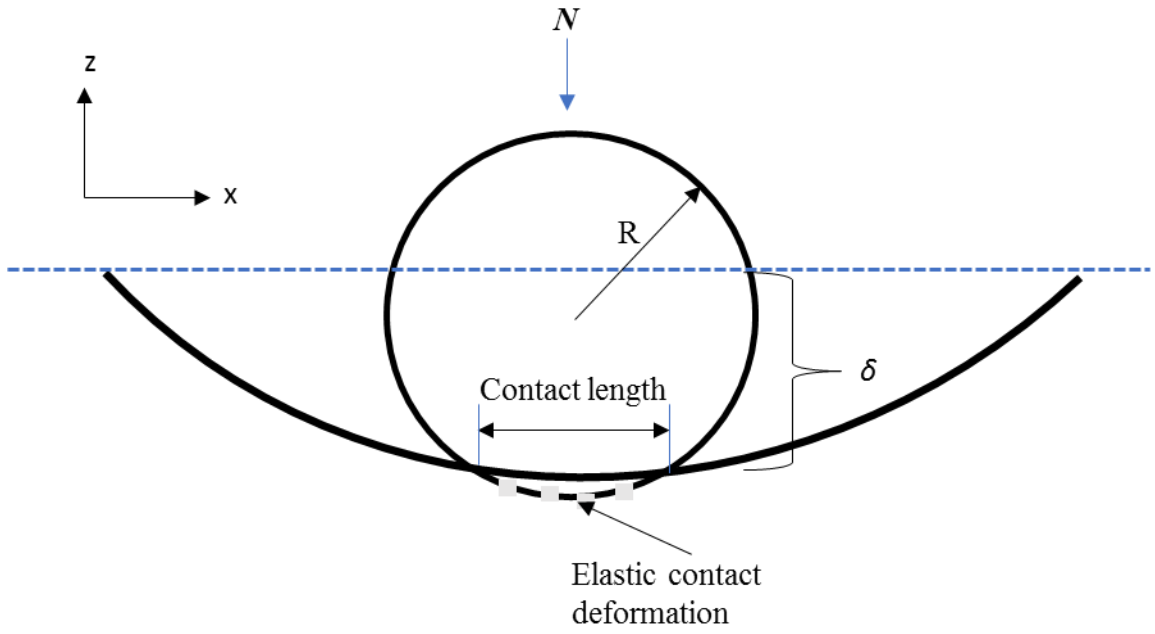

Figure 4.8 Illustration of the contact length due to the 'wrapping effect' and elastic contact deformation.

4.4.2 The effect of crossing angle

In the previous section, it is found in the case of a perpendicular contact that although pre-tension influences the bending stiffness of the fibre as well as the contact length, the elastic deformation in fibre-fibre contacts due to normal load is the dominating effect in the formation of the contact area and of the friction force. In this section another parameter, the fibre orientation (crossing angle), is studied. Here, the effect of crossing angle – the interdependency between pre-tension and fibre crossing angle – is evaluated.

Figure 4.9 shows the fibre deflection of the A2 fibre as a function of the pre-tension load at various crossing angles at 10 mN normal load. Note that the fibre deflection is measured during the experiment based on the load-displacement data given by the sensor. Results show that at a constant pre-tension load, the fibre deflection is nearly constant with increasing crossing angle. But due to the 'wrapping effect', the fibre deflection is decreased with increasing pre-tension load. This is in agreement with Figure 4.10 where the friction force decreases with increasing pre-tension load. It is observed that although

the pre-tension influences fibre deflection, the value of the friction force is not very different.

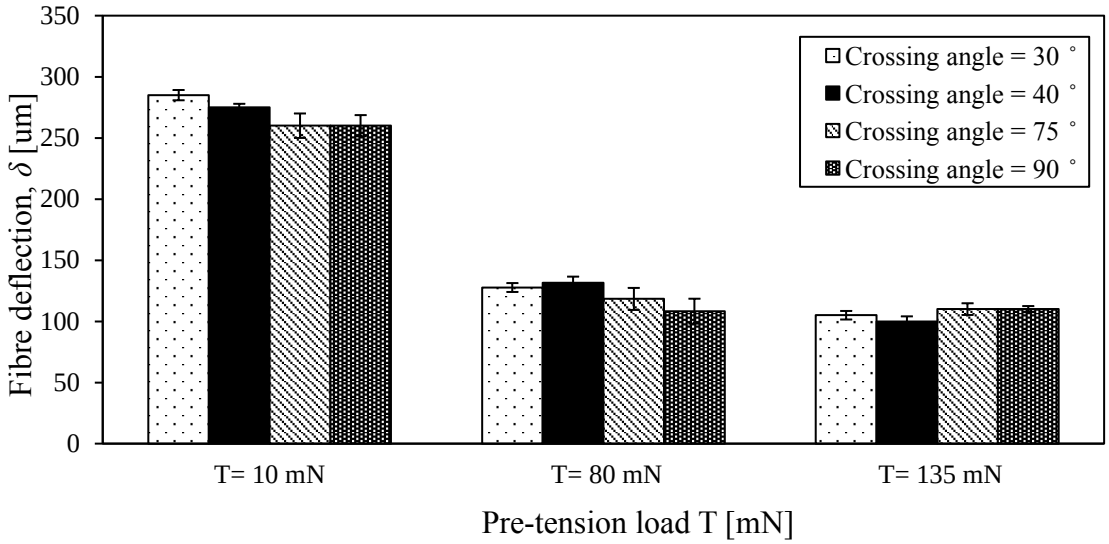

Figure 4.9 Fibre deflection as a function of pre-tension load at 10 mN normal load.

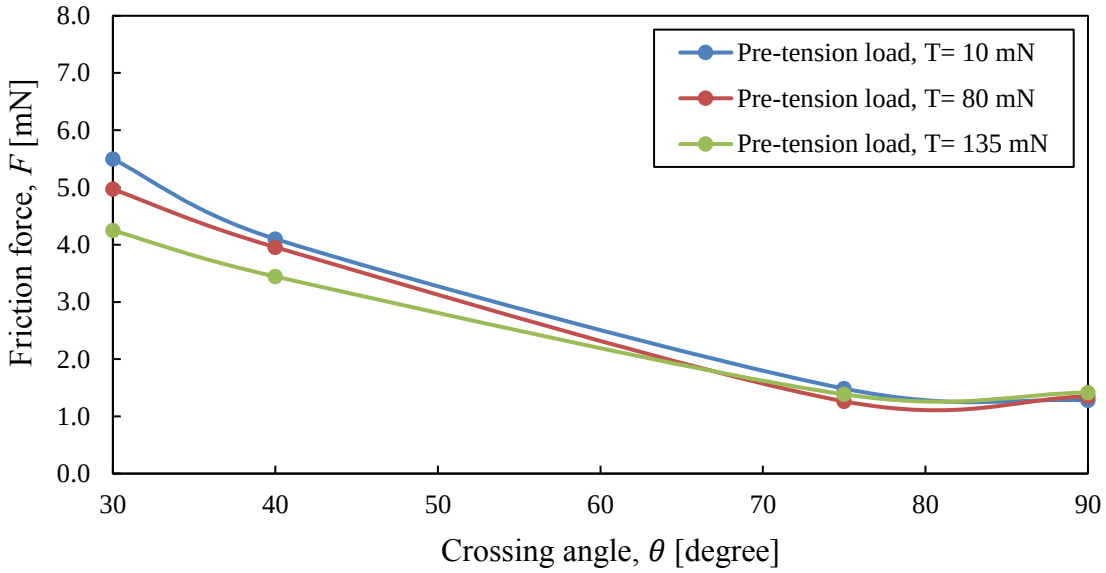

Figure 4.10 Friction force as a function of the crossing angle at various pre-tension load (with standard deviation less than 0.05 mN).

Using equation (5.1), it is found that the maximum calculated contact length at high normal load (15 mN) and low pre-tension load (10 mN) is about 1.3 µm. As the crossing angle tends to affect the friction due to the elastic deformation in the contact as described by Hertz, the validity of the Hertzian assumption on the size of the contact radius due to the effect of crossing angle is calculated. The minimum value of the contact radius at high

normal load (10 mN) is about 2.18 µm, which is less than the radius of the fibre of 6.1 µm but higher than the contact length predicted with the taut wire model (1.3 µm). So, it is suggested that when considering the friction and contact behaviour at different crossing angles, the effect of pre-tension can be ignored as the fibre bending stiffness influence is small. In this case, the crossing angle affects friction and not the pre-tension. This means that the elastic deformation in the contact, as for example described by Hertz, can be used to explain the frictional behaviour in contrast to a 'wrapping effect' as discussed in taut wire theory. Therefore, the Hertzian elliptical contact model is used to relate the friction force behaviour with the size of the contact area between fibres as the crossing angle changed. The approximate method that is proposed by Greenwood [3] is used to calculate the contact area. So, the contact area between fibres at crossing angles between $0° < \theta < 90°$ is calculated by finding the length of the semi-axes a_{ell} and b_{ell} [3] as described in Chapter 2 and rewritten as follows:

$$a_{ell} = \left(\frac{3k_{ell}^2 \varepsilon N R_e}{\pi E^*}\right)^{\frac{1}{3}} \qquad b_{ell} = \left(\frac{3\varepsilon N R_e}{\pi k_{ell}^2 E^*}\right)^{\frac{1}{3}} \tag{5.3}$$

where k_{ell} is the axis ratio (a_{ell}/b_{ell}), ε is an ellipticity ratio, *N* is the normal load, R_e is the effective radius, E^* is the contact modulus and *R* is the fibre radius. The axis ratio is $k_{ell} = 1.0339({}^{R_b}/_{R_a})^{0.636}$ and the ellipticity ratio, $\varepsilon = 1.0003 + 0.5968\left({}^{R_a}/_{R_b}\right)$.

Figure 4.11 shows the theoretical calculations of the contact area *A* as a function of the crossing angle for the A2 fibre. From the calculations, the contact area is reduced significantly as the crossing angle between the fibres increases. The reduction of the area of contact with the crossing angle shows an agreement with the friction force results depicted in Figure 4.12. The friction force is reduced with the crossing angle at 135 mN pre-tension load at a standard deviation less than 0.03 mN. This shows that the crossing angle has a significant effect on the area of contact between the fibres at a high pre-tension load. More results can be found in Paper D.

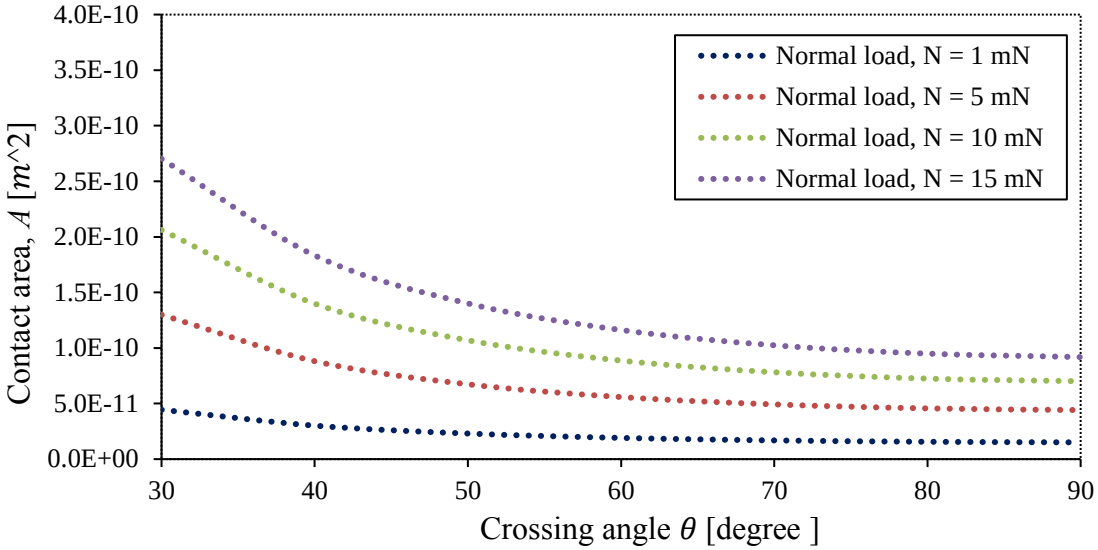

Figure 4.11 Contact area *A* between two fibres in contact as a function of the crossing angle at various normal loads.

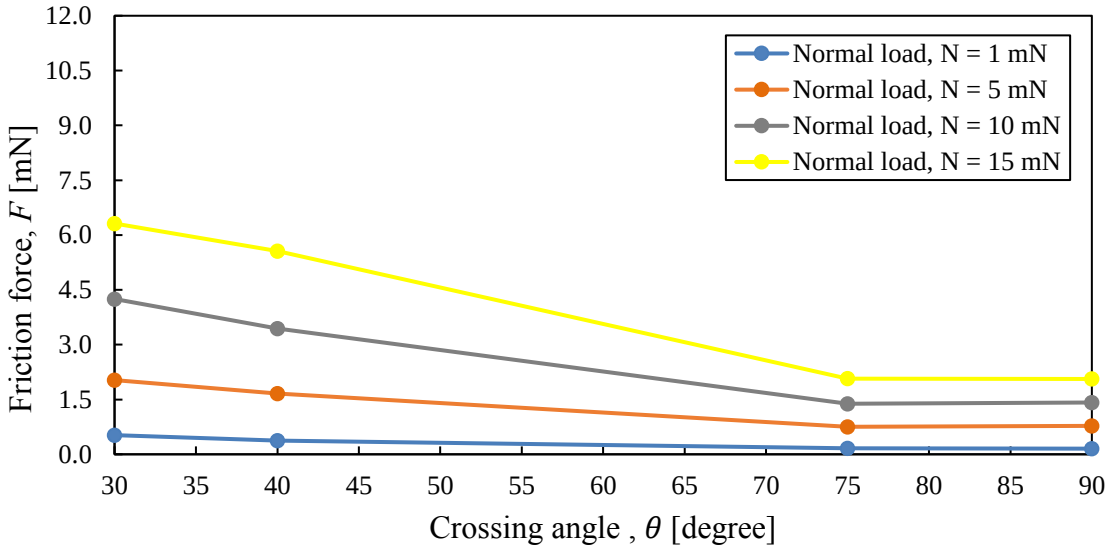

Figure 4.12 Friction force as a function of the crossing angle of the A2 at 135 mN pre-tension load.

4.4.2.1 Friction force model comparison

Using the friction model $F = \tau A + P$, equation (2.38) in Chapter 2, the predicted friction force is calculated and compared with the experimental results by ignoring the ploughing effect, P and choosing a fitting and constant value for the interfacial strength τ. Results are shown in Figure 4.13. In this model, the value of interfacial shear strength τ used is 10 MPa and 20 MPa [5]. The straight line indicates the measured friction force in the experiment and the dotted line shows the predicted friction force. The normal load that is

applied to the fibres is 10 mN at 135 mN pre-tension load. It can be seen that the value of τ = 20 MPa appears to fit the friction force result.

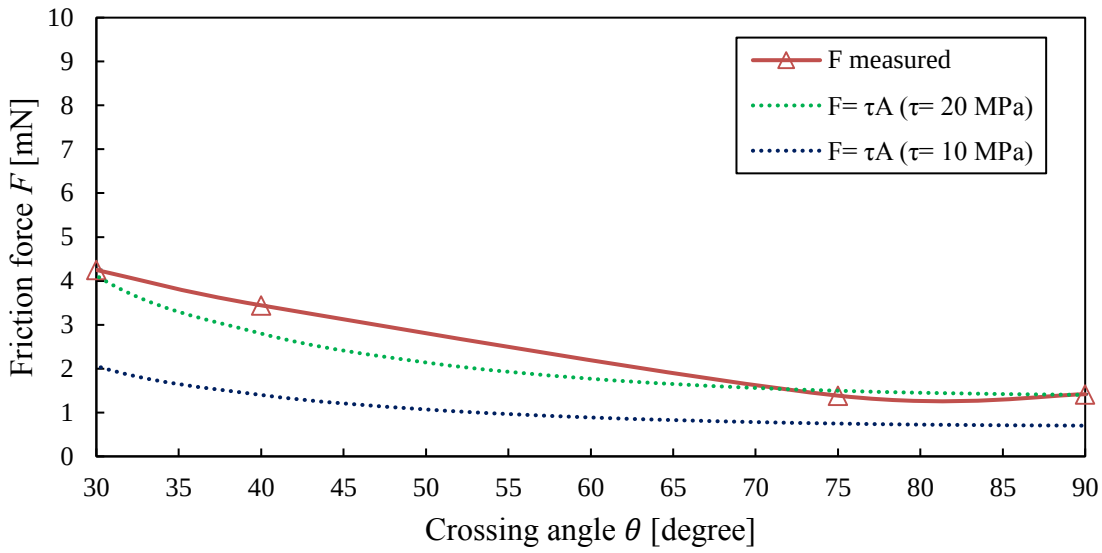

Figure 4.13 Predicted friction force as a function of crossing angle for various τ values.

4.4.3 The effect of elastic modulus

Figure 4.14 shows the friction force of low and high modulus fibre with similar sizing under 50 mN pre-tension at varying normal load. The friction force of the low modulus (LM) fibre type is found to be slightly higher than the high modulus (HM) fibre type under similar conditions. The fibre with low elastic modulus has a lower bending stiffness; therefore during loading the LM fibre generates a large deformation in the area of contact and consequently increases the friction force. According to Gupta [6], the resistance to bending is determined by:

$$Resistance\ to\ bending = \left[\frac{1}{4\pi\beta_0}\right]\frac{\varepsilon E d^2}{\rho} \tag{5.4}$$

where ε is the shape factor, E is the modulus, d is linear density, ρ is the density and β_0 is a constant that depends on the units in which E, d and ρ are expressed. Here it can be seen that, apart from the elastic modulus, there are other parameters which influence the fibre bending stiffness and elastic deformation in contact. Due to these interdependent parameters, measured friction forces are found to differ by 34%.

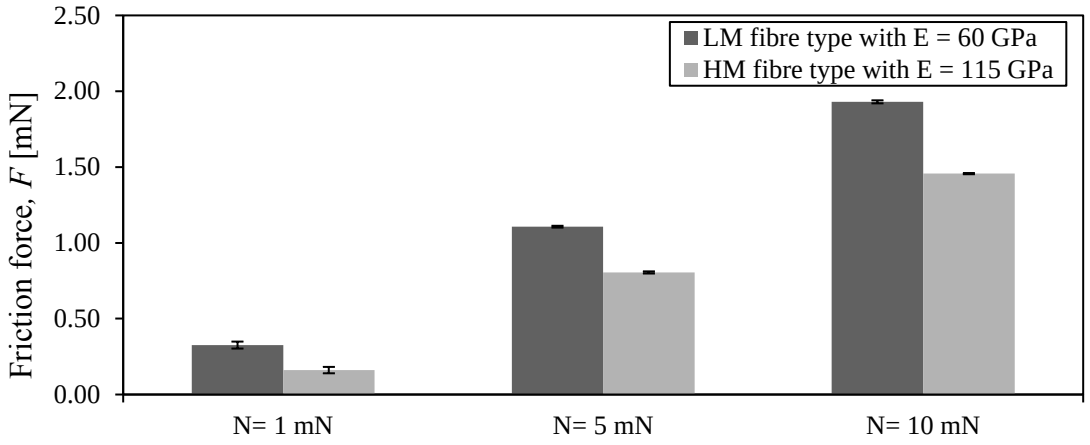

Figure 4.14 The effect of elastic modulus in friction force of two different fibre types under 50 mN pre-tension loads.

4.4.4 The effect of normal load

Figure 4.15 shows the friction force as a function of normal load at various pre-tension loads at $\theta = 90°$. The same normal load range has been used by Tourlonias *et al.* [7] on a contact between single carbon fibres. In the range of normal loads used, the friction force is approximately proportional to the normal load, although for the determination of the exact behaviour more data points would be needed. Our results are also in agreement with [8], where also the friction force has been found to approximately follow Coulomb's law.

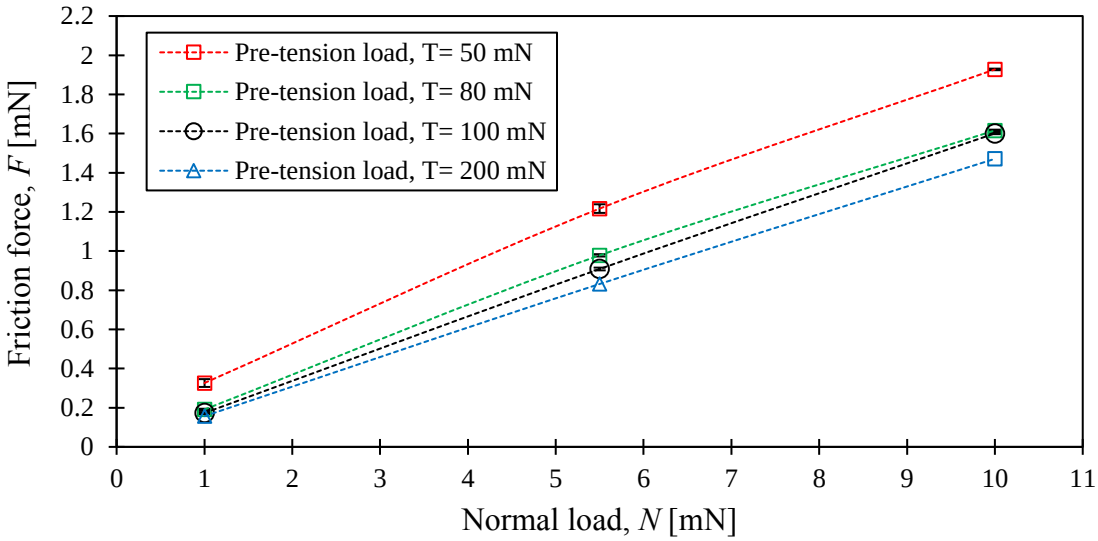

Figure 4.15 Friction force as the function of normal load for HM fibre type, $\theta = 90°$.

4.4.5 The role of surface energy with friction between two single aramid fibres in contacts

When the surfaces of the fibres are brought into contact, a tangential force is required to initiate a motion between the fibres. This force is composed of the applied normal force as well as the adhesion force. According to most adhesion models including Johnson-Kendall-Robert (JKR) [9], Derjaguin-Muller-Toporov (DMT) [10], and Maugis-Dugdale (MD) [11], the adhesion force is proportional to the role of adhesion. One fundamental property for work of adhesion is the surface energy. Therefore, it is interesting to correlate the role of surface energy found in Chapter 3 to the frictional behaviour between two single aramid fibres.

Table 4.3 shows the coefficient of friction results of the A1 and A2 type of fibre. It can be seen that the coefficient of friction of A1 (untreated fibre) is slightly lower than of A2 (treated fibre). Since the friction force is proportional to the area of contact i.e. $F = \tau A$ [12,13], assuming there is no ploughing taking place at the contact interface, friction is caused only by the shear in the microcontact. Assuming a certain value for τ as the shear strength in the contact interface, a large area of contact (at equivalent pressures) results in a higher friction force i.e. higher coefficient of friction. Here, the interfacial bond strength per unit area at the fibre-fibre interface could be related directly to the surface energy per unit area γ of a fibre as done in [14]. In a perpendicular contact, the area of contact between two interacting fibres, *A*, can be easily derived from the JKR circular contact model as described earlier in Chapter 2 and rewritten as [9]:

$$A_{JKR} = \left(\frac{3\pi R^*}{4E^*}\right)^{2/3} \left(N + 3\pi\Delta\gamma R + \sqrt{6\pi\Delta\gamma RN + (3\pi\Delta\gamma R)^2}\right)^{2/3} \tag{5.6}$$

Table 4.3 Friction measurement results.

Fibre type	A1	A2	OC
Normal load [mN]	Coefficient of friction, μ	Coefficient of friction, μ	Coefficient of friction, μ
10	0.135	0.142	0.170
15	0.128	0.132	0.150

The theoretical values of the area of contact between fibres obtained from the JKR theory at 10 mN and 15 mN applied normal load are shown in Table 4.4.

Table 4.4 Estimation of the contact area interfaces obtained from the JKR contact model.

Normal load applied, N [mN]	Area of contact, A_{JKR} (m^2)	
	10	15
A1	1.854×10^{-11}	2.425×10^{-11}
A2	1.877×10^{-11}	2.455×10^{-11}
OC	9.851×10^{-11}	1.281×10^{-10}

Using this information, the role of the fibre's total surface energy within the contact interfaces, which is the product of the surface energy per unit area γ and the area of contact, A, was assessed. The results of the surface energy γA have been used to correlate with the coefficient of friction μ. Figure 4.16 shows the coefficient of friction for fibre interactions as a function of the total surface energy in the area of contact of A1 and A2. For the same amount of the applied load to the contact (N = 10 mN, T = 10 mN), the coefficient of friction of the A1 fibre is found to be lower than that of the A2 fibre. At 10 mN normal applied load, the total surface energy of fibre in area of contact, the γA for the A1 fibre is estimated to be 6.06×10^{-13} J. However, for the A2 fibre the γA is about 1.4 times larger than the A1. Certainly, if the γ is low, the interfacial strength per unit area is weak and so does the adhesion and friction force.

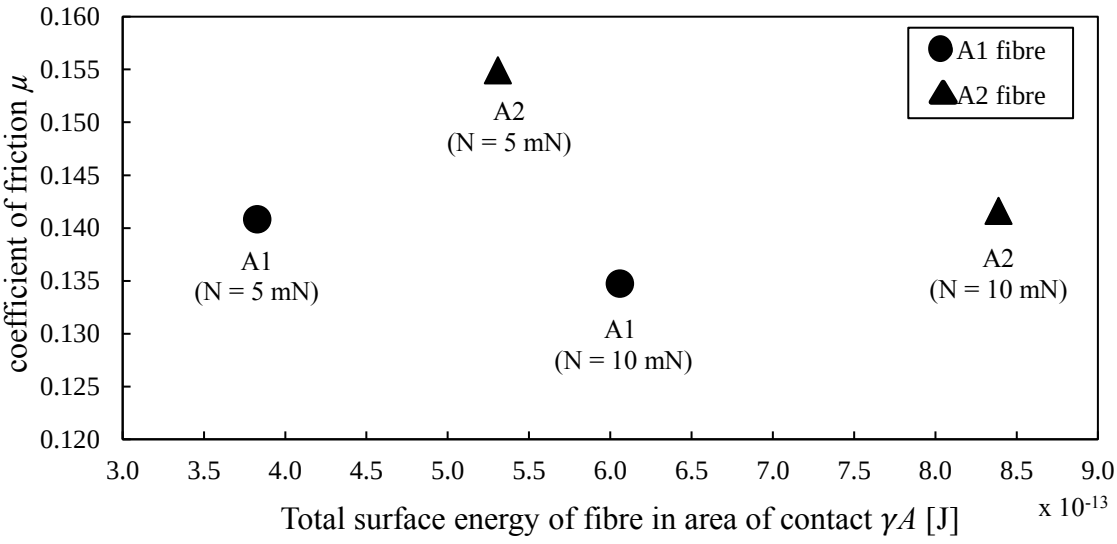

Figure 4.16 Coefficient of friction as a function of total surface energy of fibre in area of contact at 10 mN and 15 mN normal applied load.

The size of the fibre thickness also influences the total surface energy of fibre in the area of contact. Table 4.5 shows the result of the total surface energy of fibre in area of contact between two treated fibres, the A2 and OC with different thickness, 12 µm and 140 µm, respectively. Note that fibre with a larger thickness generates a larger contacting area and consequently produces a higher total surface energy in the area of contact. From Table 4.5 it can be seen that at a specific normal applied load the OC fibre has a higher total surface energy than the A2 fibre.

Table 4.5 Effect of the fibre thickness in total surface energy of fibre in the area of contact.

Fibre type	A2	OC
Fibre thickness [µm]	12	140
Normal load [mN]	γA (μ)	γA (μ)
10	8.39 x 10^{-13} J (0.142)	25.5 x 10^{-13} J (0.170)
15	11 x 10^{-13} J (0.132)	155 x 10^{-13} J (0.150)

A high surface energy at the contact would result in a high adhesive bonding in normal direction and thus it can be expected that a high friction force is required to break the bond in tangential direction. Thus, the coefficient of friction μ is shown to be approximately proportional to γA as was also done by Miyoshi [14] in a study between ceramic-metal couples in vacuum. To reduce friction, the total surface energy between the fibre contact interfaces must therefore be minimized.

4.5 Summary

The newly developed experimental setup to measure the friction force between fibres has been discussed. The designed setup is capable of measuring the friction force of single fibres under pre-tension at various crossing angles. Using this developed setup, the friction signal shows good data reproducibility with a very small variation of the friction force in between the different cycles of the friction experiment. The results from surface characterization shows that the roughness of the fibre surface reduces when the pre-tension load is applied. Also, the pre-tension load changes the bending stiffness of the fibre and influences the fibre deflection during loading. A high pre-tension increases the fibre stiffness and reduces the fibre deflection as well as the contact length between the fibres. However, this ‘wrapping effect’ is small in comparison with the elastic deformation in the fibre-fibre contact. Therefore, it is assumed that the friction force is governed by elastic

contact deformation and the contribution of the ‘wrapping effect’ is relatively small. The effect of the crossing angle on the friction force was studied by performing experiments on the A2 fibre at 135 mN pre-tension load. The results show that the friction force reduces as the crossing angle increases. Since it is difficult to measure the contact area between fibres, the contact area due to the changes in crossing angle in these experiments is calculated using the approximate Hertzian elliptical contact model, and in these experiments, it has been found to be larger than the wrapping length, showing that contact deformation dominates over the wrapping length. The predicted contact area can be related to the measured friction force if a constant shear stress in the contact is assumed. The constant interfacial shear strength properties τ = 10 MPa and 20 MPa are used to predict the friction force of the A2 fibre at different crossing angles. For these values, it has been found that friction model result fits the measured friction force. The elastic modulus also influences the friction force as a lower E modulus will result in more deformation and therefore a larger contact area. Also, within the tested normal load range, the friction force is found to approximately follow Coulomb’s law. Finally, the total surface energy between the fibre contact interfaces has been correlated with the friction force measured.

References

[1] Yaqoob MA. de Rooij MB. Schipper DJ. Design of a vacuum based test rig for measuring micro adhesion and friction force. *WTT Transaction and Built Environment*, 2012; (14):261–274.

[2] Charles I. *Applied mechanics for engineers*. The Cambridge University Press 1951:54-66.

[3] Greenwood JA. Analysis of elliptical Hertzian contacts. *Tribology International* 1997; 30[3]: 235-237.

[4] Johnson KL. *Contact mechanics*. Cambridge Uni Press. 1985.

[5] Cornelissen B. Rietman B. Akkerman R. Frictional behaviour of high performance fibrous tows: friction experiments. *Composites Part A: Applied Science and Manufacturing* 2013; 44:95–104.

[6] Gupta BS. Textile fiber morphology, structure and properties in relation to friction. in Friction in textiles materials. Ed. Gupta Bs. Woodhead Publishing. 2008.

[7] Tourlinas M. Bueno M-A, Poquillon D. Friction of carbon tows and fine single fibers. *Composites Part A: Applied Science and Manufacturing*. 2017; 98: 116-123.

[8] Mulvihill D. Smerdova O. Sutcliffe M. Friction of carbon fibre tows. *Composites Part A: Applied Science and Manufacturing* 2016; 93:185–198.

[9] Johnson KL. Kendall K. Roberts A D. Surface energy and the contact of elastic solids. *Proceeding Royal Society London A* 1971, 324: 301–313 4

[10] Derjaguin BV. Muller VM. Toporov YP. Effect of contact deformations on the adhesion of particles. *Journal of Colloid Interface Science* 1975, 53: 314–325 5

[11] Maugis D. Adhesion of spheres: The JKR-DMT transition using a Dugdale model. *Journal of Colloid Interface Science* 1992, 150: 243–269.

[12] Bowden FP. Tabor D. *Friction and lubrication of solids*. Oxford, Clarendon Press. 1954.

[13] Bowden FP. Tabor D. *Friction: An introduction to tribology*. Anchor Press. New York.1973.

[14] Miyoshi K. Considerations in vacuum tribology (adhesion, friction, wear, and solid lubrication in vacuum). *Tribology International* 1999; 32; 605-616.

Chapter 5

Adhesion Force Measurements

5.1 Introduction

This chapter discusses the experimental results of the adhesion force between fibres using the atomic force microscope. The adhesion force between fibres is measured at various relative humidity levels and fibre orientations (crossing angle). The AFM tipless cantilever was functionalized by attaching a small fibre sample to create a fibre on fibre contact condition. In this chapter, the experimental setup and procedures will be discussed. Further, the adhesion force measured will be compared with the theoretical calculations. The content of this chapter is based on paper E.

5.2 Materials

Twaron® aramid fibre without surface finishing (untreated fibre) with a linear mass density of 1.6 dtex supplied by Teijin Aramid B.V (The Netherlands) have been used in this study. The axial modulus of elasticity of the fibre is 109 GPa. The transverse modulus of the fibre is much lower and is equal to 1.6 GPa. The diameter of the fibre used is 12 µm. AFM roughness measurement on the fibre surface revealed a rms roughness of 1.6 nm over a scan size of 3 µm x 3 µm.

5.3 Modified cantilever

A tipless cantilever (TL-FM from Nanosensors) has been functionalized by directly attaching a small piece of Twaron® aramid fibre to it. A small amount of two-component adhesive epoxy resin was spread over the cantilever tip. Then the aramid substrate was glued to the tip using the motorized micromanipulator and was left for at least 24 hours to fully cure the epoxy. Figure 5.1 shows the modified tip including the small piece of the Twaron® aramid fibre attached.

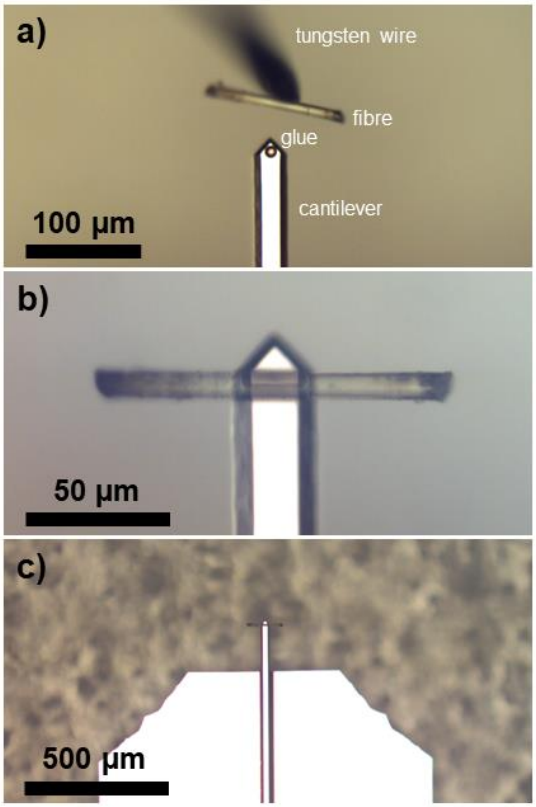

Figure 5.1 Modified cantilever attached with Twaron® aramid fibre using a micromanipulator: (a) A fibre being transferred to the cantilever and (b, c) Fixed at its final position by UV-cured glue.

5.4 Adhesion force measurements and tip calibration

The adhesion force measurements were carried out using the Multimode 8 AFM with the Nano Scope V controller and JV scanner (Bruker). The schematic setup can be found in Figure 5.2. At first, it is important to calibrate the deflection stiffness of the modified tip with attached aramid fibre on a rigid material. In this calibration procedure, a cleaned silicon wafer is used as a reference sample. After the deflection sensitivity is calibrated, the spring constant of the modified tip is measured. The deflection sensitivity of the modified tip measured is between 73.81 nm V^{-1} to 105 nm V^{-1} and the spring constant is between 2.52 Nm^{-1} to 3.23 Nm^{-1}.

To perform adhesion force measurements between two single fibres, a second fibre sample is glued on the silicon wafer using double-sided tape (Tesafix, Tesa AG, Germany) and that wafer is later fixed on a small plate using the same double-sided tape. The fibre is placed randomly on the wafer to emulate various crossing angles between the modified tip and the fibre sample during the measurements. The modified tip is brought into contact with the fibre by extending the piezo vertically, then retracting the piezo and calculating the

force required to separate from the fibre. For each sample, the adhesion force measurement is repeated three times in which each force was an average of 200 measurements. All measurements were performed in room temperature (21°C ± 1°C).

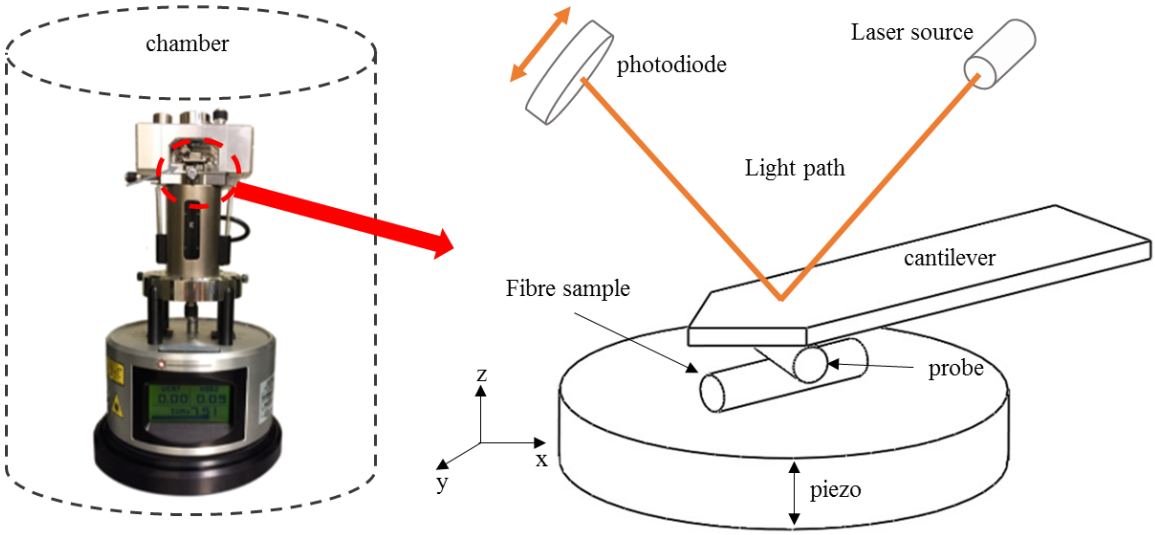

Figure 5.2 A schematic setup of the crossed fibre-fibre arrangement used in the AFM.

5.5 Result & discussion

5.5.1 The effect of relative humidity

The relative humidity dependence on the adhesion force was explained in Section 2.3.2. A theoretical model based on a sphere-sphere contact geometry was discussed for fibres in perpendicular contact. The adhesion experiments were performed to compare the capillary force measured with the theoretical calculations. A humidity chamber has been used to house the AFM (see Figure 5.2). The RH was measured using the humidity sensor which is placed in the chamber. The RH is controlled by flushing a stream of mixed (pure) N_2 and N_2 saturated with water vapor into the chamber. As mentioned in [1], water is considered in a structured form or an ordered form until 3 monolayers of water molecules. Only at higher thickness values there is a transition from ordered to bulk behaviour and consequently meniscus behaviour. Thus, at low RH, the Kelvin equation cannot be used to calculate the adhesion force. The force acting on the sphere (see Figure 5.3) due to the meniscus formation (capillary neck) when the meniscus is in equilibrium was shown in Section 2.3.1 and rewritten as follows [2]:

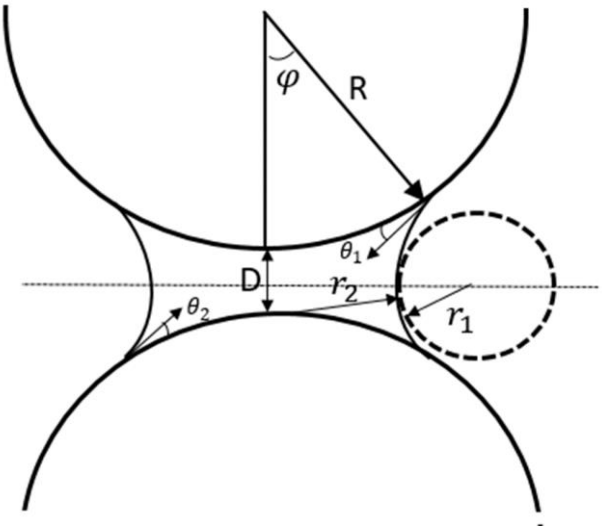

Figure 5.3 Geometry of the sphere-sphere contact with a meniscus formation [3].

$$F_c = F_s + F_p \tag{5.3}$$

$$F_p = -P_{cap}\pi({r_2}^2 - a^2) = -\left[-\frac{R_g T}{V_m} log\left(\frac{p}{p_s}\right)\right]\pi(R^2 - sin^2\varphi - a^2) \tag{5.4}$$

$$F_s = -2\pi\gamma_L r_2 \sin(\theta_1 + \varphi) = -2\pi\gamma_L R \sin\varphi sin(\theta_1 + \varphi) \tag{5.5}$$

where F_c is the total adhesion force, F_p is the capillary pressure since the pressure inside the capillary is lower than the pressure in the other vapour phase, F_s is the surface tension force, θ_1 is the contact angle, φ is the filling angle and *a* is the contact radius of the solid-solid contacting surfaces which can be calculated using e.g. Hertz theory [4].

Figure 5.4 shows the variation in the force measured to separate two single aramid fibres at perpendicular contact. The adhesion force is plotted as a function of relative humidity. At low RH (≤ 50%), the adhesion force is constant. However, at 50% RH and above, there is a significant increase in adhesion force. Studies done on several other materials including glass and silicon surfaces also show that there is a significant effect of RH on the capillary force [5-6]. In those experiments, the adhesion force shows a clear threshold at around 30 – 40% RH. Also, according to [7], between 1 - 40% RH no capillary neck is developed, and the adhesion is dominated by the van der Waals force. At 40% RH, a capillary neck is

formed and between 40 – 70% RH, the adhesion force is formed by both van der Waals and capillary forces. In this regime the adhesion force increases with increasing RH. Sample B is further analyzed using two different procedures; (i) a force measurement from low RH to high RH, (ii) a force measurement from high RH to low RH to evaluate the reproducibility of the results, but also to analyze potential non-equilibrium effects in the experiments. Figure 5.5 shows the result of the adhesion force as a function of relative humidity for increasing and decreasing RH. Here, it is found that both ways give the similar trend thus it can be suggested that the experimental error due to the measurement procedure is relatively small and there is no hysteresis effect due to e.g. the contact not being in equilibrium at a certain humidity. Thus, it can be concluded that for aramid fibre-fibre contact, capillary neck formation is started at about 50% RH, with the *Kelvin radius*, r_k is close to 2 nm.

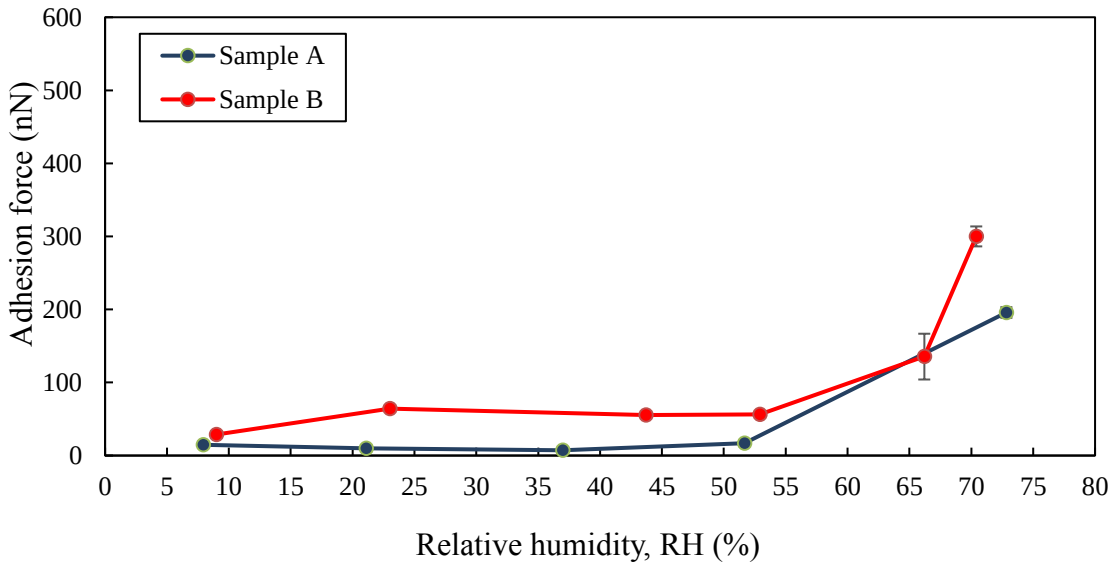

Figure 5.4 The effect of relative humidity on adhesion force between single aramid fibres.

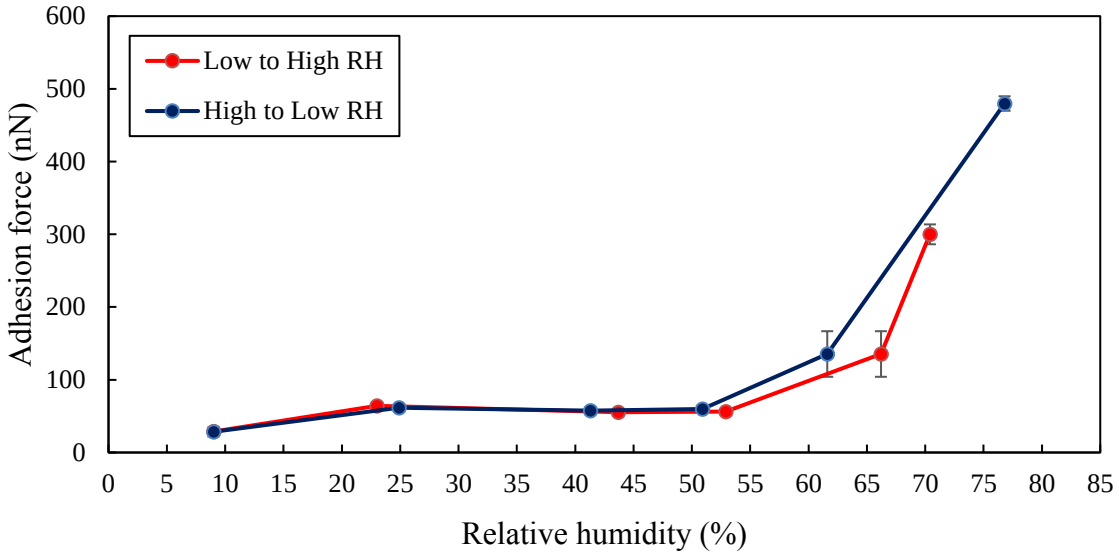

Figure 5.5 Validation on the experimental procedures for sample B.

To compare the experimental results obtained, the total capillary force at high relative humidity level (77% RH) is calculated using the model as mentioned above. The filling angle φ is calculated implicitly using Young-Laplace and Kelvin equations along with the geometrical analysis of the sphere-sphere contact as shown in Figure 5.3 and is given as [3];

$$\frac{\Delta p}{\gamma_L} = \left(\frac{1}{r_1} + \frac{1}{r_2}\right) = -\frac{R_g T}{V_m \gamma_L} log\left(\frac{p}{p_s}\right) \tag{5.6}$$

$$-\frac{R_g T}{V_m \gamma_L} log\left(\frac{p}{p_s}\right) = \frac{\cos(\theta_1 + \varphi) + cos\theta_2}{D + R(1 - cos\varphi)} + \frac{1}{R\ sin\varphi} \tag{5.7}$$

Assuming the distance between the spheres, D is 0.2 nm, the filling angle φ at 77% RH can be calculated to be 1.54°. The calculated adhesion force, which is dominated by the capillary force, can be calculated to be equal to 6.17 x10^{-7} N while the measured adhesion force is equal to 4.79 x10^{-7} N. So, the calculated force is relatively close to the measured value. A possible reason that the measured adhesion force is less than predicted by the model might be surface roughness, which for these fibres is in the order of nanometres as discussed before in Chapter 3.

5.5.2 The effect of crossing angle in dry conditions

To study the effect of the crossing angle on the adhesion force, the measurements have been performed at dry conditions or at very low humidity level. At this condition, the van der Waals force is dominating the capillary force. The experiments have been carried out on randomly oriented fibres at 8% RH. The example of the crossing angle configuration between the modified tip and the fibre sample is shown in Figure 5.7(a). The crossing angle is considered as the angle between the fibre that is attached to the tip and fibre sample. Figure 5.8 shows the adhesion force as a function of the crossing angle. It can be seen that the experimental values of the adhesion force are reduced as the crossing angle between the fibres in increased. According to Hertz's contact model [4], when two identical cylinders are brought into contact at 90° with respect to each other, the geometrical shape of the contact area would be circular and if the cylinders are parallel to each other, the contact zone takes a rectangular shape. However, if the cylinders are brought into contact at different angles within the limits above, the contact area is expected to have an elliptical shape as in Figure 5.7(b). Within this limit, the adhesion is found to increase as the contact area increase i.e. the crossing angle reduces [8]. Thus, in this study it is assumed that the crossing angle changes the contact area of the fibre-fibre contact interface and influences the adhesion force. The finite contact area between fibres has been explained using Johnson-Kendall-Roberts (JKR) contact model [9] in Section 2.3.2 as:

$$A_{JKR} = \pi\left(\frac{3R}{4E^*}\right)^{2/3}\left(N + 3\pi\Delta\gamma R + \sqrt{6\pi\Delta\gamma RN + (3\pi\gamma\Delta R)^2}\right)^{2/3} \tag{5.8}$$

where R is the fibre radius, E^* is the contact modulus, N is the normal load and $\Delta\gamma$ is the work of adhesion. In this model, it is assumed that the adhesive force is within the contact area and therefore the force to separate the surfaces at point contact ($\theta = 90°$) can be calculated using the following equation [9]:

$$F_a = \frac{3}{2}\pi\Delta\gamma R \tag{5.9}$$

where $\Delta\gamma$ is the work of adhesion and R is the relative radius. For elliptical contacts ($0° < \theta < 90°$), Johnson and Greenwood [10] have extended the JKR for a point contact

theory to the general elliptical adhesive contact model. In this model, it is assumed that the contact area remains elliptical, but the eccentricity varies continuously with load. The adhesion force is substantially less than the value for a point contact and can be calculated as follows [10];

$$F_{adh} = 2\pi a_{ell} b \left[P_1 - \frac{1}{3}\left(\alpha {a_{ell}}^2 + \beta {b_{ell}}^2\right)\right] \tag{5.10}$$

where P_1 is the pressure (5.11), α and β are the pressure coefficients (5.12) and, a_{ell} and b_{ell} are the semi-major and minor axes of the elliptical adhesive contact [10].

$$P_1 = \frac{\alpha {a_{ell}}^{5/2} - \beta {b_{ell}}^{5/2}}{{a_{ell}}^{1/2} - {b_{ell}}^{1/2}} \tag{5.11}$$

$$\alpha = \frac{E^*}{2b_{ell}\ R_e}\alpha' \text{ and } \beta = \frac{E^*}{2b_{ell}\ R_e}\beta' \tag{5.12}$$

$${a_{ell}}^{2/3} = 2R_e \sqrt{\frac{2\Delta\gamma}{\pi E^*}} \frac{(b_{ell}/a_{ell})^{\frac{1}{2}}(1 - (b_{ell}/a_{ell})^{\frac{1}{2}})}{\beta'(b_{ell}/a_{ell})^2 - \alpha'} \tag{5.13}$$

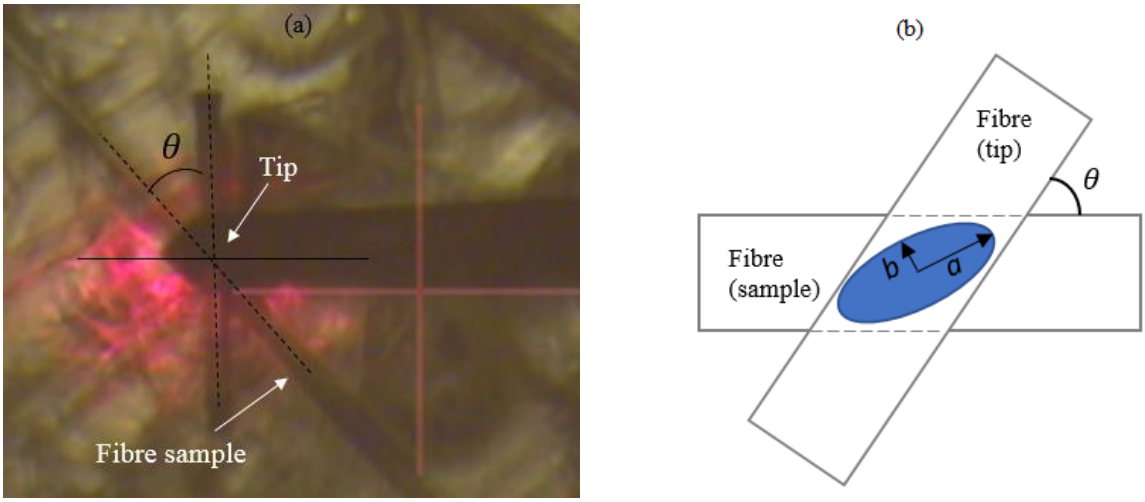

Figure 5.7 Fibre-fibre crossed arrangement (a) real setup (b) geometrical contact area shape.

Using the JKR elliptical contact model above, the adhesion force is calculated and plotted as a dash line in Figure 5.8. As can be seen from the figure, results from the calculations show a similar trend as the results obtained from experiments. In both cases the adhesion force is reduced, in a very similar way, with increasing crossing angle. The contact area of the ellipse reduces as it goes from being a slim elliptical (30°) to circular (90°) contact. It can be seen that the magnitude of the adhesion force measured is approximately 2.5 times less than the magnitude of the calculated model. Note that, in the JKR adhesive elliptical model, the surface is assumed to be smooth. However, in this experiment the fibre that has been used has a certain roughness in the order of nanometers . According to [11], the capillary force decreases more than two orders of magnitude if the rms roughness is increased a few nanometers in the range of 1- 10 nm. In other works [12,13] it is also reported that the value of the adhesion as a function of the rms roughness is decreasing by a factor of 5 if the roughness increased from 0.2 to 4 nm. So, the deviation between model and experiments can well be explained by the roughness effect.

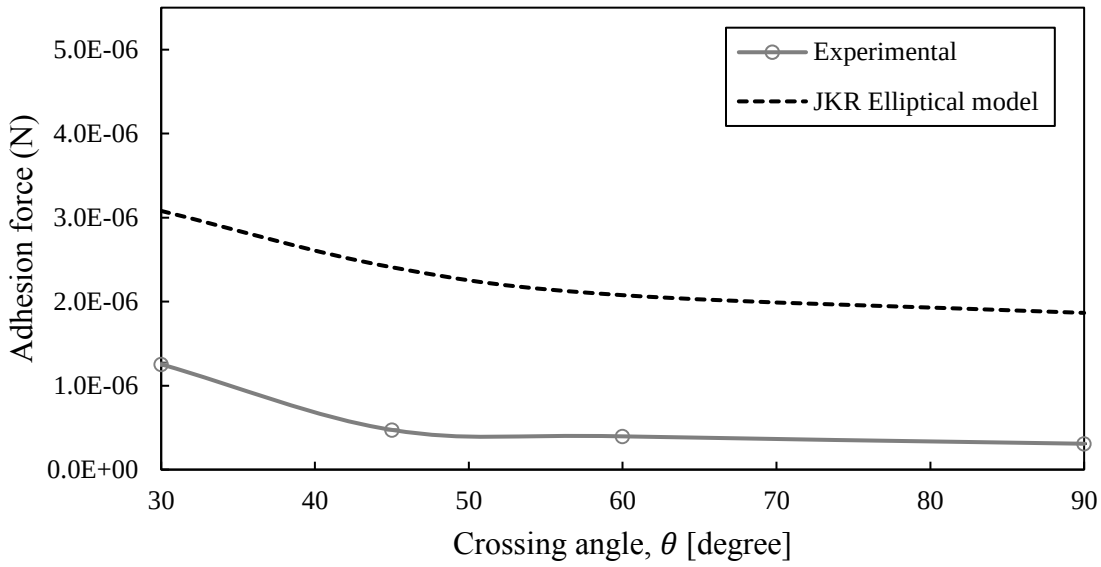

Figure 5.8 The effect of crossing angle on the adhesion force at 8% RH.

Also, a similar experiment has been carried out in ambient at a relative humidity of nearly 40% RH. Here, the influence of humidity on the adhesion force together with the crossing angle has been investigated. Figure 5.9 shows the measurement result of two different samples tested at different crossing angles. The result shows that the adhesion force has a minimum at 40° crossing angle. Numerical studies [14,15] have shown that at elliptical contact ($0° < \theta < 90°$), the shape of the capillary neck is distorted and non-symmetric. In this regime, the capillary force is reduced with the crossing angle due to the changes in the wetted length of the capillary neck [14,15]. Also, studies found that the surface-free torque is measured at parallel and perpendicular contact, while at 40 - 45° the capillary torque is maximum due to narrow capillary neck shape [14].

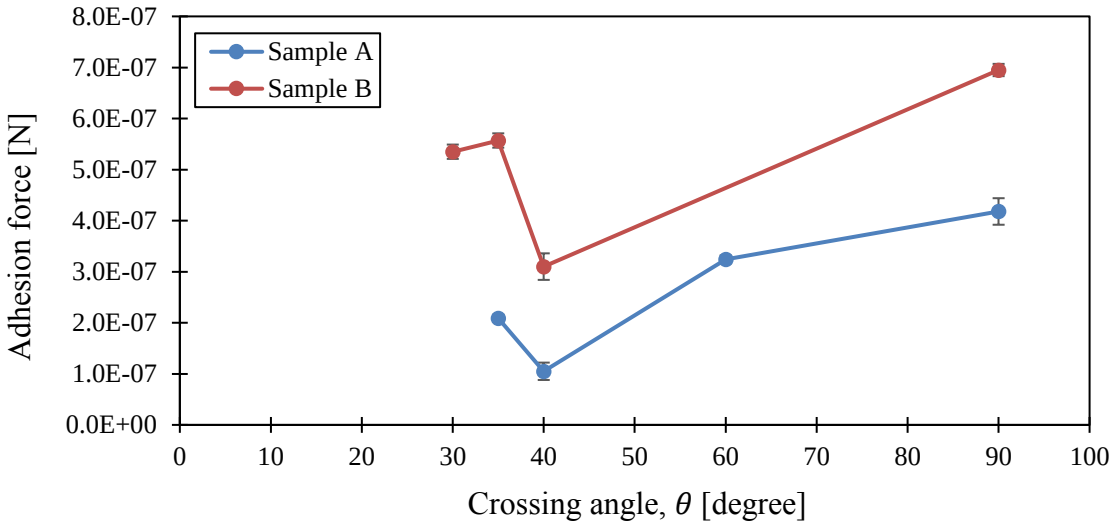

Figure 9 The effect of crossing angle on the adhesion force at 40%RH.

5.6 Summary

Experiments have been performed to study the effect of relative humidity and crossing angle of the A1 fibre on the adhesion force. Result show that the adhesion force is changed when the RH changes from 8% to 77%. The adhesion force shows a clear threshold at about 50% RH, above which the adhesion force increases with the increasing relative humidity. Calculations of the meniscus using the Young-Laplace and Kelvin equations have been compared to the measured adhesion force at 77% RH. In dry conditions, the measured adhesion force is found 2.5 times less than the predicted values using the JKR elliptical adhesive model for different crossing angles. However, the surface roughness is assumed to reduce the adhesion force in the experiment, explaining the over prediction by the model based on smooth contacts. The adhesion force at various crossing angles has also been measured in ambient (40% RH). The results show that at about 40° crossing angle, the adhesion force is minimum which can be explained by the maximum capillary torque between contact surfaces.

References

[1] Asay SAS. Wahl KJ. Colton RJ. Nanoindentation ad contact stiffness measurement using force modulation with a capacitive load-displacement transducer. *Review of Scientific Instruments* 1999. 70 (5); 2408-2416.

[2] Xiao X. Qian Li. Investigation of humidity-dependent capillary force. *Langmuir* 2000; 16; 8153-8158.

[3] Dormann M. Schmid H-J. Simulation of Capillary bridges between particles. *Procedia Engineering* 2015:102; 14-23.

[4] Johnson KL. Contact mechanics. Cambridge Uni Press. 1985.

[5] Wong C. Ye W. Hou Y. Zhao J. Yin J. Mechanism of Adhesion between Polymer Fibers at Nanoscale Contacts. *Langmuir* 2010; 28; 4663−4671.

[6] Jones R. Pollock HM. Cleaver JAS, Hodges CS. Adhesion force between glass and silicon surfaces in air studied by AFM: Effects of relative humidity, particle size, roughness and surface treatment. *Langmuir* 2002; 18; 8054-8055.

[7] He M. Blum AS. Aston DE. Buenviaje C. Overney RM. Critical phenomena of water bridges in nanoasperity contacts. *Journal of Chemical Physics 2001*; 114(3):1355-1360.

[8] Sumer B. Onal CD. Aksak B. Metin S. An experimental analysis of elliptical adhesive contact. *Journal of Applied Physics* 2010; 11(107); 1-7.

[9] Johnson KL. Kendall K. Robert AD. Surface energy and the contact of elastics solids. in *Proceedings Royal Society London Series A Mathematical and Physics Science*, 1971;324(1558); 247-390.

[10] Johnson KL. Greenwood JA. An approximate JKR theory for elliptical contacts *Journal of Physics D: Applied Physics* 2005; 38:1042.

[11] van Zwol PJ. Palasantzas G. de Hosson JTM. Influence of random roughness on the adhesion between metal surfaces due to capillary condensation. *Applied Physics Letters* 2007; 91:101905.

[12] Ata A. Rabinovich YI. Singh RK. Role of surface roughness in capillary adhesion. *Journal of Adhesion Science and Technology* 2002; 16(4); 337-346.

[13] Rabinovich YI. Alder JJ. Esayanur MS. Ata A. Singh RK. Moudgil BM. Capillary forces between surfaces with nanoscale roughness. *Advances in Colloid and Interface Science* 2002; 96; 213-230.

[14] Bedarkar A. Wu X-F. Capillary torque in a liquid bridge between two angled-filaments. *Journal of Applied Physics* 2009; 106:113527.

[15] Soleimani M. Hill RJ. Van de Ven TGM. Capillary force between flexible filaments. *Langmuir* 2015:31; 8328-8334.

Chapter 6

Conclusions & Recommendations

In this chapter, a general reflection on the friction and adhesion behaviour will be discussed in the discussion section. The main findings of the experimental investigation discussed in the previous chapters are summarized in the next section. Finally, some recommendations for further research are given.

6.1 Discussion

This thesis addresses the dynamic frictional behaviour and adhesion between fibres at microscale (filament level) for aramid fibres. The friction force and adhesion force between single aramid fibres in contact has been determined experimentally. Due to the low thickness and geometrical shape, measuring the contact area between aramid fibres is challenging. However, it has been seen that the contact area between fibres is very important in influencing the behaviour of friction and adhesion. From model calculations, both the pre-tension load and crossing angle have been shown to influence the contact area significantly. For example, the changes in 'bending stiffness' of the fibre due to pre-tension influence the conformability between the fibres. Also, the crossing angle between fibres has been shown to have an effect on the contact area. The changes in fibre orientation (crossing angle) give a significant difference in the size and geometrical shape of the contact area and thus influence not only friction but also adhesion. Many researchers have been developing a contact model with and without the contribution of adhesion at elliptical contact ($0° < \theta < 90°$). However, almost no studies have been done on measurements of the contact area specifically between fibres.

Although clear relations between the (calculated) contact area and (measured) friction and adhesion behaviour have been found, there is currently no available method, to the best of the author's knowledge, to directly measure the contact area. For a full validation of the models and theories, a suitable method to measure the contact area between individual fibres is required.

6.2 Conclusions

The main objective of this thesis is to understand the friction and adhesion behaviour between individual fibres. The current study was focused mainly on the friction and adhesion behaviour between two single aramid fibres. Since the study at filament level requires knowledge about surface properties, surface roughness, wetting behaviour and surface energy of single aramid fibres, these properties have been investigated as well. The major conclusions from the research can be summarized as follows:

Frictional behaviour between two single aramid fibres

1. With the developed setup, the friction force measured produces reproducible data with standard deviation of all fibres measured at less than 0.5 mN. The setup also enables friction force measurements at various crossing angles.
2. The model describing the theory of taut wire, as described in Chapter 2, can be used to estimate the macroscopic bending of the aramid fibre. More particularly, an estimation of the contact length (wrapping effect) can be calculated using this model. However, the predicted contact length is small in comparison with the radius of contact predicted with the Hertzian contact model. This shows the elastic contact deformation in the contact dominates over the ‘wrapping effect’.
3. For an elliptical contact, a contact area calculated using a Hertzian elliptical contact model for different crossing angles differs only by a constant factor from the measured friction force. Thus, the results agree with a ‘constant interface strength’ model for friction.
4. The experimental results show the dependency of the friction force on the elastic modulus. Fibres with a low elastic modulus show a higher friction force in comparison with the fibre with a higher elastic modulus. This is due to the influence of the E modulus on the elastic deformation of the contact. A lower E modulus will result in a large contact area between the fibres.
5. The friction force is following by approximation Coulomb’s law (i.e. $F = \mu N$) with the normal load range applied.

Surface energy of aramid fibre

The surface energy of a single aramid fibre can be determined using the Wilhelmy method.

1. Due to the contact angle hysteresis (CAH) phenomena, the advancing contact angle is found to be higher than the receding contact angle. The CAH in this study might be caused by the surface chemical properties, i.e. surface heterogeneity and the shape of the fibre end.
2. The surface of the Twaron® aramid fibres is polar, exhibiting hydrophilic behaviour.
3. Coating the fibre surface influences the surface energy.

Adhesion

1. The formation of the capillary neck between fibre surfaces in humid conditions is important as it influences the adhesion force. The adhesion force has been shown to increase with humidity between 50 - 77% RH.
2. When comparing the calculated adhesion force with the measured force, it has been shown that the measured adhesion force is 2.5 times less than the calculated force using the JKR adhesive contact model. This can be explained by the effects of surface roughness reducing the adhesion force.
3. The maximum capillary torque at 40 - 45° crossing angle reduces the capillary force. The capillary torque results reduce the length of the meniscus and therefore reduce the capillary force.

6.3 Recommendations

Further work is required to extend the understanding of the friction and adhesion behaviour between fibres. Several recommendations will be made for future improvements related to experimental work.

1. Controlling both top and bottom fibre with the same pre-tension load and the same fibre length could reduce the interdependency between parameters and will improve the analysis.
2. An analysis of the frictional behaviour between fibres under different conditions (range of sliding speed and increased number of cycles) should be performed to see the effect of wear on the frictional behaviour and to draw conclusions on the lifetime of the coatings applied on the fibres.
3. An experimental study on the frictional behaviour at nano-scale, perhaps in a suitable Atomic Force Microscope (with calibration of the lateral force) would be useful in order to correlate the adhesion and friction behaviour under similar conditions.
4. A suitable approach and dedicated setup to measure the 'real' contact area between fibres (cylinder on cylinder contact should be developed). Several approaches can be used such as:
    - The principle of film transfer from the fibre to another could be used. A thin film could be applied to one of the fibre surfaces. When contact is made with the other fibre surface, the film is transferred at the point of contact and will be clearly visible when the fibres are separated. However, the thickness of the film layer on the surface needs to be low as adding a relatively thick layer can lead to a larger contact area being measured than the actual size.
    - A pressure sensitive film approach can be used. In that case, a thin laminate film is placed between the contacting surfaces. When the fibres are in contact under a load, the film changes color relative to the magnitude of the pressure applied. However, in common with the previous approach, introducing a third body will change the contact conditions.
    - An electrical resistance approach to measure the contact resistance between fibres during loading. However, the fibre is very thin and, in the case of aramid non-conducting, the electrical resistance can be large in comparison with the contact resistance between them. In the case of aramid, this approach will be therefore difficult. This could be solved by the

deposition of a thin conductive coating on these fibres. The possibilities for this need to be investigated. Moreover, if it is too thick, the coating can influence the contact behaviour.

- Use could also be made of the phenomenon that the dynamic modes of a vibrating fibre will be dependent on the contact stiffness between the two contacting fibres. For this, a dynamic contact model needs to be developed and compared with the measurement results. Variations in the contact stiffness could also significantly affect eigenfrequencies and eigenmodes of the fibres. However, the effect might be slight due to the low bending stiffness of the fibres in comparison with the contact stiffness, so a feasibility study is needed first. If successful, the measured contact stiffness could be related to the contact area by for example, Hertzian contact theory.

Part B: Papers

List of papers

Paper	
A	N. Ismail, de Rooij MB, de Vries EG, Mohd Zini NH. Schipper DJ. An experimental study of friction in fibre-fibre contacts. International Journal of Materials and Product Technology 2016:53; 240-251.
B	N. Ismail, de Rooij MB, de Vries EG, Schipper DJ. Friction between single aramid fibres under pre-tension load. Submitted to Tribology International, November 2018.
C	N. Ismail, de Rooij MB, de Vries EG, Schipper DJ. Experimental study on the contact angle and surface energy of a single aramid fibre and its frictional effects. Submitted to Journal of Colloid and Interface Science, December 2018.
D	N. Ismail, de Rooij MB, de Vries EG, Schipper DJ. Effect of crossing angle on friction force between single aramid fibres. Submitted to Tribology International, December 2018.
E	N. Ismail, Hubert G, de Rooij MB, Schipper DJ, Vansco GJ. Adhesion force measurement between single aramid fibres. In preparation.

Paper A

An experimental study of friction in fibre-fibre contacts

N. Ismail*, E.G. de Vries, M.B. de Rooij, N.H Mohd Zini and D.J. Schipper.

Surface Technology and Tribology,
Faculty of Engineering Technology,
University of Twente,
P.O. box 217, 7500 AE Enschede, The Netherlands.
Faculty of Mechanical Engineering,
Universiti Teknikal Malaysia Melaka,
Hang Tuah Jaya, 76100 Durian Tunggal, Melaka, Malaysia.
*Corresponding author

Abstract

This study aims to develop a new experimental setup to measure friction between two interacting fibers. Friction experiments have been performed with two individual aramid fibers placed in perpendicular contact with each other. It is found that the setup is able to determine the frictional force between two interacting fibers of micrometers diameter. Reliable and repeatable measurement data have been obtained using different load, pre-tension and fiber length values.

1 Introduction

In recent years, it has been an important research direction to understand frictional behavior between fibers especially in fabric composites. Friction between fibers is a fundamental property that would influence the stages in the fiber bundles production process and also the final fabric composite product itself. In fact, the mechanical properties of fiber bundles are also determined by inter-fiber friction which makes friction between fibers very relevant to study. Therefore better understanding of frictional behavior between fibers is needed.

So far, several test methods have been proposed and used in the literature to determine the frictional behavior either between single fiber interactions or fiber bundle interactions. Earlier studies pioneered by Lindberg and Gralen (1948), who also developed an apparatus to measure the frictional force between single wool fibers using the twisting method. In order to characterize the frictional behavior of single fiber at low force, about 10 μN, Landwehr (1976) developed a sensitive

instrument to rub nearly parallel fibers. A capstan method was used by Roselman and Tabor (1976;1977) to analyze friction between single fiber interactions while other researchers (Cornelissen et al., 2013; Ramkumar et al, 2002) used the capstan method to investigate the frictional properties of fiber bundles.

In this article, we present a new experimental setup to investigate the frictional behavior in fiber-fiber contacts. In addition, this study is also aimed to understand the influence of pre-tension in fibers on the frictional behavior. The study is focused on the measurement of the dynamic friction coefficient.

2 Friction

Friction can be defined as the force of resistance encountered when two bodies are brought into contact and allowed to slide against each other. The coefficient of friction is defined as follows;

$$F_f = \mu F_N \tag{1}$$

where F_f is the friction force and μ is the coefficient of friction. It is reported that the coefficient of friction is influenced by the physical and chemical properties of the contacting surfaces (Cornelissen et al., 2012).

3 Force Measuring Mechanism (FMM)

In this study the frictional behavior between two interacting fibers will be investigated experimentally in terms of frictional force measured using a specific setup. The setup incudes a friction force mechanism (FFM) designed by Yaqoob (2012). This mechanism is a two degree of freedom system that can measure the normal and friction force independently. The mechanism consists of eight compound parallelogram frictionless hole-hinge flexure mechanisms. This force measuring mechanism (FMM) is relatively insensitive to the thermal disturbances and manufacturing errors due to its symmetry. The stiffness in both the normal as well as the tangential direction of the FMM is equal to 3.75 mN/μm. Further details regarding the FMM can be found in Yaqoob (2012).

4 Experiment

4.1 Measurement setup

The measurement setup for fibre-fibre contact is illustrated in Figure 1. The setup consists of top and bottom holders to hold the fiber specimens. The top holder consists of two pins which are inserted and connected to the cylinder body. The total dimension of top holder is 20 mm in length. The distance between two pins results in a length of the top fiber of 2 mm. As for the bottom holder, there are also two pins attached vertically from the base plate. The distance between the two pins represents the fiber length. There are two sets of bottom holders available that can hold the fibre in 2.5 mm and 6 mm in length respectively. Low viscosity glue was used to attach the fibre specimens to the holder. The top holder is mounted on the positioning stage so that the normal load F_N can be applied. The applied normal force F_N and frictional force F_f are measured independently by the capacitive sensors in the FMM. The accuracy of the capacitive sensors is 2 nm with a measuring range of 50 µm. The capacitive sensors are mounted on the force measuring mechanism (FMM) as shown in Figure 2. Both normal and frictional forces can be calculated with the help of both capacitive sensors by measuring the deflection in the FMM in X and Z directions and using the calibrated stiffness of the FMM. With this setup, the maximum normal load that can be applied is 100 mN.

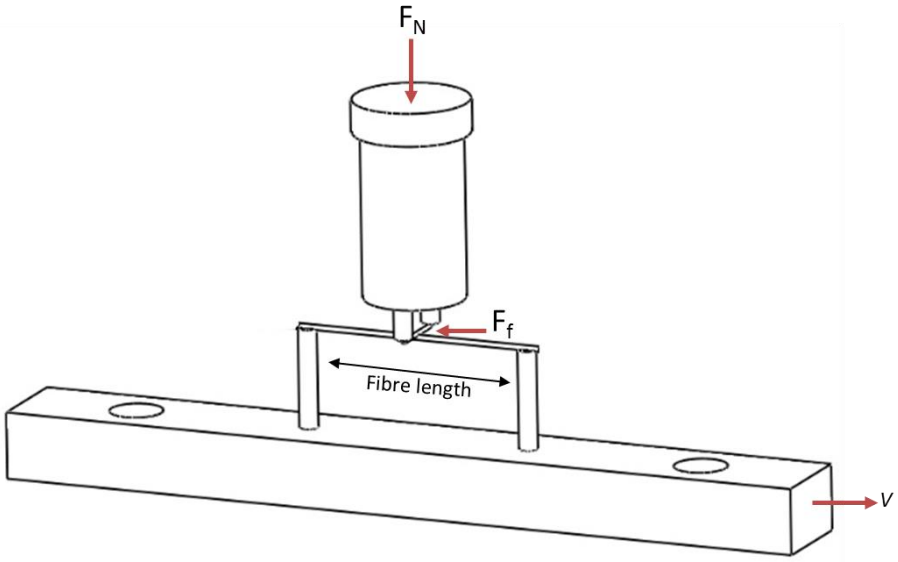

Figure 1 Schematic arrangement of the crossed fibres.

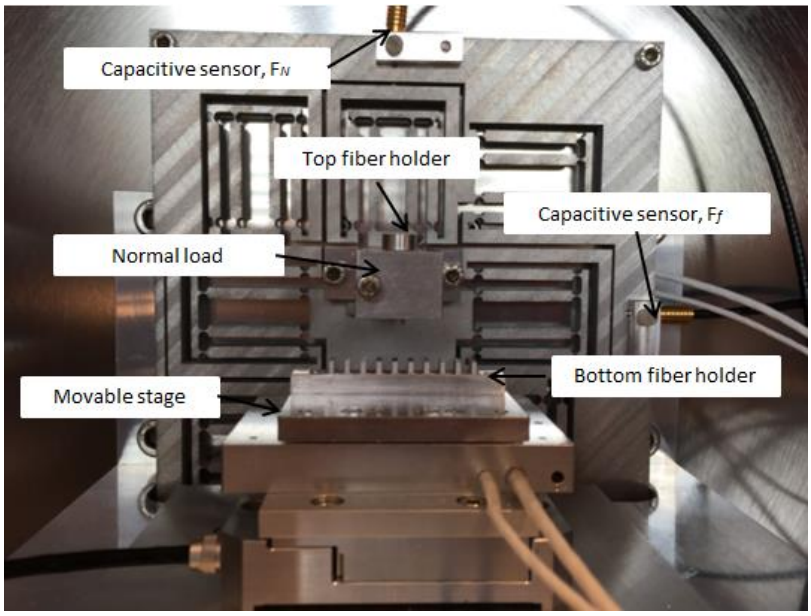

Figure 2 Measurement setup.

The bottom holder is placed on a movable flat stage where the sliding speed, *v* can be controlled. The fibers are placed crossing each other in perpendicular at 90˚ skew angle as illustrated in Figure 3.

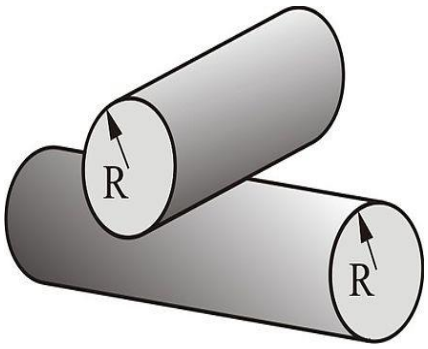

Figure 3 Fibre arrangements in 90˚skew angle.

As mentioned earlier, this study also aims at the influence of fiber tension on friction. Therefore during the tests, one end of the bottom fibre is attached to a dead weight to induce the pre-tension. Two different weights were applied to the fibre. The weights used were 2 g and 3 g, resulting in forces of 20 mN and 30 mN. In this study, the pre-tension that was applied to the fibre specimens is assumed to be uniformly distributed. Table 1 summarizes the relevant parameters and settings of the friction experiment.

Table 1 Experimental parameters.

Description	Symbol	Unit	Value
Normal load	F_N	[mN]	1-10
Pre-tension load	T	[mN]	20 & 30
Sliding velocity	v	[mm/s]	0.002
Sliding distance	d	[mm]	0.2
Fibre length: Top	L_T	[mm]	2
Fibre length: Bottom (short fiber)	L_{Bs}	[mm]	2.5
(long fiber)	L_{BL}		6
Relative humidity	RH	[%]	43 - 64

4.2 Material used in the measurements

Generally, in structural composite materials such as Continuous Fiber Reinforced Polymers (CFRPS), fibre materials such as aramid, carbon and E-glass are used as tow materials. In this study, aramid fibres were selected as the testing materials. The material properties of the aramid fibres are described as in Table 2. The measurement of the individual fibre diameter has been conducted using Scanning Electron Microscopy (SEM) as illustrated in Figure 4. The aramid fibres provided by the manufacturer are in a tow bundle. From this bundle, the fibres are separated manually in the laboratory. For bottom fibre specimens, the individual fibre are cut in two different lengths which are 2.5 mm and 6 mm and will be referred to ‘short’ and ‘long’ fibres in this study. During the measurement setup, all fibers are allowed to cure for 24 hours after gluing on the holder before performing measurements. There is no cleaning procedure carried out onto the fibre specimens. Section 4.3 describes the measurement procedure for the friction experiments and explains how the point contact was realized.

Table 2 Manufacturer data of the aramid fiber used in friction experiment.

Properties	Unit	Value
Filament diameter	µm	10
Young's modulus	GPa	60 - 80
Linear density	dtex	420 - 3360
Tenacity	mN/tex	1650 - 2200
Elongation at break	%	3.0 - 4.4

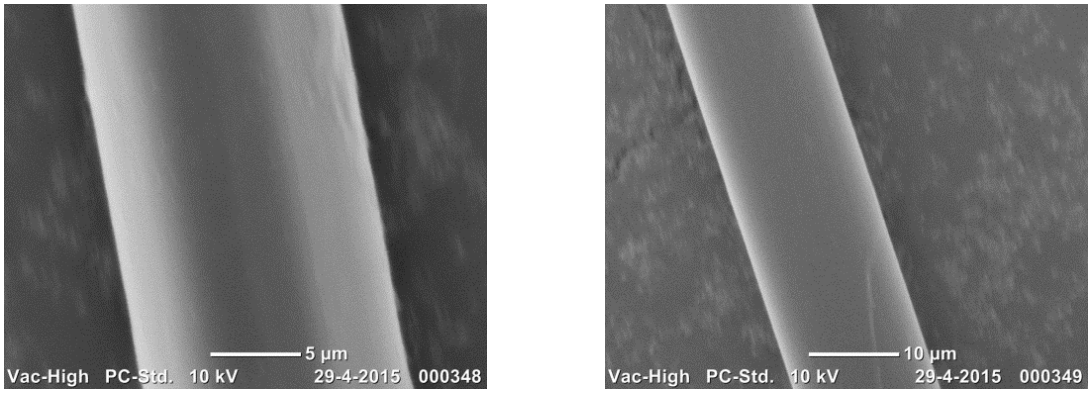

(a) (b)

Figure 4 (a) and (b) Images of the fibre used.

4.3 Experimental procedure

The holder was first cleaned with acetone before gluing the fibre onto it. One end of the fibre was glued, while the other end was attached to a dead weight to realize the pre-tension. It was assumed that after 24 hours, the pre-tension load was well distributed along the fibre. After that, the other end of the fiber was glued. The experiments were carried out with several parameters in order to have better understanding of frictional behavior of single aramid fibre interaction. Every experiment was repeated three times. A detailed experimental matrix of friction measurements is given in Table 3.

To perform friction measurements, it is important to find the point of initial contact between the two fibres accurately. This to make sure that the measured and actual forces that are applied to the sample are the same in every experiment. The first

step is to find the contact roughly while the top fibre approaches the bottom fibre with a certain velocity, v_1. As the top fibre is approaching the bottom a few microns before the contact, the velocity is then changed to a lower velocity, v_2. An optical camera with high magnification is used to capture the image of the fibre-fibre contact point as shown in Figure 5. After the contact is made, the normal load is applied, and the movable stage is moved with a defined sliding velocity and distance in a reciprocal movement. Multi-pass friction loops can be set to control repeatability and running in effects. This results in a frictional loop as shown in Figure 6. The environmental conditions were monitored during the measurement. The room temperature and relative humidity were recorded every 30 minutes. From that, it was found that during the measurements, the room temperature varied from 24 ^{o}C to 25.6 ^{o}C and the relative humidity ranged from 42.7 %RH to 63.1 %RH.

Table 3 Experimental matrix of friction measurements.

Sample ID	Fiber length [mm]	Pre-tension load [mN]
ID-1	6	30
ID-2	6	20
ID-3	2.5	30
ID-4	2.5	20

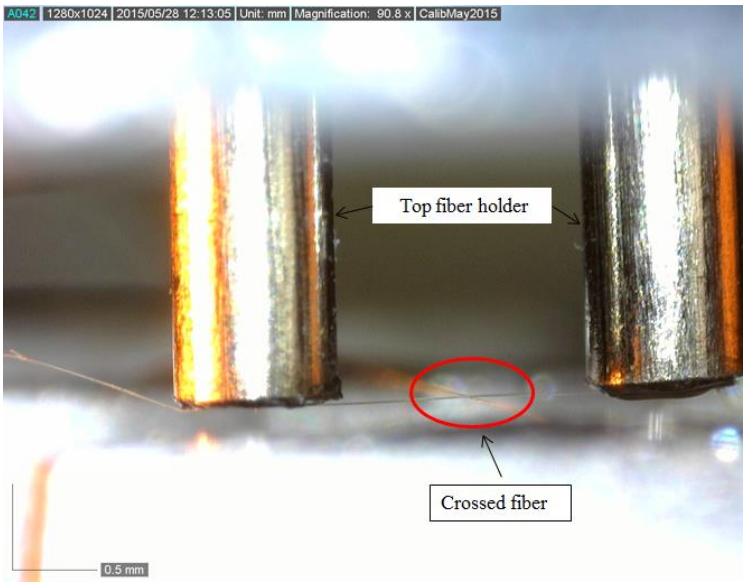

Figure 5 Point contact between crossed fibres.

5.0 Results and Discussion

Figure 6(a) shows the friction measurement curves of a long fibre with 30 mN pre-tension load at 8 mN normal load and Figure 6(b) shows the friction measurement results of the short fibre with 20 mN pre-tension load at 10 mN normal load. It can be seen that there is a transient response during the initial stage. This is related to the lateral stiffness of the FMM as well as the fibre-fibre contact. After that, the fibres started sliding and the signal was steady both in forward and backward sliding direction. During the first cycle, the average value of the frictional force is slightly different from the other three cycles. The same trends is observed in all measurements. The difference between the values can be explained by the presence of the impurities on the fibre surface that may affect frictional conditions. After the first cycle these impurities are removed. This results in a steady state conditions with a stable value of the frictional force for subsequent cycles. From the results in Figure 6, it can be seen that the differences in frictional force level between cycles are very small. The frictional force measured under different fiber length, normal load and pre-tension load are given in Table 4. The measured frictional force for each condition was the average of total 400 µm sliding distance forward and backward. Each condition was repeated four times to ensure reproducibility of the data. Standard deviation from the average was reported for each condition. The low standard deviation shows that the measurements value obtained are accurate and reliable.

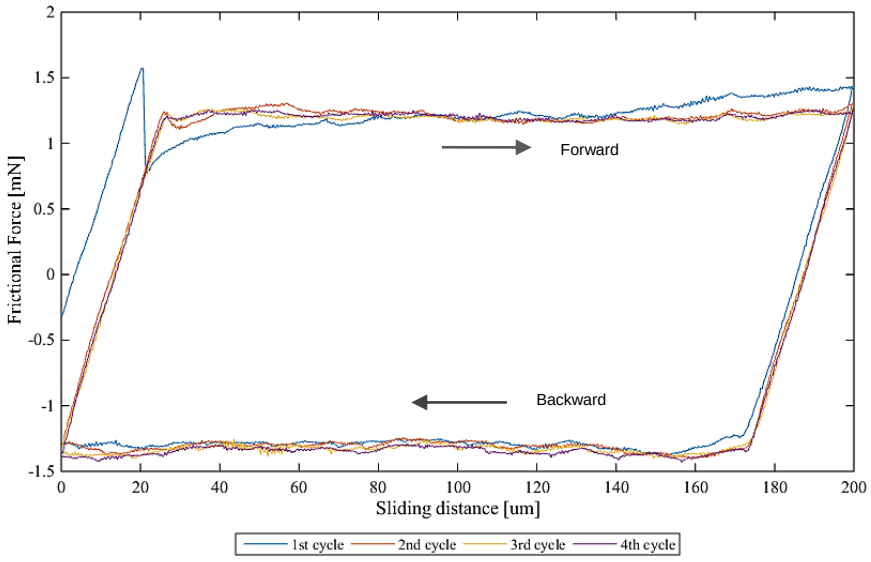

(a)

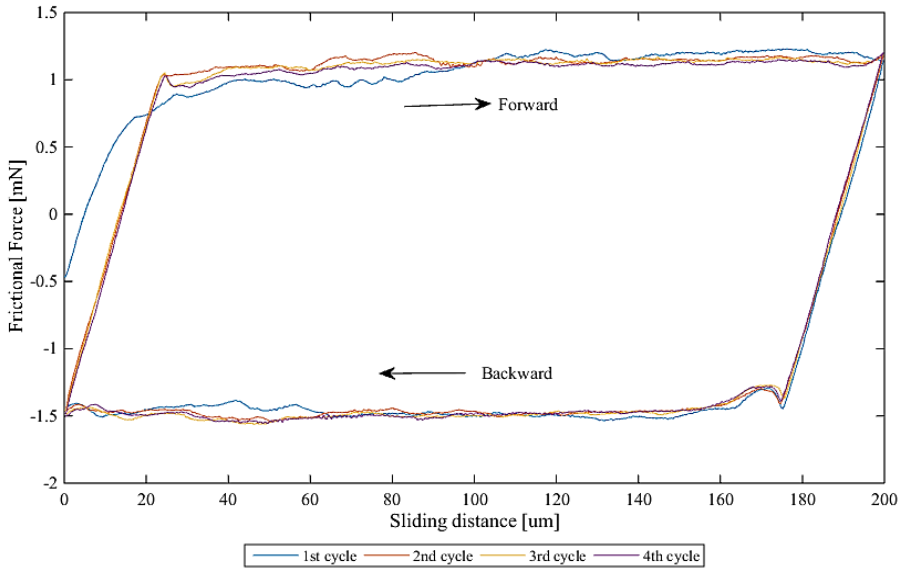

(b)

Figure 6 (a) Friction measurement (a) with 30 mN pre-tension load at 8 mN normal load (b) with 20 mN pre-tension load at 10 mN normal load.

Table 4 Frictional force in mN measured under different fiber length, normal and pre-tension load.

Fiber length [mm]	Pre-tension load [mN]	Normal load [mN]				
		1	3	5	8	10
6	20	0.153(0.010)	0.396(0.016)	0.609(0.004)	0.889(0.013)	1.235(0.062)
	30	0.229(0.005)	0.528(0.020)	0.704(0.014)	1.261(0.008)	1.319(0.053)
2.5	20	0.163(0.023)	0.374(0.025)	0.648(0.022)	0.998(0.010)	1.293(0.006)
	30	0.201(0.078)	0.409(0.028)	0.697(0.055)	1.107(0.093)	1.375(0.144)

The values within the parentheses refer to the standard deviation values.

5.1 Effect of applied load on coefficient of friction

According to Amonton's law (Archard, 1957), friction is proportional to the applied load with the coefficient of friction, μ as follows:

$$\mu = \frac{F_f}{F_N} \tag{2}$$

where F_f is the friction force and F_N is the normal load. However, according to the Hertz theory for single asperity contact, the area of contact for a point contact is proportional to the applied normal load to the power of 2/3 as follows:

$$A = \pi . \left(\frac{3}{4}\frac{R}{E^*}\right)^{2/3} . {F_N}^{2/3} \tag{3}$$

where *R* is the radius, *E** is the reduced elastic modulus of the contacts. By assuming that no ploughing occurs at single asperity contact (Bowden and Tabor, 1950), the frictional force is proportional to the contact area and if the shear stress is constant, the normal load dependency of the frictional force equals $F_f \propto {F_N}^{\frac{2}{3}}$ for a point contact. Therefore the friction coefficient shows the following proportionality with load for a point contact:

$$\mu = \frac{F_f}{F_N} \rightarrow \mu \propto \frac{{F_N}^{2/3}}{F_N} ; \mu \propto {F_N}^{-1/3} \tag{4}$$

which shows that the friction coefficient is proportional to the applied normal load to the power of -1/3. Also in this study, it was found that the friction coefficient reduced with applied normal load as shown in Figure 7. In this figure the power law curve fits to the measurements have been plotted as follows:

$$\mu = k{F_N}^{-\beta} \tag{5}$$

where μ is the coefficient of friction, *k* and β are constants and F_N is the normal load. From the experiments, it was found that the value of β lies between 0.1 and 0.2

depending on the pre-tension load as seen in Figure 8. These results are in good agreement with the study done by Lincoln (1952) where it was shown that the value of β typically lies between 0 and 1/3 for fibre-fibre contacts. The β value obtained show that the frictional behavior in fibre-fibre contacts behave between a point contact and a random rough surface (Greenwood and Williamson, 1966).

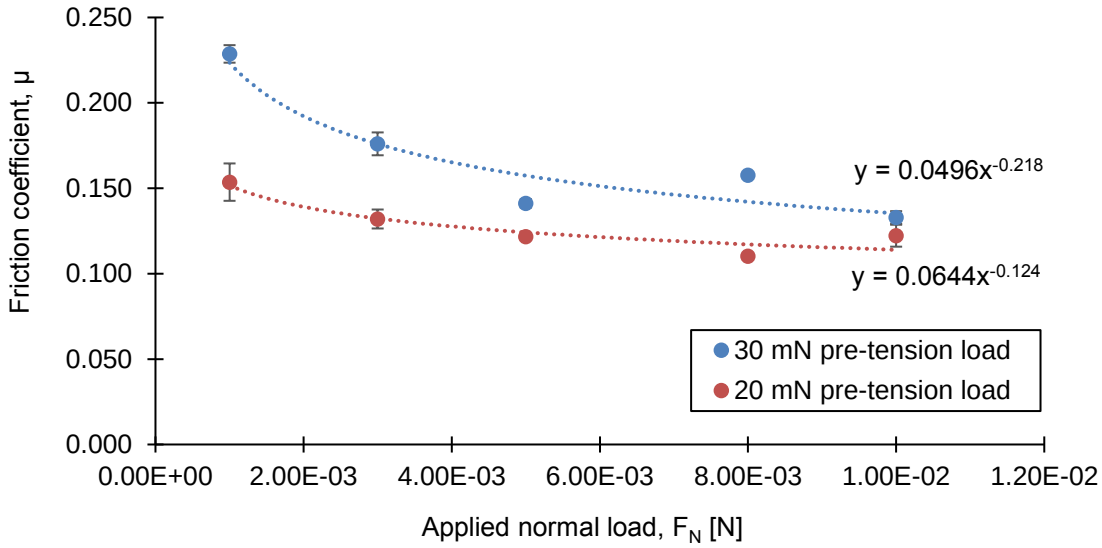

Figure 7 Friction coefficient, μ as a function of the applied normal load. The power law curve fits the data along with the governing equation. The error bar represents the standard deviation, fibre length 6 mm.

5.2 Effect of pre-tension load on coefficient of friction

Figure 8 shows the effect of pre-tension load on the friction coefficient of fibre-fibre contacts. The friction measurements at 30 mN pre-tension load showed larger variations in the measured coefficient of friction under similar conditions. As the pre-tension load increases, the friction coefficient also increases. It was observed that at different fiber lengths the magnitude of the friction coefficient also follows a similar trend.

5.3 Effect of fiber length on coefficient of friction

Figure 9 shows the change in friction coefficient with fibre length. The effect is more evident at the longer fibre used in the study. In the fibre-fibre contact, the applied

normal load causes the bottom fibre to bend and as a result an increase in contact area. In this study, the effect of fibre length exhibits a similar behavior as with the effect of pre-tension on the frictional behavior as both increase the coefficient of friction.

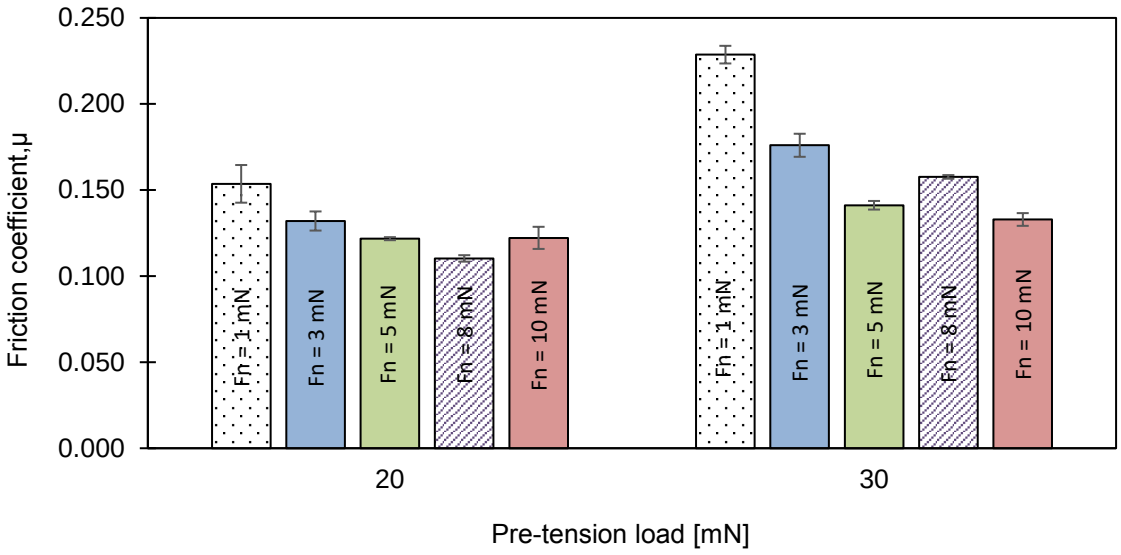

Figure 8 Effects of pre-tension loads at 6 mm fiber length.

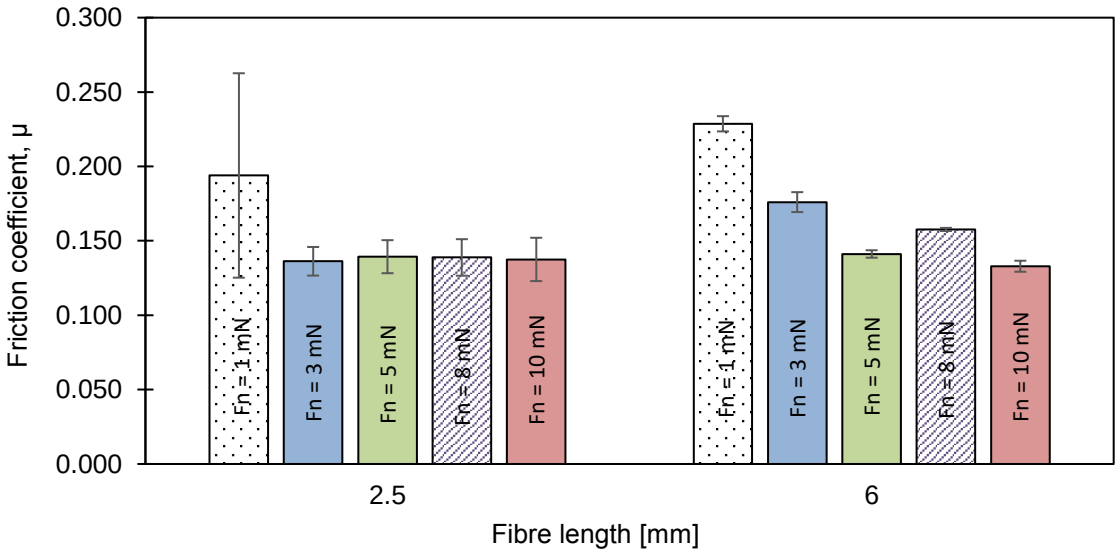

Figure 9 Effect of fibre length at 30 mN pre-tension load.

6 Conclusion

A new experimental setup to measure friction between fibre-fibre contact has been successfully developed and tested. The measurement results show that the friction coefficient is reduced with normal applied load and follows a power law as a function of load. It has been found that the frictional behavior of the fibre-fibre contact is in transitional region between random rough surface and a point contact. Besides, it is revealed that the pre-tension load and fiber length also have a great influence on the frictional behavior. These two parameters contribute to change the contact area surface during fibre-fibre interaction.

Acknowledgements

The authors would like to acknowledge Malaysia Education Ministry and Universiti Teknikal Malaysia Melaka (UTeM) for the financial support to the corresponding author.

References

Archard, J.F., 1957, Elastic deformation and the laws of friction, *Proceedings of Royal Society of London. A*, 243, pp.190-205, DOI: 10.1098/rspa.1957.0214.

Bowden, F.P. and Tabor, D., 1950,The friction and lubrications of solids, *Oxford University Press*, London.

Cornelissen, B., Rietman. B. and Akkerman. R., 2013, Frictional behavior of high performance fibrous tows: Friction experiments, *Composites Part A: Applied Science and Manufacturing*, Vol. 44, pp. 95-104.

Gralen, N. and Olofsson, B., 1947, Measurement of friction between single fibers, *Textile Research Journal*, Volume 17, No. 9, pp. 488-496.

Greenwood, J.A. and Williamson, J.B.P., 1966, Contact of nominally flat surfaces, *Proceedings of Royal Society of London. Series A, Mathematical and Physical Sciences*, pp.300-319.

Landwehr, R.C., 1976. Sensitive instrument to measure the friction between single fibers in various media. *Review of Scientific Instruments*, 47(12), p.1461.

Lincoln, B.,1952, Frictional and elastic properties of high polymeric materials, *Journal of Applied Physics*, 3, pp.260-263.

Lindberg, J. and Gralen, N., 1948. Measurement of Friction Between Single Fibers: II. Frictional Properties of Wool Fibers Measured by the Fiber-Twist Method. *Textile Research Journal*, 18(5), pp.287–301.

Ramkumar, S.S., Shastri, L.,Tock, R.W, Shelly, D.C., Smith, M.L. and Padmanabhan, S., 2002, Experimental Study of the Frictional Properties of Friction Spun Yarns. *Journal of Applied Polymer Science*, 88, pp. 2450–2454.

Roselman, I. and Tabor, D., 1977. The friction and wear of individual carbon fibres. *Journal Physics*, 10., pp. 1181-1194

Roselman, I. and Tabor, D., 1976. The friction of carbon fibres. *Journal Physics*, 9, pp.2517-2532.

Yaqoob, M. A, de Rooij, M.B, and Schipper, D.J., 2012, Design of a vacuum based test rig for measuring micro adhesion and friction force, *WIT Transaction and Built Environment*, DOI. 10.2495/HPSM120231.

Paper B

Friction between single aramid fibres under pre-tension load

Nurhidayah ISMAIL [1,2*], Matthijn B. de ROOIJ [1], Erik G. de VRIES [1], Nurul Hilwa MOHD ZINI[1,2],and Dik J. SCHIPPER[1]

[1]Laboratory for Surface Technology and Tribology, Department Mechanics of Solids, Surfaces and Systems (MS3), Faculty of Engineering Technology, University of Twente, Drienerlolaan 5, 7522 NB, Enschede, The Netherlands.

[2]Centre for Advanced Research on Energy, Faculty of Mechanical Engineering, University Teknikal Malaysia Melaka, Hang Tuah Jaya, 76100 Durian Tunggal, Melaka, Malaysia.

Abstract

Understanding the friction mechanism at microscale (filament level) of fibrous material is important as it is one of the key roles in governing the behaviour of fibre assemblies at meso- and macroscale. However, mechanical stress such as tension may also influence the frictional behaviour between fibres. Therefore, in this study the frictional behaviour of fibre-on-fibre contact under pre-tension is explored. A new experimental setup was successfully developed to measure the friction force between two single fibres (Twaron® aramid fibres) at perpendicular contact. Although pre-tension influences the bending stiffness of the fibre, the results show that the effect of pre-tension on the contact length is relatively small. The elastic deformation of the contact dominates over the 'wrapping effect', generating the contact area over which the interfacial shear takes place. The elastic modulus and linear density of the aramid fibres also have a significant influence on the frictional behaviour.

1 Introduction

Aramid fibres are often found in high-performance applications such as in some composites, ballistics, aerospace, protective clothing, ropes and cables applications. This is due to its combination of high strength and high stiffness properties as well as the high strength-to-weight ratio, about five times higher than steel. Unfortunately, the fibre may expose to a series of mechanical stresses for instance friction during

processing or handling stages, which lead to its structural deformation and deteriorate the physical and mechanical performance of a final product.

In general, the fibre is produced in the form of individual continuous filaments which are bundled together forming the tows. These yarns are then intercrossed to form a woven fabric. The processes show that the individual continuous filaments, are basically the contacting and interacting bodies and subjected to frictional effects. Therefore, a thorough understanding of the frictional behaviour between fibres at filament level is necessary, especially for the complex structures like woven fabrics.

It is important to note that, the friction plays a dual role. An excessive frictional force, either fibre against fibre or fibre against tool, can deteriorate the physical characteristics of the fibre itself, e.g., defibrillation that lead to fibre breakage. This breakage is crucial as it influences the strength properties of the fibre yarns and fabric [1-3]. On the contrary, for the spun yarn, a higher inter-fibre friction will increase the yarn strength, but if the tension exceeds the friction level, a high possibility of rupturing and slipping of fibres exists. For example, in some dynamically loaded applications such as in mooring lines, the friction between fibres may cause a premature failure of the fibre ropes and hence influence the mechanical properties and the ropes lifespan [4,5]. Vertical tension because of the rope weight as well as a dynamic response which is excited by longitudinal oscillation due to wave motion will generate the internal friction in fibres ropes. Thus, understanding the friction and tension between fibres at microscale level is needed as it has a great influence on the structural and properties of a final product such as a rope and a woven fabric.

Many researchers have developed various methods to study the friction between fibres and have been reviewed by several authors [6,7]. One of the fundamental methods is to measure friction based on the principle of rubbing fibre against another fibre in linear motion [8-12]. This method is commonly used for concentrated point, line and disperse contacts between fibres, yarns (tows) and fabrics. For example, this method has been adapted in measuring the friction force between single fibres of different materials such as carbon [13], polyamide [14], polyester [14] and polyethylene [15], and tow against tow or metal contact [16]. Meanwhile, Gralen, Olofsson and Lindberg [17-19] have used a twist method to study the frictional

behaviour in textile materials. In their experiments, two fibres were twisted together by a certain number of turns, and the friction force would be only measured during slippage. If measuring at high velocities or when a lubricant is present at the fibre interface, a capstan method is the most common way to measure friction between fibres. In this method, a fibre is wrapped over a cylindrical body and the frictional force that is developed is calculated based on a normal force generated by the tension exerted at both fibres end. Roselman and Tabor [20] have used this method to study friction behaviour at microscale level, while Cornelissen et al. [21] and Chakladar et al. [22] used this method to study at mesoscale level. Other factors that affecting the friction such as surface roughness [21], tow angle and tow size [22] have been also investigated through this method.

There are many papers on the friction between fibres, however, to the best of the author's knowledge, the effect of pre-tension loads on the frictional behaviour at microscale has not yet been discussed in detail even though it is a relevant issue in many applications. For example, in a continuous composite manufacturing process, low and high pre-tension during winding may result in poor mechanical properties and catastrophic failure, respectively. Therefore, this study aims at investigating the frictional behaviour between single fibres in contact with the influence of pre-tension. The 'fibre-on-fibre' term that will be used hereafter is representing the interactions between two single fibres. A new experimental setup has been developed to measure the dynamic friction of two single fibres sliding onto each other at 90° (perpendicular) contact under the influence of pre-tension and other parameter conditions such as normal load and elastic modulus.

2 Material and Method

2.1 Materials used

Two types of aramid fibres used in this study was provided by Teijin Aramid B.V. The properties of the fibres are listed in Table 1. In this study, a low Young's modulus fibre type and a high Young's modulus fibre type are called as LM and HM, respectively. Initially, the fibres were in the form of tow bundle (see Figure 1(a)), with each tow consists of thousand single filaments. Then, the fibres were manually

separated into a single filament with its Scanning Electron Microscope (SEM) image is shown in Figure 1(b).

Table 1 Manufacturer data of the material properties of the aramid fibres used in the friction experiments.

Description [unit]	LM	HM
Elongation at break [%]	4.4	2.9
Linear density [dtex]	1.2	1.6
Young's modulus [GPa]	60	115
Tensile stress [GPa]	3.2	3.5
Breaking strength [N]	0.26	0.4
Fibre diameter [µm]	10.8	11.9
Finishing material	alkyl-phosphate salt	alkyl-phosphate salt

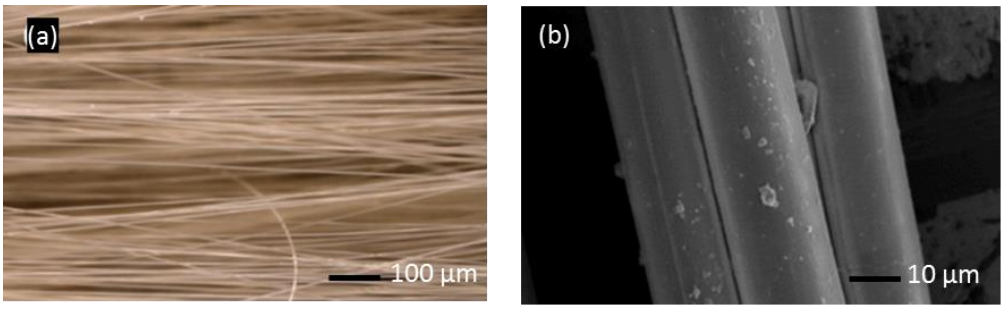

Figure 1 (a) Scanning electron microscope (SEM) images (a) tow bundle; (b) single fibre.

2.2 Surface characterization

The surface texture of the Twaron aramid fibres was examined using atomic force microscopy (AFM). The FlexAFM from Nanosurf was used to observe the surface topography and measure the roughness of the fibre surface. The ACTA cantilever form AppNano was used with a stiffness in the range of 13-77 N/m. The scanning area was set at a size of 3 µm x 3 µm.

2.3 Experimental setup

An experimental setup has been developed to measure friction between two crossed single fibres at angle of 90°. Figure 2 shows the schematic description of the experimental setup. The main setup consists of a top and bottom fibre holder, a linear stage and a set of two capacitive sensors mounted at the force measuring mechanism (FMM). The resolution of the capacitive sensor is 1 nm with a measuring range up to 50 µm. In Figure 2, the forces are calculated based on the spring stiffness concept, in which the deflection of the FMM is measured in *x* and *z* direction. A detailed explanation of the FMM can be found in Yaqoob [23]. With this load controlled setup, the maximum normal load can be applied is 100 mN with an accuracy of 8 µN.

In this study, the tension of the fibre during gluing is only controlled at the lower fibre, while for the upper fibre a minimal pre-tension is applied just to prevent the fibre from slacking. This had to be done due to the small length (2 mm) of the upper fibre. A low viscosity glue type, Loctite 401 was used for gluing the fibre at fibre holders. One end of the lower fibre is initially glued to a holder, then the other end is connected to a cable lug. The function of the cable lug is to clamp the end of the fibre into a loop shape so that the dead weight can be hooked to it to induce the pre-tension to the fibre. After the glue at the first end is cured, the dead weight is loaded to the fibre. Then the other end is glued. Next, the dead weight is removed after the glue is cured.

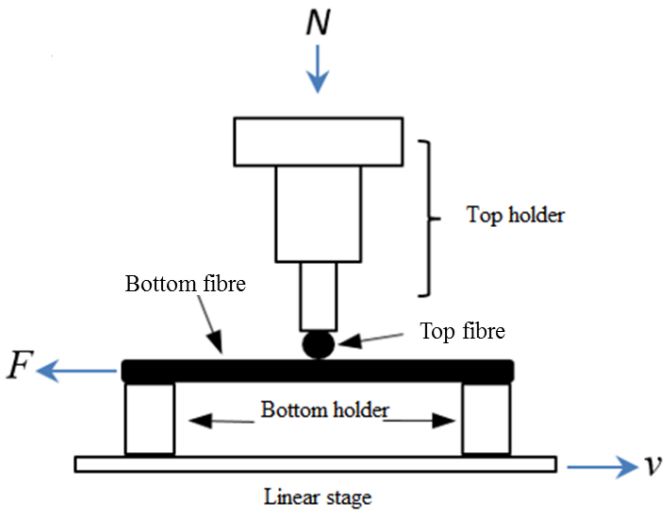

(a)

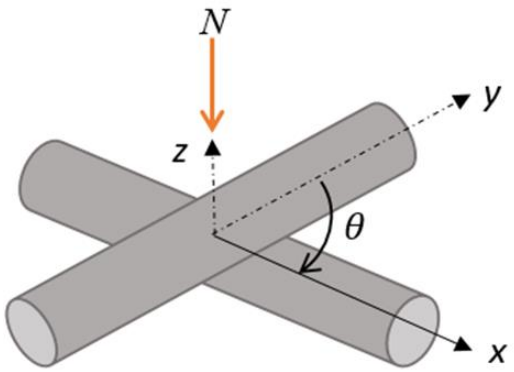

(b)

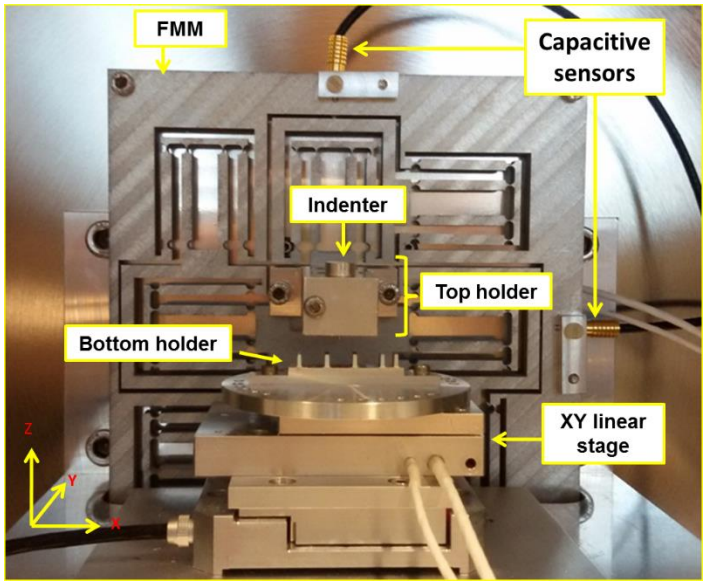

(c)

Figure 2 (a) Schematic description of friction experiment between fibres; (b) Schematic of the fibre-on-fibre contact; (c) Experimental setup.

To conduct the friction measurement, both fibres need to be brought into an initial contact. The top fibre is moved downwards approaching the bottom fibre at two different speeds; v = 0.01 mm s^{-1} to find the contact and v = 0.001 mm s^{-1} to find a few microns before the contact. During this procedure, no initial load is applied (Figure 3(a)). Therefore, the normal and friction forces are assumed zero just before contact is made. As there is no deformation in the FMM system before contact, the measured normal load is close to represent the true value. Once the final normal load is applied to the contact, the fibres start to bend as shown in Figure 3(b). The

friction force measurement is taken as the bottom fibre is sliding against the top fibre in *x* direction with the help of the stage. Multi-pass friction loops are executed to determine the repeatability and running-in effects. Table 2 shows the parameters that are used for the friction force measurements. The measurements are repeated five times for data producibility and repeatability.

Table 2 Parameters for friction measurements.

Description	symbol	value	units
Normal load	*N*	1- 10	mN
Pre-tension load	*T*	50 - 200	mN
Sliding speed	*v*	2	µm/s
Crossing angle	*θ*	90	degree
Sliding distance	*d*	100	µm
Fibre length		Top fibre: 2	mm
		Bottom fibre: 6	mm
Number of friction cycles		5	-
Relative humidity	RH		%

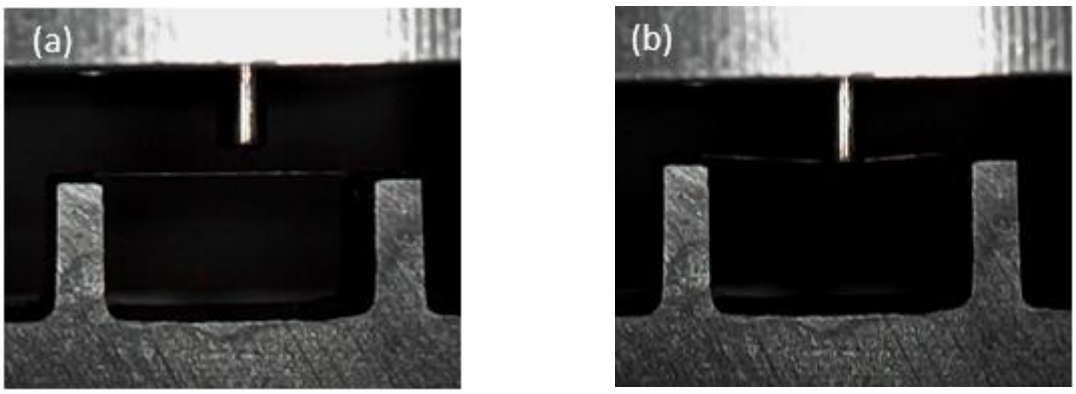

Figure 3 (a) Finding initial contact between the fibres; (b) Fibres under loading.

3 Results and discussion

3.1 Surface roughness

AFM measurements were performed to obtain the roughness of the fibre surface in three-dimensional (3D) analysis. The Sq parameter, represents the root mean square of the roughness within the measured area and is calculated using the following formula [24]:

$$S_q = \sqrt{\frac{1}{A}\iint Z^2(x,y)\,dxdy} \quad (1)$$

To observe the effect of the pre-tension on the fibre surface, a roughness measurement is performed before and after applying the pre-tension load on the fibre. The fibre sample that has been confronted with pre-tension is prepared separately from the sample for friction tests. The pre-tension fibre sample has the same length as for the friction test sample, which is cut, stretched with load for about 2 hours. Then, the load is released from the fibre and a roughness measurement is carried out using the AFM. Here, it is assumed that at a very small length, the pre-tension load would play a role on the roughness surface. Then, the fibre is placed vertically parallel to the AFM tip (see Figure 4). The fibre is scanned along the *x* direction within the scan size are of 3 µm x 3 µm with a resolution of 512 x 512 points and thus the influence of fibre orientation on the roughness measurement is therefore eliminated.

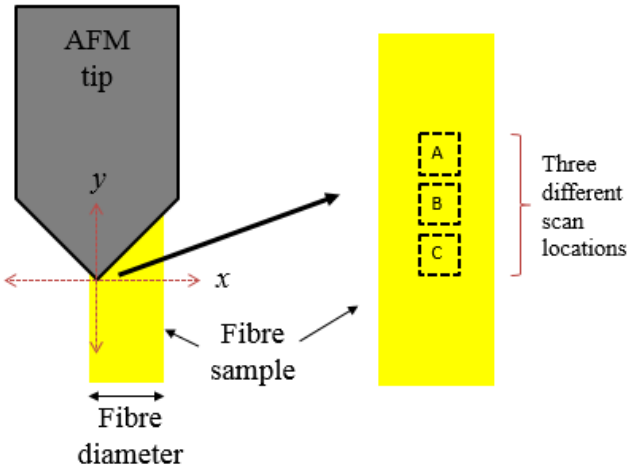

Figure 4 Illustration of the roughness measurement using AFM.

Figure 5 shows the AFM images of HM fibre type before and after applying pre-tension loads. The lines and treated particles on the surface prove that at microscale level, the fibre surface is quite rough with Sq ≈ 15.1 nm as in Fig. 5(a). With 50 mN of pre-tension load, the surface roughness is found to be reduced to Sq ≈ 11.3 nm, the AFM image is shown in Figure 5(b). By increasing the pre-tension load to 100 mN, the fibre surface changes to be even smoother, as shown in Figure 5(c) with Sq ≈ 5.6 nm. Note that the Sq value decreases asymptotic when the pre-tension load is more than 50% of the fibre breaking strength. For each pre-tension load, the roughness measurements are performed at three different locations. Figure 6 shows the overall results of the Sq value of the fibre surface for different pre-tension values. The result shows that the Sq values reduced as the pre-tension increases. Note that, in one single fibre consists hundreds of fibrils. With pre-tension this fibril elongates and hence reduce the contour peaks.

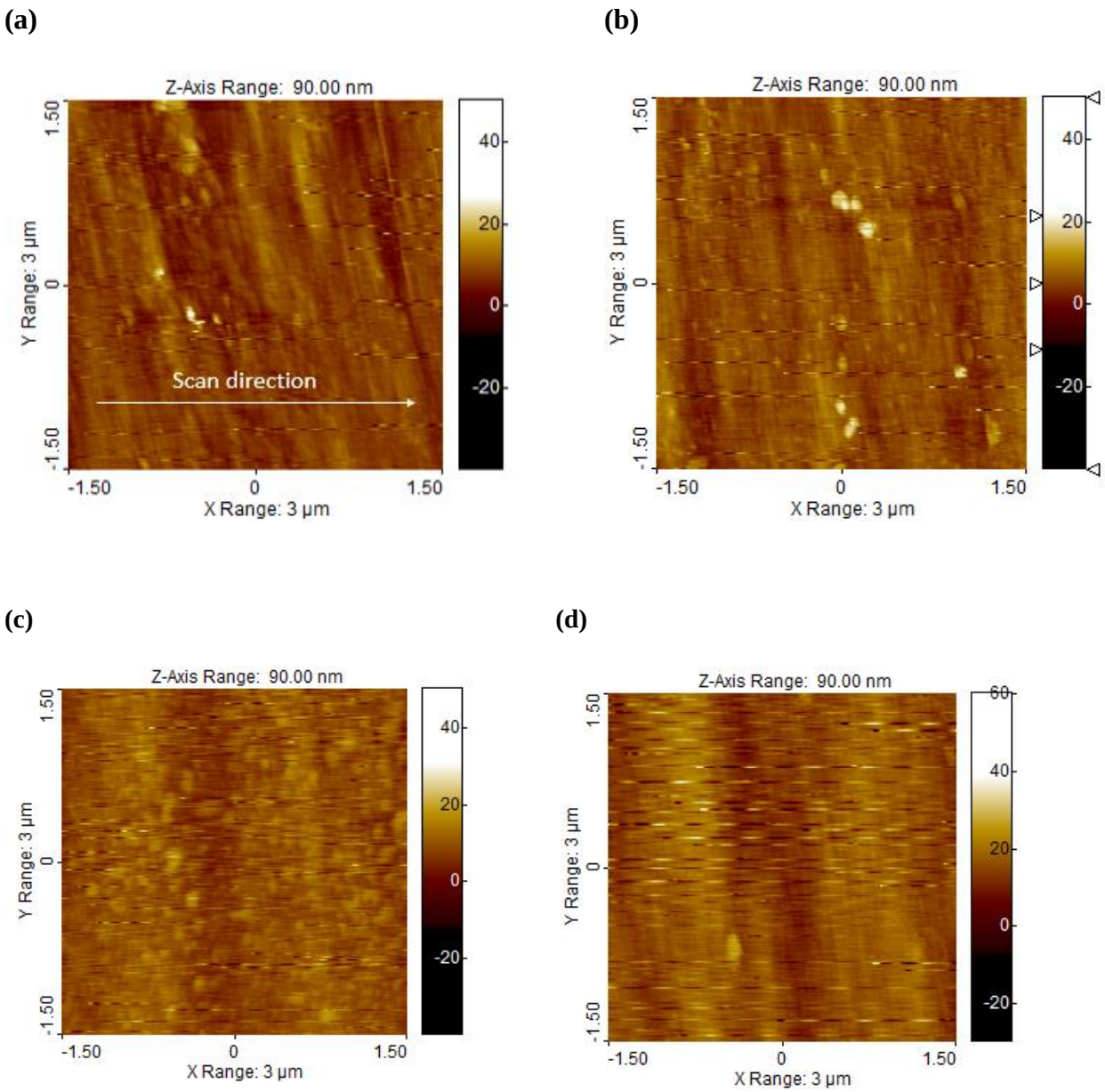

Figure 5 AFM images of HM fibre type (a) without pre-tension; (b) 50 mN pre-tension load; (c) 100 mN pre-tension load; (d) 200 mN pre-tension load.

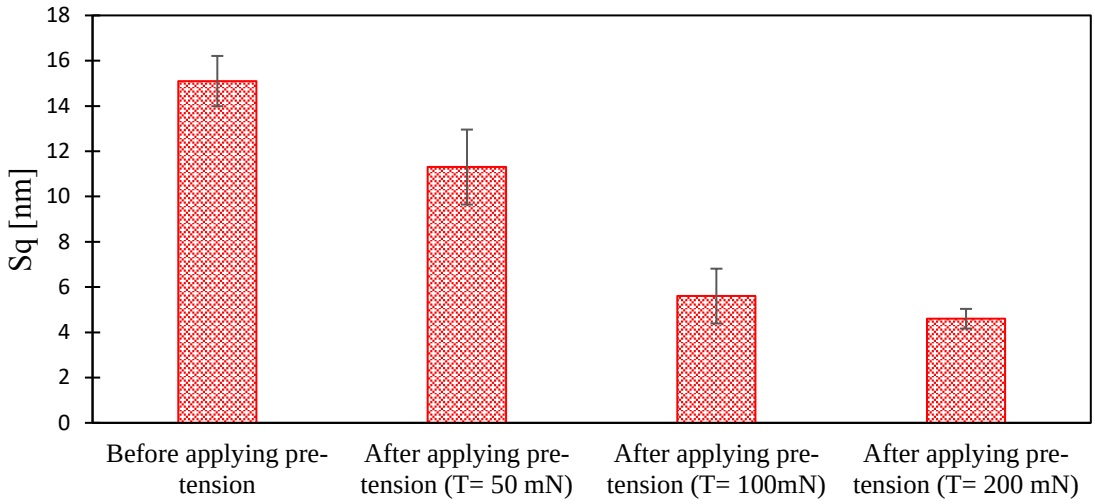

Figure 6 The effect of pre-tension on the Sq value of the fibre surface, scan area 3 µm x 3 µm.

3.2 Friction measurements

Figure 7 shows the friction force measurement signal, which measured on the HM fibre type under 10 mN normal load and a pre-tension load of 50 mN. The fibre is set to slide with a stroke of 100 µm both in forward and backward direction to complete one friction cycle. At the first 10 µm of sliding distance, the friction force signal shows a transient response when the normal load is applied to the contacting fibres. This is due to the lateral stiffness of the friction force mechanism (FFM) and the deformation of the contact. After reaching the desired normal load, the fibre starts sliding and the friction signal becomes stable. The pattern of the friction curve during forward and backward direction is similar, showing that a same value of the force is measured in both directions. Also, it is observed that the friction force values for the first cycle is slightly different from the other four cycles. This may be explained by the presence of the impurities on the fibre surface and these impurities are removed as the fibre slides. To complete one friction experiment, the friction cycle is repeated five times. The same trends can be observed in all friction tests. The friction force is calculated based on the average value of the friction force of five cycles both during forward and backward sliding. It is also can be seen from Figure 7, that the variation between each cycle is very small showing a good reproducibility, with a standard deviation, SD ≤ 0.1 mN.

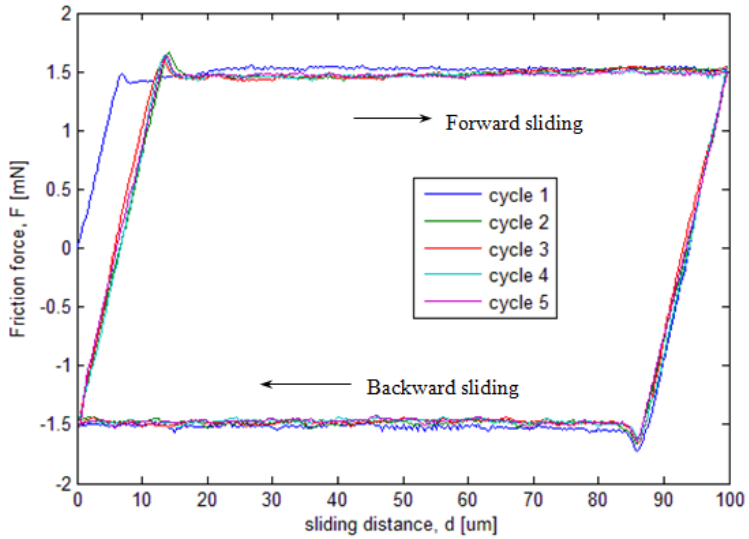

Figure 7 Typical friction force measured, *N* = 10 mN and *T* = 50 mN.

3.2.1 Geometrical analysis on the contact length due to pre-tension and the effect on friction

The contact length between the fibres is totally governed by the fibre deflection. The theory of taut wire [25] was used to have a clear view on the relationship between deflection, δ and pre-tension load, *T*. The taut wire equation is given by:

$$2\left(\frac{\delta}{L}\right)^3 A.E + \left(\frac{\delta}{L}\right)T - \frac{N}{4} = 0 \qquad (2)$$

where δ is the fibre deflection (m), *L* is the fibre length (m), *A* is the fibre cross-sectional area (m^2), *E* is the Young's modulus (Pa), *T* is the pre-tension load (N) and *N* is the normal load (N). There are two assumptions that were made in the analysis; (a) the contact length could be influenced by the deflection of the fibre and (b) the contact geometry is triangular as shown in Figure 8. This latter assumption is due to the very small contact length as compared to the fibre diameter. Also, note that a higher pre-tension will result in a lower deflection, which reduces the contact length. By using the taut wire equation (Eq. 2), the length of the contact could be determined by solving the equations in the half-plane axis that represents the fibres in the

system (see Figure 8). Due to the normal load, both fibres that are in contact start to deform at certain deflection δ. Thus, the behaviour of the lower fibre can be mathematically expressed as;

$$y = mx - \delta \tag{3}$$

and the circumference of the upper fibre that touch the lower fibre is represented by;

$$(x - x_c)^2 + (y - y_c)^2 = R^2 \tag{4}$$

where *m* is the line gradient, δ is the fibre deflection, x_c and y_c is the centre coordinates of the top fibre and *R* is the fibre radius. By solving both equations (3) and (4), the half-plane axis of the crossing point in coordinates *x* and *y* between two fibres can be determined. If it is assumed that the contact geometry is triangular, the wrapping length a_δ between two fibres in contact at a certain pre-tension and normal load can be calculated as;

$$a_\delta = \sqrt{x^2 + (-\delta_z - y)^2} \tag{5}$$

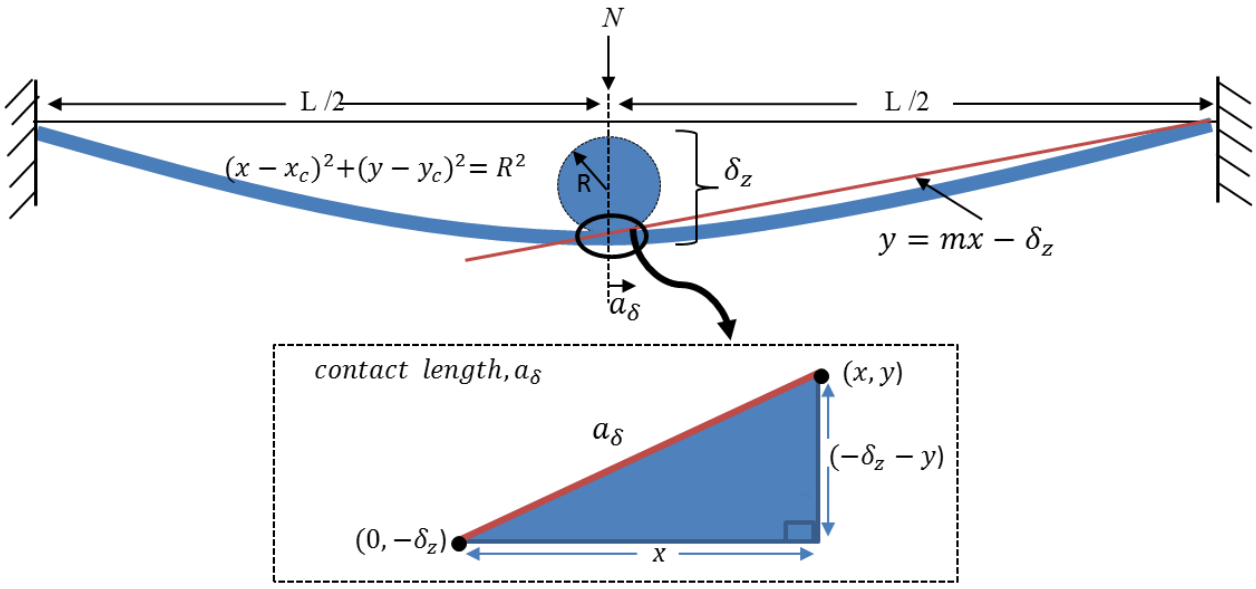

Figure 8 Fibre deflection due to the presence of pre-tension and normal load.

From the calculation using the geometrical analysis above, the results of HM and LM fibre deflection (of the lower fibre) under the influence of pre-tension and normal loads are plotted in Figure 9 (a) and (b) respectively. The calculation (theoretical model) are validated by comparing the results with the experiment data. The results of HM and LM fibres show a similar trend where the deflection of the fibre decreases with the pre-tension load. However, it is must be noted that the experimental values represent the total deflection of both upper and lower fibre, meanwhile the theoretical value only represent the deflection of the lower fibre. Therefore, the deflection of the upper fibre is the difference between the experimental and theoretical values. Interestingly, the difference between the experimental and theoretical values are found to be in the same range at least for the high normal loads at N = 5 mN and 10 mN, regardless of the fibre types. This result shows that the pre-tension of the upper fibre is constant. From equation (2), we know that if the pre-tension is constant, the only factor that contribute to the deflection is the fibre length. Moreover, as the upper fibre length is only 2 mm, so it is considered as stiff, which resulting in lower values of deflection than for the lower fibre.

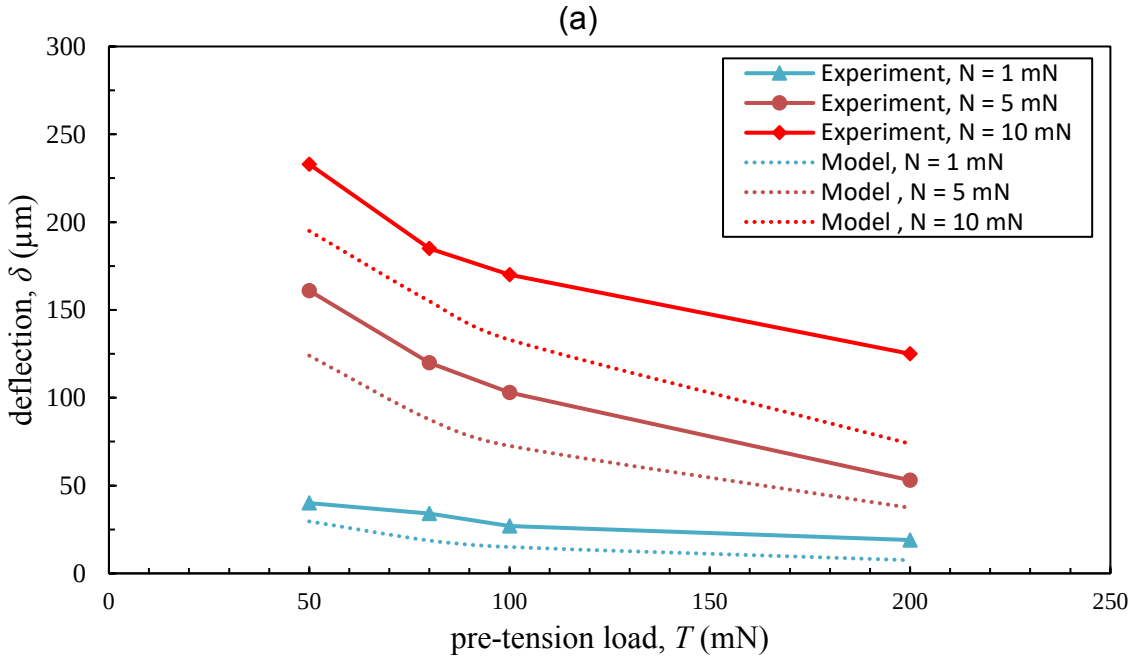

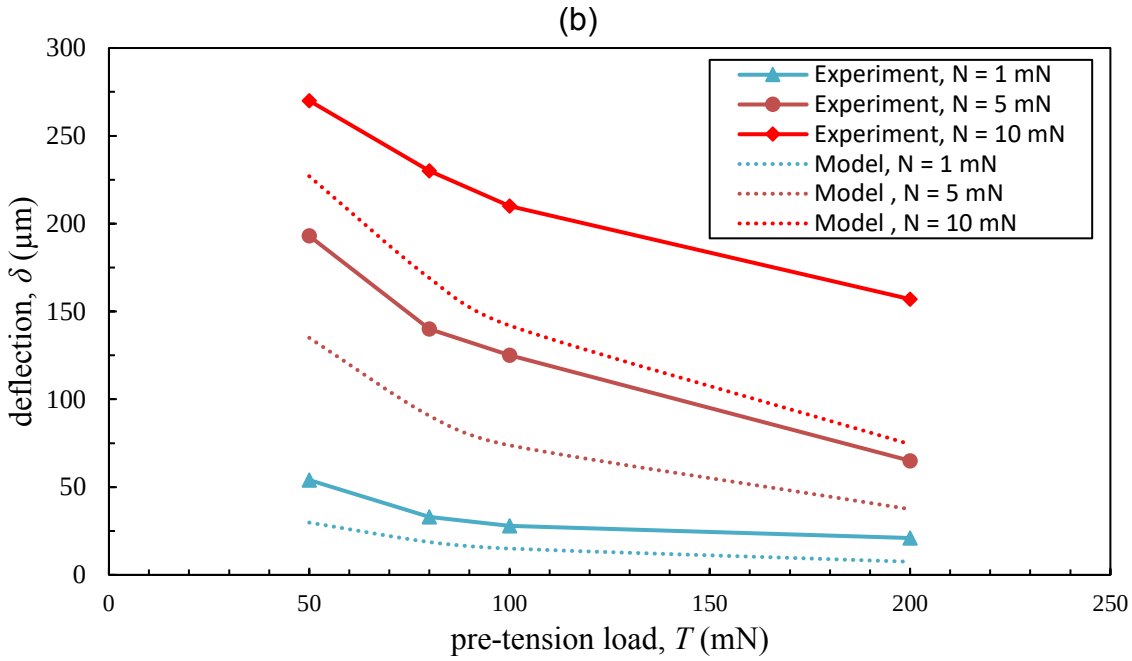

Figure 9 Comparison of the theoretical and experimental results on fibre deflection; (a) HM fibre; (b) LM fibre.

Figure 10 shows the experimental results of the friction force as a function of the pre-tension load for both the LM and HM fibre type. It can be observed that there is a gradual decrease in friction as the pre-tension load is increased, regardless of the normal load. A high pre-tension load could reduce the conformability and intimacy of the contact, which results in the decrease of the contact size and the friction force. Assuming the contact behaviour between fibres follows the Hertzian theory [26], the radius of the elastic contact deformation is compared with the calculated contact length (taut wire model). The contact radius between fibre-fibre at perpendicular contact is calculated using the equation as follows:

$$a_p = \sqrt[3]{\frac{3NR^*}{4E^*}} \tag{6}$$

where *N* is the normal load, *R** is the effective radius and *E** is the contact modulus. The contact modulus is calculated from the elastic modulus of the fibre, E_1 and E_2 and Poisson ratios v_1 and v_2 [26];

$$\frac{1}{E^*} = \frac{1-v_1^2}{E_1} + \frac{1-v_2^2}{E_2} \tag{7}$$

and the effective radius is calculated from the radius of the fibre, R_1 and R_2 [26];

$$R^* = \frac{R_1 R_2}{R_1 + R_2} \tag{8}$$

From calculations, at 1 mN, 5 mN and 10 mN normal loads, the contact radius is about 1.3 μm, 2.3 μm and 2.9 μm, respectively. Obviously, this contact radius is larger than the contact length that is due to the 'wrapping effect' between fibres which are found only 0.1 μm, 0.5 μm, 0.8 μm, respectively. Thus, in this case, the elastic deformation in fibre-fibre contact is found more significant over the 'wrapping effect' in influencing the contact area and friction force (see Figure 11). However, the role of pre-tension cannot be neglected as our result (see Figure 6) shows that the Sq values could be reduced by increasing the pre-tension load. This shown that although the influences of pre-tension on the fibre 'wrapping effect' is small, it does play a small role in changing the physical surface of the fibres and indirectly influences the size of the elastic deformation of the contact area.

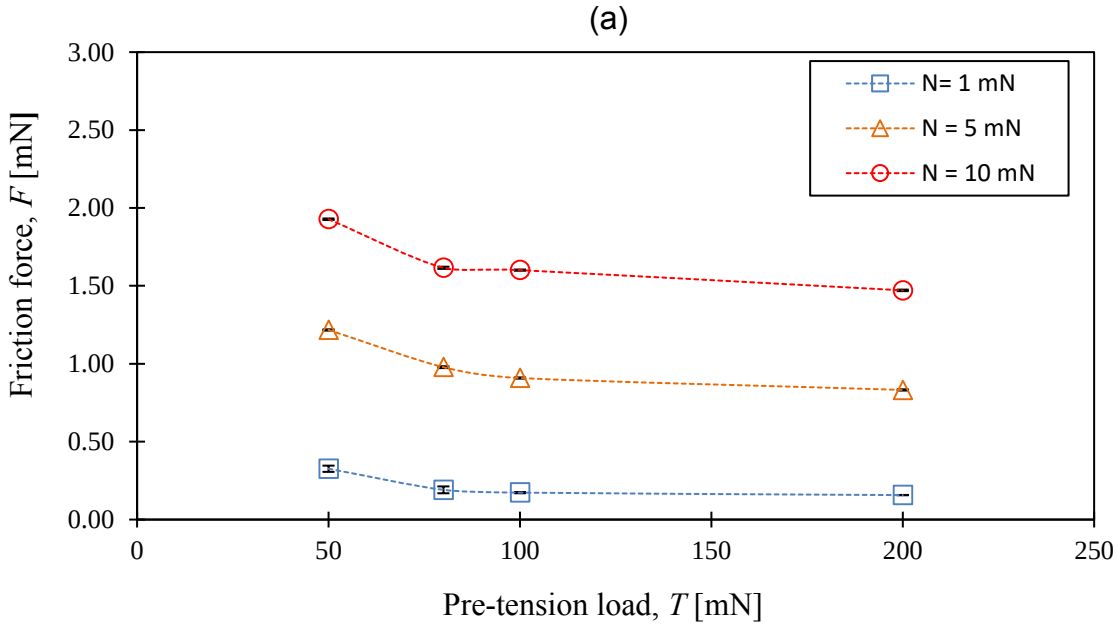

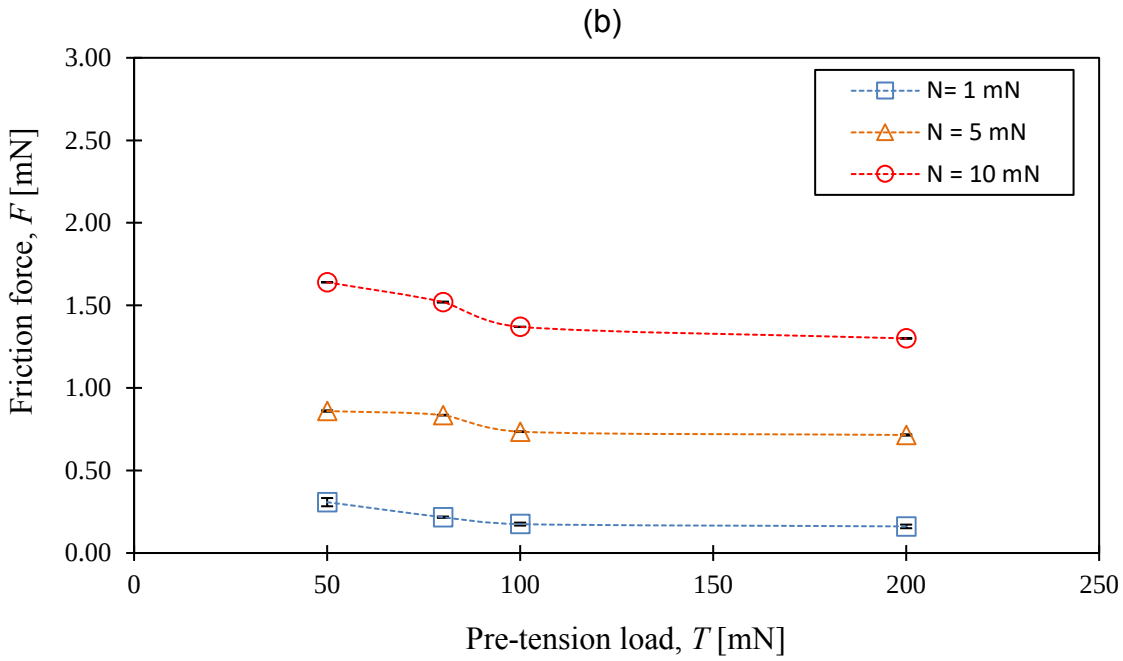

Figure 10 Friction force as a function of pre-tension load; (a) LM fibre type; (b) HM fibre type.

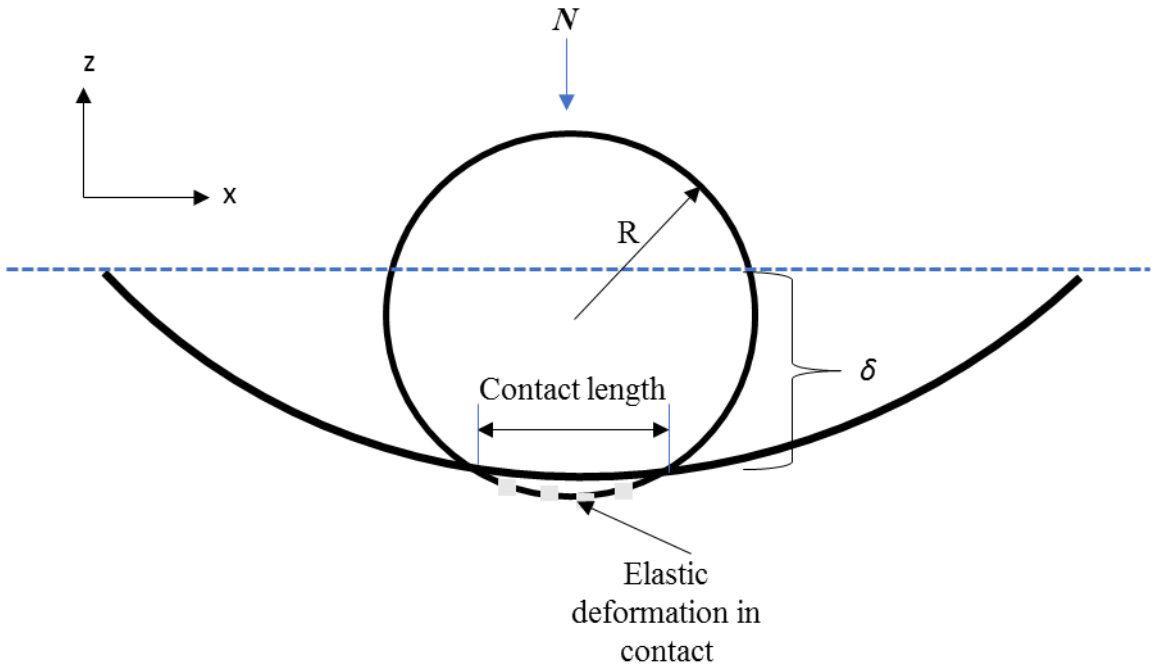

Figure 11 Illustration of the contact length due to 'wrapping effect' and elastic deformation in fibre-fibre contacts.

3.2.2 Effect of elastic modulus on friction

Figure 12 shows the friction force of the low and high modulus fibre with similar sizing under 50 mN pre-tension at varying normal load. The friction force of low modulus (LM) fibre type is found to be slightly higher than the high modulus (HM) fibre type under similar conditions. The fibre with low elastic modulus has a low bending stiffness and therefore during loading, the LM fibre have a higher deflection and generate a larger contact length between the fibres that increase the friction force as shown in Figure 12 (a). With respect to the elastic modulus values, one would expect that the friction force of LM fibre will be two times higher than the HM fibre. However, according to Gupta, the resistance to bending is determined by [7]:

$$Resistance\ to\ bending = \left[\frac{1}{4\pi\beta_0}\right]\frac{\varepsilon E d^2}{\rho} \tag{9}$$

where ε is the shape factor, E is the modulus, d is linear density, ρ is the density and β_0 is a constant which depend on the units in which E, d and ρ are expressed. So, although the elastic modulus of the LM fibre is half of the HM fibre, the size of the fibre in terms of linear density also need to be considered in influencing the contact intimacy and friction between fibres. Due to this effect the friction forces are found to differ by 34%.

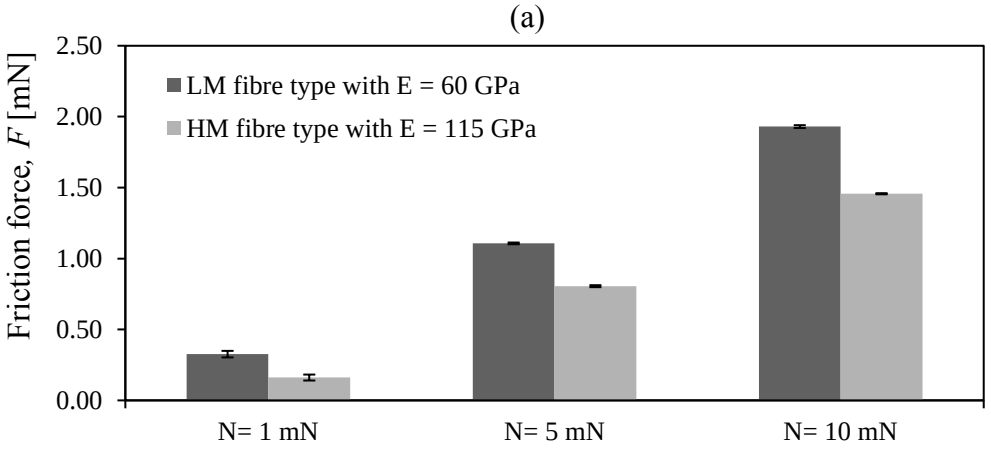

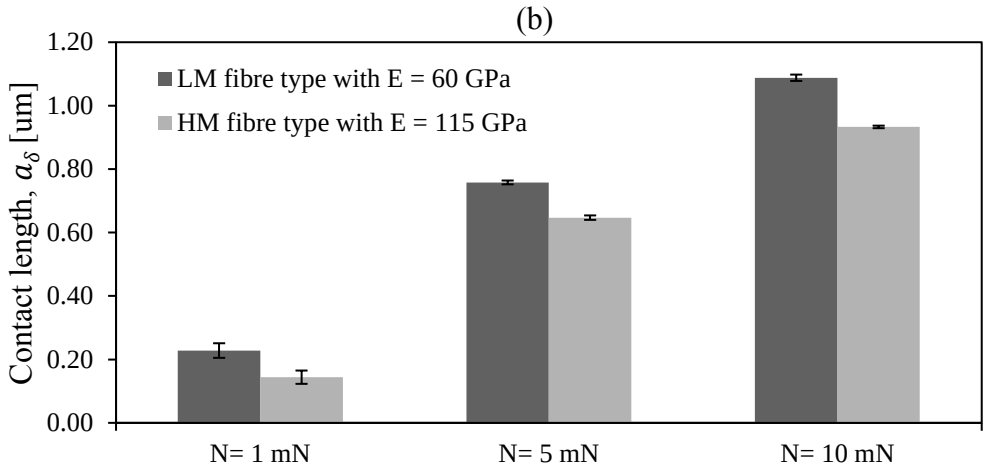

Figure 12 The effect of elastic modulus on (a) Friction force; (b) Contact length two different fibre types under 50 mN pre-tension load.

3.2.3 Effect of normal load on friction

In order to study the effect of normal load on friction, the friction forces are also measured for the HM fibre with varying normal load in the range of 1 to 10 mN at various pre-tension loads. The same normal load range has been used by Tourlonias et al. [13] in tests with single carbon fibres. The friction force as a function of normal load is shown in Figure 13. In the range of normal load tested, the friction force is found to be proportional with the normal load. These results are in agreement with [13], as the friction force is found to approximately follow the Coulomb's law.

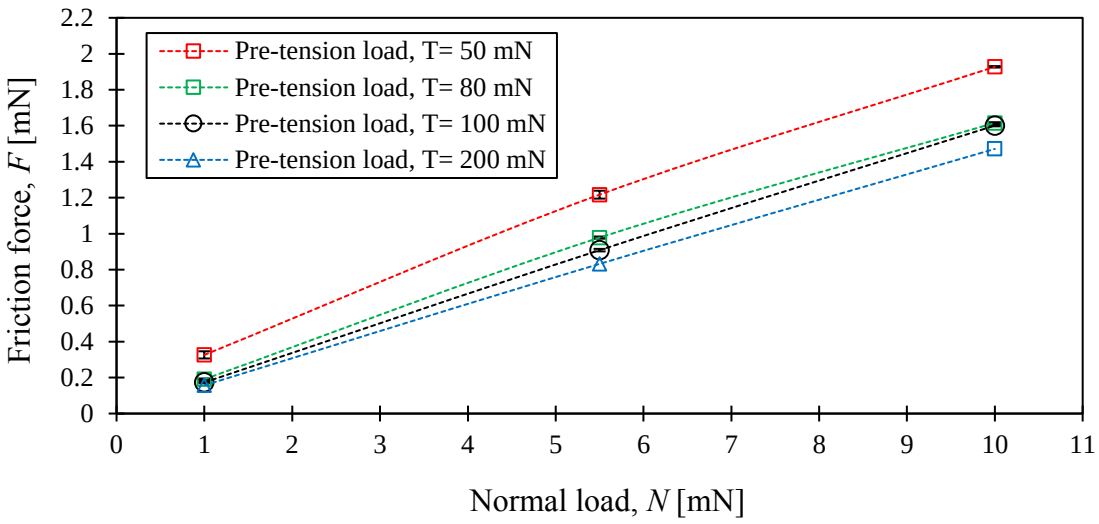

Figure 13 Friction force as a function of normal load for the HM fibre type.

4 Conclusions

The frictional behaviour between two single aramid fibres in contact under the influence of pre-tension loads have been successfully studied. An experimental setup was developed to measure the friction force of single fibres sliding perpendicular against each other in linear reciprocating motion. The friction measurements data of the single aramid fibres obtained show a good reproducibility. Also, the friction force obtained using this experimental setup and the contact length model are in agreement. As a high pre-tension load is induced to the fibre, the friction force decreases as a result of high resistance to bending of the fibre and as a consequence a reducing contact length between the fibres. However, this contact length is found to be very small compared to the contact radius of the elastic deformation of the fibre-fibre contact. It can be concluded that the elastic deformation in contact dominates the contact area and friction force significantly. Meanwhile, the effect of elastic modulus and the contribution of linear density of the fibre also increases in the friction force, in our case ~ 34%. The friction force increases linear with the normal load in the range of 1 to 10 mN.

Acknowledgement

The authors would like to thank Universiti Teknikal Malaysia Melaka and Ministry of Education Malaysia for financial support of the first author and Teijin Aramid B.V, The Netherlands for supplying the material.

References

[1] Rudov-Clark S, Mouritz AP, Lee L, Bannister MK. Fibre damage in the manufacture of advanced three-dimensional woven composites. Compos A Appl Sci Manuf 2003;34(10):963–70.

[2] Lee B, Leong KH, Herszberg I. Effect of weaving on the tensile properties of carbon fibre tows and woven composites. J Reinf Plast Compos 2001; 20:652–70.

[3] Decrette M, Mourad S, Osselin J-F, Drean J-Y. Jacquard UNIVAL 100 parameters study for high-density weaving optimization. J Ind Text 2015.

[4] Leech M. The modelling of friction in polymer fibre ropes. Int J Mech Sci 2002; 44: 621-643.

[5] Humeau C, Davies P, Engles TAP, Govaert LE, Vlasblom M, Jacquein F. Tension fatigue failure prediction for HMPE ropes. Poly Test 2018; 65:497-504.

[6] Yusekkaya ME. More about friction and its measurements. Textile Progress 2009; 41(3):141–193.

[7] Gupta BS. Friction in textile materials. Woodhead Publishing Limited, 2008.

[8] Bowden FP, Leben L. The nature of sliding and the analysis of friction. Proc R Soc London A 1939; A169; 371–391.

[9] Pascoe MW, Tabor D. The friction and deformation of polymers. Proc R Soc London A 1956; 235(1201); 210–24.

[10] Roselman IC, Tabor D. The friction of carbon fibres. J Phys D Appl Phys 1976; 9 (17):2517.

[11] Mercer EH, Makinson KR. The frictional properties of wool and other textile fibres. J Textile Inst Trans 1947; 38(5):T227–40.

[12] Howell HG. Inter-fibre friction. J Textile Inst Trans 1951; 42(12): T521–33.

[13] Tourlinas M,Bueno M-A, Poquillon D. Friction of carbon tows and fine single fibers. Compos Part A: Appl Sci Manuf. 2017; 98: 116-123.

[14] Houssem EG, Barbier G, Kocher CW, Sinoimeri A, Pumo B. Experimental evaluation of transverse friction between fibers. Trib Int 2018; 119:112-122.

[15] Briscoe BJ, Kremnitzer SL. A study of the friction and adhesion of Polyethylene terephthalate monofilaments. J Phys D: App Phys 1979; 5:505-516.

[16] Mulvihil D, Smerdova O, Sutcliffe M. Friction of carbon fibre tows. Compos Part A: Appl Sci Manuf 2016; 93:185–198.

[17] Lincoln B. Frictional and elastic properties of high polymeric materials. Brit J Appl Phys 1952 ; (3):60.

[18] Gralen N, Olofsson B. Measurement of friction between single fibers. Text Res J 1947; 17(9): 488–496.

[19] Lindberg J, Gralén N. Measurement of friction between single fibers: II. Frictional properties of wool fibers measured by the fiber-twist method. Text Res J 1948; 18(5):287–301.

[20] Roselman IC, Tabor D. The friction and wear of individual of carbon fibres. J Phys D Appl Phys 1977; 10: 1181-1194.

[21] Cornelissen B, Rietman B, Akkerman R. Frictional behaviour of high performance fibrous tows: friction experiments. Compos Part A: Appl Sci Manuf 2013; 44:95–104.

[22] Chakladar ND, Mandal P, Potluri P. Effects of inter-tow angle and tow size on carbon fibre friction. Compos Part A: Appl Sci Manuf 2014; 65; 115–124.

[23] Yaqoob MA, de Rooij MB, Schipper DJ. Design of a vacuum based test rig for measuring micro adhesion and friction force. WTT Transaction and Built Environment, 2012 ;(14):261–274.

[24] ASME B46-1. Surface texture, surface roughness, waviness and lay. 2002.

[25] Charles I. Applied mechanics for engineers. The Syndic of the Cambridge Uni Press 1951:54-66.

[26] Johnson KL. Contact mechanics. Cambridge Uni Press. 1985.

Paper C

Experimental study of the contact angle and surface energy of a single aramid fibre and its frictional effects.

Nurhidayah ISMAIL, [1,2*] Matthijn B. de. ROOIJ,[1] Erik G de. VRIES,[1] and Dik J. SCHIPPER[1]

[1]Surface Technology and Tribology Laboratory, Department Mechanics of Solids, Surfaces and Systems (MS3), Faculty of Engineering Technology, University of Twente, Drienerlolaan 5, 7522 NB, Enschede, The Netherlands.

[2]Center of Advanced Research and Energy, Faculty of Mechanical Engineering, Universiti Teknikal Malaysia Melaka, Hang Tuah Jaya, 76100 Durian Tunggal, Melaka, Malaysia.

Abstract

In this experimental study the dynamic contact angle measurement method of Wilhelmy is used to determine the surface energy of a single aramid fibre. Surface energy plays an important role in influencing the adhesion and friction behaviour between fibre-fibre contacts in composite materials. Contact angles of three different types of Twaron® aramid fibres with different treated material and thickness is measured in a series of test liquids. The contact angle hysteresis is also observed during advancing and receding the fibre into and from the liquid. Results show that the surface energy of the treated fibre is slightly higher than the non-treated fibre, about 36.7%. The fibre thickness increases the fibre surface energy. This study also found that the coefficient of friction is proportional to the product of the surface energy per unit area and the area of contact between fibre-fibre interfaces.

1 Introduction

Friction force is a force that opposes the motion of one surface (or an object) over another surface that breaks the surface contact in the sliding direction. However, within the contacting surface itself, pressure and adhesion force exist that required additional attention. Basically, the adhesion force is the main force that holds the surfaces together. The adhesion force is developed due to the adhesive bonding of the surfaces and it is typically characterized by pull-off, the force required to separate the surfaces in normal direction.

The adhesion force is one of the crucial factors in investigating the structural performance of fibrous materials. Note that at micro and nanoscale contact, the adhesion forces can be relatively high due to a high surface area-to-volume ratio [1]. In composites, the adhesion between fibres or between fibres and matrix material is an important property as it influences the function of adhesive bonding between fibres in the tow bundle, fibre to matrix and fibre coating [2-4]. Therefore, physical and chemical treatments are often applied to control the interfacial adhesion and ability to withstand the shear forces encountered during processing and use.

The adhesion behaviour depends on the surface properties of the solid surface and the interface, surface cleanliness, the area of contact and the environmental conditions as well as the surface energy. The surface energy of a solid can be determined through contact angle measurements between the solid and a series of test liquids. Several methods have been established to measure the contact angle of a solid surface, particularly a filament shape [5-8]. One of the most extensively used methods for measuring the contact angle the sessile drop method. Using this method, a proper amount of liquid is dropped onto the solid surface. Then, the contact angle is measured between the tangent to the liquid-vapour (LV) interface and the solid-liquid (SL) interface as shown in Figure 1.

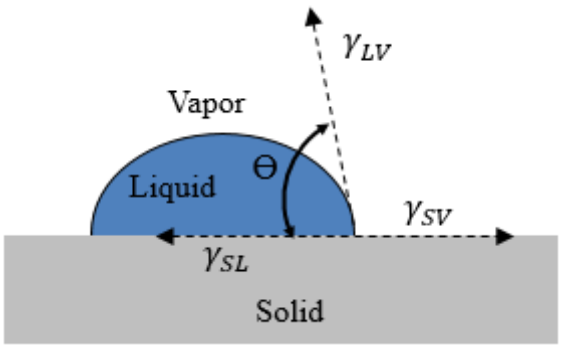

Figure 1 Contact angle measurement of a solid using the sessile drop method [9].

This method is considered a static approach as the contact angle is measured from the static drop of the liquid on the fibre surface [10]. For a flat solid surface, measuring the contact angle using the sessile drop method is practical, but for a cylindrically shaped surface such as a thin filament this method is quite challenging. Interestingly, studies done by Hao et.al [11] on a modified aramid fibre surface using

this method found that the volume of the liquid droplet influences the drop shape as well as the macroscopic contact angle between the drop and the fibre. Additionally, with a liquid that is prone to evaporate, measuring the accurate drop profile is difficult and the reproducibility is also poor. For such geometry measuring the contact angle based on the Wilhelmy method is an alternative [12]. In this method, the contact angle is deduced from the wetting force which is measured during immersion and withdrawing the fibre from the liquid. According to the literature, this method has been applied on carbon [13-14] and basalt [15] fibres but not on a flexible fibre such as aramid.

Therefore, the aim of this paper is to determine the surface energy of a single aramid fibre using the Wilhelmy method. The surface energy of different types of Twaron® aramid fibres are measured and the relation of surface energy and area of contact between two interacting fibres to friction is studied.

2 Material used

2.1 Aramid fibre

Three different types of Twaron® aramid fibres are used in this study which are provided by Teijin Aramid B.V, Arnhem, The Netherlands. Table 1 shows the material properties of a single fibre. Both A1 and A2 fibres are from the same fibre type. The only difference is that fibre A1 is a virgin fibre while the A2 fibre surface is treated with alkyl-phosphate salt. The OC fibre is treated with ethoxylated/propoxylated butanol and the thickness of the OC is almost 12 times larger than the A fibre type. Three samples were tested for each fibre type. The samples are cut from the bobbin and directly measured. The length of each sample is approximately 10 mm. The appropriate length is essential as a sample that is too long will cause the fibre to bend due to the low bending stiffness, thus the fibre will ‘swim’ on the test liquid surface during the measurement.

Table 1 The material properties of Twaron® aramid fibre.

Properties	Unit	A1	A2	OC
Elastic modulus	GPa	109	109	29.3
Linear density	dtex	1.7	1.7	210
Breaking strength	mN	390	390	15400
Fibre diameter	µm	12	12.2	140
Finish material		No	Alkyl-phosphate salt	ethoxylated/ propoxylated butanol

2.2 Test liquids

In order to assess the surface energy of the fibre, a set of liquids with a different range of polar and dispersive components needs to be used. Here, the contact angle between the fibre and the liquid was tested in three different test liquids: *n*-hexane, distilled water, and ethylene glycol. The *n*-hexane was chosen as it is nonpolar and has a low surface tension while distilled water has a high polarity component and high surface tension. Ethylene glycol was chosen as the third liquid, since it has both polar and dispersive components. The properties of the test liquids are listed in Table 2, where γ_L is the liquid surface tension, γ_L^d is the dispersive component, γ_L^p is the polar component, ρ is the liquid density and η is the liquid viscosity.

Table 2 Properties of the test liquids.

Test liquid	γ_L (mN/m)	γ_L^d(mN/m)	γ_L^p(mN/m)	ρ(g/cm^3)	η(mPas)
n-hexane	18.43	18.43	0	0.6603	0.3080
distilled water	72.80	29.10	43.70	0.9982	1.002
ethylene glycol	48.00	29.00	19.00	1.1088	21.80

3 Methods

3.1 Fibre surface characterization

The microstructure of the aramid fibres was examined using Scanning Electron Microscopy (SEM). Since the aramid fibre is a non-conductive material, a gold metallization was applied to the surface in order to improve the image quality.

Atomic Force Microscopy (AFM) was used to evaluate the surface roughness of the aramid fibre. The areal roughness measurement was performed using a Nanosurf FlexAFM. Here, ACTA cantilever types from AppNano were used. The constant of the cantilever is in the range of 13-77 N/m with a width of 30 µm, and a length of 125 µm. The scanning area was set to 3 µm x 3 µm. The fibre was placed vertically parallel to the AFM tip (see Figure 2) and the roughness measurement was performed at three different locations (A, B and C). The fibre was scanned along the *x* direction within the scan size area of 3x3 µm with a resolution of 512 x 512 points, eliminating the influence of fibre orientation on the roughness measurement.

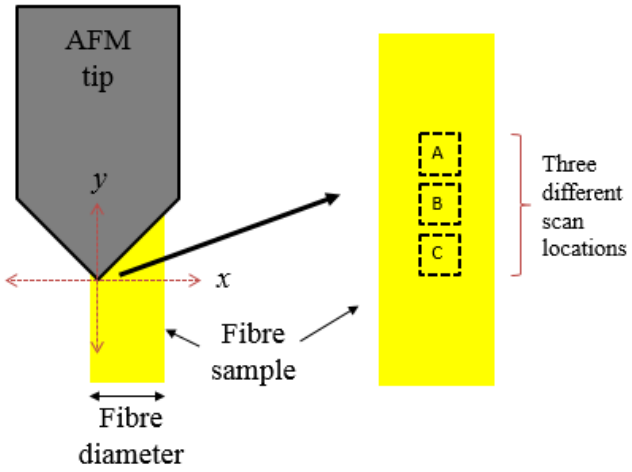

Figure 2 Illustration of the roughness measurement using AFM.

3.2 Contact angle of single aramid fibre

The contact angle of a single aramid fibre can be determined from the dynamic wetting force. The fibre is oriented perpendicular to the liquid interface and the force exerted on it during immersion and withdrawal due to wetting is measured by a tensiometer as shown in Figure 3.

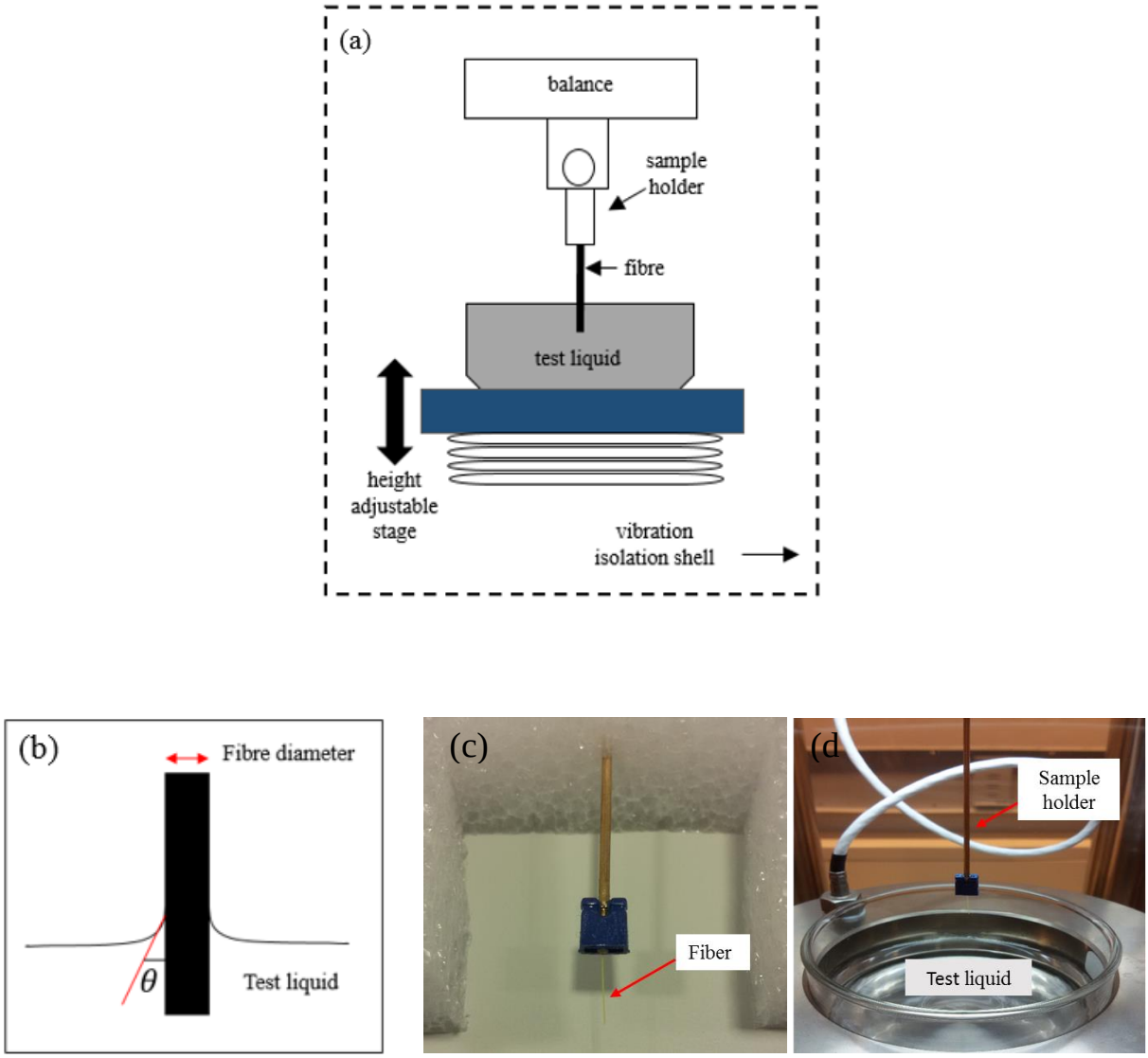

Figure 3 Experimental setup (a) DCAT 11 setup; (b) contact angle; (c) and (d) image of aramid fibre glued on the sample holder.

The force measured is a combination of the wetting force, buoyancy force and a mass which can be expressed as:

$$F_{wetting} = F_{capillary} - F_{bouyancy} + mass$$

$$= \pi D \gamma_l cos\ \theta - \rho g V_{immersed} + mg \qquad \text{(Eq.1)}$$

where γ_l is the surface tension of the test liquid, D is the diameter of the fibre and θ is the contact angle, m is the mass of the fibre, g is the gravitational acceleration, ρ is

the density of the test liquid and $V_{immersed}$ is the immersed volume of the fibre. In this case, if 5 mm of fibre is immersed in distilled water, the buoyancy force was found to be of the order of 10^{-9} N which is very small and can be ignored in comparison with the capillary force of the order of 10^{-5} N. Since the tensiometer is zeroed each time before starting the measurement, the mass contribution is zero. This means that the relationship between the force measured, *F*, and the contact angle, *θ*, becomes;

$$F_{wetting} = \pi D \gamma_l cos\theta \qquad \text{(Eq.2)}$$

In this study, the dynamic contact angle measurements were performed using DCAT 11 by DataPhysics Instruments, GmbH with a resolution of 10^{-6} g and a lifting speed ranging from 0.7 um/s to 500 mm/min. The constant speed of 0.05 mm/s was used during both immersion and withdrawal of the fibre. According to Qiu and co-workers [10], a dynamic contact angle which is measured at a speed lower than 20 mm/min is considered a static advancing contact angle. As shown in Figure 3(a), a vessel containing the test liquid is placed under the balance on an adjustable height stage. The fibre is attached to the sample holder using adhesive glue and clamped to the balance as shown in Figure 3(c) and (d). Before the measurement starts, the adjustable stage is moved up to a few millimetres below the bottom of the fibre. The force during immersion and withdrawal are then measured at constant speed. The measurement is repeated five times for each sample in a test liquid. The immersion depth is set to 5 mm and for each sample, a fresh liquid is used to avoid contamination effects.

3.3 Determination of surface energy

According to Young's equation [9], there is a relationship between the contact angle θ, the surface tension of the liquid γ_L, the interfacial tension γ_{SL} between liquid and solid and the surface free energy γ_S of the solid:

$$\gamma_S = \gamma_L \cdot cos\theta + \gamma_{SL} \qquad \text{(Eq.3)}$$

In order to be able to calculate the surface free energy of a single aramid fibre from the contact angle, the second unknown variable γ_{SL} must be determined. Building on the Fowkes method [16], the interfacial tension γ_{SL} is calculated based on the two surface tensions γ_S and γ_L and the similar interactions between the phases. These interactions are interpreted as the geometric mean of a dispersive part $\gamma^d$and a polar part γ^p of the surface tension or surface free energy, resulting in:

$$\gamma_{SL} = \gamma_S + \gamma_L - 2\left(\sqrt{\gamma_S^d \cdot \gamma_L^d} + \sqrt{\gamma_S^p \cdot \gamma_L^p}\right) \quad \text{(Eq.4)}$$

The combination of Eq. 3 and Eq. 4 leads to:

$$\gamma_L(1 + cos\theta)/2\sqrt{\gamma_L^d} = \sqrt{\gamma_s^p}\sqrt{\frac{\gamma_l^p}{\gamma_l^d}} + \sqrt{\gamma_s^d} \quad \text{(Eq.5)}$$

The contact angle value is calculated from the capillary force using Eq. 2 and inserted in the Owens-Wendt, so Eq. 5 [17]. At least two liquids with known dispersive and polar parts of the surface tension are required to determine the surface free energy of the solid, wherein at least one of the liquids must have a polar part greater than zero. According to Chapman [18], using only two liquids results in an overestimation of the dispersive component; if more liquids are used, it increases the accuracy in the determination of fibre surface energy [19].

4 Results and discussion

4.1 Surface roughness

Figure 4(a) shows the microscopic image of the surface structure of A1 obtained from SEM, and Figure 4(b), (c) and (d) show the areal surface roughness measurement performed by AFM of fibre A1, A2 and OC respectively at location B. The root mean square (RMS) value for the roughness measured are Sq ≈ 1.6 nm for A1, Sq ≈ 2.4 nm for A2 and Sq ≈ 3.7 nm for OC. Comparing two similar fibre types

A1 and A2 shows that treating the fibre surface with a coating has only a slight impact on surface roughness. At microscopic scale, the roughness is present, but in the order of nm. In Figure 4(b),(c) and (d), results revealed that there are ridges and grooves on the fibre surface.

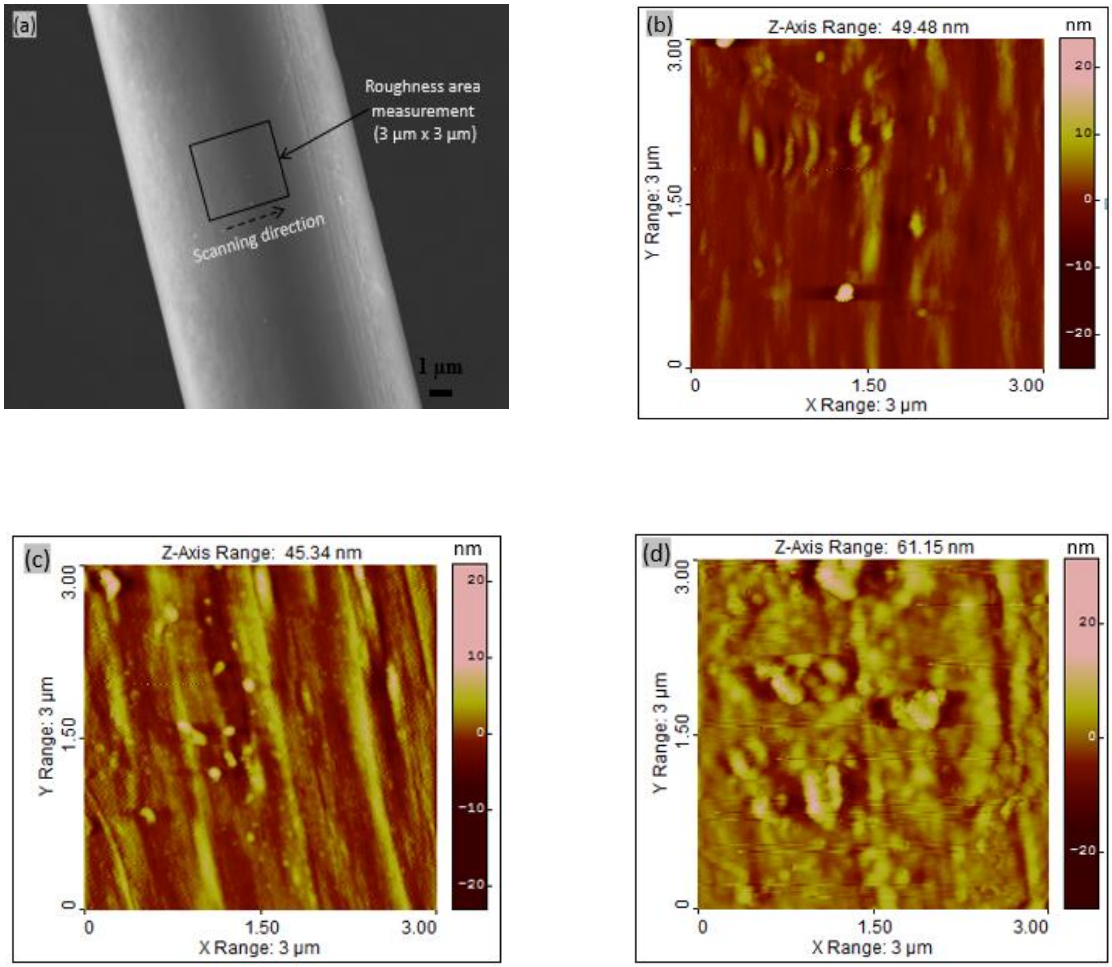

Figure 4 SEM and AFM images (a) SEM image of A2 fibre; Roughness measurements (b) A1, (c) A2 and (d) OC.

4.2 Contact angle measurements

Figure 5 shows the typical force measured as a function of the immersion depth of the OC fibre type in water. The force signal is zero at the beginning as the fibre starts to approach the test liquid. There is a significant jump in the force signal at 1.2 mm in depth as the fibre starts contacting the test liquid surface and forming the contact angle. Afterwards, the force signal shows a steady value until reaching the desired depth. Then the reverse process takes place as the adjustable stage moves in the opposite direction and a steady force signal of receding angle is measured. As the

fibre emerges from the liquid as in Figure 6(a), the force signal continues to show a gradual increase. When reaching 0.8 mm, the force signal suddenly drops to zero which appears to be exactly the same value as in the beginning of the measurement. This behaviour was due to the 'snap off' between the fibre and the test liquid. A slightly higher force just before the 'snap off' was attributed to the meniscus force during separation between the fibre and the test liquid as shown in Figure 6(b).

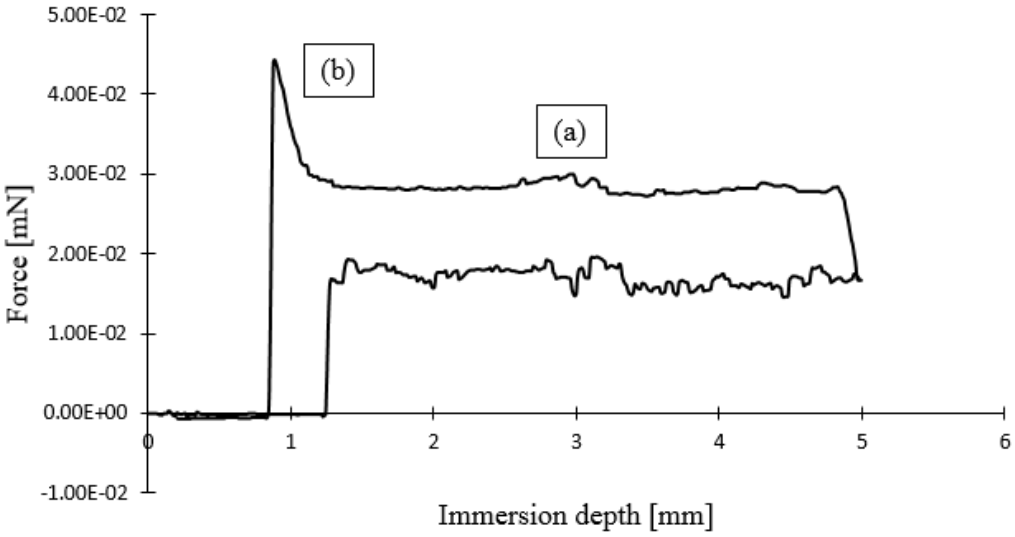

Figure 5 Typical force measurement for the OC fibre type in water.

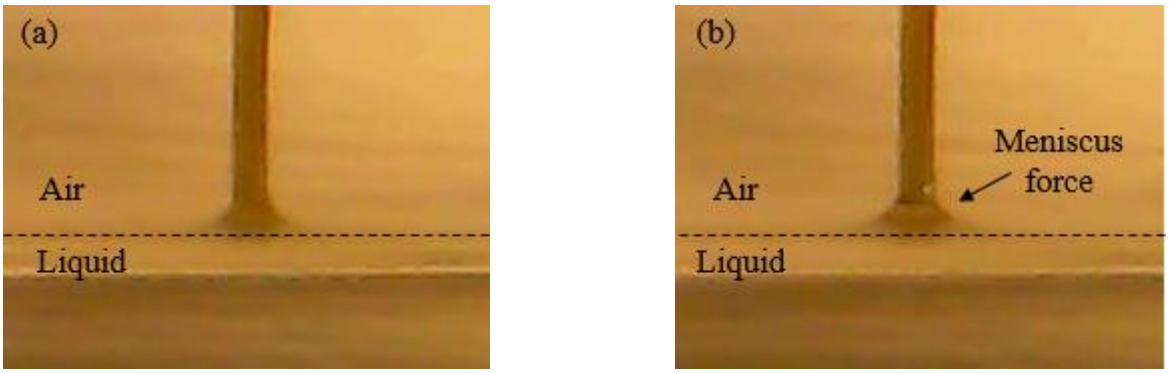

Figure 6 Real-time image of the meniscus formed between the OC and water.

Table 3 shows the measurements for both advancing and receding contact angles. An average advancing contact angle of 65.1° was obtained for untreated fibre A1. This is slightly higher than measured by Hao and co-workers (61.4°) using the

sessile drop method [11]. According to [7], the capillary force increases linearly with the diameter of the filament due to the higher wetted length, being linear with the diameter. Interestingly, our result shows that a fibre with a large thickness, the OC fibre type, has a smaller contact angle than the A1 and A2 fibre type. It is assumed that the smaller contact angle may be due to the porosity of the OC fibre, as it is composed of microfilaments or thin fibrils. Further, it is noticed that the advancing contact angles are slightly higher than receding contact angles and these differences are defined as contact angle hysteresis (CAH).

Table 3 The mean contact angle (CA) for all fibre type used in the experiment.

Fibre type	Contact angles (CA) ± SD		
	CA advancing	CA receding	CA hysteresis
A1	65.1 ± 1.4	41.9 ± 4.7	23.2
A2	61.3 ± 1.5	31.4 ± 5.6	29.9
OC	35.8 ± 0.9	12.5 ± 1.1	23.3

*SD = Standard deviation

According to the literature, it is assumed that this hysteresis is a thermodynamically occurs irreversible process which is attributed to several sources such as surface roughness [20], surface chemical heterogeneity [21, 22], liquid adsorption and desorption [23] as well as molecular rearrangement [24]. In this study, it is unlikely that the primary cause of CAH is due to the surface roughness, as from our AFM measurement results the surface can be regarded as microscopically smooth with Sq being less than 5 nm for all fibres. The molecular arrangement also cannot be connected to the CAH as the aramid fibre a highly crystalline aromatic polymer which consists of immobile molecular chains [25]. Thus, it is assumed that in this study the CAH could be from other sources such as surface chemical heterogeneity.

4.3 Surface free energy analysis

Figure 7 shows plots obtained by utilizing the values of the contact angles to determine the surface energy of single aramid fibres for the three test liquids using the Owens-Wendt method as discussed in section 3.3. All results show a reasonable

agreement with the Owens-Wendt equation (Eq. 5) with a correlation coefficient above 0.85 for all fibre types. Table 4 shows the dispersive and polar components of the fibre surface energy for a single aramid fibre calculated using the Owens-Wendt method. Overall results show that the value of the polar component is higher than the dispersive component. It is also found that the treated fibre, A2, has a total surface energy 12 mN/m greater than the A1 fibre.

(a)

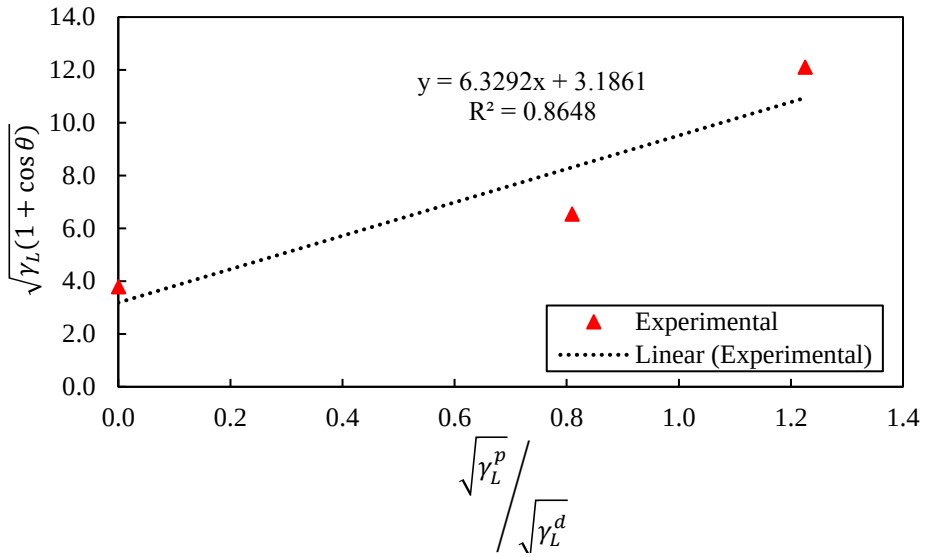

(b)

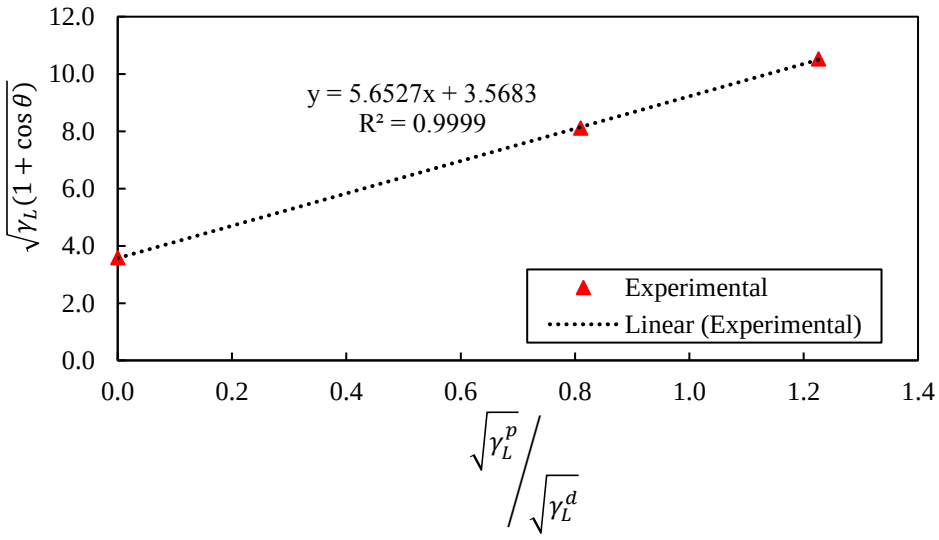

(c)

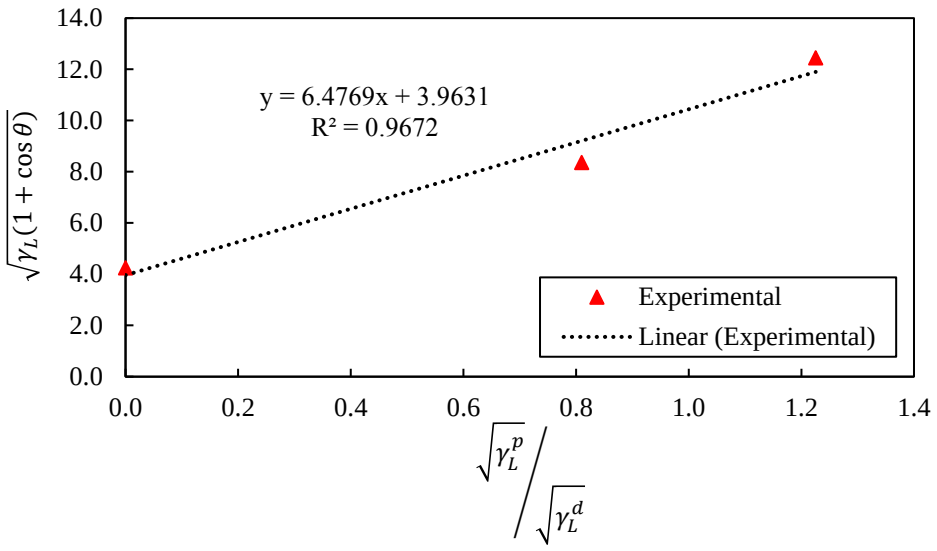

Figure 7 Linear fittings for surface energies of a single aramid fibre; (a) A1; (b) A2 and (c) OC.

Table 4 The values of surface energy and its component (dispersive and polar).

Material	γ [mN/m]	γ^d [mN/m]	γ^p [mN/m]
A1	32.69	15.01	17.68
A2	44.69	12.83	31.95
OC	59.32	14.6	44.72

5 Relation of surface energy with friction between two single aramid fibres in contact

When the surfaces of the fibres are brought into contact, a tangential force is required to initiate a motion between the fibres. This force is dependent on the applied normal force as well as the adhesion force. According to most adhesion models, Johnson-Kendall-Roberts (JKR) [26], Derjaguin-Muller-Toporov (DMT) [27], and Maugis-Dugdale (MD) [28] - the adhesion force is proportional to the role of adhesion. One of the factors that influence this adhesion force is the surface energy. Therefore, it is interesting to consider the role of surface energy on the frictional behaviour between two single aramid fibres.

Using the developed experimental setup as shown in Figure 8, the friction force is measured between two single aramid fibres in sliding contact under a load of 10 mN

and 15 mN. The measurement is carried out in ambient air at a room temperature of 20°C ± 1°C with relative humidity of 40-60 % RH and sliding speed of 2 µm s^{-1} with a sliding distance of 100 µm. Table 5 shows the coefficient of friction results of the A1 and A2 fibre. It can be seen that the coefficient of friction of the A1 (untreated fibre) is slightly lower than the A2 (treated fibre).

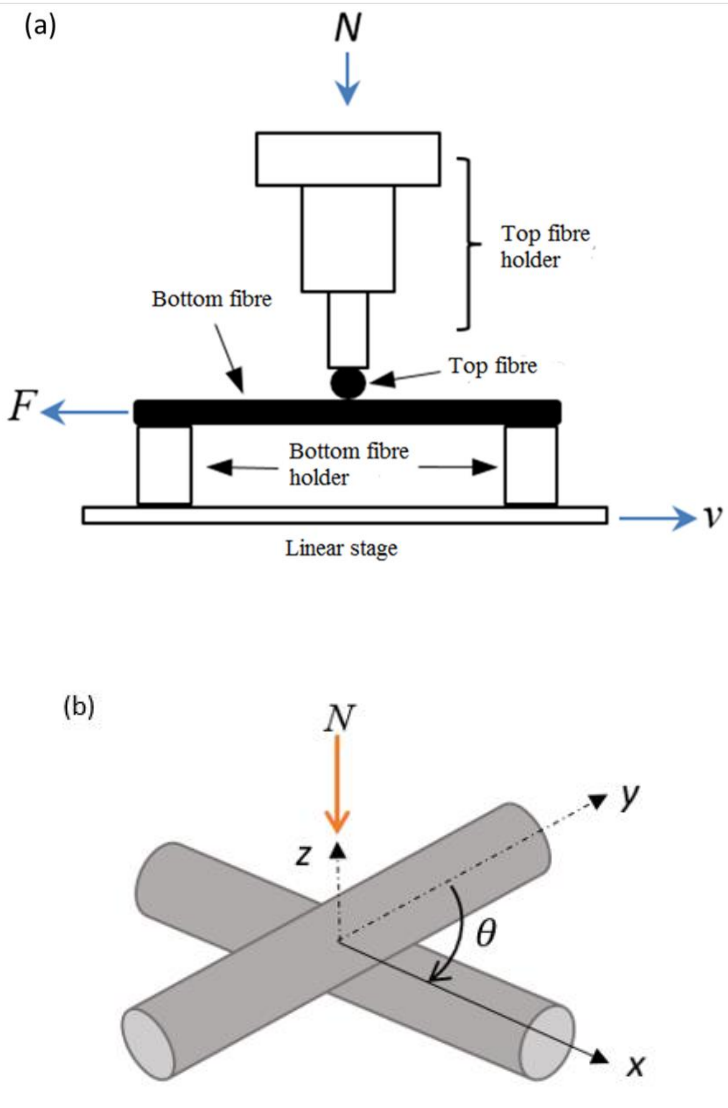

Figure 8 Friction between two single fibres (a) Experimental setup (b) fibre-fibre arrangement.

Table 5 Experimental friction results.

Fibre type	A1	A2
Normal load [mN]	Coefficient of friction, μ	Coefficient of friction, μ
1	0.155	0.177
5	0.141	0.155
10	0.135	0.142
15	0.128	0.132

Since friction force is proportional to the area of contact, i.e. $F = \tau A$ [29,30]; assuming that no ploughing occurs at the contact interface; and friction is caused only by the shear in the microcontact, where τ is the shear strength of the contact interface, a large area of contact (at equivalent pressures) results in a higher friction force, i.e. a higher coefficient of friction. Here, the interfacial bond strength per unit area at the fibre-fibre interface could be directly related with the surface energy per unit area γ of a fibre as was done in [31] for ceramic-metal couples in vacuum. In this analysis, the contact area between two fibres sliding at a perpendicular contact, *A*, can be easily derived from the JKR circular contact model as [26]:

$$A = \left(\frac{3\pi R^*}{4E^*}\right)^{2/3} \left(N + 3\pi\Delta\gamma R + \sqrt{6\pi\Delta\gamma RN + (3\pi\Delta\gamma R)^2}\right)^{2/3} \quad \text{(Eq.6)}$$

with

$$\frac{1}{E^*} = \frac{1 - v_1^2}{E_1} + \frac{1 - v_2^2}{E_2} \quad \text{(Eq.7)}$$

and

$$R^* = \frac{R_1 R_2}{R_1 + R_2} \quad \text{(Eq.8)}$$

where *N* is the normal load (N), $v_1 = v_2$ is the Poisson ratio of aramid fibre, $E_1 = E_2$ is the elastic modulus (GPa), $R_1 = R_2$ is the fibre radius (m) and $\Delta\gamma$ is the work of adhesion or the surface energy of the fibre. The calculated values of the area of

contact between fibres obtained from the JKR theory for the A1 and A2 fibre at 1 mN to 15 mN applied normal load are shown in Table 6.

Table 6 The calculated contact area between fibres obtained from the JKR circular contact model.

Fibre type	Area of contact, A_{JKR} (m^2)			
Normal load applied, N [mN]	1	5	10	15
A1	4.073×10^{-12}	1.172×10^{-11}	1.854×10^{-11}	2.425×10^{-11}
A2	4.139×10^{-12}	1.188×10^{-11}	1.877×10^{-11}	2.455×10^{-11}

Using this information, the role of the fibre's total surface energy within the contact interfaces, which is the product of the surface energy per unit area γ and the area of contact, *A,* was assessed. The results of the coefficient of friction μ obtained in Table 5 are used to correlate friction with the value of the total surface energy in the area of contact γA. Figure 9 shows the coefficient of friction of the A1 and A2 fibre as a function of total surface energy in the area of contact at 10 mN pre-tension load with various normal applied loads.

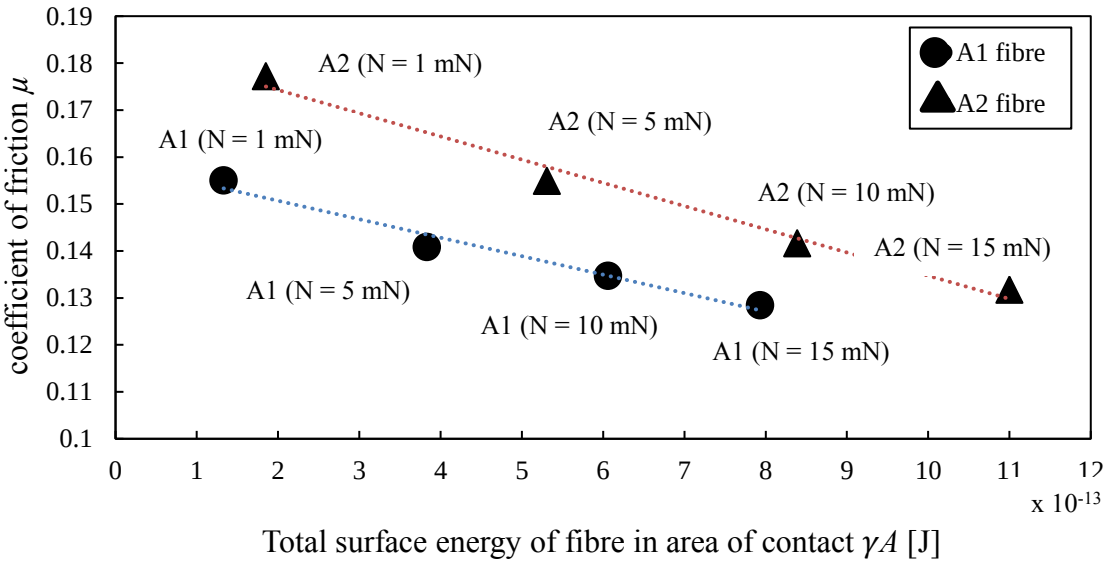

Figure 9 Coefficient of friction as a function of total surface energy of a fibre in the area of contact of the A1 and A2 fibre at 10 mN pre-tension load with various normal applied loads.

At specific applied normal load conditions, it can be seen that the coefficient of friction increased as the total surface energy in area of contact interface increased. For example, at 10 mN applied normal load (see Figure 9), the results show that the coefficient of friction μ of high surface energy fibre (A2) is 0.142, while for the low surface energy fibre (A1), the coefficient of friction μ is found to be 0.135. It should be noted that the effect of surface energy of the fibre plays a role in increasing the friction behaviour at the same applied load (10 mN), and the surface energy per unit area of the A2 fibre is 8.39 x 10^{-13} J, which is slightly higher than the surface energy per unit area of the A1 fibre, 6.06 x 10^{-13} J. Certainly, if γ is high, the interfacial bond strength per unit area is strong and so is the adhesion and therefore the friction. Thus, the coefficient of friction μ is shown to be approximately proportional to γA, as was found by Miyoshi [32] in a study between ceramic-metal couples in vacuum.

Table 7 shows the estimated total surface energy of fibre in the area of contact between two treated fibres, the A2 and OC with different thickness, 12 µm and 140 µm, respectively. The result shows that at 10 mN normal applied load, the coefficient of friction μ of the OC fibre is 0.170 while the A2 fibre is 0.142. Note that, fibre with larger thickness generates a larger contact area. The estimated contact area of the OC fibre obtained using the JKR circular contact model in Eq. 6 is 9.851 x 10^{-11} m^2, which is five times larger than the estimated contact area of the A2 fibre. As a consequence, this result in a high total surface energy of the fibre in the area of contact.

Table 7 Estimated total surface energy of fibre in area of contact γA.

Fibre type	A2	OC
Normal load [mN]	γA (μ)	γA (μ)
10	8.39 x 10^{-13} J (0.142)	25.5 x 10^{-13} J (0.170)
15	11 x 10^{-13} J (0.132)	155 x 10^{-13} J (0.150)

6 Conclusions

This study aims to assess the surface free energy of single aramid fibres and correlate it with the friction behaviour between fibre-fibre contacts. The surface energy was determined by utilizing the dynamic contact angle measurements using the Wilhelmy method. Three different Twaron® aramid fibres, different (treated) material and thickness, are tested with a series of test liquids. The advancing contact

angle is shown to be larger than the receding contact angle which causes the phenomenon of contact angle hysteresis. It is assumed that the hysteresis is due to the surface chemical properties such as the chemical heterogeneity which effects the variation in contact angle during advancing and receding. The surface energy of the Twaron® aramid fibres is polar, exhibiting a hydrophilic behaviour. The treated fibre surface is found to have a greater surface energy than the untreated fibre (virgin) of the same material. Also, the fibre with a larger thickness is found have a larger contact area size and a higher total surface energy in the area of contact. It should be noted that the surface energy plays a role in the friction behaviour. The coefficient of friction is found to increase with high total surface energy between fibre-fibre areas of the contact interface.

Acknowledgments

The authors would like to thank Universiti Teknikal Malaysia Melaka and Ministry of Education Malaysia for providing financial support to one of the authors, and also Teijin Aramid B.V for material supply.

References

[1] Qiang S, Shing-Chung W, Wei Y, Jianwen H, Jie Z, Jinghua Y. Mechanism of Adhesion between Polymer Fibers at Nanoscale Contacts. Langmuir 2012;28; 4663−4671.

[2] Lange de PJ, Akker PG, Mader E, Gao SL, Prasithphol W, Young RJ. Controlled interfacial adhesion of Twaron aramid fibres in composites by the finish formulation. J. Comp Sci and Tech 2007;67: 2027-2035.

[3] Liu L, Huang YD, Zhang ZQ, Jiang ZX, Wu LN. Ultrasonic treatment of aramid fibre surface and its effect on the interface of aramid/epoxy composites. J. App Surf Sci 2008; 254:2594-2599.

[4] Caixia J, Ping C, Wei L, Bin L, Qian W. Surface treatment of aramid fiber by air dielectric barrier discharge plasma at atmospheric pressure. J App Surf Sci 2011; 257:4165-4170.

[5] Miller B, Penn LS, Hedvat S. Wetting force measurements on single fibres. Coll. Surfaces 1983, 6(1);49-61.

[6] Hseih Y-L, Wu M, Andres D. Wetting characteristics of Poly(p-phenyleneterephthalamide) single fibres and their adhesion to epoxy. J Coll Interface Sci. 1991;144(1);127-144.

[7] van de Velde K, Kiekens P. Wettability and surface analysis of glass fibers, Indian J. Fiber Text Res 2000;25(1);8-13.

[8] Barraza HJ, Hwa MJ, Blakley K, O'Rear EA, Grady BP. Wetting behaviour of Elastomer modified glass fiber, Langmuir 2001;17(17);5288-5296.

[9] Young T. III An essay on cohesion of fluids. Phil. Trans. Roy. Soc. (London) 1805; 5: 65.

[10] Yuan Y, Lee TR. Contact angle and wetting properties. Surface Sci 2013; 51:3-34.

[11] Hao W, Yao X, Ke Y, Ma Y, Li F. Experimental characterization of contact angle and surface energy on aramid fibers. J. Adhesion Sci and Tech 2013; 27(9): 1012-1022.

[12] Wu S. In: Polymer interface and adhesion. New York: Marcel Dekker; 1982. p.264.

[13] Si Q, Carlos AF, Dongxing Z, Aart Willem VV, David S. Wettability of a single carbon fiber. Langmuir 2016; 32:9697-9705.

[14] Jian W, Carlos AF, Dongxing Z, Xungai W, Aart Willem VV, David S. Wettability of carbon fibres at micro- and mesoscales. Carbon 2017; 120:438-446.

[15] Monica FP, Maria CS, Pierre-Jacques L, Fabrizio S, Jacopo T, Sylvain D. Surface characterisation and wetting properties of single basalt fibres. J Compos Part B 2017; 109:72-81.

[16] Fowkes FM. Contact angle, wettability and adhesion. Washington DC: American Chemical Society;1964, p. 99.

[17] Owens DK, Wendt RC. Estimation of the free surface energy of polymers. J App Pol Sci 1969; 13: 1741-1747.

[18] Chapman II GB. Non-destructive Evaluation of adhesive bonds using 20 MHz and 25 kHz ultrasonic frequencies on metal and polymer assemblies. Author House; 2014, ISBN 978-1-4969-2553-4.

[19] Pasquini D, Belgacem MN, Gandini A, da Silva Curvelo AA. Surface esterification of cellulose fibres: characterization by drift and contact angles measurement. J Colloid Interface Sci 2006;295(1): 79-83.

[20] Xiadong W, Xiaofenand P, Buxuan W. Contact angle hysteresis and hysteresis tension on rough solid surface, Chinese J. Chem. Eng. 2004; 12 (5):615.

[21] Eral HB, 'tMannetje DJCM. Oh JM. Contact angle hysteresis: A review of fundamentals and applications. J Colloid PolymSci 2013;291(2): 243-260.

[22] Neumann AW, Good RJ. Thermodynamics of Contact Angles I. Heterogeneous Solid Surface. J. Colloid Interface Sci 1972;38(2):341-358.

[23] Sedev RV, Petrov JG, Neumann AW. Effect of swelling of a polymer surface on advancing and receding contact angles. J. Colloid and Interface Sci 1996; 180:36-42.

[24] Schwartz AM. Contact Angle Hysteresis: A Molecular Interpretation. J. Colloid Interface Sci 1980;75(2):404-408.

[25] Lynn SP, Bernard M. A study of the primary cause of Contact Angle Hysteresis on Some Polymeric Solid. J Colloid and Interface Sci. 1980; 78(1): 238-241.

[26] Johnson KL, Kendall K, Roberts A D. Surface energy and the contact of elastic solids. Proc R Soc Lond A, 1971, 324: 301–313 4

[27] Derjaguin B V, Muller V M, Toporov Y P. Effect of contact deformations on the adhesion of particles. J Colloid Interface Sci, 1975, 53: 314–325 5

[28] Maugis D. Adhesion of spheres: The JKR-DMT transition using a Dugdale model. J Colloid Interface Sci, 1992, 150: 243–269.

[29] Bowden FP, Tabor D. Friction and lubrication of solids. Oxford, Clarendon Press. 1954.

[30] Bowden FP, Tabor D. Friction: An introduction to tribology. Anchor Press. New York.1973.

[31] Miyoshi K. Considerations in vacuum tribology (adhesion, friction, wear, and solid lubrication in vacuum). Trib Int 1999;32;605-616.

Paper D

Effect of crossing angle on friction force between two single aramid fibres in contact

Nurhidayah ISMAIL [1,2*], Matthijn B. de ROOIJ [1], Erik G. de VRIES [1] and Dik J. SCHIPPER[1]

[1]Laboratory for Surface Technology and Tribology, Department Mechanics of Solids, Surfaces and Systems (MS3), Faculty of Engineering Technology, University of Twente, Drienerlolaan 5, 7522 NB, Enschede, The Netherlands.

[2]Centre for Advanced Research on Energy, Faculty of Mechanical Engineering, Universiti Teknikal Malaysia Melaka, Hang Tuah Jaya, 76100 Durian Tunggal, Melaka, Malaysia

Abstract

In a non-crimp fabric (NCF), the orientation of fibres is crucial to improving the mechanical properties of the fabric. However, this orientation may cause a variation of fibre contact configurations, influencing the frictional behaviour between fibres. In this paper, the significance of fibre orientation (crossing angle) on the frictional behaviour between single aramid fibres is explored experimentally using a dedicated setup. Two fibres were placed crossing each other at various crossing angles (30° to 90°). The friction force was found to decrease with increasing crossing angle. The Hertzian elliptical calculation of the contact area resulted in an area - crossing angle (A- θ) curve which differs only by a constant factor from the measured force crossing angle (F- θ) curves. Consequently, the results can be explained by a constant interfacial shear strength of the friction model as well as a Hertzian type of contact, despite the fibrous nature of the contacting fibres. Additionally, the effect of pre-tension on the friction force has been investigated.

1 Introduction

In non-crimp fabrics (NCF), fibre tows are arranged in a different orientation to provide more isotropic properties of the fabric and to have a better drapability during the Liquid Composite Moulding (LCM) process. However, the combination of multiple layers of fibres with different orientations stacked in one fabric exposes the fibres to several contact modes such as line, point and elliptical contact. These contact

modes are important as they are expected to influence the real contact area between contacting surfaces, adhesion and also friction behaviour.

In the friction model which is described by Bowden and Tabor [1,2], the friction force *F* is simply given by:

$$F = \tau A + P \tag{1}$$

where *τ* is the interfacial shear strength, *A* is the real contact area and *P* is the ploughing component. If the ploughing component *P* is ignored and the shear strength *τ* is constant, the friction force *F* is proportional to the real contact area *A*. Thus, if this theory also holds for fibres, it is necessary to study the relationship between the contact area of fibre on fibre contact and the friction force behaviour.

To date, several studies have been done on the friction behaviour between fibres, however the studies are limited to the line [3-8] and point [3-5, 9-11] contact modes, being respectively parallel and perpendicular contacting fibres. Studies of elliptical contacts have been made, but these studies focus on the friction behaviour of the fibres at tow (mesoscale level) [5] and different materials such as elastomeric poly (dimenthysiloxane) (PDMS) [12]. To the best of the author's knowledge, there is no detailed study on the frictional behaviour between aramid fibres in an elliptical contact at microscale. This paper therefore aims to study the frictional behaviour between two single aramid fibres in contact at various crossing angles in the range of 30° to 90°. A series of experiments was conducted under normal and pre-tension loads. Here, the fundamental theory of the Hertzian elliptical contact is used to investigate the relationship between the crossing angle, contact area of the fibres and the friction force. Additionally, the role of normal and pre-tension load on the contact area between fibres is investigated.

2 Theoretical background

In the Hertzian contact theory [13], there are three types of the contact configurations or contact modes: (i) line, (ii) point and (iii) elliptical contact. A line contact is formed when two cylinders are placed in parallel ($\theta = 0°/180°$) to each other and a point

contact ($\theta = 90°$) is formed when two cylinders cross each other perpendicularly. The elliptical contact (see Figure 1) is formed when the two cylinders cross each other at an angle between 0° and 90°.

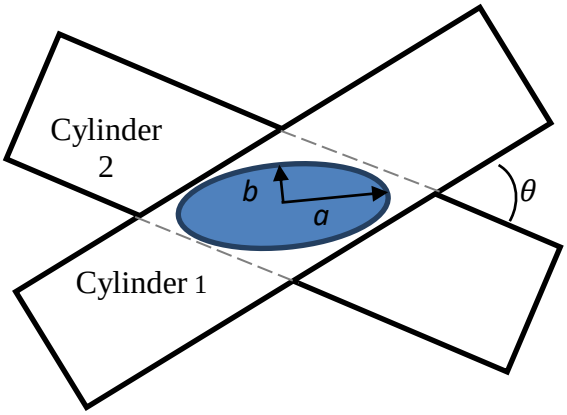

Figure 1 The geometrical contact area shape at elliptical contact.

When two smooth cylinders of equal radius are brought into contact, they will initially touch either at a point or along a line. With the application of the normal load, elastic deformation enlarges these into contact areas. Here, the shape and the size of the geometrical area of contact is influenced by the contact modes. Assuming Hertzian contacts and therefore semi-infinite bodies, two fibres at line, point and elliptical contact modes generate respectively a rectangular, circular and ellipse shaped area of the contact. Whether or not Hertzian theory can be used to predict the contact between fibres has to be validated, as obviously fibres have small dimensions and might therefore not behave as semi-infinite bodies. The line and point contact mode effectively act as the maximum and minimum limits of the size of the contact area for the crossing angle between 0° to 90°. In experiments, the friction force is found to be 2.5 times greater for the line contact arrangement than for the point contact situation between carbon tows [3,5] and 1.7 to 3.2 higher between fibres [4].

Thus, it is interesting to relate the measured friction force with the calculated size of the area of contact between the fibre-fibre interfaces as a function of the crossing angle. For a line contact, the rectangular shape of the contact area can be calculated as:

$$A = bL \tag{2}$$

where *L* is the contact length and *b* is the contact width. According to Hertz, *b* can be calculated as [13]:

$$b = \sqrt{\frac{4NR_e}{\pi L E^*}} \tag{3}$$

where *N* is the normal load, R_e is the effective radius and *E** is the contact modulus. The contact modulus is calculated from the elastic modulus of the fibre, E_1 and E_2, and Poisson ratios v_1 and v_2[13]:

$$\frac{1}{E^*} = \frac{1 - v_1^2}{E_1} + \frac{1 - v_2^2}{E_2} \tag{4}$$

and the effective radius is calculated from the radius of the fibre, R_1 and R_2 [13]:

$$R_e = \frac{R_1 R_2}{R_1 + R_2} \tag{5}$$

According to Hertz, if two fibres cross each other perpendicularly, ($\theta = 90°$), the circular shaped contact area can be directly calculated as:

$$A = \pi a^2 \tag{6}$$

where *a* is the radius of the contact according to [13]:

$$a = \sqrt[3]{\frac{3NR_e}{4E^*}} \tag{7}$$

In the case of two cylinders at elliptical contact, the ellipse contact area can be calculated by determining the semi-axes length of the ellipse shape, *a* and *b* (see Figure 1). The principal relative radii of curvature between bodies can be related to the crossing angle θ and defined as follows [13]:

$$R_a = \frac{R}{1 - \cos\theta} \tag{8}$$

$$R_b = \frac{R}{1 + \cos\theta} \tag{9}$$

where the effective radius is given by:

$$R_e = \sqrt{R_a R_b} \tag{10}$$

Within the elliptical contact area, the pressure distribution can be expressed as:

$$P = p_o\sqrt{1 - (x/a)^2 - (y/b)^2} \tag{11}$$

$$(x/a)^2 + (y/b)^2 \leq 1$$

$$p_o = \frac{3N}{2\pi ab} \tag{12}$$

where *P* is the pressure, p_o is the maximum pressure, *N* is the normal load, and *a* and *b* are the semi-axis lengths of the ellipse area. The relations between the geometric constant and semi-axes are given by [13]:

$$\frac{R_a}{R_b} = \frac{(a/b^2)E(e) - K(e)}{K(e) - E(e)} \tag{13}$$

and

$$\frac{1}{2}\left(\frac{1}{R_a R_b}\right)^{1/2} = \frac{p_o}{E^*}\frac{b}{a^2 e^2}[\{(a^2/b^2)E(e) - K(e)\}\{K(e) - E(e)\}]^{1/2} \quad (14)$$

where *E*(e) and *K*(e) are the complete elliptic integrals of the first and second kind respectively [13]. The parameter *e* is the eccentricity of the contact ellipse given by:

$$e^2 = 1 - b^2/a^2 \quad (15)$$

With the equivalent contact radius $c = (ab)^{\frac{1}{2}}$ and substitution of p_o from equation (12) into (14), we can obtain:

$$c^3 = \frac{3NR}{4E^*}\frac{4}{\pi e^2}(b/a)^{3/2}[\{(a^2/b^2)E(e) - K(e)\}\{K(e) - E(e)\}]^{1/2} \quad (16)$$

By numerical integration of the elliptical integral *E*(e) and *K*(e), the size of the elliptical contact can be calculated. However, due to the inconvenience of solving the numerical integration of the elliptical integral, an approximate relation has been developed. Greenwood has proposed an approximate equation to calculate the Hertzian elliptical contact area [14,15]. This method worked well for mildly elliptical contacts – the length of the semi-axes *a* and *b* of the ellipse can be calculated as [14]:

$$a = \left(\frac{3k^2\varepsilon N R_e}{\pi E^*}\right)^{(\frac{1}{3})} \qquad b = \left(\frac{3\varepsilon N R_e}{\pi k^2 E^*}\right)^{(\frac{1}{3})} \quad (17)$$

where *k* is the axis ratio (*a*/*b*), ε is the ellipticity ratio, *N* is the normal load, R_e is the effective radius, E^* is the contact modulus and *R* is the fibre radius. Using the axis ratio, $k = 1.0339(^{R_b}/_{R_a})^{0.636}$ and ellipticity ratio $\varepsilon = 1.0003 + 0.5968(^{R_a}/_{R_b})$, the

area of the elliptically shaped contact at various crossing angles can be directly calculated.

3 Experimental details

3.1 Aramid fibres

This study used three different samples of Twaron® aramid fibres, (referred as A1, A2 and OC, in this study) from Teijin Aramid B.V (Arnhem, The Netherlands). Note that the A1 and A2 fibre samples are from the same fibre type, but the A2 fibre is treated (coated) with alkyl-phosphate salt. The material properties and SEM images of each fibre type are shown in Table 1 and Figure 2 respectively.

Table 1 The material properties of the aramid fibres.

Properties	Unit	A1	A2	OC
Elastic modulus	GPa	109	109	29.3
Linear density	dtex	1.7	1.7	210
Breaking strength	mN	390	390	15400
Elongation at break	%	3.2	4.4	2.9
Fibre diameter	µm	12	12.2	140
Finish material		No	Alkyl-phosphate salt	ethoxylated/ propoxylated butanol

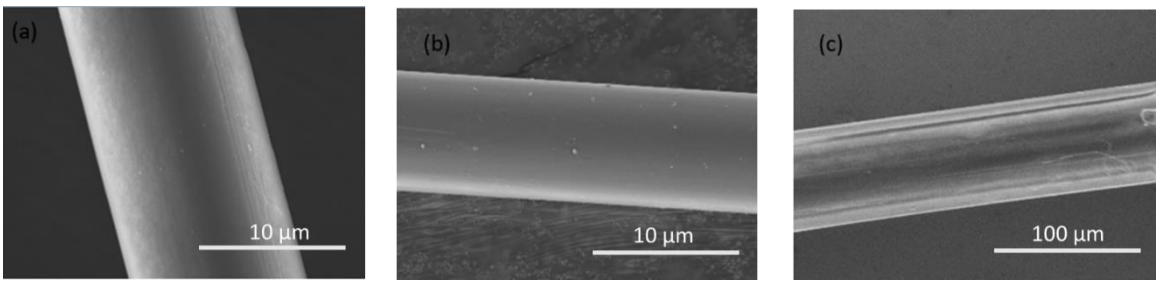

Figure 2 SEM images of Twaron® aramid fibre types that are used in this study: (a) A1; (b) A2 and (c) OC fibre.

3.2 Sample preparation

In each experiment, two fibre samples are prepared. The samples are described here as top and bottom fibre (see Figure 3(a)). The length of the top and bottom fibres are 2 and 6 mm respectively. Using a low viscosity glue (Loctite 401), both

fibres are glued on their specific fibre holders. The top fibre is glued with just enough pre-tension to avoid the fibre from slacking, meanwhile the bottom fibre is glued with varying pre-tension loads ranging from 1 to 300 mN. The pretension is realized by first gluing one end of the fibre, after which the pretension is applied by a dead weight. Then the second end is glued, and the dead weight is removed after the glue is cured.

3.3 Friction Setup

Figure 3(a) and (b) show the schematic and real experimental setups that were used to measure the friction force. Figure 3(c) shows the crossed fibre arrangement at a specific angle of $30°$. In this study, the friction force between those two fibres is measured at a crossing angle of 30°, 40°, 50°, 75° and 90° under various normal and pre-tension loads. To provide different angles, the bottom fibre is fixed in a horizontal position, while the top fibre is rotated clockwise. The friction force measurements are taken when the bottom fibre is sliding against the top fibre at constant speed and sliding distance. Three samples are tested for each crossing angle. Multi-pass friction loops are executed where the friction measurements are repeated five times for each sample. The experimental parameters that were used for the friction force measurement are listed in Table 2.

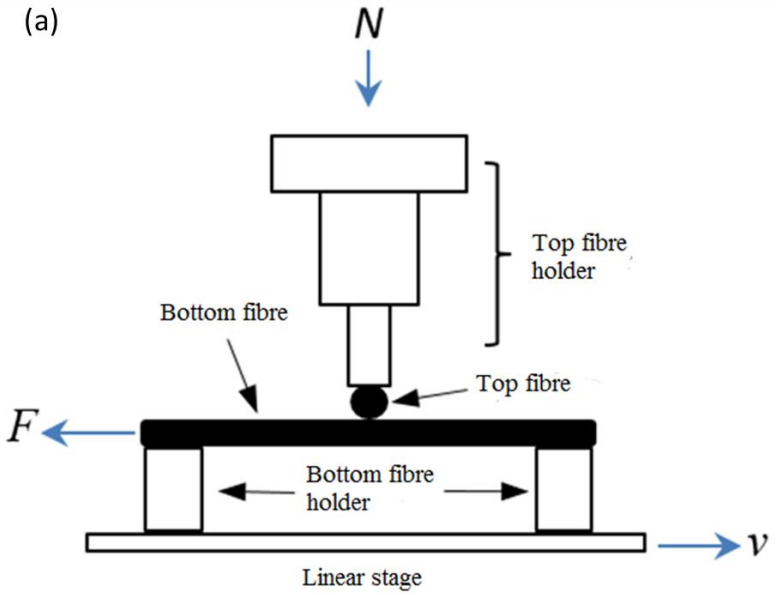

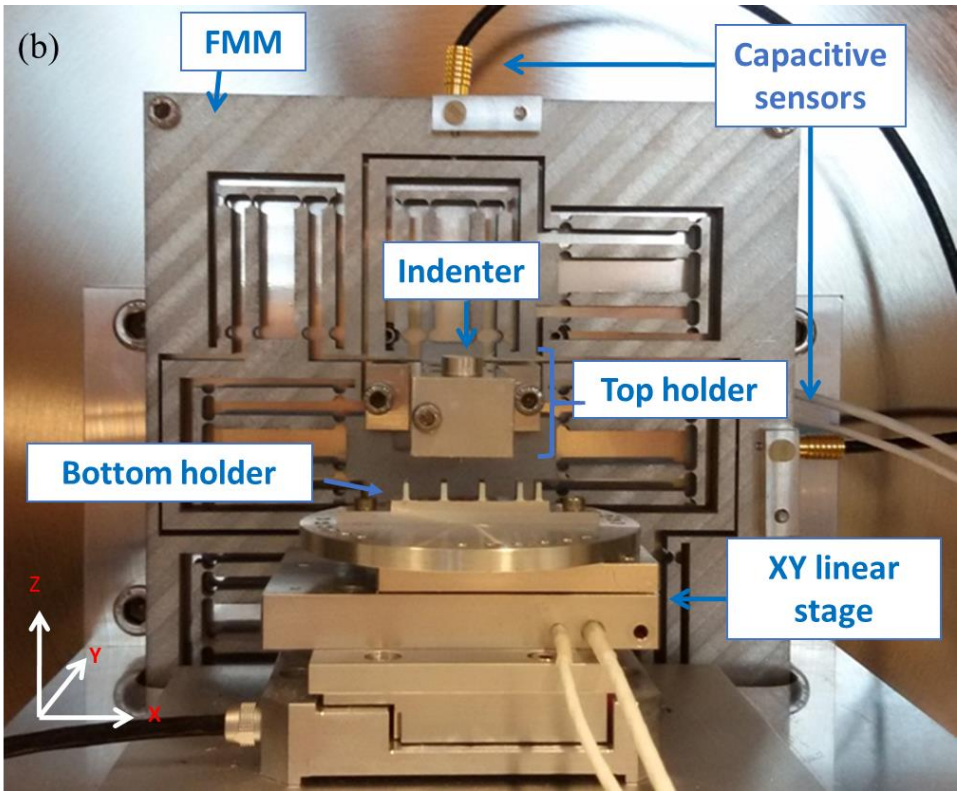

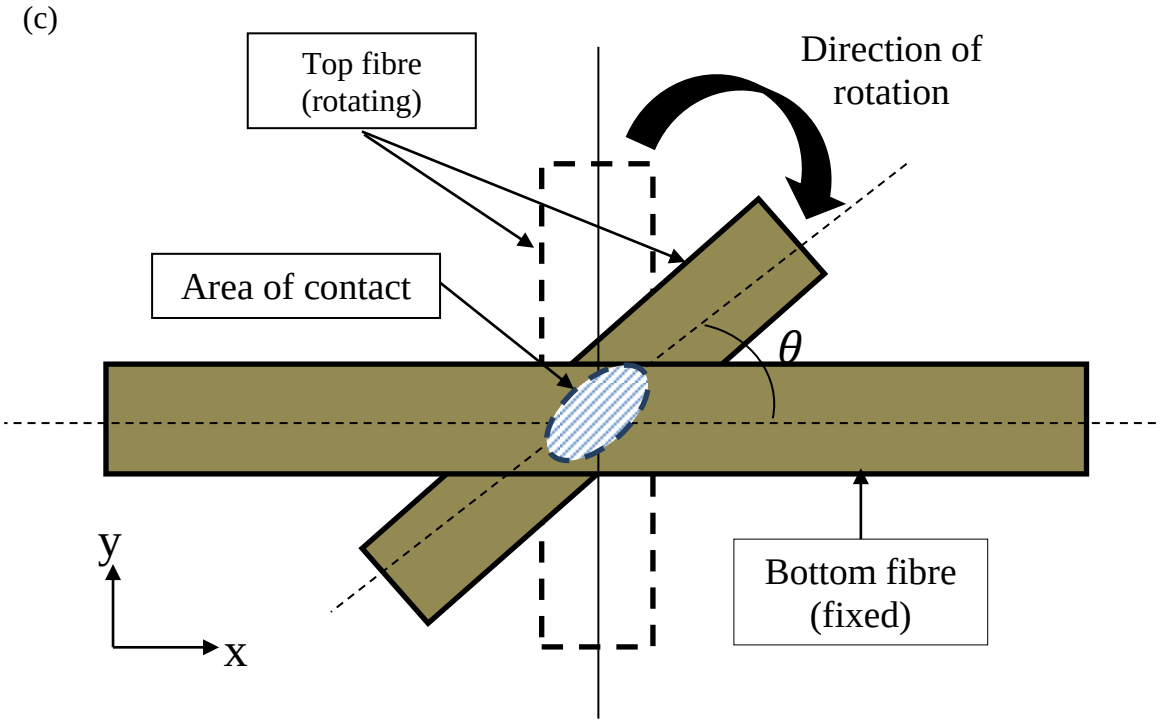

Figure 3 Friction between fibres (a) Schematic diagram of the setup (b) Real setup (c) Top view of crossed fibre arrangement.

Table 2 Parameters for friction measurements.

Description	symbol	value	units
Normal load	*N*	1- 50	mN
Pre-tension load	*T*	50 - 200	mN
Sliding speed	*v*	2	µm/s
Crossing angle	*θ*	30 - 90	degree
Sliding distance	*d*	100	µm
Fibre length	*La*	Upper fibre: 2	mm
	Lb	Lower fibre: 6	mm
Number of friction cycles		5	
Temperature		20 ± 2	°C
Relative humidity	RH	30 - 40	%

4 Results and discussion

4.1 Friction force measurements

Figure 4 is an example of the raw data of the force - distance curve signal measured between two similar A1 fibres with 5 mN normal load at a 40° crossing angle. Results show that the friction force curve for each cycle during forward and backward sliding are equal. The negative signs for the friction force during sliding represent the backward direction. It is noticeable that the friction force of the first cycle shows a slightly lower value than to the rest of the four cycles. This could be due to removal of contamination that is present on the fibre surface. Thus, the average of the friction force in this study is calculated based on the next four cycles (cycle numbers 2-5). Within these four cycles, the variation is very small with the standard deviation less than 0.05 mN. This shows that the friction measurements are highly reproduceable. Also, after an initial static friction force, the dynamic friction force is constant over the sliding length.

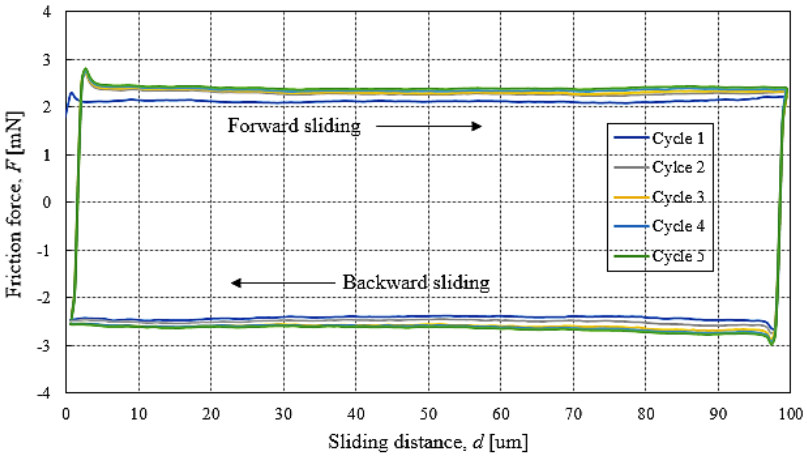

Figure 4 Raw data of force-distance curve signal measured between two similar A1 fibres at 5 mN normal load, pre-tension load is 10 mN, $\theta = 40°$ and RH = 33 %.

4.2 The effect of crossing angle

Figure 5 shows the average friction force as a function of the crossing angle for the OC, A1 and A2 fibre at various normal load. The results show that the friction force is reduced as the crossing angle increases from 30° to 90° for all fibre types, regardless of the fibre diameter and treatment of the fibre surface. It is assumed that this friction force is influenced by the role of the crossing angle that changes the contact area. Consequently, the Hertzian elliptical contact model is used to relate the friction force behaviour to the size of the contact area between the fibres as the crossing angle changes. The approximate contact area method that is proposed by Greenwood [14] is used and the contact area between fibres at crossing angles between $0° < \theta < 90°$ is calculated using equation (17) [14]. Figure 6 shows the theoretical calculations of the contact area *A* as a function of the crossing angle for the A1 fibre. Note that the measured diameter of the A2 fibre is about 0.2 µm (see Table 1) larger than the A1 fibre, which has little effect on the theoretical calculations of the contact area. From Figure 6, the contact area is reduced gradually as the crossing angle increases. It can also be seen that at the same parameter condition (normal load and pre-tension load) the friction force measured for the A2 fibre is slightly greater than for the A1 fibre. It is assumed that this might be associated with the physical properties of the fibre such as roughness and the surface energy as the A1 fibre is a virgin fibre while the A2 fibre is a treated fibre.

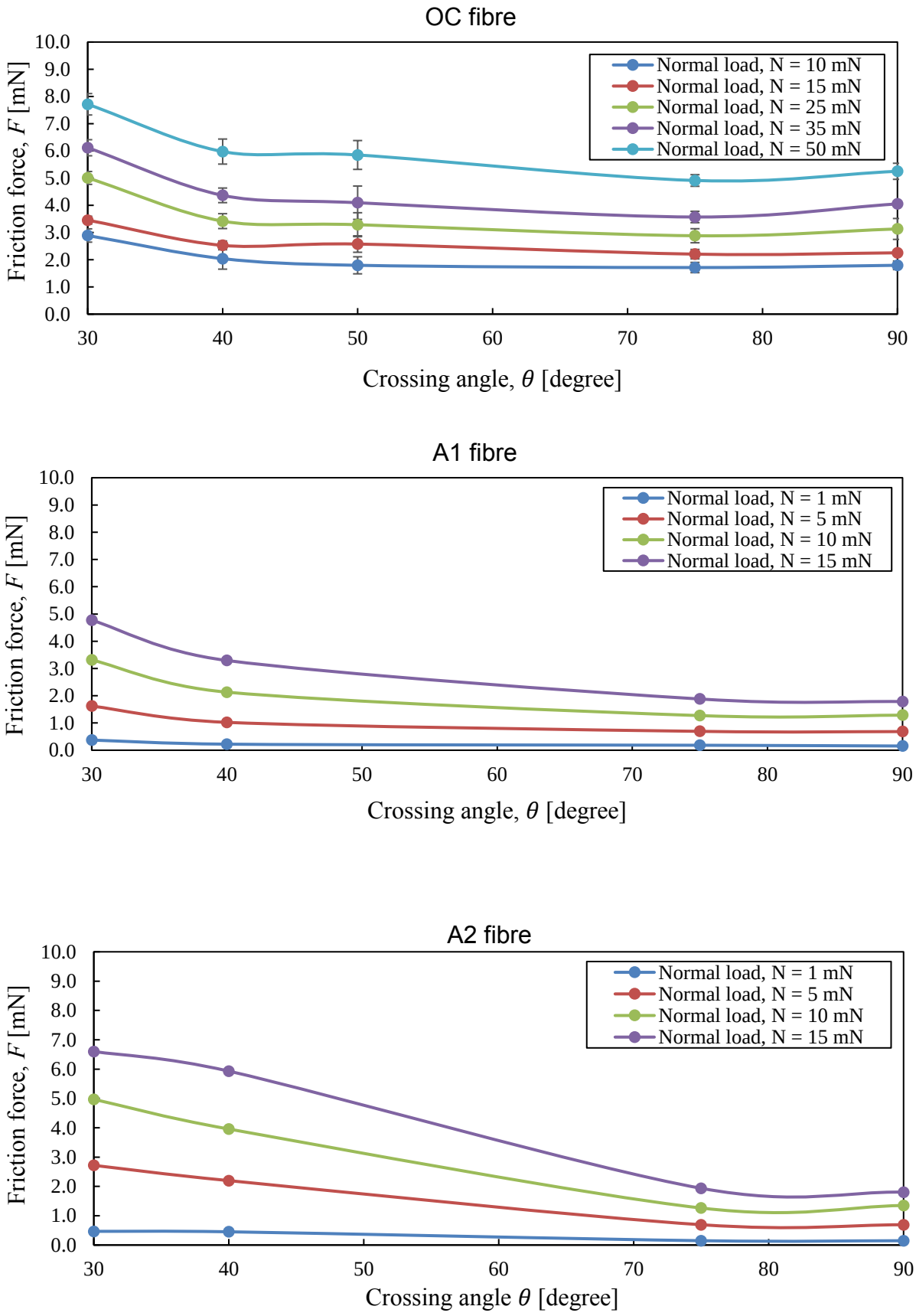

Figure 5 Friction force as a function of crossing angle. ***OC fibre****:* at 200 mN pre-tension load. ***A1 fibre****:* at 80 mN pre-tension load. ***A2 fibre****:* at 80 mN pre-tension load.

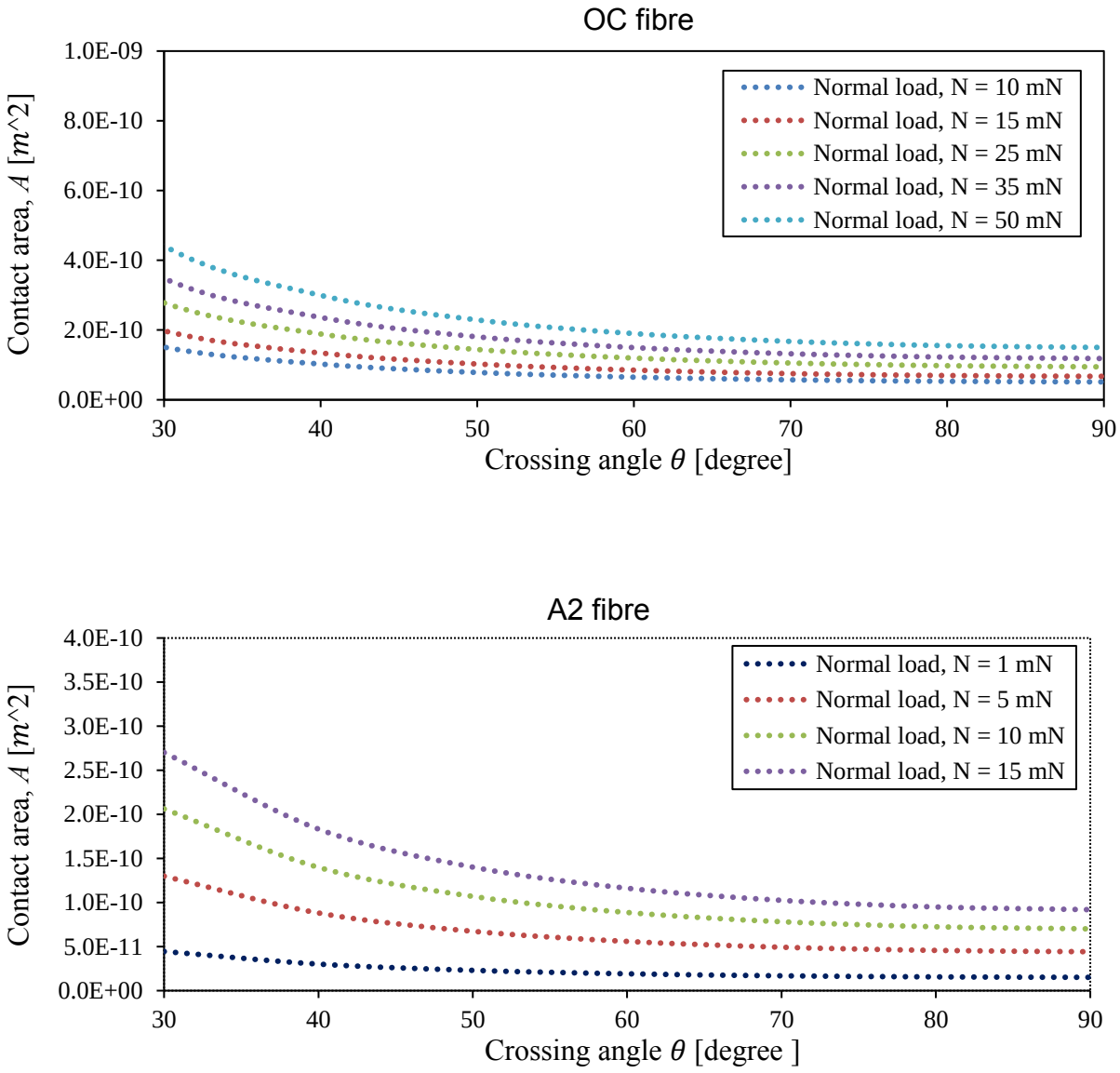

Figure 6 Contact area *A* between two fibres in contact as a function of the crossing angle at various normal loads.

4.3 Comparison with the friction force model

Using the friction model $F = \tau A$, the predicted friction force is calculated and compared with the measured friction force. The friction force between fibres can be calculated using the predicted values of the contact area *A* in Figure 6 combined with the interfacial shear strength τ. In this calculation, the value of constant interfacial shear strength τ used is 10 MPa and 20 MPa [16]. In Figure 7, a comparison is made of the predicted friction force with interfacial strength τ equal to respectively 10 MPa and 20 MPa, without the contribution of adhesion between fibres. The straight line indicates the measured friction force in the experiment and the dotted line shows

the predicted friction force. The normal load that is applied to all fibres is 10 mN with a pre-tension load of 200 mN (OC fibre) and 135 mN (A1 and A2 fibre). It can be observed that the friction in a fibre-fibre contact, assuming Hertzian contact behaviour, can be explained with the same value of the shear strength for both coated fibres (OC and A2). The shear strength for the coated fibre-fibre contacts is found to be higher at a value of around 20 MPa. The validity of the Hertzian assumption will be further evaluated in the next section.

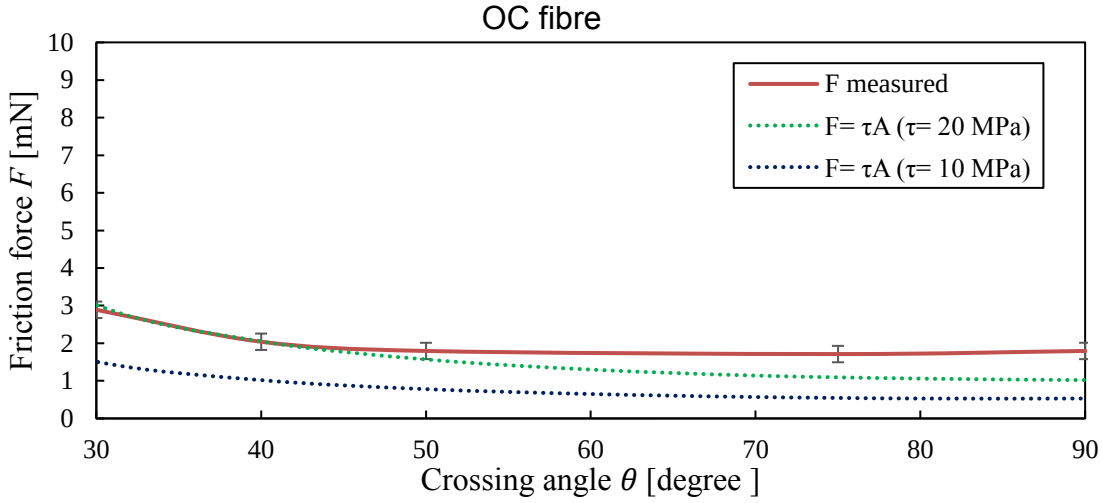

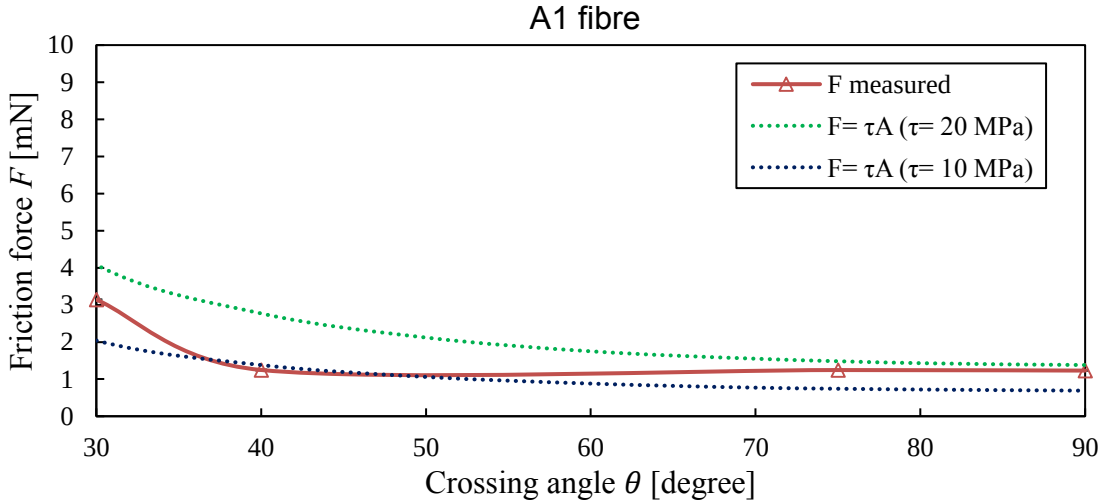

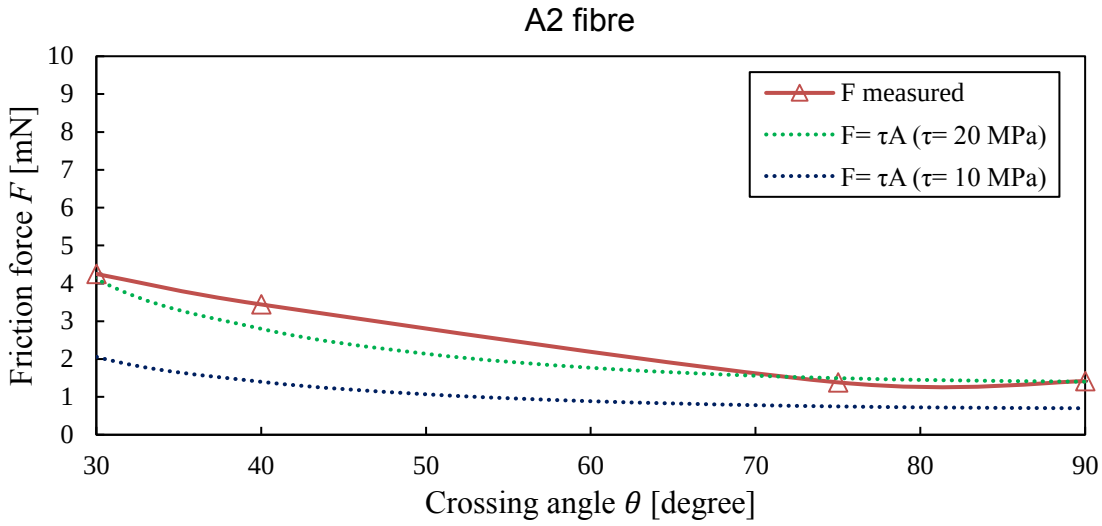

Figure 7 Predicted friction force as a function of crossing angle for various τ values.

4.4 Evaluation of the contribution of the normal load and pre-tension load.

In this section, the interdependency of the pre-tension load and normal load with crossing angle is evaluated. Due to the pre-tension, the bending stiffness of the fibre will change and therefore influence the conformability between the contacting fibres. This can potentially lead to a different frictional behaviour. Potential reasons for this are a different contact area, geometrical and physical changes at the fibre surface, and the roughness changes or compaction due to the fibrillar nature of the fibre. Figure 8 shows the effect of normal load on the measured fibre deflection. At a constant crossing angle, the fibre deflection increases as the normal load increases. The higher the normal load applied on the fibre, the higher the macroscopic bending of the fibre and the more deformation in the contact.

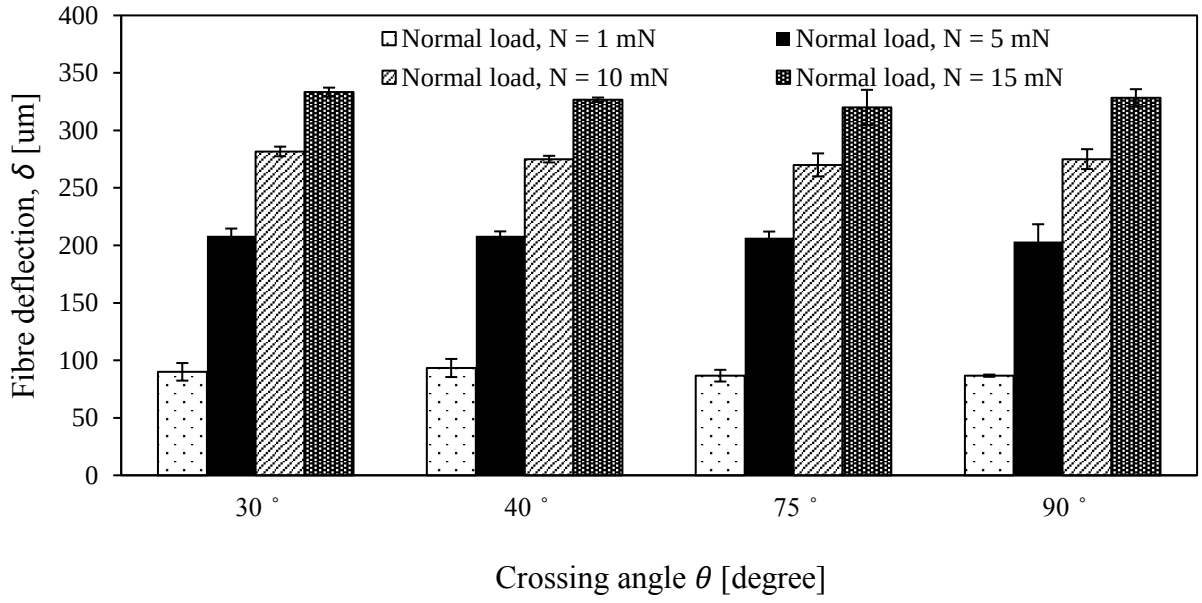

Figure 8 The fibre deflection as a function of crossing angle and various normal loads at 10 mN pre-tension load.

From the taut wire theory, the deflection of the fibre under pre-tension as well as an applied normal load can be calculated as follows [17]:

$$2\left(\frac{\delta_z}{L_t}\right)^3 A_t.E + \left(\frac{\delta_z}{L_t}\right)T - \frac{N}{4} = 0 \tag{18}$$

where δ_z is the fibre deflection, L_t is the fibre length, A_t is the fibre cross-sectional area, *E* is the Young's modulus, *T* is the pre-tension load and *N* is the normal load. To study the relationship between pre-tension and contact length between contacting fibres, the deflection of the fibre must first be determined. Figure 10 shows the diagram of the fibre deflection due to pre-tension and normal load. Due to the application of a normal load, both fibres that are in contact deform at a certain deflection δ_z. Thus, mathematically the behaviour of the lower fibre can be represented, assuming a straight line between the centre of the contact and the end of the top fibre as:

$$y = mx - \delta_z \tag{19}$$

and the circumference of the bottom fibre that touches the top fibre is represented by (see Figure 9):

$$(x - x_c)^2 + (y - y_c)^2 = R^2 \tag{20}$$

where *m* is the line gradient, δ_z is the fibre deflection, x_c and y_c are the coordinates of the centre of the contact and *R* is the fibre radius. If it is assumed that the contact geometry is triangular, the contact length a_δ between two fibres in contact at δ_z can be calculated, by evaluating the crossing points of equations (19) and (20) in the half plane axis, as:

$$a_\delta = \sqrt{x^2 + (-\delta_z - y)^2} \tag{21}$$

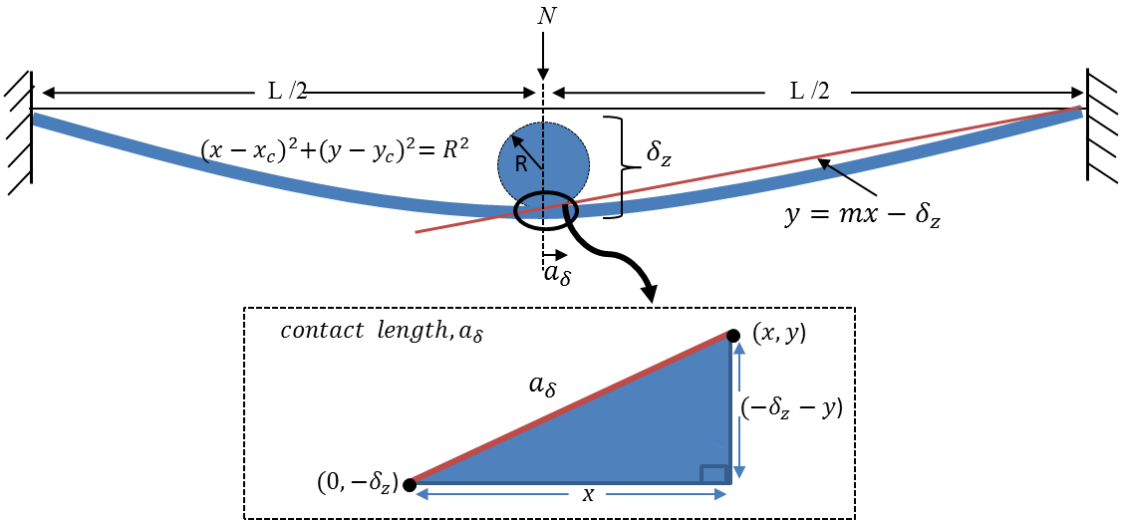

Figure 9 Diagram of the fibre deflection.

Figure 10(a) shows the fibre deflection of the same fibre (A2) at various pre-tension loads. The result shows that the deflection of the fibre is reduced with increasing pre-tension load. Note that, the fibre deflection is the deflection of both fibres (top and bottom) measured during the experiment based on the load-displacement data given by the sensor. Interestingly, it can be seen that at constant pre-tension load, the fibre

deflection is nearly constant with the crossing angle. However, it is shown in Figure 10 (b) that the friction force is reduced with the crossing angle. It can also be seen that, although the fibre deflection is influenced by the pre-tension, the effect on the friction force is small. This means that the 'wrapping effect' does not explain the friction measured. Using the theory of taut wire as described above, the contact length between the fibres under loading conditions (normal and pre-tension load) is calculated. It is found that the maximum contact length is 1.30 μm. Assuming the contact between the fibres at different crossing angles is elastic and following the Hertz theory, the calculated contact radius using equation (7) is found to be around 2 μm which is larger than the contact length predicted with the taut wire theory but still less than the radius of the fibre. This means that elastic deformation in the contact dominates the wrapping effect. Additionally, elastic deformation in the contact as described by Hertz can explain the friction behaviour at different crossing angles, although the deformation is quite large in comparison with the radius of the fibre, which violates the underlying assumption of semi-infinite bodies and small deformations in the Hertzian theory.

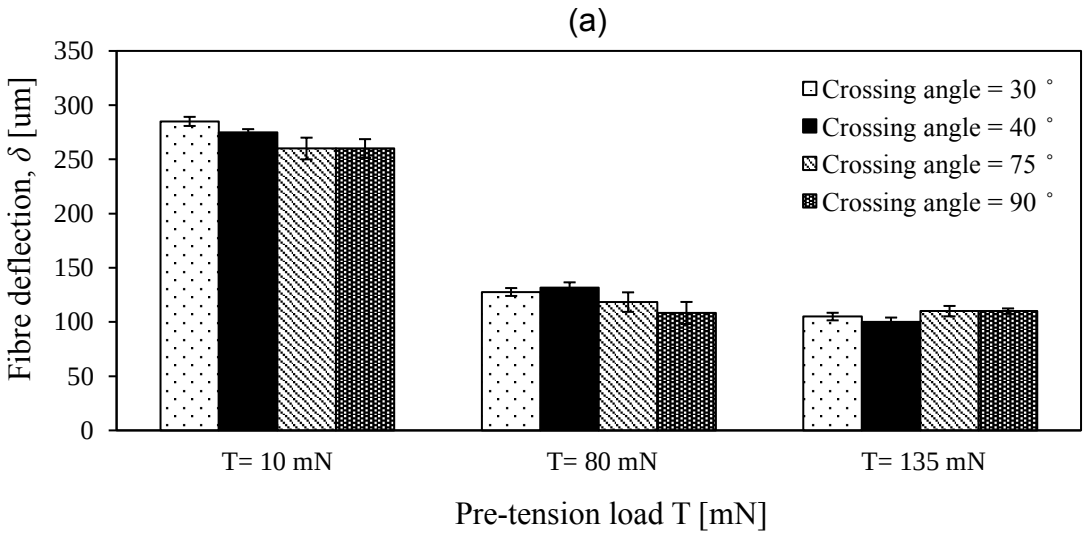

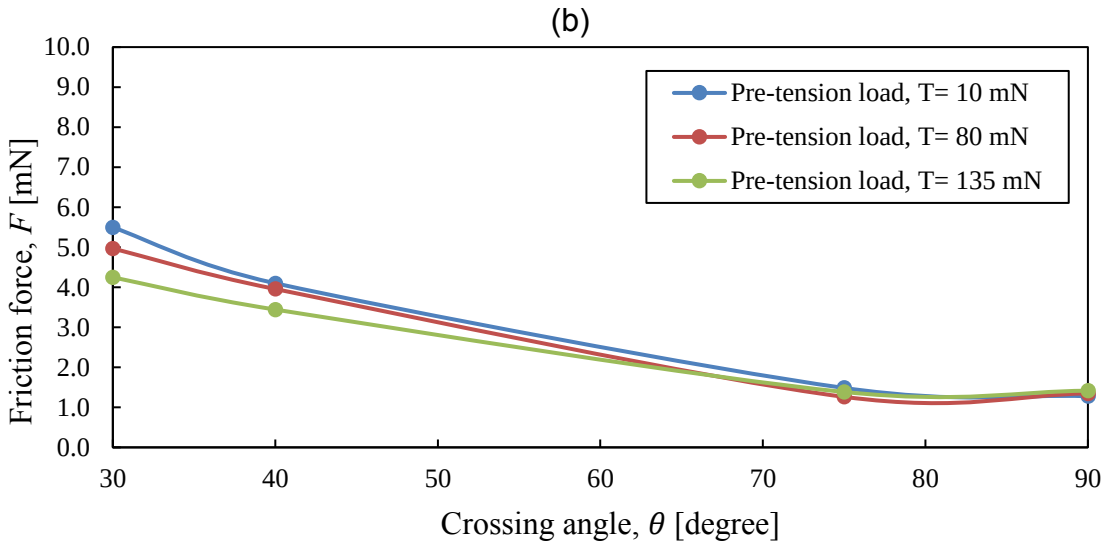

Figure 10 The A2 fibre with 10 mN applied normal load (a) Fibre deflection as a function of pre-tension load (b) Friction force as a function of crossing angle at various pre-tension loads (the standard deviation is less than 0.05 mN).

5 Conclusions

This study aims to investigate the effect of the crossing angle on the frictional force behaviour between two single aramid fibres. The experiments were performed using three different types of Twaron® aramid fibres at various crossing angles, normal loads and pre-tension loads. It is found that the friction force decreases as the crossing angle increases between 30° and 90°. The size of the contact area at various contact angles is calculated using the Hertzian elliptical contact model. Since the measured friction force and the calculated contact area curve give a similar trend differing only by a constant factor, the results are in good agreement with the assumption of a constant interfacial shear strength for the friction model. The value of τ for the OC and A2 fibre contact is found to be 20 MPa, while for the A1 fibre the value of τ is 10 MPa. The friction force is found to decrease as the pre-tension load increases, although bending of the fibre indicated by the measured deflection is influenced by it. With a constant pre-tension load and fibre deflection, the friction force decreases with the crossing angle. Thus, it is suggested that the formation of the contact area at an elliptical contact is not associated mainly with pre-tension. The analysis shows that elastic deformation in the contact dominates over a 'wrapping effect' which can be considered as a secondary effect.

Acknowledgement

The authors would like to thank Universiti Teknikal Malaysia Melaka and Ministry of Education Malaysia for providing financial support to the first author and Teijin Aramid B.V, The Netherlands, for supplying the material.

References

[1] Bowden FP, Tabor D. Friction and lubrication of solids. Oxford, Clarendon Press. 1954.

[2] Bowden FP, Tabor D. Friction: An introduction to tribology. Anchor Press. New York.1973.

[3] Cornelissen B, Rietman B, Akkerman R. Frictional behaviour of high performance fibrous tows: Friction experiments. Compos A Appl Sci Manuf 2013; 44:95–104.

[4] Mulvihil D, Smerdova O, Sutcliffe M. Friction of carbon fibre tows. Compos A Appl Sci Manuf 2016; 93:185–198.

[5] Chakladar ND, Mandal P, Potluri P. Effects of inter-tow angle and tow size on carbon fibre friction Compos A Appl Sci Manuf 2014; 65; 115–124.

[6] Lincoln B. Frictional and elastic properties of high polymeric materials. Brit J Appl Phys 1952; (3):60.

[7] Gralen N, Olofsson B. Measurement of friction between single fibers. Text Res J 1947; 17(9): 488–496.

[8] Lindberg J, Gralen N. Measurement of friction between single fibers: II. Frictional properties of wool fibers measured by the fiber-twist method. Text Res J 1948; 18(5):287–301.

[9] Briscoe BJ, Kremnitzer SL. A study of the friction and adhesion of Polyethylene terephthalate monofilaments. J Phys D: App Phys 1979; 5:505-516.

[10] Briscoe BJ, Wrinkler A, Adams MJ. A statistical analysis of the frictional forces generated between monofilaments during intermittent sliding. J Phys D: App Phys 1985; 18: 2143-2167.

[11] Tourlinas M, Bueno M-A, Poquillon D. Friction of carbon tows and fine single fibers. Compos Part A: Appl Sci Manuf. 2017; 98: 116-123.

[12] Sumer B, Onal CD, Aksak B, Sitti M. An experimental analysis of elliptical adhesive contact. J App Phys. 2010; 107:113512.

[13] Johnson KL. Contact mechanics. Cambridge Uni Press. 1985.

[14] Greenwood JA, Formulas for moderately elliptical Hertzian contacts, Transactions of the ASME, J Trib. 1985; 107 (4); 501-504.

[15] Greenwood JA. Analysis of elliptical Hertzian contacts. Tribology International 1997, 3(30); 235-237.

[16] Cornelissen B, de Rooij MB, Rietman B, Akkerman R. Frictional behaviour of high performance fibrous tows: a contact mechanics model of tow–metal friction. Wear 2013; 305(1–2):78–88.

[17] Charles I. Applied mechanics for engineers. The Syndic of the Cambridge University Press 1951:54-66.

Paper E

Adhesion Force Measurements between Single Aramid Fibres

Nurhidayah ISMAIL [1,3*], Hubert GOJZEWSKI [2], Matthijn B. de ROOIJ [1], Dik J. SCHIPPER[1] and G. Julius VANCSO [2].

[1]Laboratory for Surface Technology and Tribology, Department Mechanics of Solids, Surfaces and Systems (MS3), Faculty of Engineering Technology, University of Twente, Drienerlolaan 5, 7522 NB, Enschede, The Netherlands.

[2]Materials Science and Technology of Polymers, Faculty of Science and Technology, University of Twente, Drienerlolaan 5, 7522 NB, Enschede, The Netherlands.

[3]Centre for Advanced Research on Energy, Faculty of Mechanical Engineering, Universiti Teknikal Malaysia Melaka, Hang Tuah Jaya, 76100 Durian Tunggal, Melaka, Malaysia.

Abstract

Adhesion between fibre surfaces is an important property as it influences the function of adhesive bonding between fibres and structural integrity of end products made out of fibres, like a rope. The adhesion force between fibres will depend on many factors like the surface energy and relative humidity. In this study, the adhesion force between two single aramid fibres was measured by atomic force microscopy (AFM) with a small piece of aramid fibre attached to the tipless cantilever. At 50% - 77% RH, a significant increase in the adhesion force has been found. The Kelvin equation is used to compare the measurement result. Meanwhile, at dry conditions (8% RH) the adhesion force is decreased with increasing crossing angle. This can be explained by a change in the contact area. The adhesion force measured is compared to a theoretical calculation of the Johnson-Kendall-Roberts model for an elliptical contact.

1 Introduction

The adhesion force between fibres determines final macroscopic mechanical properties of the fibrous structured bulk materials [1]. It is also a critical factor for the integrity and stability of a fibre network [2]. Thus, the adhesion interactions are important in designing and controlling the application of the nonwoven fabric. The

adhesion phenomenon, observed at micro- and nanoscale, is driven primarily by two facts: high surface area-to-volume ratio and water capillary condensation.

The adhesion force between aramid fibres is significant in production processes as well as products made out of these fibres. Examples are the wet forming process for manufacturing the aramid paper sheet in electrical insulation for motors, generators and transformers applications [2]. The aramid fibres are hydrophilic [3], thus at ambient conditions, capillary forces are a dominant component of the adhesion force [4]. Capillary condensation in fibre contacts determines the magnitude of the capillary forces and is primarily dependent on the radius and surface energy of the fibres as well as the amount of water, represented by the relative humidity [5]. While the radius and surface energy are fixed in the final material texture of aramid fibres, the relative humidity drives the capillarity among fibres and thus the interactions in the fibre structure. Additionally, in a final textured material the fibres may contact each other under a define crossing angle such as in a non-crimp fabric (NCF) and in fibre ropes and cables. As a matter of fact, the fibre-fibre adhesion force is then a function of its contact area as well [6]. However, to our knowledge, the effect of crossing angle between fibres on adhesion has not been investigated experimentally. However, as these contacts are present in many fibrous structures, it is of importance to study this.

Adhesion between fibres can be determined experimentally or using a well-established contact mechanics model such as Johnson-Kendall-Robert (JKR) [7] or Derjaguin-Muller-Toporov (DMT) [8]. In 1979, Briscoe and his co-workers have developed an experimental setup to measure the adhesion force between Polyethylene-terephthalate monofilaments [9]. In their experiment, the adhesion force is measured based on the bending analysis of the monofilaments. However, inaccurate determination of the effective fibre length could lead to an inaccurate adhesion force value. Today, with modern technology, a direct measurement of the adhesion force is feasible by means of an atomic force microscopy (AFM) using a micro fabricated cantilever, terminated with a sharp tip, that senses the sample-surface interaction forces. The AFM cantilever can be modified by attaching a colloidal particle or a different object. Ducker et al. [10] have been developing a colloidal probe by attaching a 3.5 µm radius of glass sphere to a cantilever. Using the same technique, researchers have modified AFM probes with different materials.

While attracting a spherical particle to a cantilever is satisfactorily developed [11], attracting objects of other geometries remain challenging due to a technical reason of micro-handling and precise positioning [10]. Although, some natural and synthetic crossed fibre systems have been studied using an AFM, including human hair [12,13], polyamides [14], polyester [15] and Electrospun polycaprolactone (PCL) [16], single aramid fibres were not investigated. Zhang et al. [17] have performed an interesting study on adhesion between the aramid fibres and aramid fibrid, however, the authors did not control quantitatively the aramid fibres attracted to the cantilever (the AFM tip was put in contact with many fibres in the aramid film). Thus, the contact area and crossing angles could not be controlled.

In this study, the measurements of the adhesion force between two single aramid fibres in contact with respect to each other is explored. The AFM tip is modified by attaching a non-treated Twaron® aramid fibre on the tipless cantilever. We fully control the number of contacting fibres (2 crossed fibres; well-defined crossed-cylinder geometry), fibre crossing angles (from 30 to 90°), and the experimental conditions (temperature and relative humidity, RH, in the range of 8 – 77 %). Three combinations are considered to measure and analyze the adhesion forces: (1) perpendicularly crossed fibres at varied humidity, (2) fibres at varied crossing angles at dry conditions (RH = 8%), and (3) fibres at varied crossing angles at RH = 40%. The effect of relative humidity and crossing angle on the adhesion force are also compared with the approximate contact model of Johnson-Kendall-Roberts [18].

2 Experimental Details

2.1 Material

Twaron® aramid fibre without surface finishing (untreated fibre) with a linear mass density of 1.6 dtex supplied by Teijin Aramid B.V, The Netherlands is used in this study. The elastic modulus of the fibre is 109 GPa with a thickness of 12 µm. AFM roughness measurement on the fibre surface revealed a rms roughness of 1.6 nm over a scan size of 3 µm x 3 µm.

2.2 Preparation of the modified tip

Picket-shaped tipless cantilevers (TL-FM from Nanosensors, nominal spring constant of 2.8 N/m) were functionalized by a directly attaching of Twaron® aramid fibre on it. The aramid fibre was cut by a laser (~ 120 µm in length), diluted in water and drop-coated on a freshly cleaved mica surface, and left to dry. Manipulations were performed under an optical microscope (Olympus BX60) using a home-made XYZ micromanipulator with chemically-adjusted (via etching) curvature of the end-radius of a tungsten wire (World Precision Instruments, Inc.). Two tungsten wires were etched at 30 V in 1 M KOH water solution, and immersed in ethanol and dried under nitrogen, in order to transfer the adhesive (glue) and single fibres in two separated steps. First, a small drop of UV-cured glue (Optical Adhesive 81, Norland Products, Inc.) was deposited on the cantilever (Fig. 1a). Then, a single fibre was transferred (via capillary condensation between the fibre and wire) from mica substrate to the cantilever and precisely positioned, i.e. symmetrically at the end of the cantilever (Fig. 1b-c). Prepared cantilevers were photocured using high intensity UV lamp (Hamamatsu LC8, type 02A) for 6 minutes in air. The quality of the modified cantilevers was carefully checked by optical imaging. On the one hand, the amount of glue was large enough to hold the fibres property during the adhesion studies, on the other hand, small enough to do not contaminate the contacting – in the crossed fibre adhesion experiments – part of the fibre.

To prepare samples, aramid fibres were cut by a scalpel and dropped on a support. The support contained the silicon wafer with epoxy glue that was (intentionally) partly cured to fix the fibres on the surface but to avoid getting them drown. Randomly distributed fibres emulated various crossing angles in the AFM experiment. We paid attention that the number of dropped fibres is small enough to avoid crossed, a thus tilted, fibres. However, the studied crossed-cylinder geometry is a “self-adjusting” system; a possible tilt of a fibre shall not influence the interaction geometry.

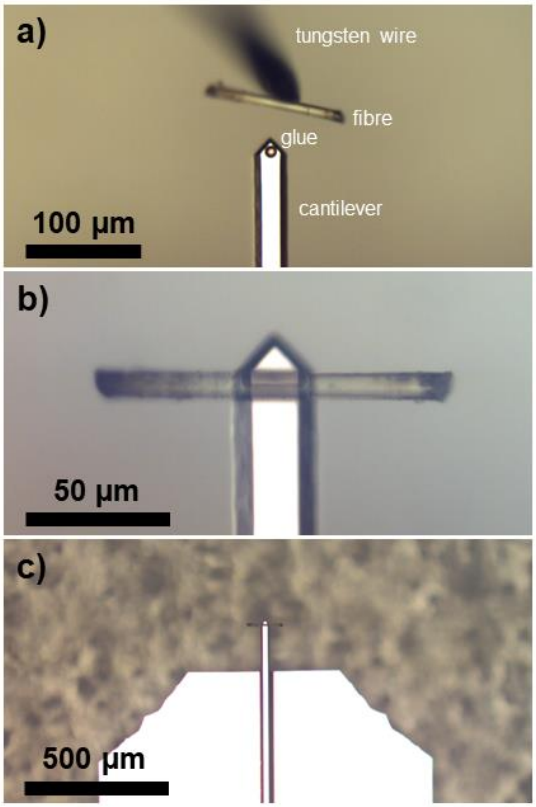

Figure 1 Modified cantilever attached with Twaron® aramid fibre using micromanipulator: (a) a fibre being transferred to the cantilever and (b, c) fixed at its final position by the UV-cured glue.

2.3 Control of relative humidity

A home-made humidity chamber (Perspex) was implemented to the AFM station. To adjust the relative humidity, a stream of (pure) N_2 and N_2 saturated with water vapor were mixed and directed to the chamber. The saturated vapor is obtained by N_2 bubbles through a *frit* (glass tube) into water. The streams are controlled mechanically via valves. The humidity sensor is placed inside the chamber, close the AFM head, for monitoring the relative humidity during the experiments. At each humidity the system was left free for about 10 min to stabilize the RH value.

2.4 AFM experimental setup and cantilever calibration

The adhesion force measurements were carried out using Multimode 8 AFM retrofitted with Nano Scope V controller and JV scanner (Bruker). An illustration of the experimental setup can be found in Fig. 2. The deflection sensitivity of the modified cantilevers was measured on a rigid sample (Piranha cleaned silicon wafer)

and ranged from 73.8 - 105.0 nm/V from one. The cantilever spring constant was measured by the thermal tune method and ranged from 2.52 – 3.23 N/m [18]. We did not correct this value due to a possible off-end loading effect [19], because all the fibres were located almost at the very end of the rectangular part of cantilevers, where an AFM tip normally sits as well in the tip-containing cantilevers. However, we estimated the uncertainty of cantilever spring determination to be less than 8% for fibres located less than 6 μm off a typical tip position. A standard Force Spectroscopy (FS) mode was operated to bring the fibre in contact and to record force-distance curves. A self-written analysis software was used to calculate the adhesion forces. Typically 200 force-distance curves were recorded at a constant and low unloading rate (ramp frequency of 1 Hz) to avoid adhesion force vs. unloading rate dependence [20] and any kinetic effects on the capillarity formation and rupture [20]. Due to the geometry (relatively high width and low length, resulting in high lateral spring constant) of the cantilever itself, torsional motions during the fibre-fibre interactions were reduced. Additionally, we also paid a lot of attention to the symmetry of the fibre-fibre contact during the experiments to reduce the lateral deflection signal upon the cantilever bending. All measurements were performed in a room temperature of 21°C ± 1°C.

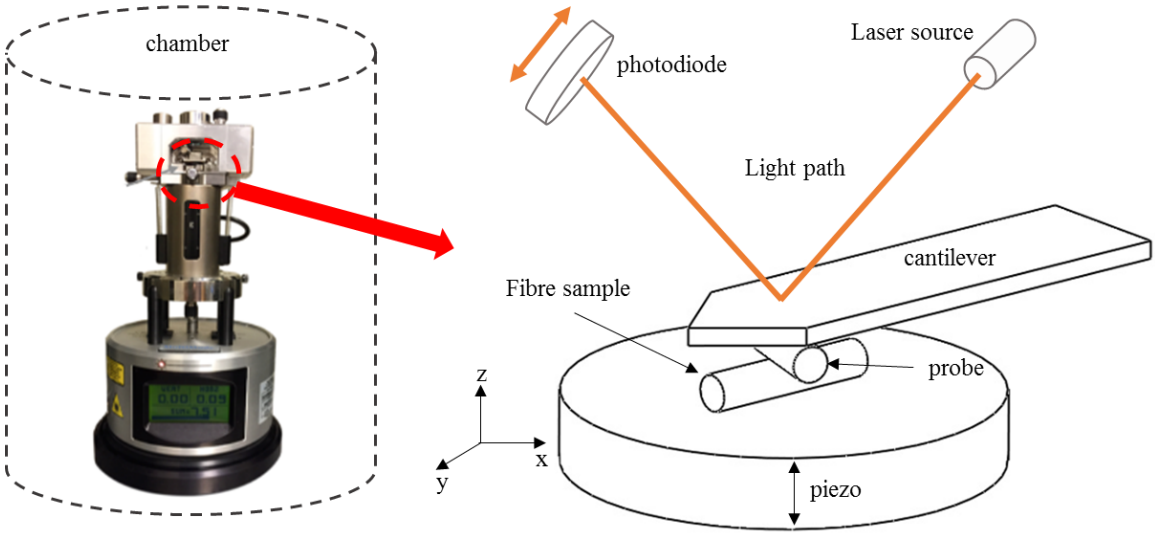

Figure 2 A schematic setup of the crossed fibre-fibre arrangement used in the AFM.

3 Results and discussion

3.1 Force-distance curve

Figure 3 shows a typical force-distance curve obtained between the cantilever-containing fibre and the fibre fixed on the substrate at perpendicular contact at a relative humidity of 70.0%. The dot-line represents the approach trace while the straight-line the retract trace. The minimum in the approach trace indicates the fibre-fibre interactions to be attractive. When the cantilever-containing fibre gets in contact with the fibre on the substrate, both are pressed against each other up to a maximum load of ~ 70 nN, resulting in a decent contacting area. During the cantilever retraction, its detachment is achieved when the spring force overcomes the adhesion force.

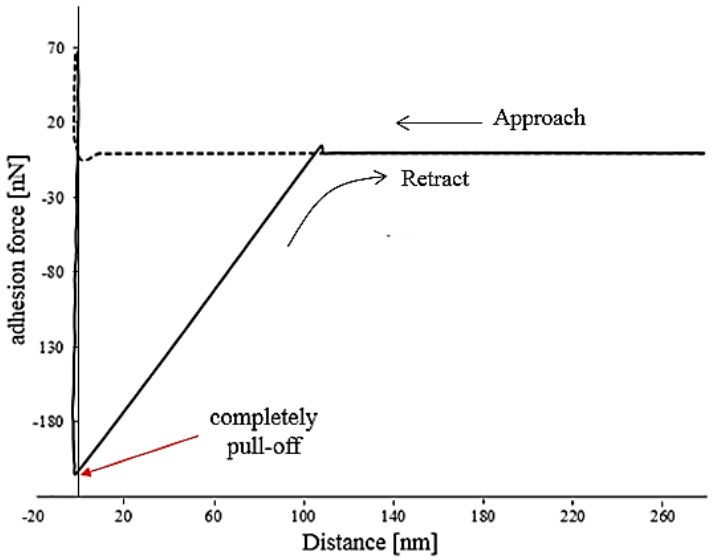

Figure 3 Force-distance curve recorded for crossing aramid fibres at a perpendicular contact at 70% relative humidity.

3.2 The effect of water capillary condensation

According to the literature [21,22], the interaction surfaces of two crossed cylinders at perpendicular contact is equivalent to a geometry of sphere near a flat surface. Derjaguin [23] approximates the effective radius of geometry sphere-sphere by half of the sphere radii, basically originating from the Hertzian theory. In humid conditions, the surface force will be affected by the presence of the water between

the contacting surfaces. The liquid condenses forming a meniscus between the tip and sample surface. The formation of meniscus or capillary neck leads to an attractive force, thus force that need to separate the two fibres in contact is dominant by the capillary force. Here, to calculate the capillary force, a sphere-sphere geometry (see Figure 4) is used to formulate the mathematical equations. When the water meniscus arises, the pressure that is generated by the curvature of the meniscus surface can be derived using the Young-Laplace pressure equation [21];

$$P_{cap} = \gamma_L \left(\frac{1}{r_1} + \frac{1}{r_2}\right) \approx \frac{\gamma_L}{r_k} \qquad \text{(Eq. 1)}$$

where γ_L is the liquid surface tension (water) and r_1 and r_2 are curvature radii that defined the curved surface as shown in Figure 4.

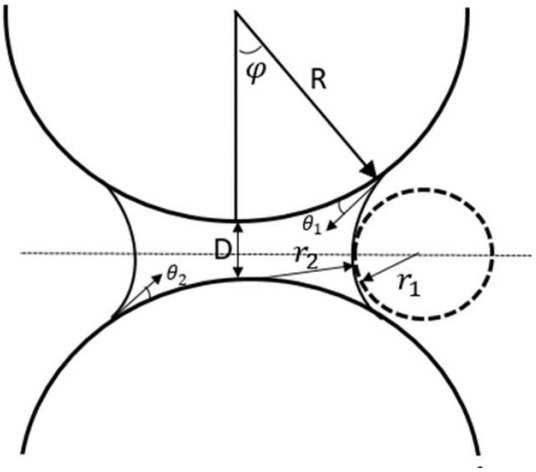

Figure 4 Geometry of the sphere-sphere contact with a meniscus formation [24].

As the RH increases, the amount of liquid in the system increases and, as a result, the meniscus will grow with the increasing of the meniscus radius, r_2. Using the Kelvin equation, the mean radius of curvature of the condensed meniscus or known as *Kelvin radius*, r_k can be calculated by [25]:

$$\left(\frac{1}{r_1}+\frac{1}{r_2}\right)^{-1} = r_k = -\frac{\gamma_L V}{R_g T log\left(\frac{p}{p_s}\right)} \quad \text{(Eq. 2)}$$

where p/p_s is the relative humidity (RH), V is the molar volume, R_g is the gas constant and T is the absolute temperature. For water, γ_L = 73 mJ/m^2 at T = 293K, this gives $\gamma_L V/R_g T$ = 0.54 nm [21]. When the meniscus is in equilibrium, the force acting on the sphere due to meniscus formation is given as [25];

$$F_c = F_s + F_p \quad \text{(Eq. 3)}$$

$$F_p = -P_{cap}\pi({r_2}^2 - a^2) = -\left[-\frac{R_g T}{V_m} log\left(\frac{p}{p_s}\right)\right]\pi(R^2 - sin^2\varphi - a^2) \quad \text{(Eq. 4)}$$

$$F_s = -2\pi\gamma_L r_2 \sin(\theta_1 + \varphi) = -2\pi\gamma_L R \sin\varphi sin(\theta_1 + \varphi) \quad \text{(Eq. 5)}$$

where F_p is the capillary force since the pressure inside the capillary is lower than the pressure in the other vapour phase, F_s is the surface tension force, $\theta_1$is the contact angle, φ is the filling angle and a is the contact radius of the solid-solid contacting surfaces which can be calculated using e.g. Hertz theory [26].

Figure 5 shows a variation in the force measured to separate two single aramid fibres at perpendicular contact as a function of relative humidity, measured from low to high, and *vice-versa*. As a general trend, one can observe that at moderate RH (20 – 50%) the adhesion force shows a *plateau*, with a rather constant value of the adhesion force. At low RH, i.e. below ~ 20%, the adhesion force drops. However, at ~ 50% RH and above, there is a significant increase in adhesion force. Taking into account a noticeable surface roughness of the fibres (see in Figure 6), we can address three regimes as the following [27]:

i. RH below 20%: the interactions are driven by the van der Waals forces with some capillary bridges formed at the outmost fibre asperities. Even at low

relative humidity, a water layer can still be present that allows the formation of capillary bridges.

ii. RH 20-50%: the interactions are driven by capillary bridges that are formed at many asperities. One continuous capillary neck is not formed yet. The van der Waals forces are present; however, the capillary force is already a few times higher than the van der Waals force.

iii. RH above 50%: A continuous capillary neck is formed. The menisci are merged into one apparent capillarity. The adhesion force versus relative humidity relation shows a steep transition and the van der Waals forces can be neglected as significantly screened by capillary forces.

Additionally, the results indicate a loop (hysteresis) in the capillarity above ~ 50% RH. One can attribute this to hysteresis of the water contact angle of the studied fibres [28]. It can be said that for the untreated Twaron® aramid fibre a capillary neck formation is started at about 50% RH. The *Kelvin radius*, r_k is about 2 *n*m, resulting in a significant fibre-fibre interaction transition.

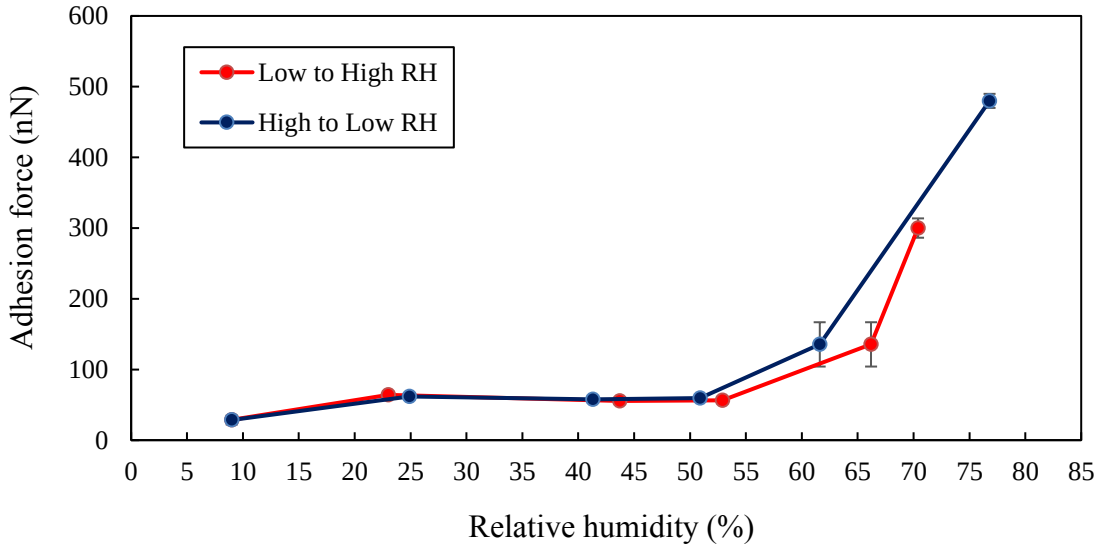

Figure 5 The effect of relative humidity on adhesion force.

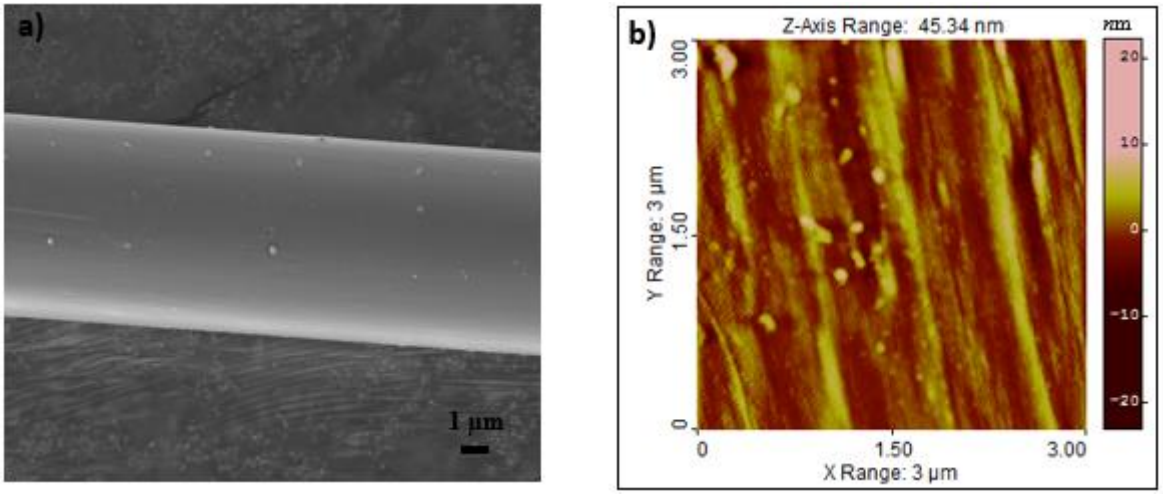

Figure 6 Fibre surface: (a) SEM image (b) roughness measurement with rms ~ 1.6 nm.

It is interesting to compare the adhesion force in a regime where the capillary condensation of the water is maximum. The filling angle φ at 77% RH is calculated implicitly using the Young-Laplace and Kelvin equations along with the geometrical analysis of the sphere-sphere contact as shown in Figure 4 and is given as [25];

$$\frac{\Delta p}{\gamma_L} = \left(\frac{1}{r_1} + \frac{1}{r_2}\right) = -\frac{R_g T}{V_m \gamma_L} log\left(\frac{p}{p_s}\right) \quad \text{(Eq. 6)}$$

$$-\frac{R_g T}{V_m \gamma_L} log\left(\frac{p}{p_s}\right) = \frac{\cos(\theta_1 + \varphi) + cos\theta_2}{D + R(1 - cos\varphi)} + \frac{1}{R\ sin\varphi} \quad \text{(Eq. 7)}$$

Assuming the distance between the spheres, *D* is 0.2 nm, the calculated filling angle at 77% RH is 1.54°. The calculated adhesion force which is dominated by the capillary force is then equal to 6.2 x10^{-7} N while the measured adhesion force is 4.8 x10^{-7} N.

3.3 The effect of crossing angle in dry conditions

To study the effect of the crossing angle on the adhesion force, the measurements were performed in dry conditions or at very low humidity level. At this condition, the van der Waals force is dominant over the capillary force. The test is carried out on randomly oriented fibres in 8% RH. The example of the crossing angle configuration between the modified tip and the fibre sample is shown in Figure 7 (a). The crossing angle is considered as the angle between the fibre that is attached to the tip and fibre sample. Figure 8 shows the adhesion force as a function of the crossing angle. It can be seen that the experimental values of the adhesion force are reduced as the crossing angle between fibres in increased. According to Hertz's contact model [26], when two identical cylinders are brought into contact at 90° with respect to each other, the geometrical shape of the contact area would be circular and if the cylinders are parallel to each other, the contact zone would take a rectangular shape. However, if the cylinders are brought into contact at different angles within the limits above, the contact area is expected to have an elliptical shape as in Figure 7 (b). Within these limits, the adhesion increases as the contact area increase i.e. the crossing angle reduces [6]. Thus, in this study it is assumed that the crossing angle will change the contact area of the fibre-fibre contact interface and consequently influence the adhesion force. The physical contact behaviour due to the crossing angle is also explained using Johnson-Kendall-Roberts (JKR) adhesive contact model [7]. An important result of the JKR model is that it predicts a finite contact area between surfaces under zero normal load. This area can be calculated as follows [7];

$$A_{JKR} = \pi\left(\frac{3R}{4E^*}\right)^{2/3}\left(N + 3\pi\Delta\gamma R + \sqrt{6\pi\Delta\gamma RN + (3\pi\Delta\gamma R)^2}\right)^{2/3} \qquad \text{(Eq. 8)}$$

where R is the fibre radius, E^* is the contact modulus, N is the normal load and $\gamma\Delta$ is the work of adhesion between fibres. The JKR model assumes the adhesive forces are confined inside the contact area and thus the adhesion force at point contact ($\theta = 90°$) can be calculated using the following equation [7]:

$$F_a = \frac{3}{2}\pi\Delta\gamma R \quad \text{(Eq. 9)}$$

where $\Delta\gamma$ is the work of adhesion and R is the relative radius. For an elliptical contact ($0° < \theta < 90°$), Johnson and Greenwood [18] have extended the JKR for a point contact theory to the general elliptical adhesive contact model. In this model, the assumption is made that the contact area remains elliptical, but the eccentricity varies continuously with load. The adhesion force is substantially less than the value for a point contact and can be calculated as follows [18];

$$F_a = 2\pi ab\left[P_1 - \frac{1}{3}(\alpha a^2 + \beta b^2)\right] \quad \text{(Eq. 10)}$$

where P_1 is the pressure distribution (Eq. 11), α and β are the coefficient in pressure (Eq. 12) and a is the mean radius for an elliptical adhesive contact (Eq.13).

$$P_1 = \frac{\alpha a^{5/2} - \beta b^{5/2}}{a^{1/2} - b^{1/2}} \quad \text{(Eq. 11)}$$

$$\alpha = \frac{E^*}{2bR_e}\alpha' \text{ and } \beta = \frac{E^*}{2bR_e}\beta' \quad \text{(Eq. 12)}$$

$$a^{2/3} = 2R_e\sqrt{\frac{2\Delta\gamma}{\pi E^*}}\frac{(b/a)^{\frac{1}{2}}(1-(b/a)^{\frac{1}{2}})}{\beta'(b/a)^2 - \alpha'} \quad \text{(Eq. 13)}$$

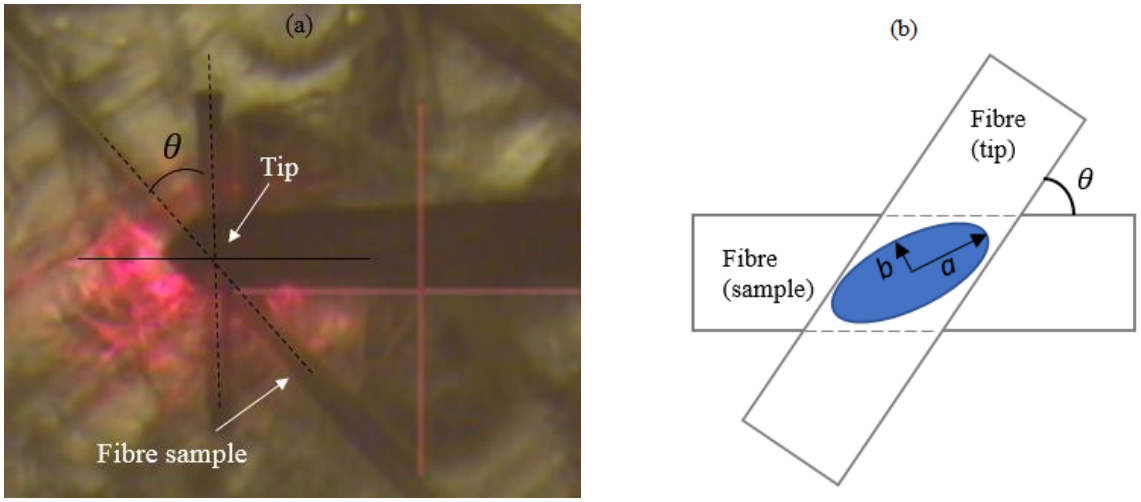

Figure 7 Fibre-fibre contact (a) Crossed fibre arrangement (b) Geometrical contact area shape.

Using the JKR elliptical contact model above, the calculated and measured adhesion force are plotted in Figure 8. Result from the calculation model shows the same trend as the experimental value in the sense that the adhesion force is reduced as the crossing angle is increased. The contact area of the ellipse reduces as it goes from slimly elliptical (30°) to circular (90°) contact. Note that, the adhesion force measured is approximately 2.5 times less than the value of the calculated model. One possible reason to explain this difference is the physical properties of the fibre surface. Note that in JKR model, the solid surface is considered to be smooth. However in real measurement, the surface of the fibre have a certain roughness. As result, when two fibre surfaces get into contact, the real contact is only established at asperities which can drastically reduce the adhesion force. The influences of surface roughness have been reported in [4] and in a study on a glass sphere found that the adhesion force is decreased by a factor of 5 if the roughness is changed from 0.17 nm to 1.6 nm [29].

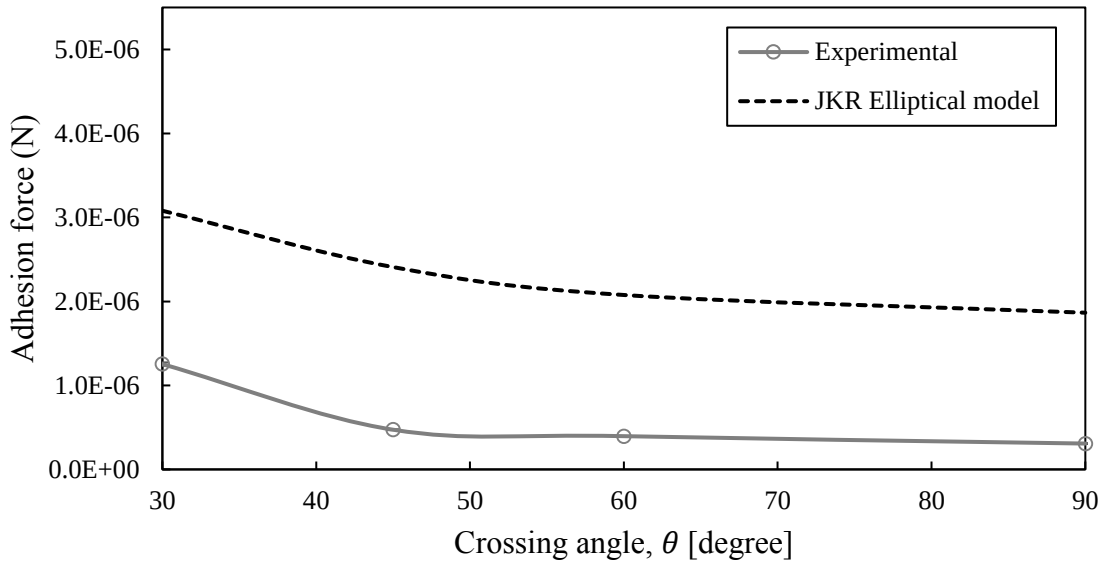

Figure 8 The effect of crossing angle on the adhesion force at 8%RH.

Also, a similar test has been carried out under ambient conditions at a relative humidity of nearly 40% RH. Then, the influence of water capillary condensation on the adhesion force at different the crossing angles will be investigated. Figure 9 shows the measurement results of two different samples tested at different crossing angles. Results show that the adhesion force is decreasing at around 30° to 40°.

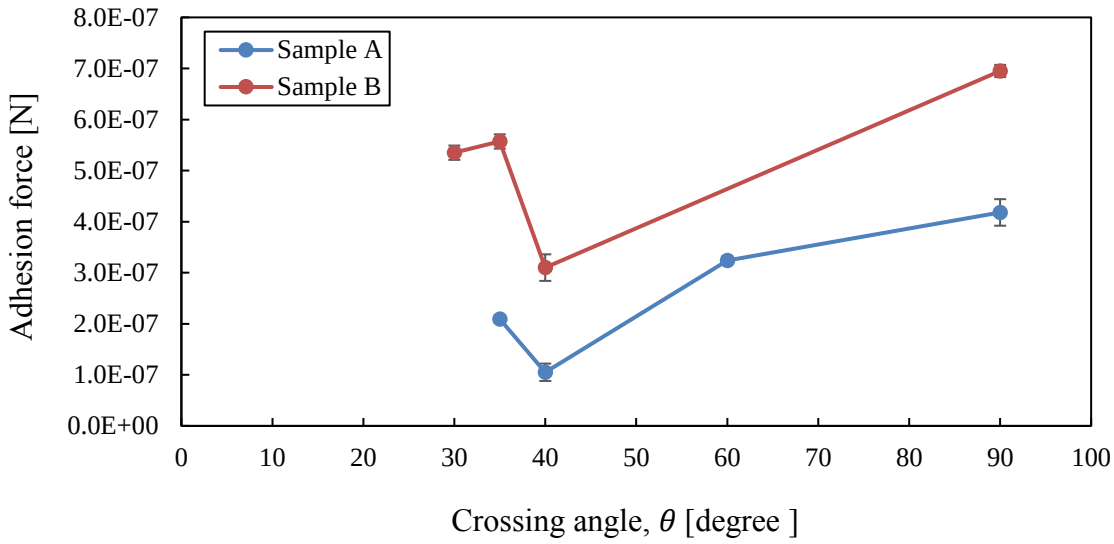

Figure 9 The effect of crossing angle on the adhesion force at 40% RH.

At crossing angles higher than 40°, the adhesion force shows an increase with increasing crossing angle. So, interestingly, the adhesion force is found to be minimum at around 40° crossing angle. This condition can be explained by the influence of the capillary torque that is induced when there is a capillary neck or meniscus bridges at two angle-position filaments [30]. In numerical studies, Bedarkar and Wu [30] and Soleimani et al. [31] have shown that at around 45° crossing angle, the capillary torque is maximum as the contact tends to rotate due to the distort shape of the capillary neck between the contact. So, this will reduce the force that need to separate the contact in normal direction that is the adhesion force.

4 Conclusions

This study is related to the measurement of the adhesion force between two single aramid fibres. A tipless AFM cantilever was functionalized by attaching a non-treated Twaron® aramid fibre. The adhesion force measurements on a fibre-fibre contact were performed at various relative humidity levels and fibre crossing angles. At 90° crossing angle, the effect of relative humidity on the adhesion force was first studied. The adhesion force is low below 20% RH, at moderate 20-50% RH, and reveals a steep transition above 50% RH due to an interplay of the capillary bridges at the asperities of the fibres. It is assumed that the capillary neck is formed at about 50% RH and the capillary force dominates the adhesion. At 77% RH, the measured adhesion force is compared with the Young-Laplace and Kelvin equations. It is found that the measured adhesion force is in the same order of magnitude as the calculated adhesion force. In dry conditions, the effect of crossing angle on adhesion force is also studied. The experimental results are compared with the JKR adhesive elliptical contact model. Results show the adhesion force obtained from the model is 2.5 times higher than the measured adhesion force values. We address the differences to be due to the fibre surface roughness. Meanwhile, in ambient conditions (~40% RH), the adhesion force is found to be minimum at 40-45°crossing angle due to the maximum capillary torque.

Acknowledgement

The authors would like to thank Universiti Teknikal Malaysia Melaka and Ministry of Education Malaysia for financial support of the first author and Teijin Aramid B.V, The Netherlands for supplying the material.

References

[1] Qiang S, Shing-Chung W, Wei Y, Jianwen H, Jie Z, Jinghua Y. Mechanism of Adhesion between Polymer Fibers at Nanoscale Contacts. Langmuir 2012; 28; 4663−4671.

[2] Bhatia A. Electrical electronics insulation conference, and electrical manufacturing & coil winding conference proceedings 1995; 409–410.

[3] Hao W. Yao X. Ke Y. Ma Y. Li F. Experimental characterization of contact angle and surface energy on aramid fibers. J Adh Sci and Tech 2013; 27(9): 1012-1022.

[4] Butt H-J, Kappl M. Normal capillary forces. Advances in Colloid and Interface Science 2009; 146; 48-60.

[5] Butt H-J, Kappl M. Surface and interfacial force. Wiley-VCH Berlin. 2010.

[6] Sumer B. Onal CD. Aksak B. Metin S. An experimental analysis of elliptical adhesive contact. J App Phys 2010; 11(107); 1-7.

[7] Johnson KL, Kendall K, Robert AD. Surface energy and the contact of elastics solids. in Proc Roy Soc Lond. Series A, Math and Phys Sci, 1971; 324(1558); 247-390.

[8] Derjaguin, B. V.; Muller, V. M.; Toporov, Y. P. Effect of contact deformations on the adhesion of particles. J. Colloid Interface Sci. 1975; 53, 314−326.

[9] Briscoe BJ, Kremnitzer SL. A study of the friction and adhesion of Polyethylene terephthalate monofilaments. J Phys D: App Phys 1979; 5:505-516.

[10] Ducker WA. Senden TJ. Pashely RM. Direct measurement of colloidal forces using an atomic force microscope. Nature 1991; 353; 239-241.

[11] Huang F, Li K, Kulachenko A. Measurement of interfiber friction force for pulp fibers by atomic force microscopy. J Mater Sci 2009; 44; 3770-3776.

[12] Max E, Hafner W. Bartels FW, Sugiharto A, Wood C, Fery A. A novel AFM based method for force measurements between individual hair strands. Ultramicroscopy 2010; 110; 320-324.

[13] Mizuno H, Luengo GS, Rutland MW. Interactions between Crossed Hair Fibers at Nanoscale. Langmuir 2010; 26(24); 18909-18915.

[14] Zhang Z, Wu C, Chei H, Hou J, Jia J. Friction behavior of nano-textured polyimide surfaces measured by AFM colloidal probe. App Surf Sci 2014; 320; 328-333.

[15] Qiang S, Shing-Chung W, Wei Y, Jianwen H, Jie Z, Jinghua Y. Mechanism of adhesion between polymer fibres at nanoscale contacts. Langmuir 2012; 28; 4463-4671.

[16] Mizuno H. Kiellin M. Nordgren N. Petterson T. Wallqvist V. Fielden M. Rutland MV. Friction measurement between polyester fibres using fibre probe SPM. Aust J Chem 2006; 59(6); 390-393.

[17] Zhang S. Zhang M. Li K. Adhesion force between aramid fibre and aramid fibrid by AFM. Polymer Bulletin 2011; 66(3); 351-362.

[18] Johnson KL. Greenwood JA. An approximate JKR theory for elliptical contacts. J Phys D: App Phys 2005; 38:1042.

[19] Hutter JL. Bechhoefer J. Calibration of atomic-force microscope tips. Rev Sci Inst 1993; 64; 1868.

[20] Gojzewski H, Kappl M, Kircher G, Koczorowski W, Butt H-G, Ptak A. Nanoadhesion on rigid methyl-terminated biphenyl thiol monolayers: a high-rate dynamic force spectroscopy study. ChemPhysChem 2013; 14; 543-549.

[21] Israelachvili JN, Intermolecular and surface forces, 3rd ed., Academic Press, Burlington, MA, 2011.

[22] Eriksson JC, Ljunggren S. Odberg L. Adhesive forces between fibers due to capillary condensation of water vapor. J Colloid Interface Sci 1992; 152(2); 368-375.

[23] Derjaguin B. Studies on friction and adhesion IV. Theory of the adhesion of small particles. Colloid J 1934; 69(2); 155-164.

[24] Dormann M. Schmid H-J. Simulation of Capillary bridges between particles. Proc Eng 2015:102; 14-23.

[25] Xiao X. Qian Li. Investigation of humidity-dependent capillary force. Langmuir 2000; 16; 8153-8158.

[26] Johnson KL. Contact mechanics. Cambridge Uni Press. 1985.

[27] He M. Blum AS. Aston DE. Buenviaje C. Overney RM. Critical phenomena of water bridges in nanoasperity contacts. J Chem Phys 2001; 114(3):1355-1360.

[28] De Souza EJ. Gao L. McCarthy TJ. Arzt E. Crosby AJ. Effect of contact angle hysteresis on the measurement of capillary forces. Langmuir 2008; 24(4); 1391-6.

[29] Rabinovich YI. Alder JJ. Ata A. Singh RK. Moudgil BM. Adhesion between nanoscale rough surfaces II. Measurement and comparison with theory. J Colloid Interface Sci 2000; 232; 17-24.

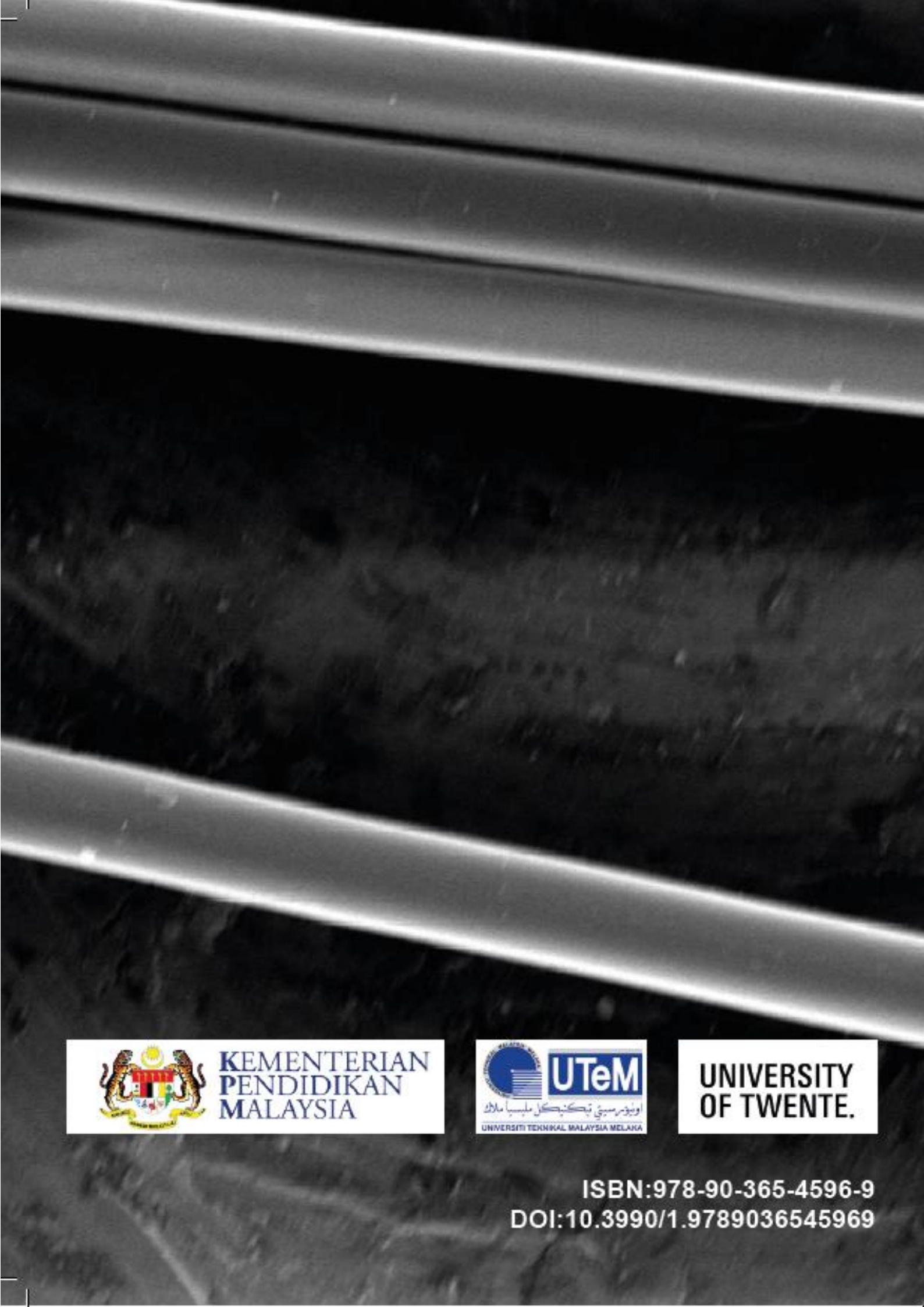

ISBN:978-90-365-4596-9
DOI:10.3990/1.9789036545969